Efficient asymptotic preserving schemes for BGK and ES-BGK models on cartesian grids




PhD Thesis in Fluid Dynamics and Applied Mathematics

Politecnico di Torino
Department of Mechanical and Aerospace Engineering

University of Bordeaux
Bordeaux Institut of Mathematics and INRIA Bordeaux Sud-Ouest, Team MEMPHIS

Efficient Asymptotic Preserving Schemes for BGK and ES-BGK models on Cartesian Grids

Author:
Florian Bernard

Supervisors:
Prof. Gabriella Puppo
Prof. Angelo Iollo

Examining committee

Prof. Domenic D'Ambrosio	Professor	Politecnico di Torino
M. Thierry Goudon	Senior Research Scientist	INRIA Sophia Antipolis
Prof. Luc Mieussens	Professor	University of Bordeaux
Prof. Alberto Milazzo	Professor	University of Palermo
Prof. Giovanni Russo	Professor	University of Catania

March 9th, 2015

"La semplicità è la più grande sofisticatezza"

— Leonardo da Vinci

Acknowledgement

I would like to first thank the people that gave me the opportunity of doing this PhD thesis, my supervisors Gabriella Puppo and Angelo Iollo. It was a great pleasure to work with these two nice people and to learn from them along these three years.

This PhD thesis wouldn't have been possible without the financial support of the French-Italian University and the "Cluster of Excellence" CPU, so I want to mention them.

Thanks to the commission and in particular Thierry Goudon and Giovanni Russo who have accepted to review my thesis.

A special acknowledgement goes to Optimad Engineering and all the people there for supporting me during my time in Italy. They also helped me a lot to go through this PhD and in particular to learn a bit of Italian and I know it wasn't always easy! It was a great pleasure to have shared this memorable experience with all of you and I'll hope it is just the beginning...

All the people from IMB also deserve their spot in this part for having shared so many lunches and breaks with me around the coffee machine (even when it didn't work...)! Thank you to all the former MC2 team, the MEMPHIS and MONC teams, the PhD students and post-docs. The atmosphere in the new corridor is really enjoyable and stimulating. I have of course a special thought for the people that shared my office and supported my mood reactions against my code (that might come from my Italian company...)!

I also have to thank all my friends outside IMB, from Bordeaux, Normandy or other places. You were a refreshing air and you were always available when I needed it especially for having "a" drink or being part of my travelling craziness.

Finally, the last but not the least support, my family and in particular my parents. You trusted me along all these years and gave me the opportunity of studying until my PhD. Thank you very much for always being here and helpful. Thank you to all my family for the moral support, the last years were not so easy and I wish some persons were still here to see the end of this part of my life.

UNIVERSITÉ FRANCO ITALIENNE | UNIVERSITÀ ITALO FRANCESE

OPTIMAD ENGINEERING

Contents

List of Symbol

α	Adaptation coefficient
$\mathbf{a}$	Force acting on a particle per unit of mass (acceleration)
δ	Exponent of the viscosity law
D	Drag coefficient
f	Density distribution function
γ	Ratio of specific heats
$\mathcal{G}_f$	Gaussian distribution function
$\mathcal{T}$	Symmetric tensor of the ES-BGK model
$\mathbf{q}$	Heat flux
κ	Heat conductivity coefficient
$\mathbf{m}$	Collisional invariant
λ	Mean free path
$\mathcal{M}$	Molar mass
$\mathcal{R}$	Universal gas constant
M_f	Maxwellian distribution function
m'	Mass of a particle
Ω	Control volume in the one-particle phase space
τ	Relaxation time
ρ	Gas density
$\rho\Theta$	Pressure tensor
σ	Molecule diameter
Θ	Opposite stress tensor
$\mathbf{a}$	Force acting on a molecule per unit of mass (acceleration)
$\mathbf{e}$	Outward pointing normal

$\mathbf{F}$	Force acting on the molecules/particles
$\mathbf{n}_w$	Outward pointing normal to the interface
μ	Gas viscosity
$\mathbf{U}$	Macroscopic velocity of the gas
$\boldsymbol{\xi}$	Microscopic velocity of a molecule
$\boldsymbol{\xi'}$	Microscopic velocity of a particle
$\mathbf{c}$	Peculiar (or thermal) velocity
$\tilde{\Theta}$	Viscous tensor
$\Omega_{\boldsymbol{\xi}}$	Control volume in the velocity space
$\Omega_{\mathbf{x}}$	Control volume in the physical space
$\mathbf{x}$	Space position
D	Number of space dimensions
d	Number of translational degrees of freedom
E	Total energy
k_b	Boltzmann constant
Kn	Knudsen number
M	Mach number
m	Molecule mass
N	Number of molecules
p	Scalar pressure
Pr	Prandtl number
R	Specific gas constant
T	Gas temperature
t	Time variable

Introduction

Context and scope of the study

A common feature of complex flows is the presence of both rarefied and hydrodynamic regimes in the same field. This is particularly true in industry when dealing with vacuum pumps or hypersonic atmospheric re-entry vehicles for instance. For such applications, this crucial effect makes difficult to reproduce experiments in real conditions. This difficulty justify the use of numerical simulations. For example, in vacuum pumps, when the pressure becomes too low, the behaviour of each gas molecule can significantly differ from the average, macroscopic behaviour of the flow due to the large distance between each molecule. This flow regime is qualified as rarefied. On the contrary, when the gas molecules are really close to each other compared to the problem characteristic length, they tends to behave similarly as the macroscopic flow. The flow regime is said hydrodynamic.

Rarefied regimes are more complicated to simulate because more physical phenomena are involved at different scales. For the hydrodynamic regime, considering only the macroscopic scale is enough. But in the rarefied regime, the macroscopic scale can be the consequence of different microscopic states and lead to different solutions over time.

The objective of this work is the simulation of complex rarefied flows with a particular care on the asymptotic behaviour towards the hydrodynamic regime and on the viability of the numerical modeling for realistic test cases. The adaptability of the schemes to High Performance Computing (HPC) is an essential aspect taken into account in order to reduce the computational time requirements for the simulation of complex cases. The numerical schemes and the methods we develop will allow a smooth transition in the solution between the two regimes and have to preserve the correct solution in the limit of the rarefied and the hydrodynamic regimes. In particular, this has to be true even up to the wall of possible immersed bodies. In this PhD thesis, different geometries will be considered going for simple fixed bodies (step, Blunt body) to more complex moving and deformable structures. Thus, we will also focus on the ability of the numerical methods further developed to handle these phenomena.

In particular, we will devote our investigation to two relevant industrial problems: the particle dynamics in a nozzle plume of a satellite thruster in a rarefied environment and a re-entry capsule. The case of the nozzle plume has been investigated by [39] and shows that after firing, particle dust pollutes a collar even in front of the nozzle (see figure 1). In a real environment, this phenomenon implies a pollution of optical devices (lenses, mirrors or solar panels) carried by the satellite. It is the first time this problem is faced from a numerical point of view. For this special test case, the numerical model and the numerical method should describe correctly the hydrodynamic regime as well as the rarefied regime even in the same field. All the schemes and methods presented and the coupling the gas flow model with a particle transport model have been fully developed in this work and implemented in a numerical simulation code.

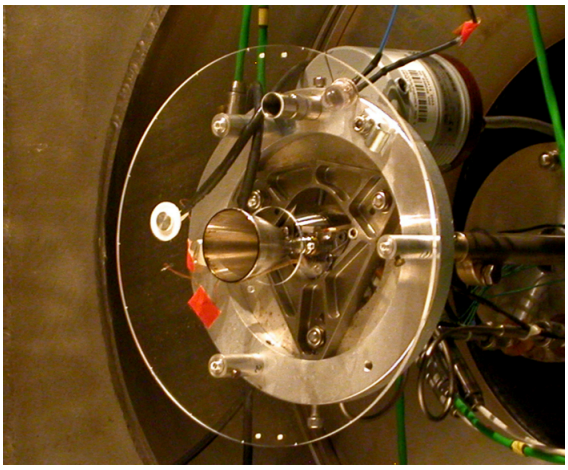

(a) Clean collar (before firing).

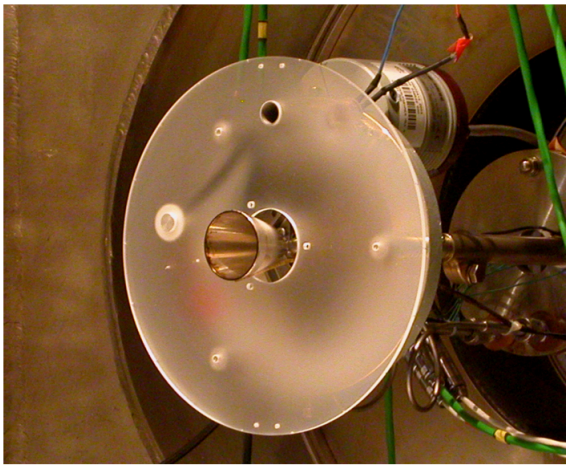

(b) Contaminated collar (after firing).

Figure 1: Effect of nozzle plumes in rarefied environment (extracted from figure 12 in [39]).

Numerical modelling

The specificity of such flows is that classical fluid dynamics equations such as *Navier-Stokes equations* or *compressible Euler equations*, cannot describe properly the flow dynamics. Considering the behaviour of each gas molecules is out of reach because of the computational requirements. Hence one can adopt a statistical point of view of the thermodynamic state of the gas molecules. The resulting equation is known as the *Boltzmann equation* and is valid for both rarefied and hydrodynamic regimes. Because this equation is more general than macroscopic models, it is more complex and makes its resolution very challenging.

The Boltzmann equation considers a statistical description of the gas through a distribution function of the gas molecules. It considers two physical phenomena: mass conservation in phase space and collisions between the molecules. Mass conservation is ensured at the continuous level through the introduction of the microscopic velocities of the gas molecules as independent variables. It implies that the distribution function has six variables in the phase space in 3D (three in the physical space and three in the velocity space). This high dimensionality of the equation and the complexity of the collision term, make the resolution of the Boltzmann equation very heavy. Attempts were made to get the direct numerical solution of the Boltzmann equation [89]. The authors used a Monte Carlo sampling technique to reduce the effort of computing the collision operator. This idea was also developed by Bird to build one of the most popular method used to solve this equation, the Direct Simulation Monte Carlo (DSMC, [16]). The main assumption is an uncoupling between the motion of the gas molecules and the collision process during a small time step. It uses a probabilistic approach where the gas is represented as a set of computational gas molecules. These molecules are moved over a distance according to the time step. The collision process will then act on a set of these particles. Although the molecule movement is easily computed, this method suffer from the same drawback as classical kinetic theory and then, Boltzmann equation. It assumes molecular chaos and cannot be applied for dense gas flows or with a strong limitation on the time step. Moreover, the probabilistic approach can generate stochastic noise. Another possibility to solve the Boltzmann equation

are deterministic models that do not suffer from these drawbacks. In this work, we will focus on two different deterministic models: the BGK model [15] and the ES-BGK model [64], [65]. They are solved with a Discrete Velocity Method (DVM) introducing a discretization of the velocity space. However, the cost is higher than DSMC in the rarefied regime and it would benefit from computational time optimization techniques especially to simulate 3D test cases. In particular, massive parallel computations can significantly reduce the computational time. In this sense, we will develop our schemes on Cartesian grids in order to get the best performance as possible in a HPC environment.

The last problem we face in this work is closely related to the applications we investigate. The simulation of the ejection of incompletely burned particles in a rarefied nozzle plume implies the introduction of a particle transport model.

Organization of the thesis

The PhD thesis is organized as follows. The **first chapter** is devoted to the Boltzmann equation and how it can be derived from molecular dynamics under some particular assumptions. Some important properties are given as well as the models used in this work: the BGK model and the ES-BGK model. They are introduced under their classical form but also under the form implemented in the code.

In **chapter 2**, the discretization is introduced. The numerical schemes in space and time are presented with some classical boundary conditions used. We also introduce the notion of asymptotic preserving schemes which represent a key point of this work.

The first contribution of this work is proposed in **chapter 3**. Standard test cases are used to emphasis the need of a proper treatment of the boundary conditions to preserve the asymptotic limit of the model at the discrete level. A new boundary condition satisfying this requirement is proposed and devised on a Cartesian grid with special care on the accuracy. The method is also applied to moving geometries. Validations in 1D and 2D are presented with respect to analytical solutions. The test case of a nozzle plume in rarefied environment is also investigated and quantitatively compared to experimental results.

Chapter 4 is devoted to techniques improving the computational time required to solve complex test cases. In particular, a local velocity grid approach is presented giving significant reduction of the cost for different test cases in different regimes.

In **chapter 5**, 3D test cases are presented. In particular, the re-entry of an Apollo capsule is simulated.

Finally, in **chapter 6**, a particle transport model is introduced leading to the investigation of particle dynamics in rarefied nozzle plumes. The model is based on experimental observation and a novel method to solve it is proposed. This method is validated with respect to analytical solutions. Results are also compared to experiment qualitatively. Based on these results, preliminary conclusion can be made to explain the phenomenon of the particle pollution around satellite thrusters presented previously.

Chapter I

The Boltzmann Equation

In this chapter, the Boltzmann equation and some related models are presented with important properties that we will use in this work. Section I.1 will focus on a short overview of the derivation of the Boltzmann equation from molecular dynamics. For a complete dissertation on molecular dynamics and collisional models, we refer the reader to [16], [26], [27] or [108]. More details on the theory presented can also be found in [1]. Section I.2 is devoted to the BGK model which is used in the largest part of this work. It is presented in details to clearly fix the notations and the equations that are actually used in the code. The Shakov model is presented in section I.3. Even if this model is not used in this work, it is worth presenting it to show how some drawbacks of the BGK model can be cured easily (even if other properties are lost) and because it is quite used in the literature. Finally, another model of the Boltzmann equation, the ES-BGK model is presented in section I.4 which will be widely used in the numerical results.

I.1 Description and properties of the Boltzmann equation

In this section, we present the Boltzmann equation with some important properties. We first show how the Boltzmann equation can be derived from molecular dynamics concepts and a statistical approach. Important features are then presented with some possible extensions to more complex gases. Here, we use the term *particles* to describe the gas particles that are basically atoms or molecules.

I.1.1 Derivation of the Boltzmann equation

During the XVIIIth century, Daniel Bernoulli first described a gas as a large number of small particles. This idea gave the basis of the kinetic theory of gas. By considering the motion of each particle (atoms or molecules), macroscopic quantities such as temperature, pressure, viscosity or thermal conductivity can be explained. Let us consider a set of N particles with d translational energy degrees of freedom characterized by their mass m_i, their position $\mathbf{x}_i \in \mathbb{R}^D$ (D being the number of space dimensions) and their velocity $\boldsymbol{\xi}_i \in \mathbb{R}^d$. The time evolution of the system according to Newton's law is described in terms of $(D+d)N$ ordinary differential equations. Let $\mathbf{F}_i$ denote the sum of all the forces acting on the i-th particle:

$$\left\{ \begin{array}{l} \dot{\mathbf{x}}_i = \boldsymbol{\xi}_i \\ \dot{\boldsymbol{\xi}}_i = \dfrac{1}{m_i}\mathbf{F}_i \end{array} \right. , i = 1...N \tag{I.1}$$

Considering such an approach for realistic systems requires to solve these equations for an amount of particles around Avogadro's number ($\mathcal{N}_A = 6.022.10^{23}$). It is also necessary to

accurately give the initial conditions for every particle (position and microscopic velocity). This amount of data is prohibitive even for nowadays calculators because of the memory requirements and the computational time. It is also impossible to get the initial data in a practical way for such quantity of particles. Even if it would be possible, the initial data would be hardly accurate and would dramatically impact the whole calculation.

For the above reasons, a statistical approach is more suitable. The underlying idea is to consider a distribution function $f = f(\mathbf{x}, \boldsymbol{\xi}, t)$ that represents the particles density distribution. The number of particles contained in a volume $[\mathbf{x}, \mathbf{x} + d\mathbf{x}]$ that have a velocity in $[\boldsymbol{\xi}, \boldsymbol{\xi} + d\boldsymbol{\xi}]$ at time t can be expressed as:

$$\delta n = N f(\mathbf{x}, \boldsymbol{\xi}, t) d\mathbf{x} d\boldsymbol{\xi} \tag{I.2}$$

Let us now consider a control volume $\Omega = \Omega_{\mathbf{x}} \times \Omega_{\boldsymbol{\xi}} \subseteq \mathbb{R}^{D+d}$. To derive the equation for the time evolution of f, we only consider binary collisions (diluted gas assumption) and that mass, momentum and kinetic energy are conserved during each collision. We assume also that the external forces do not depend on the microscopic velocity. Then, the time variation of the number of particles in Ω is due to:

1. the flux of particles with velocity $\boldsymbol{\xi}$ through the boundary surfaces of $\Omega_{\mathbf{x}}$
2. the flux of particles in Ω of which microscopic velocities have been modified by the external forces (flux through the boundary surfaces of $\Omega_{\boldsymbol{\xi}}$).
3. collisions that modify the microscopic velocities of a particle with $\boldsymbol{\xi}$ initially in $\Omega_{\boldsymbol{\xi}}$

Then, with (I.1)

$$\frac{d}{dt}\int_{\Omega} N f(\mathbf{x}, \boldsymbol{\xi}, t) d\Omega + \int_{\Omega_{\boldsymbol{\xi}} \cup \delta\Omega_{\mathbf{x}}} \boldsymbol{\xi} \cdot \mathbf{e}_{\mathbf{x}} f d\Omega + \int_{\Omega_{\mathbf{x}} \cup \delta\Omega_{\boldsymbol{\xi}}} \frac{1}{m} \mathbf{F} \cdot \mathbf{e}_{\boldsymbol{\xi}} f d\Omega = \int_{\Omega} N Q(f, f) d\Omega \tag{I.3}$$

where the right hand side represents the gain of particles in Ω due to the collisions. $\mathbf{e}_{\mathbf{x}}$ and $\mathbf{e}_{\boldsymbol{\xi}}$ are respectively the outward pointing normal to $\Omega_{\mathbf{x}}$ and $\Omega_{\boldsymbol{\xi}}$. Q is an operator that depends on the distribution function and represents locally the effects of the interaction between the gas particles. Let us consider the following hypothesis:

Binary collisions. The gas is considered diluted enough to have only binary collisions. In other words, collisions cannot involve more than two particles at a time. It means that the diameter of the particles is considered much lower than the mean free path between the particles. If n_{loc} is local density of gas particles of diameter σ, we have:

$$n_{loc}\sigma \ll 1$$

Localised collisions in space and time. This hypothesis considers that the characteristic time of the collisions is much lower than the characteristic time of the flow. Thus, the collisions are localised in a position $\mathbf{x}$ at a time t.

Molecular chaos. It means that the velocity of two particles are not correlated. The joint probability density function of a particle that has velocity $\boldsymbol{\xi}$ and a particle that has velocity $\boldsymbol{\xi}_\star$ is the product of the distribution function f in $\mathbf{x}$ for the two microscopic velocities $\boldsymbol{\xi}$ and $\boldsymbol{\xi}_\star$:

$$f^{(2)}(\mathbf{x}, \boldsymbol{\xi}, \mathbf{x}_\star, \boldsymbol{\xi}_\star, t) = f(\mathbf{x}, \boldsymbol{\xi}, t) f(\mathbf{x}_\star, \boldsymbol{\xi}_\star, t)$$

where $f^{(2)}(\mathbf{x}, \boldsymbol{\xi}, \mathbf{x}_\star, \boldsymbol{\xi}_\star, t)$ is the probability of finding a particle in $\mathbf{x}$ at velocity $\boldsymbol{\xi}$ at time t and a particle in $\mathbf{x}_\star$ at velocity $\boldsymbol{\xi}_\star$ at the same time.

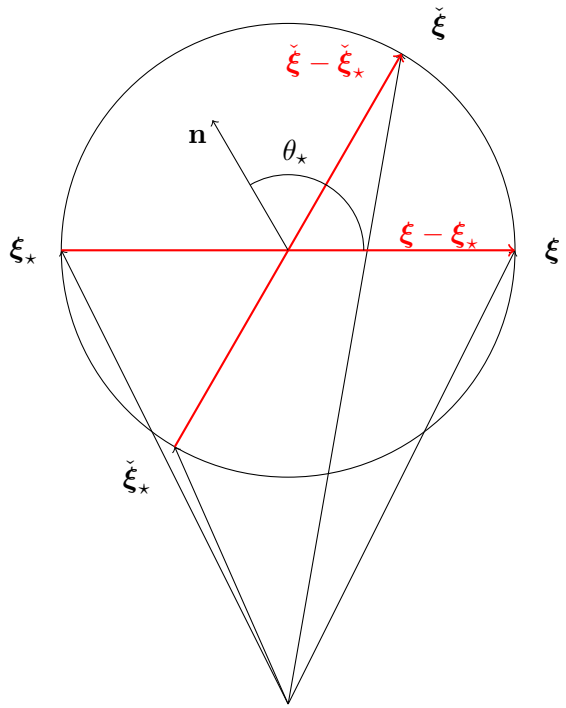

Figure I.1: Parametrization of the cross section

Elastic collisions. We consider that the momentum and kinetic energy are conserved. With a constant mass for the particles with $\boldsymbol{\xi}$ and $\boldsymbol{\xi}_\star$ the pre-collisional velocities and $\check{\boldsymbol{\xi}}$ and $\check{\boldsymbol{\xi}}_\star$ the post-collisional velocities:

$$\boldsymbol{\xi} + \boldsymbol{\xi}_\star = \check{\boldsymbol{\xi}} + \check{\boldsymbol{\xi}}_\star \tag{I.4}$$
$$|\boldsymbol{\xi}|^2 + |\boldsymbol{\xi}_\star|^2 = |\check{\boldsymbol{\xi}}|^2 + |\check{\boldsymbol{\xi}}_\star|^2 \tag{I.5}$$

We then have

$$|\boldsymbol{\xi} - \boldsymbol{\xi}_\star| = |\check{\boldsymbol{\xi}} - \check{\boldsymbol{\xi}}_\star|$$

From these expressions it is possible to express the velocities after the collision depending on the velocities before the collision and a parameter $\mathbf{n} = \frac{\boldsymbol{\xi} - \check{\boldsymbol{\xi}}}{|\boldsymbol{\xi} - \check{\boldsymbol{\xi}}|}$ (see figure I.1) such that:

$$\begin{cases} \check{\boldsymbol{\xi}} = \boldsymbol{\xi} + (\boldsymbol{\xi}_\star - \boldsymbol{\xi}) \cdot \mathbf{n})\mathbf{n} \\ \check{\boldsymbol{\xi}}_\star = \boldsymbol{\xi}_\star - (\boldsymbol{\xi}_\star - \boldsymbol{\xi}) \cdot \mathbf{n})\mathbf{n} \end{cases}$$

It is then possible to obtain the scattering cross section $s(|\boldsymbol{\xi} - \boldsymbol{\xi}_\star|, \theta_\star)$ depending on the two pre-collisional velocities and the deflection angle $\theta_\star$ for a given collisional model (Hard Sphere, Variable Hard Sphere, Maxwellian molecules). The scattering cross section s gives the probability of the collision between particles that have $\boldsymbol{\xi}$ and $\boldsymbol{\xi}_\star$ as microscopic velocity. We also mention that other parametrizations are possible. For more details on the calculation of the scattering cross section for different collisional models, we refer the reader to [1], [26].

Collision micro-reversibility. This hypothesis implies that the probability for a couple of particles that have velocities $(\boldsymbol{\xi}, \boldsymbol{\xi}_\star)$ to collide and have resulting velocities $(\check{\boldsymbol{\xi}}, \check{\boldsymbol{\xi}}_\star)$ is the same as the probability for a couple of particles that have velocities $(\check{\boldsymbol{\xi}}, \check{\boldsymbol{\xi}}_\star)$ to collide and have resulting

velocities $(\boldsymbol{\xi}, \boldsymbol{\xi}_\star)$.

Considering these previsou five hypothesis, we can then give an expression for the collision operator $Q(f, f)$ [27]:

$$Q(f,f)(\mathbf{x},\boldsymbol{\xi},t) = \int_{\mathbb{R}^3}\int_{\mathbb{S}^2} (\check{f}\check{f}_\star - f f_\star) s(|\boldsymbol{\xi}-\boldsymbol{\xi}_\star|,\theta_\star)|\boldsymbol{\xi}-\boldsymbol{\xi}_\star| d\mathbf{n} d\boldsymbol{\xi}_\star \tag{I.6}$$

where $\mathbf{n}$ is the parameter giving the post-collisional velocities from the pre-collisional velocities defined previously and $\check{f}_\star = f(\mathbf{x}, \check{\boldsymbol{\xi}}_\star, t)$ with equivalent notation for $f_\star$ and $\check{f}$.

By assuming the control volume to be time independent and because $\mathbf{a} = \frac{1}{m}\mathbf{F}$ does not depend on $\boldsymbol{\xi}$, the equation (I.3) can be recast as:

$$\int_\Omega N[\frac{\partial f}{\partial t} + \boldsymbol{\xi}\cdot\nabla_{\mathbf{x}} f + \mathbf{a}\cdot\nabla_{\boldsymbol{\xi}} f] d\Omega = \int_\Omega N Q(f,f) d\Omega \tag{I.7}$$

Finally, we will consider the mass density distribution function defined as: $\hat{f} = mNf$ and $\hat{Q}(\hat{f},\hat{f}) = Q(f,f)$. Since (I.7) holds for each control volume Ω, a minimum requirement of smoothness on f implies that ($\hat{}$ are dropped for simplicity):

$$\frac{\partial f}{\partial t} + \boldsymbol{\xi}\cdot\nabla_{\mathbf{x}} f + \mathbf{a}\cdot\nabla_{\boldsymbol{\xi}} f = Q(f,f) \tag{I.8}$$

Equation (I.8) is known as the *Boltzmann equation* named after Ludwig Eduard Boltzmann, the Austrian physicist who devised it in 1872.

I.1.2 Properties of the Boltzmann equation

I.1.2.1 Macroscopic quantities

When simulating a flow, one wants to recover macroscopic quantities such as density, velocity, temperature, energy or pressure. These quantities can be calculated from the Boltzmann equation through the distribution function f. Let us consider $f(\mathbf{x}, \boldsymbol{\xi}, t)$ the mass density distribution function. We have the following properties:

$$\begin{pmatrix} \rho(\mathbf{x},t) \\ \rho(\mathbf{x},t)\mathbf{U}(\mathbf{x},t) \\ E(\mathbf{x},t) \end{pmatrix} = \int_{\mathbb{R}^d} f(\mathbf{x},\boldsymbol{\xi},t)\mathbf{m}(\boldsymbol{\xi}) d\boldsymbol{\xi} \quad \text{with} \quad \mathbf{m}(\boldsymbol{\xi}) = \begin{pmatrix} 1 \\ \boldsymbol{\xi} \\ \frac{1}{2} \mid \boldsymbol{\xi} \mid^2 \end{pmatrix} \tag{I.9}$$

ρ is the density and $\mathbf{U} = (u, v, w)$ is the macroscopic velocity. Here E is the total energy obtained as follows:

$$E(\mathbf{x},t) = \frac{d}{2}\rho(\mathbf{x},t) R T(\mathbf{x},t) + \frac{1}{2}\rho(\mathbf{x},t) \mid \mathbf{U}(\mathbf{x},t) \mid^2 \tag{I.10}$$

with T the temperature and R the specific gas constant. This constant can be expressed with the universal gas constant $\mathcal{R}$ or with the Boltzmann constant k_b:

$$R = \frac{\mathcal{R}}{\mathcal{M}} = \frac{k_b}{m} = \frac{\mathcal{N}_A k_b}{\mathcal{M}}$$

where $\mathcal{M}$ is the molar mass of the gas, m the mass of one molecule and $\mathcal{N}_A$ the Avogadro's number ($\mathcal{N}_A = 6.02214129 \times 10^{23}\ mol^{-1}$). We consider a monoatomic gas for which the ratio of specific heats γ can be calculated as:

$$\gamma = 1 + \frac{2}{d}$$

In the following, $d = 3$ and therefore γ=5/3.

Other macroscopic quantities can be of interest. The stress tensor Θ is linked to the third order moment of the distribution function f while the heat flux $\mathbf{q}$ is calculated as the fourth order moment. If the peculiar velocity $\mathbf{c}$ is defined as $\mathbf{c} = \boldsymbol{\xi} - \mathbf{U}(\mathbf{x}, t)$:

$$\begin{aligned} \Theta(\mathbf{x}, t) &= \frac{1}{\rho(\mathbf{x}, t)} \int_{\mathbb{R}^d} \mathbf{c} \otimes \mathbf{c} f(\mathbf{x}, \boldsymbol{\xi}, t) d\boldsymbol{\xi} \\ \mathbf{q}(\mathbf{x}, t) &= \int_{\mathbb{R}^d} \frac{1}{2} \mathbf{c} \cdot |\mathbf{c}|^2 f(\mathbf{x}, \boldsymbol{\xi}, t) d\boldsymbol{\xi} \end{aligned} \tag{I.11}$$

It is also possible to define the scalar pressure p and the viscous tensor $\tilde{\Theta}$:

$$p = \frac{1}{d} tr(\rho \Theta) \tag{I.12}$$

$$\tilde{\Theta} = pI - \rho \Theta \tag{I.13}$$

I.1.2.2 The collision operator and the $\mathcal{H}$ theorem

The collision operator Q has some interesting properties. During elastic collisions, some quantities are conserved. In particular, if we consider the vector $\mathbf{m}(\boldsymbol{\xi}) = (1, \boldsymbol{\xi}, \frac{1}{2}|\boldsymbol{\xi}|^2)$, it is possible to prove that:

$$\int_{\Omega_{\boldsymbol{\xi}}} \mathbf{m}(\boldsymbol{\xi}) Q(f, f) d\boldsymbol{\xi} = 0 \tag{I.14}$$

The vector $\mathbf{m}(\boldsymbol{\xi})$ is called the vector of collision invariants (see [26]). This property can be used to determine the distribution functions verifying $Q(f, f) = 0$. These functions are the Maxwellian distributions:

$$Q(f, f) = 0 \Leftrightarrow f = A \exp(-C|\boldsymbol{\xi} - B|^2) \tag{I.15}$$

where $A \in \mathbb{R}$, $B \in \mathbb{R}^d$, $C \in \mathbb{R}$ are independent of $\boldsymbol{\xi}$ but are determined uniquely by the macroscopic quantities ρ, $\mathbf{U}$, T. More specifically, we can prove that the Maxwellian distribution minimizes the $\mathcal{H}$-function defined as:

$$\mathcal{H}(f) = \int_{\mathbb{R}^d} f \log f d\boldsymbol{\xi} \tag{I.16}$$

Under the constraints given by the three first moments of the distribution function, the minimum of the $\mathcal{H}$-function is obtained for:

$$M_f[\rho, \mathbf{U}, T] = \frac{\rho}{(2\pi RT)^{d/2}} \exp\Big(- \frac{|\boldsymbol{\xi} - \mathbf{U}|^2}{2RT} \Big) \tag{I.17}$$

in the sense that, given ρ, U , T, let $DH = \{f \geq 0 : \int_\Omega f m(\boldsymbol{\xi}) d\boldsymbol{\xi} = [\rho, U, T]\}$, then $\mathcal{H}(M) = \min_{f \in DH} \mathcal{H}(f)$. This quantity is particularly useful to prove one of the most important results for the Boltzmann equation: the $\mathcal{H}$ theorem.

H-theorem. *Let f be the solution of the Boltzmann equation* (I.8)*. For an isolated ideal gas in a enclosed domain Ω such that:*

$$\int_{\partial\Omega}\int_{\mathbb{R}^d}(\boldsymbol{\xi}-\boldsymbol{u}_b).\boldsymbol{e}flogfd\boldsymbol{\xi}dS=0$$

where $\boldsymbol{u}_b$ is the velocity of the boundaries of Ω and $\boldsymbol{e}$ the outward pointing normal to $\partial\Omega$, the following inequality holds true:

$$\frac{dH}{dt}\leqslant 0$$

where $H[f]=\int_\Omega \mathcal{H}d\Omega$

The proof of this theorem can be found for instance in [1]. The theorem states that the time evolution of the isolated system described by the Boltzmann equation tends to decrease the H-function. In other words, once the minimum of the H-function is reached, the system is at steady state and the $\mathcal{H}$ theorem ensures that the system remains at equilibrium. Since the Maxwellian distribution minimizes the $\mathcal{H}$-function, the $\mathcal{H}$ theorem implies that the Maxwellian is the solution of the space homogeneous problem ($\nabla_{\mathbf{x}}\equiv 0$) once the steady state is reached. For the space non-homogeneous problem, the solution is a relaxation towards an equilibrium varying in time because of the competition between collisions (right hand side of the Boltzmann equation) and the free transport of the particles (left hand side of the Boltzmann equation).

I.1.2.3 The hydrodynamic limit

As the number of particles increases, the behaviour of each particle becomes less significant for the flow and macroscopic models such as compressible Euler equations or Navier-Stokes equations are viable. To know whether or not these models can be used properly, a parameter is introduced named the Knudsen number Kn. It is defined as the ratio between the mean free path between the particles λ and the physical characteristic length of the problem L:

$$Kn=\frac{\lambda}{L} \tag{I.18}$$

Physically, it tells how packed are the particles. If the mean free path is much smaller than the characteristic length of the problem, the number of collisions per unit time is so large that the system reaches equilibrium faster than the transport destroys it. This kind of regime is referred to *hydrodynamic regime* and macroscopic models are valid. Conversely, the *rarefied regime* takes place when the low number of collisions per unit time makes preponderant the molecular transport. The structure of the equilibrium is lost and the macroscopic models cannot represent correctly the phenomena.

Macroscopic equations are recovered from the Boltzmann equation multiplying the equation by the vector $\mathbf{m}(\boldsymbol{\xi})=(1,\boldsymbol{\xi},\frac{1}{2}|\boldsymbol{\xi}|^2)$ and integrating in velocity space:

$$\begin{aligned}
&\frac{\partial\rho}{\partial t}+\nabla_{\mathbf{x}}\cdot\int_{\Omega_{\boldsymbol{\xi}}}\boldsymbol{\xi}fd\boldsymbol{\xi}+\mathbf{a}\cdot\int_{\Omega_{\boldsymbol{\xi}}}\nabla_{\boldsymbol{\xi}}fd\boldsymbol{\xi}=0\\
&\frac{\partial\rho\mathbf{U}}{\partial t}+\nabla_{\mathbf{x}}\cdot\int_{\Omega_{\boldsymbol{\xi}}}\boldsymbol{\xi}\otimes\boldsymbol{\xi}fd\boldsymbol{\xi}+\mathbf{a}\cdot\int_{\Omega_{\boldsymbol{\xi}}}\nabla_{\boldsymbol{\xi}}\boldsymbol{\xi}fd\boldsymbol{\xi}=0\\
&\frac{\partial E}{\partial t}+\nabla_{\mathbf{x}}\cdot\int_{\Omega_{\boldsymbol{\xi}}}\frac{1}{2}|\boldsymbol{\xi}|^2\boldsymbol{\xi}fd\boldsymbol{\xi}+\mathbf{a}\cdot\int_{\Omega_{\boldsymbol{\xi}}}\nabla_{\boldsymbol{\xi}}\frac{1}{2}|\boldsymbol{\xi}|^2fd\boldsymbol{\xi}=0
\end{aligned} \tag{I.19}$$

where ρ, $\mathbf{U}$ and E are defined from (I.9) and property (I.14) is used.

This set of equations describes the evolution of the three first moments of f but it is not in a closed form. Indeed, the convective term depends on the moment of higher order (moment of order i depends on the $(i+1)-th$ moment). However, it is possible to rewrite the system in the following form:

$$\begin{aligned}
&\frac{\partial \rho}{\partial t} + \nabla_{\mathbf{x}} \cdot (\rho \mathbf{U}) = 0 \\
&\frac{\partial \rho \mathbf{U}}{\partial t} + \nabla_{\mathbf{x}} \cdot (\rho \mathbf{U} \otimes \mathbf{U} + pI) = \rho \mathbf{a} + \nabla_{\mathbf{x}} \tilde{\Theta} \\
&\frac{\partial E}{\partial t} + \nabla_{\mathbf{x}} \cdot (\mathbf{U}(E+p)) = \mathbf{a} \cdot \rho \mathbf{U} - \nabla_{\mathbf{x}} \mathbf{q} + \nabla_{\mathbf{x}} (\tilde{\Theta} \mathbf{U})
\end{aligned} \tag{I.20}$$

The above system is similar to compressible Navier-Stokes equations except that it is still not closed. The heat flux vector $\mathbf{q}$ and the viscous tensor $\tilde{\Theta}$ are not expressed in terms of other macroscopic quantities. For example, it is not possible to postulate that the heat flux depends on the gradient of the temperature.

An interesting idea to find the relationship defining the heat flux and the stress tensor is to look at which assumption the density distribution function f must fulfil in order to recover the Navier-Stokes system of equations. To do so, a solution is the use of the Chapman-Enskog expansion [29].

We assume that the distribution function can be expanded as:

$$f = M_f + \sum_{k=1,2,\ldots} (Kn)^k f^{(k)} \tag{I.21}$$

where M_f is the equilibrium function defined by the first three moments of the distribution function and the $f^{(k)}$ are bounded as Kn goes to 0.

For $Kn << 1$, $f \simeq M_f$. It corresponds to a 0-th order expansion. Because of the symmetry of the equilibrium distribution function with respect to $(\boldsymbol{\xi} - \mathbf{U})$, odd moments are zero and then we get the following constitutive relationship:

$$\tilde{\Theta} = 0 \qquad \text{and} \qquad \mathbf{q} = 0 \tag{I.22}$$

The system (I.20) closed with the relations (I.22) gives the compressible Euler equations. If we now keep first order term (terms corresponding to $f^{(1)}$) we get:

$$\begin{aligned}
&\tilde{\Theta}_{i,j} = \mu\left(\frac{\partial \mathbf{U}_i}{\partial \mathbf{x}_j} + \frac{\partial \mathbf{U}_j}{\partial \mathbf{x}_i}\right) - \frac{2}{D}\mu \sum_{k=1,2,..D} \frac{\partial \mathbf{U}_k}{\partial \mathbf{x}_k} \quad i,j = 1,2,..,D \\
&\mathbf{q} = -\kappa \nabla_x T
\end{aligned} \tag{I.23}$$

These expressions used in (I.20) gives the compressible Navier-Stokes equations except that the bulk viscosity is not involved. From this analysis it is also possible to express the heat conductivity κ:

$$\kappa = \frac{15}{4} R\mu \tag{I.24}$$

giving that for a monoatomic gas ($c_p = \frac{5}{2}R$), the Prantdtl number is:

$$Pr = \frac{\mu c_p}{\kappa} = \frac{2}{3} \tag{I.25}$$

Some additional relationship between viscosity, particles cross section can be recovered with the same analysis but won't be discussed here. For more details we refer the reader to [26] or [29].

I.1.3 Extension to more complex gas

The Boltzmann equation as presented previously (I.8) is valid for monoatomic gases (energy degrees of freedom are only translational) and does not consider gas mixtures. Even if such gases are not considered in this work, we briefly give an overview on how this model can be extended to more complex flows. Extending to these cases the numerical methods presented in this thesis is an important perspective.

I.1.3.1 Polyatomic gas

The Boltzmann equation can be extended to the case of diatomic or polyatomic gases by adding degrees of freedom. In (I.8), the mass density distribution function, only considers translational internal energy (microscopic velocity). But in the case of diatomic or polyatomic gases, rotational and vibrational internal energies have to be added. This can be done through a new variable in the distribution function taking into account the internal energy of the molecules. The collision term in the Boltzmann equation is then modified to conserve the total energy (internal energy and kinetic energy) during the collision process. Elastic (each energy is conserved) and inelastic (transfer between the two energies) collision are then distinguished. Polyatomic gas flows can be simulated for instance with the Larsen-Borgnakke model [18].

I.1.3.2 Gas mixture

In the case of gas mixture, different distribution functions f_i are used for each species. The collision operator is also modified as the sum of the collision operators $Q_{i,j}(f_i, f_j)$ between the gas molecules of each species. The conservation relations for mass and energy need to be modified in the case of gas molecules of different mass. We refer the reader to [57] for more details.

I.1.3.3 Granular flows

The kinetic theory and in particular the Boltzmann equation is also widely used for granular flows. These flows are characterized by strong interactions between the particles and mostly determine the dynamics. Example of such flows are found in the simulation of avalanches, sediment transport or in mining operations. Even with a dense flow of particles, the dynamics can be quite different from a fluid flow. In particular, collisions are considered inelastic and the invariant presented in (I.5) are not valid. A restitution coefficient e is added in the parametrization:

$$\begin{cases} \check{\boldsymbol{\xi}} = \boldsymbol{\xi} + \dfrac{1+e}{2}(\boldsymbol{\xi}_\star - \boldsymbol{\xi}) \cdot \mathbf{n})\mathbf{n} \\ \check{\boldsymbol{\xi}}_\star = \boldsymbol{\xi}_\star - \dfrac{1+e}{2}(\boldsymbol{\xi}_\star - \boldsymbol{\xi}) \cdot \mathbf{n})\mathbf{n} \end{cases}$$

The hypothesis of uncorrelated pre-collisional velocities should also be omitted as well as the localised collisions in space. The collisional operator becomes then more complicated to analyse than the classical collisional operator (see [113]). In the case of the Hard Sphere model, the collision operator becomes:

$$\begin{aligned} Q_G(f,f) = & r^2 \int_{\mathbb{R}^3} \int_{\mathbb{S}^2} \Big(\frac{1}{e^2} G(\mathbf{x}, \mathbf{x} - r\mathbf{n}) f(\mathbf{x}, \check{\boldsymbol{\xi}}) f(\mathbf{x} - r\mathbf{n}, \check{\boldsymbol{\xi}}_\star) \\ & - G(\mathbf{x}, \mathbf{x} + r\mathbf{n}) f(\mathbf{x}, \boldsymbol{\xi}) f(\mathbf{x} + r\mathbf{n}, \boldsymbol{\xi}_\star) \Big) |\boldsymbol{\xi} - \boldsymbol{\xi}_\star| d\mathbf{n} d\boldsymbol{\xi}_\star \end{aligned}$$

with r the radius of the particles and G the correlation function such that:

$$f^{(2)}(\mathbf{x}, \boldsymbol{\xi}, \mathbf{x}_\star, \boldsymbol{\xi}_\star, t) = G(\mathbf{x}, \mathbf{x}_\star) f(\mathbf{x}, \boldsymbol{\xi}, t) f(\mathbf{x}_\star, \boldsymbol{\xi}_\star, t)$$

One can note that the case $e = 1$ and $G = 1$ corresponds to the standard collision operator.

We have presented the Boltzmann equation used to simulate flows in the rarefied regime. Unfortunately, simulating the Boltzmann equation as it is written in (I.8) is almost computationally prohibitive for realistic test cases because of the discretization of the collision operator. Direct Simulation Monte Carlo [16] is a very popular method widely used in industry for rarefied flows simulation. It is suitable in the rarefied regime but the cost of the method as we approach the hydrodynamic regime dramatically increases. Since we are interested also in the limit towards the continuous regime, this methods does not seems appropriate to our concerns. However, it is possible to derive approximated models more suitable to computations. In the following, we present three popular deterministic models used in the literature.

I.2 The BGK model

In this section, the BGK model from Bhatnagar, Gross and Krook [15] is presented with some important features. For the sake of completeness and to allow the reader to fully reproduce the numerical results, the BGK model is presented in its dimensionless form. We also describe a procedure to reduce the number of degrees of freedom in one and two dimensions.

I.2.1 The dimensionless BGK model

The BGK model is an approximation of the Boltzmann equation derived under particular assumptions:

(i) the distribution function f is a small departure from the equilibrium distribution function: $f = M + \delta f$.

(ii) the relaxation time τ and the cross section s do not depend on the microscopic velocities

Because of the first assumption, the BGK model is particularly viable for moderate and small Knudsen numbers, in the kinetic regime (roughly $Kn < 1$). As for the Boltzmann equation, the Chapman-Enskog expansion [29] ensures the asymptotic limit towards Navier-Stokes equation for small Knudsen numbers ($Kn \simeq 10^{-3}$) and towards compressible Euler equations for $Kn \to 0$. However, this analysis leads to one of the main drawbacks of this model. The Prandtl number obtained with the BGK model is not correct for a monoatomic gas. The Chapman-Enskog expansion on the BGK model gives a Prandtl number of 1 instead of 2/3 (see (I.25)).

Let us consider that there are no external or internal forces acting on the system so that $\mathbf{a} = \mathbf{0}$ in (I.8). The collision term is linearized around the Maxwellian distribution function and the resulting model is:

$$\frac{\partial f}{\partial t}(\mathbf{x}, \boldsymbol{\xi}, t) + \boldsymbol{\xi} \cdot \nabla_{\mathbf{x}} f(\mathbf{x}, \boldsymbol{\xi}, t) = \frac{1}{\tau}(M_f(\mathbf{x}, \boldsymbol{\xi}, t) - f(\mathbf{x}, \boldsymbol{\xi}, t)) \tag{I.26}$$

where τ is the relaxation time and M_f is the Maxwellian distribution function. It is obtained as follows:

$$M_f(\mathbf{x}, \boldsymbol{\xi}, t) = \frac{\rho(\mathbf{x}, t)}{(2\pi RT(\mathbf{x}, t))^{d/2}} \exp\Big(- \frac{| \boldsymbol{\xi} - \mathbf{U}(\mathbf{x}, t) |^2}{2RT(\mathbf{x}, t)} \Big) \tag{I.27}$$

where R is the specific gas constant and $T(\mathbf{x},t)$, $\mathbf{U}(\mathbf{x},t)$ and $\rho(\mathbf{x},t)$ are macroscopic values of temperature, velocity and density.

The relaxation time for the BGK model can be written as [85]:

$$\tau^{-1} = c_0 \rho T^{1-\delta}$$

where c_0 is a constant that depends on the reference conditions and δ is the exponent of the viscosity law of the gas. The constant c_0 can be expressed as :

$$c_0 = \frac{RT_0^{\delta}}{\mu_0}$$

where μ_0 is the reference viscosity of the gas at the reference temperature T_0.

Let's take the following dimensionless parameters:

$$\hat{t} = \frac{t}{t_0} \quad \hat{\mathbf{x}} = \frac{\mathbf{x}}{L} \quad \hat{\boldsymbol{\xi}} = \frac{\boldsymbol{\xi}}{(RT_0)^{1/2}} \qquad \hat{\mathbf{U}} = \frac{\mathbf{U}}{(RT_0)^{1/2}}$$
$$\hat{\rho} = \frac{\rho}{\rho_0} \quad \hat{T} = \frac{T}{T_0} \quad \hat{f} = \frac{f}{\rho_0/(RT_0)^{d/2}} \quad \hat{M}_f = \frac{\hat{\rho}}{(2\pi\hat{T})^{d/2}} \exp\Big(- \frac{|\hat{\boldsymbol{\xi}} - \hat{\mathbf{U}}|^2}{2\hat{T}} \Big)$$

It leads to the dimensionless form of the BGK equation (hats will be dropped for simplicity):

$$S_t \; \partial_t f + \boldsymbol{\xi}.\nabla_x f = \frac{1}{Kn_\infty} \rho T^{1-\delta} (M_f - f) \tag{I.28}$$

with

$$S_t = \frac{L}{(RT_0)^{1/2} t_0} \qquad Kn_\infty = \frac{\lambda}{L} \quad \text{with} \quad \lambda = \frac{\mu_0}{\sqrt{RT_0}\rho_0} \tag{I.29}$$

S_t is the so-called Strouhal number usually set to 1 (by choosing an adapted time scale) and Kn_∞ is the Knudsen number in reference condition where λ is the mean free path.

One can also define a local Knudsen number which corresponds to the relaxation time in dimensionless form:

$$\frac{1}{\tau} = \frac{1}{Kn_{local}} = \frac{1}{Kn_\infty} \rho T^{1-\delta}$$

I.2.2 BGK reduced model

The multi-dimensionality of the BGK model (and of kinetic models in general) makes the computations very slow. A discretization has to be considered in space and in velocity which makes a six-dimensions problem in 3D plus time. When dealing with 1D or 2D problem, space dimensions can be omitted (2 in 1D and 1 in 2D). The same dimensions can actually be omitted also in velocity by considering a constant macroscopic velocity in these directions which is a viable approximation in most cases. The obtained model is qualified as "reduced model" and is strictly identical to the genuine one. Instead of one distribution function of 4 dimensions in 1D plus time (respectively 5 in 2D), the model uses two distribution functions of 2 dimensions plus in 1D (respectively 4 in 2D). The resulting model is computationally faster and requires less memory. The method to established the reduced model is presented for the BGK model in the 1D and 2D cases. Full details of the calculations are presented in annexe A.

I.2.2.1 1D case

Let's consider the dimensionless BGK model with $S_t = 1$:

$$\frac{\partial f}{\partial t}(\mathbf{x}, \boldsymbol{\xi}, t) + \boldsymbol{\xi} \cdot \nabla_{\mathbf{x}} f(\mathbf{x}, \boldsymbol{\xi}, t) = \frac{1}{\tau}(M_f(\mathbf{x}, \boldsymbol{\xi}, t) - f(\mathbf{x}, \boldsymbol{\xi}, t)) \tag{I.30}$$

A 1D problem is considered so $D = 1$, $\boldsymbol{\xi} = (\xi_u, \xi_v, \xi_w)^T$ and $\nabla_{\mathbf{x}} = (\partial_x, 0, 0)^T$. Equation (I.30) becomes in 1D:

$$\frac{\partial f}{\partial t}(x, \boldsymbol{\xi}, t) + \xi_u \partial_x f(x, \boldsymbol{\xi}, t) = \frac{1}{\tau}(M_f(x, \boldsymbol{\xi}, t) - f(x, \boldsymbol{\xi}, t)) \tag{I.31}$$

In 1D, thanks to the Chu reduction [33], it is possible to reduce the number of independent variables in velocity space. Let:

$$\phi(x, \xi_u, t) = \int_{\mathbb{R}^2} f(x, \boldsymbol{\xi}, t) d\xi_v d\xi_w$$
$$\psi(x, \xi_u, t) = \int_{\mathbb{R}^2} \frac{1}{2}(\xi_v^2 + \xi_w^2) f(x, \boldsymbol{\xi}, t) d\xi_v d\xi_w$$

The 1D reduced model is obtained by multiplying equation (I.31) by function $\mathbf{m}_1(\boldsymbol{\xi}) = (1, \xi_u, \frac{1}{2}|\boldsymbol{\xi}|^2)^T$ and integrating it with respect to ξ_v and ξ_w. Since the macroscopic velocity space has only one dimension:

$$\int_{\mathbb{R}^3} f(\boldsymbol{\xi}) \mathbf{m}_1(\boldsymbol{\xi}) d\boldsymbol{\xi} = \begin{pmatrix} \int_{\mathbb{R}} \phi(\xi_u) d\xi_u \\ \int_{\mathbb{R}} \xi_u \phi(\xi_u) d\xi_u \\ \int_{\mathbb{R}} \frac{1}{2}\xi_u^2 \phi(\xi_u) d\xi_u + \int_{\mathbb{R}} \psi(\xi_u) d\xi_u \end{pmatrix} = \begin{pmatrix} \rho \\ \rho u \\ E \end{pmatrix} \tag{I.32}$$

where the dependence on x and t is dropped for simplicity.

It leads to the 1D reduced model expressed with the two functions ϕ and ψ:

$$\begin{cases} \partial_t \phi(x, \xi_u, t) + \xi_u \partial_x \phi(x, \xi_u, t) = \frac{1}{\tau}(M_\phi(x, \xi_u, t) - \phi(x, \xi_u, t)) \\ \partial_t \psi(x, \xi_u, t) + \xi_u \partial_x \psi(x, \xi_u, t) = \frac{1}{\tau}(M_\psi(x, \xi_u, t) - \psi(x, \xi_u, t)) \end{cases} \tag{I.33}$$

where $M_\phi = \int_{\mathbb{R}^2} M_f d\xi_v d\xi_w$ and $M_\psi = \int_{\mathbb{R}^2} \frac{1}{2}(\xi_v^2 + \xi_w^2) M_f d\xi_v d\xi_w$. In the continuous case, these expressions can be calculated exactly:

$$\begin{cases} M_\phi(\boldsymbol{\xi}) = \dfrac{\rho(x,t)}{\sqrt{2\pi T(x,t)}} \exp\Big(- \dfrac{(\xi_u - u(x,t))^2}{2T(x,t)} \Big) \\ M_\psi(\boldsymbol{\xi}) = \dfrac{(d-1)T(x,t)}{2} \dfrac{\rho(x,t)}{\sqrt{2\pi T(x,t)}} \exp\Big(- \dfrac{(\xi_u - u(x,t))^2}{2T(x,t)} \Big) = \dfrac{(d-1)T(x,t)}{2} M_\phi \end{cases}$$

$u(x,t)$ and $T(x,t)$ are respectively the macroscopic velocity and macroscopic temperature.

I.2.2.2 2D case

In 2D, the same approach can be used multiplying the 2D equation by $\mathbf{m}_2(\boldsymbol{\xi}) = (1, \xi_u, \xi_v, \frac{1}{2}(\xi_u^2 + \xi_v^2))^T$ and integrating it on the third component of the velocity:

$$\phi(x, y, \xi_u, \xi_v, t) = \int_{\mathbb{R}} f(x, y, \boldsymbol{\xi}, t) d\xi_w$$
$$\psi(x, y, \xi_u, \xi_v, t) = \int_{\mathbb{R}} \frac{1}{2}\xi_w^2 f(x, y, \boldsymbol{\xi}, t) d\xi_w$$

This leads to the 2D reduced model expressed with the two functions ϕ and ψ:

$$\begin{cases} \partial_t \phi(X, \boldsymbol{\xi}_2, t) + \boldsymbol{\xi}_2 \cdot \nabla \phi(X, \boldsymbol{\xi}_2, t) = \dfrac{1}{\tau}(M_\phi(X, \boldsymbol{\xi}_2, t) - \phi(X, \boldsymbol{\xi}_2, t)) \\ \partial_t \psi(X, \boldsymbol{\xi}_2, t) + \boldsymbol{\xi}_2 \cdot \nabla \psi(X, \boldsymbol{\xi}_2, t) = \dfrac{1}{\tau}(M_\psi(X, \boldsymbol{\xi}_2, t) - \psi(X, \boldsymbol{\xi}_2, t)) \end{cases} \tag{I.34}$$

where $X = (x, y)$, $\boldsymbol{\xi}_2 = (\xi_u, \xi_v)^T$, $M_\phi = \int_{\mathbb{R}} M_f d\xi_w$ and $M_\psi = \int_{\mathbb{R}} \frac{1}{2}\xi_w^2 M_f d\xi_w$. In the continuous case, these expressions can be calculated exactly:

$$\begin{cases} M_\phi = \dfrac{\rho(X,t)}{2\pi T(X,t)} \exp\Big(- \dfrac{|\boldsymbol{\xi}_2 - \mathbf{U}(X,t)|^2}{2T(X,t)} \Big) \\ M_\psi = \dfrac{(d-2)T(X,t)}{2} \dfrac{\rho(X,t)}{2\pi T(X,t)} \exp\Big(- \dfrac{|\boldsymbol{\xi}_2 - \mathbf{U}(X,t)|^2}{2T(X,t)} \Big) = \dfrac{(d-2)T(X,t)}{2} M_\phi \end{cases}$$

were $\mathbf{U}(X,t) = (u, v)^T$ and $T(X,t)$ are respectively the macroscopic velocity and macroscopic temperature.

The moments of f can be obtained by multiplying the reduced function ϕ and ψ by $\mathbf{m}_2$ and integrating over the reduced velocity space:

$$\int_{\mathbb{R}^3} f(\boldsymbol{\xi}_2) m_2(\boldsymbol{\xi}_2) d\boldsymbol{\xi}_2 = \begin{pmatrix} \int_{\mathbb{R}^2} \phi(\boldsymbol{\xi}_2) d\boldsymbol{\xi}_2 \\ \int_{\mathbb{R}^2} \xi_u \phi(\boldsymbol{\xi}_2) d\boldsymbol{\xi}_2 \\ \int_{\mathbb{R}^2} \xi_v \phi(\boldsymbol{\xi}_2) d\boldsymbol{\xi}_2 \\ \int_{\mathbb{R}^2} \frac{1}{2}|\boldsymbol{\xi}_2|^2 \phi(\boldsymbol{\xi}_2) d\boldsymbol{\xi}_2 + \int_{\mathbb{R}^2} \psi(\boldsymbol{\xi}_2) d\boldsymbol{\xi}_2 \end{pmatrix} = \begin{pmatrix} \rho \\ \rho u \\ \rho v \\ E \end{pmatrix}$$

We have presented in details the BGK model since it is widely used in this work. Although it is a relatively simple model to simulate rarefied flows it does not give the correct Prandtl number for monoatomic gases as said previously. To fix this issue, attempt have been made in [19] or in [110] by modifying the BGK model but they make the model very complex from a numerical point of view. We now present two models similar to the BGK model but with a modification of the equilibrium function to recover the correct Prandtl number for monoatomic gases.

I.3 The Shakov model

The Shakov model [106] has been derived with the same consideration used for the BGK model. To recover the correct Prandtl number, the idea is to multiply the Maxwellian distribution function by a polynomial function depending on the Prandtl number and the heat flux. With respect to the BGK model, it has also the advantage of preserving the correct heat flux given by the Boltzmann equation. The dimensionless form of the model, also called S-BGK, is the following:

$$\frac{\partial f}{\partial t}(\mathbf{x}, \boldsymbol{\xi}, t) + \boldsymbol{\xi} \cdot \nabla_{\mathbf{x}} f(\mathbf{x}, \boldsymbol{\xi}, t) = \frac{1}{\tau}(M_{fs}(\mathbf{x}, \boldsymbol{\xi}, t) - f(\mathbf{x}, \boldsymbol{\xi}, t)) \tag{I.35}$$

with M_{fs} the Maxwellian obtained as follows:

$$M_{fs}(\mathbf{x}, \boldsymbol{\xi}, t) = M_f(\mathbf{x}, \boldsymbol{\xi}, t)\Big[1 + \frac{(1 - Pr)}{5p(\mathbf{x}, t)T(\mathbf{x}, t)} \mathbf{c} \cdot \mathbf{q}(\mathbf{x}, t)\Big(\frac{|\mathbf{c}|^2}{T(\mathbf{x}, t)} - 5\Big)\Big] \tag{I.36}$$

where M_f is the actual Maxwellian distribution function of the BGK model, p the pressure and $\mathbf{q}$ the heat flux.

If the Prandtl number is set to 1, the BGK model is recovered. The polynomial function is used to conserve the correct heat flux (fourth moment of f). However, one drawback of this model is that the positivity of the distribution function is not ensured. Although this model is almost as simple as the BGK model it provides the correct Prandtl number and that it is quite used in the literature, we prefer using another model that respects the positivity of the distribution.

I.4 The ES-BGK model

The ES-BGK model of Holway [64], [65], as Shakov's model, contains explicitly the correct Prandtl number. It is very similar to the BGK model, but it has been proven [3] to satisfy the three basic requirements of the Boltzmann equation, non-negative distribution functions, of predicting a correct Prandtl number and of respecting the H-theorem. It is similar to the BGK model the only difference being the relaxation term. The equilibrium function is no longer the Maxwellian distribution but an anisotropic Gaussian distribution function:

$$\frac{\partial f}{\partial t} + \boldsymbol{\xi} \cdot \nabla_{\mathbf{x}} f = \frac{1}{\tau}\Big(\mathcal{G}_f - f\Big) \tag{I.37}$$

with τ the relaxation time given by:

$$\frac{1}{\tau} = \frac{c_0 \rho T^{1-\delta}}{1-\nu}$$

$c_0 = \frac{RT_0^{\delta}}{\mu_0}$ is the same coefficient as in the relaxation time for the BGK equation depending on the reference temperature and reference viscosity of the gas. ν is a parameter set such that the correct Prandtl number is recovered in the hydrodynamic limit. For such models, it has been proven in [4] that the model is valid (satisfy the $\mathcal{H}$-theorem) for $-\frac{1}{2} \leq \nu < 1$. Also, the Chapman-Enskog expansion performed on the ES-BGK model gives that:

$$Pr = \frac{1}{1-\nu} \tag{I.38}$$

The correct value for the Prandtl number is then recovered for the lower possible value of ν, meaning $\nu = -\frac{1}{2}$.

The equilibrium distribution function is a calculated as follows:

$$\mathcal{G}_f(\mathbf{x}, \boldsymbol{\xi}, t) = \frac{\rho(\mathbf{x}, t)}{\sqrt{\det(2\pi \mathcal{T}(\mathbf{x}, t))}} \exp\Big(- \frac{(\boldsymbol{\xi} - \mathbf{U}(\mathbf{x}, t))^T \mathcal{T}^{-1} (\boldsymbol{\xi} - \mathbf{U}(\mathbf{x}, t))}{2} \Big)$$

The symmetric tensor $\mathcal{T}$ is defined as:

$$\mathcal{T}(\mathbf{x}, t) = \frac{1}{Pr} RT(\mathbf{x}, t) I + (1 - \frac{1}{Pr}) \Theta(\mathbf{x}, t)$$

where I is the identity matrix. It is easy to see that:

$$\mathcal{T}(\mathbf{x}, t) = \frac{1}{\rho(\mathbf{x}, t)} \int_{\mathbb{R}^3} \mathbf{c} \otimes \mathbf{c} \mathcal{G}_f d\boldsymbol{\xi}$$

Note that at equilibrium, $f = \mathcal{G}_f$ and then $\Theta = \frac{1}{Pr} RTI + (1 - \frac{1}{Pr})\Theta$ so $\Theta = RTI$. Therefore, $f = \mathcal{G}_f = M_f$. The fundamental equilibrium property given by the H-theorem is then satisfied.

If the Prandtl number is set to 1, the BGK model previously presented is recovered.

In the following, we will use the dimensionless form of the ES-BGK model. The expression of the relaxation time and of the tensor $\mathcal{T}$ becomes:

$$\frac{1}{\tau} = \frac{Pr}{Kn_\infty}\rho T^{1-\delta} \tag{I.39}$$

$$\mathcal{T}(\mathbf{x},t) = \frac{1}{Pr}T(\mathbf{x},t)I + (1-\frac{1}{Pr})\Theta(\mathbf{x},t) \tag{I.40}$$

As for the BGK model, a reduction is possible in 1D and 2D. The mechanism is exactly the same as presented in section I.2.2 and won't be discussed here. However, it is worth noting that such a reduction implies that the tensor Θ is still symmetric but with zeros on the extra-diagonal part corresponding to the reduced dimensions. The details of the calculations are found in annexe C. The equations are the following for a general case of reduced model in a D space dimension:

$$\begin{aligned}\phi &= \int_{\mathbb{R}^{d-D}} f \prod_{k=D+1,d} d\xi_k \\ \psi &= \int_{\mathbb{R}^{d-D}} \frac{1}{2}\sum_{l=D+1,d} \xi_l^2 f \prod_{k=D+1,d} d\xi_k\end{aligned} \tag{I.41}$$

The macroscopic quantities are recovered as follows:

$$\int_{\mathbb{R}^d} f(\boldsymbol{\xi}_D)\mathbf{m}_D(\boldsymbol{\xi})d\boldsymbol{\xi} = \begin{pmatrix} \int_{\mathbb{R}^D}\phi(\boldsymbol{\xi}_D)d\boldsymbol{\xi}_D \\ \int_{\mathbb{R}^D}\boldsymbol{\xi}\phi(\boldsymbol{\xi}_D)d\boldsymbol{\xi}_D \\ \int_{\mathbb{R}^D}\frac{1}{2}|\boldsymbol{\xi}_D|^2\phi(\boldsymbol{\xi}_D)d\boldsymbol{\xi}_D + \int_{\mathbb{R}^{d-D}}\psi(\boldsymbol{\xi}_D)d\boldsymbol{\xi}_D \\ \int_{\mathbb{R}^D}\mathbf{c}_D\otimes\mathbf{c}_D\phi(\boldsymbol{\xi}_D)d\boldsymbol{\xi}_D \end{pmatrix} = \begin{pmatrix} \rho \\ \rho\mathbf{U}_D \\ E \\ \rho\Theta_D \end{pmatrix} \tag{I.42}$$

In these equations $\boldsymbol{\xi}_D$ and $\mathbf{c}_D$ have the same the dimension of the reduced velocity space ($= D$), Θ_D is the reduced pressure tensor of dimension $D\times D$ and $\mathbf{m}_D(\boldsymbol{\xi}) = (1, \boldsymbol{\xi}_D, \frac{1}{2}|\boldsymbol{\xi}_D|^2, \mathbf{c}_D\otimes\mathbf{c}_D)^T$. Dimensions omitted are the reduced dimensions. As presented in annexe C the reduced Gaussian distribution functions are:

$$\begin{aligned}\mathcal{G}_\phi &= \frac{\rho}{\sqrt{\det(2\pi\mathcal{T}_D)}}\prod_{i,j=1}^{D}\exp\Big(-\frac{(\xi_i-U_i)(\xi_j-U_j)\mathcal{T}_{D\,i,j}^{-1}}{2}\Big) \\ \mathcal{G}_\psi &= \frac{\sum_{k=D+1,d}\mathcal{T}_{Dk,k}}{2}\mathcal{G}_\phi\end{aligned} \tag{I.43}$$

where ξ_k and U_k are the k-th components of the vectors $\boldsymbol{\xi}$ and $\mathbf{U}$ respectively. $\mathcal{T}_D$ is the reduced tensor of dimension $D\times D$ defined by $(\mathcal{T}_D)_{i,j} = \mathcal{T}_{i,j}$ for $i,j = 1,..,D$.

The second equilibrium distribution function is computed with the sum of the diagonal terms of $\mathcal{T}$ on the reduced dimensions. This sum is computed with the second reduced distribution function ψ as:

$$\begin{aligned}\sum_{k=D+1,d}\Theta_{k,k} &= \frac{1}{\rho}\int_{\mathbb{R}^{d-D}} 2\psi \prod_{k=D+1,d} d\xi_k \\ \sum_{k=D+1,d}\mathcal{T}_{k,k} &= \frac{d-D}{Pr}T + (1-\frac{1}{Pr})\sum_{k=D+1,d}\Theta_{k,k}\end{aligned} \tag{I.44}$$

In this first chapter, the Boltzmann equation has been presented with some important properties. Computations of solutions of the Boltzmann equations are very intensive due to the

collision operator. DSMC [16] is probably more efficient but comes with stochastic noise that is hard to be reduced. Moreover, the cost becomes prohibitive as the hydrodynamic regime is approach. In this work, we prefer using deterministic models. In this sense, two models have been introduced: the BGK model and the ES-BGK model. They both respect some properties of the Boltzmann equation (positivity of the distribution function, $\mathcal{H}$-theorem) but only the ES-BGK model predicts the correct Prandtl number. In these models, only three energy degrees of freedom for the gas molecules are considered meaning that the gas is modelled as a monoatomic gas composed of identical particles. However, the relative simplicity of the two models allows a first step in the study of flows where rarefied and hydrodynamic regimes coexist at a reasonable cost and accuracy. We now present the numerical methods used to solve these models.

Chapter II

Numerical Methods for Kinetic Models

This chapter is devoted to the presentation of the numerical method used in the following. The numerical method is a deterministic scheme based on a discrete velocity space (DVM). First we describe the discretization in velocity, then we proceede with the space discretization, and finally we give the time integration scheme, verifying also the asymptotic properties of the scheme as $Kn \to 0$. For the time integration scheme, we distinguish the case of the BGK model and the one of the ES-BGK model. The last section presents different types of boundary conditions for kinetic models and how to impose them.

II.1 The discretization in velocity space

In this section, we present the discrete velocity space discretization for the BGK and the ES-BGK models. Conceptually, the method used for the two model is similar. For the sake of completeness, the method is presented for the two models separately.

II.1.1 Case of the BGK model

By construction the distribution function f and the Maxwellian distribution function M_f satisfy:

$$\int_{\mathbb{R}^3} M_f \mathbf{m}(\boldsymbol{\xi}) d\boldsymbol{\xi} = \begin{pmatrix} \rho \\ \rho \mathbf{U} \\ E \end{pmatrix} = \int_{\mathbb{R}^3} f \mathbf{m}(\boldsymbol{\xi}) d\boldsymbol{\xi}$$

This is essential to ensure conservation of mass, momentum and energy because by multiplying (I.30) by $\mathbf{m}(\boldsymbol{\xi})$ and integrating in velocity space one should recover conservation laws:

$$\partial_t \int_{\mathbb{R}^3} \mathbf{m}(\boldsymbol{\xi}) f(\boldsymbol{\xi}) d\boldsymbol{\xi} + \partial_x \int_{\mathbb{R}^3} \boldsymbol{\xi} \mathbf{m}(\boldsymbol{\xi}) f(\boldsymbol{\xi}) d\boldsymbol{\xi} = 0$$

In the discrete case, a bounded velocity space $\Omega_{\boldsymbol{\xi}}$ has to be introduced such that it contains all the important informations of the distribution functions at any time and in any position in physical space. It is assumed that:

$$\lim_{\xi_\alpha \to \pm\infty} \xi_\alpha^k f(\boldsymbol{\xi}) = 0 \tag{II.1}$$

for every $k \geqslant 0$ and every component ξ_α of $\boldsymbol{\xi}$. In particular, $\Omega_{\boldsymbol{\xi}}$ has to be chosen such that the distribution function is negligible outside $\Omega_{\boldsymbol{\xi}}$. Then, $\Omega_{\boldsymbol{\xi}}$ has to be discretized and the integrals

are evaluated by quadrature on the discrete space. Let $\langle ., . \rangle$ denote the quadrature rule and

$$\begin{pmatrix} \rho \\ \rho \mathbf{U} \\ E \end{pmatrix} = \langle f(\boldsymbol{\xi}), \mathbf{m}(\boldsymbol{\xi}) \rangle$$

be the discrete moments of f. Now:

$$\langle M_f(\boldsymbol{\xi}), \mathbf{m}(\boldsymbol{\xi}) \rangle \neq \begin{pmatrix} \rho \\ \rho \mathbf{U} \\ E \end{pmatrix}$$

and conservation would not hold.

Based on the work of Cabannes et al. [24] on entropic Maxwellian states, Mieussens proved in [85] that a discrete Maxwellian can be expressed as $\widetilde{M}_f = \exp(\boldsymbol{\alpha} \cdot \mathbf{m}(\boldsymbol{\xi}))$ and such that:

$$\langle \widetilde{M}_f(\boldsymbol{\xi}), \mathbf{m}(\boldsymbol{\xi}) \rangle = \begin{pmatrix} \rho \\ \rho \mathbf{U} \\ E \end{pmatrix}$$

This form holds true also in the continuous case for the exact Maxwellian of the BGK model with:

$$\boldsymbol{\alpha}_c = \left(\ln(\frac{\rho}{(2\pi T)^{d/2}}) - \frac{|\mathbf{U}|^2}{2T}, \frac{\mathbf{U}}{T}, -\frac{1}{T} \right)$$

For the 1D BGK reduced model, this expression becomes :

$$\langle \widetilde{M_\phi}, \mathbf{m}_1(\boldsymbol{\xi}) \rangle + \langle \widetilde{M_\psi}, \mathbf{e}_3 \rangle = \langle f, \mathbf{m}_1(\boldsymbol{\xi}) \rangle \tag{II.2}$$

with $\mathbf{e}_3 = (0, 0, 1)^T$.

In 2D, the discrete Maxwellians of ϕ and ψ are such that:

$$\langle \widetilde{M_\phi}, \mathbf{m}_2(\boldsymbol{\xi}) \rangle + \langle \widetilde{M_\psi}, \mathbf{e}_4 \rangle = \langle f, \mathbf{m}_2(\boldsymbol{\xi}) \rangle \tag{II.3}$$

with $\mathbf{e}_4 = (0, 0, 0, 1)^T$.

Equation (II.2) and (II.3) are a non linear system in $\boldsymbol{\alpha}$ which can be solved with a Newton-Raphson method (see annexe B). The solution in the continuous case ($\boldsymbol{\alpha}_c$) will be the starting value for the Newton-Raphson algorithm.

II.1.2 Case of the ES-BGK model

In the case of the ES-BGK model, the assumption (II.1) is also true and the discrete form of the Gaussian can also be expressed as [85]:

$$\widetilde{\mathcal{G}}_f = \exp(\boldsymbol{\alpha} \cdot \mathbf{m}^{ES}(\boldsymbol{\xi}))$$

where $\mathbf{m}^{ES}(\boldsymbol{\xi}) = (1, \boldsymbol{\xi}, \frac{1}{2}|\boldsymbol{\xi}|^2, \mathbf{c} \otimes \mathbf{c})$.

The discrete system to solve is slightly larger since the third order moment of the distribution function has to be conserved. Hence:

$$\langle \widetilde{\mathcal{G}}_f(\boldsymbol{\xi}), \mathbf{m}^{ES}(\boldsymbol{\xi}) \rangle = \begin{pmatrix} \rho \\ \rho \mathbf{U} \\ E \\ \rho \mathcal{T} \end{pmatrix}$$

Conserving the fourth moment (or third order moment) adds six equations in 3D: one for each diagonal component, one for each extra diagonal component in the upper (or lower) part of the matrix $\rho\mathcal{T}$ since the tensor is symmetric. Actually, with the fourth moment, the equation on the energy becomes a linear combination of the three equations on the diagonal components of $\mathcal{T}$, the equations on the momentum and on the density. It is then removed from the resolution of the non linear system. Thus, for the 1D ES-BGK reduced model, the non linear system to solve is composed of four equations. It has six equations in 2D (instead of four for the BGK model) and ten in 3D (instead of five for the BGK model).

The resolution of the discrete Gaussian is then more costly in the case of the ES-BGK model especially in 3D. But as for the BGK model, it makes the scheme more robust since it always conserves mass momentum and energy independently of the quadrature rule. Moreover, because of the exact discrete conservation, it is possible to use coarse grids in velocity space, thus reducing the overhead due to the solution of the non linear system.

At the continuous level, the conservation is ensured with:

$$\boldsymbol{\alpha}_c = \left(\ln(\frac{\rho}{\sqrt{\det(2\pi\mathcal{T})}}), 0, 0, 0, -\frac{\mathcal{T}^{-1}_{1,1}}{2}, -\frac{\mathcal{T}^{-1}_{2,2}}{2}, -\frac{\mathcal{T}^{-1}_{3,3}}{2}, -\mathcal{T}^{-1}_{1,2}, \mathcal{T}^{-1}_{1,3}, \mathcal{T}^{-1}_{2,3}\right)$$

where $\mathcal{T}^{-1}_{i,j}$ stands for the i,j component of the tensor $\mathcal{T}^{-1}$. As in the case of the BGK model, this value is used for the initialization of the Newton-Raphson algorithm (see annexe D).

II.1.3 The velocity grid discretization

Now that the discrete model in velocity space has been presented, we develop how the velocity grid is set. It is done independently of the kinetic model used (BGK or ES-BGK model).

II.1.3.1 The Gauss-Hermite quadrature rule

Using the Gauss-Hermite polynomial basis can seem an optimal approach to define the velocity grid since it is particularly adapted to Gaussian distribution function. Indeed, it allows a very precise integration of a Gaussian function with very few points. Thus, the underlying idea is to consider that the distribution function is closed to a Maxwellian and then, can be integrated with the Gauss Hermite quadrature method. In the 1D case:

$$\int_{-\infty}^{+\infty} f(x,\xi_u,t)\varpi(\xi_u)d\xi_u = \sum_{i=1}^{n}\omega_i f(x,\xi_{ui},t)$$

where f is the distribution function, $\varpi = e^{-\xi_u^2}$ (with a change of variable if needed) the weight function equal to ω_i for $\xi_u = \xi_{ui}$ and n is number of points of the velocity grid:

$$\omega_i = \frac{2^{n-1}n!\sqrt{\pi}}{n^2[H_{n-1}(\xi_{ui})]^2}$$

with H_n are the Hermite polynomials that have ξ_{ui} as roots.

Usually, to have a good accuracy, few points are required. Close to the hydrodynamic regime, a grid with 10 points in each directions gives approximatively a quadrature error on f around 10^{-18}.

The main advantage of this quadrature rule is that the velocity grid is adjusted to the Maxwellian and then reduces the maximum velocity of the grid and also the total number of grid points required. However, ensuring conservation is not easy and the algorithm for

the discrete Maxwellian can diverge especially far from the hydrodynamic regime where the distribution function is not a Maxwellian any more. Moreover, computing a new velocity grid and new weights at each time step is computationally costly and requires interpolations of the distribution function on the new grid. For these reasons, this quadrature rule is not used in this work.

II.1.3.2 The trapezoidal rule

In our case, the trapezoidal quadrature rule is used because it has spectral accuracy for smooth and periodic functions on a uniform grid. For this reason we use a uniform grid symmetric with respect to 0 and such that f is negligible outside the grid. In 1D:

$$\mathcal{G}_v = (\xi_u^i)_{i=-n..n} \quad \text{with} \quad \xi_u^i = i\Delta\xi_u$$

The boundaries (ξ_u^{min} and ξ_u^{max}) and the mesh size of the velocity grid is usually determined according to two criteria:

$$\mathcal{G}_v = (\xi_u^i)_{i=-n_v..n_v} \quad \text{such that} \begin{cases} \xi_u^{max} = |u|^{max} + 5\sqrt{T_{max}} \\ \xi_u^{min} = -\xi_u^{max} \\ \Delta\xi_u \leq \sqrt{T_{min}} \end{cases} \tag{II.4}$$

with $|u|^{max}$ the maximum absolute value of the macroscopic velocity and T_{max} the maximum temperature over space and time. The velocity grid is then taken symmetric with respect to zero. The first condition ensures that most of the Maxwellian distribution function (more than 99.99%) is contained in the grid for every space cell at any time t. The last condition ensures that the Maxwellian distribution function is always defined on at least three grid points.

For multidimensional cases, the same discretization is performed independently in all directions.

II.2 Space discretization

In computational fluid dynamics, two kind of grids are generally used: unstructured grids and Cartesian grids. On one hand, unstructured grids have the advantage of fitting a possible body immersed in the flow. Using a finite volume scheme on such a grid makes easy the enforcement of boundary conditions on the body since they can be imposed exactly. On the other hand, if the body is moving, a new mesh has to be generated at each time step to fit the new position of the body which is complex and costly. Moreover, geometrical informations are required such as cell edges size, normals, and can be prohibitive in terms of memory. Cartesian grids have no such requirements and are easily generated. Schemes on Cartesian grids are also simpler and more suitable for massive parallel computations. But unlike unstructured grids, imposing the boundary conditions at a reasonable accuracy is challenging and will be a key point in this work.

Even if most of this work is done on Cartesian grids, let us introduce first the scheme in a general form on structured grids since some computations are done on body-fitted grids (curvilinear meshes). It is presented for the BGK model in 2D. The scheme is identical for the ES-BGK model.

The discretization of $\Omega_{\mathbf{x}}$ on a structured grid gives:

$$\Omega_{\mathbf{x}} = \bigcup_{\substack{i=1..n \\ j=1..m}} \Omega_{\mathbf{x}}^{i,j}$$

such that (x_i, y_j) are the coordinates of the center of cell (i, j) and $(x_{i+1/2}, y_j)$ are the coordinates of the center of the interface between cells (i, j) and $(i+1, j)$ (see figure II.1).

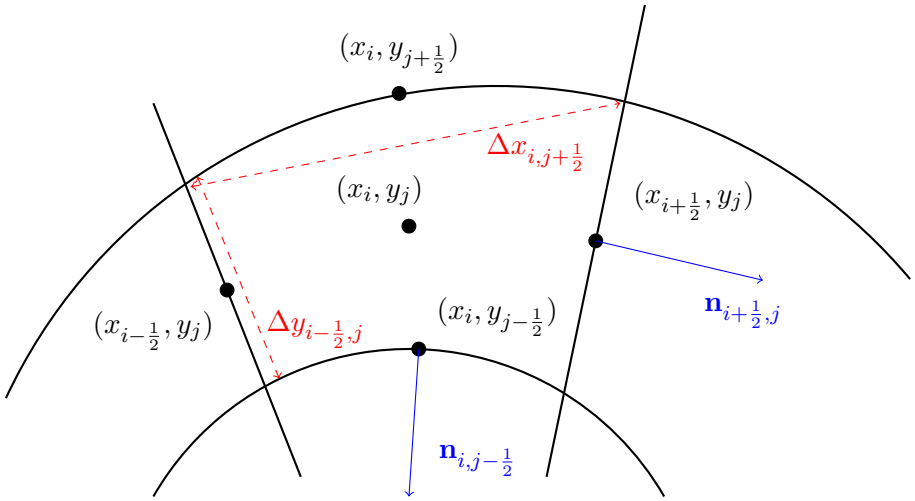

Figure II.1: Cell (i, j) of a structured grid.

On a space cell $\Omega_{\mathbf{x}}^{i,j}$, eq.(I.34) is integrated with a finite volume method assuming no external forces for simplicity:

$$\frac{\partial f_{i,j}}{\partial t} + \boldsymbol{\xi} \cdot \int_{\partial\Omega_{\mathbf{x}}^{i,j}} f \mathbf{n}_{\partial\Omega_{\mathbf{x}}^{i,j}} d\sigma = \frac{1}{\tau_{i,j}}(M_{f_{i,j}} - f_{i,j}) \tag{II.5}$$

where $f_{i,j} = \frac{1}{|\Omega_{\mathbf{x}}^{i,j}|}\int_{\Omega_{\mathbf{x}}^{i,j}} f dxdy$ and $M_{f_{i,j}} = \frac{1}{|\Omega_{\mathbf{x}}^{i,j}|}\int_{\Omega_{\mathbf{x}}^{i,j}} \widetilde{M}_f dxdy$.

The equation can be simply rewritten in terms of fluxes at each numerical interface (between two cells):

$$\frac{\partial f_{i,j}}{\partial t} + \frac{1}{|\Omega_{\mathbf{x}}^{i,j}|}(\Delta y_{i+\frac{1}{2},j} F_{i+\frac{1}{2},j} - \Delta y_{i-\frac{1}{2},j} F_{i-\frac{1}{2},j} + \Delta x_{i,j+\frac{1}{2}} F_{i,j+\frac{1}{2}} - \Delta x_{i,j-\frac{1}{2}} F_{i,j-\frac{1}{2}}) = \frac{1}{\tau_{i,j}}(M_{f_{i,j}} - f_{i,j}) \tag{II.6}$$

with $F_{i+\frac{1}{2},j}$ the numerical flux between cell $\Omega_{\mathbf{x}}^{i,j}$ and cell $\Omega_{\mathbf{x}}^{i+1,j}$ (with a similar notation for the other fluxes) which is expressed as :

$$F_{i+\frac{1}{2},j} = \max(0, \boldsymbol{\xi} \cdot \mathbf{n}_{i+\frac{1}{2},j}) f_{i,j} + \min(0, \boldsymbol{\xi} \cdot \mathbf{n}_{i+\frac{1}{2},j}) f_{i+1,j} \tag{II.7}$$

On a uniform Cartesian grid, the scheme is simpler. If $\Omega_{\mathbf{x}} = [x_{in}, x_{out}] \times [y_{in}, y_{out}]$ is a box and discretized with $n \times m$ cells (where x_{in}, x_{out}, y_{in} and y_{out} are the boundary of the domain):

$$\begin{cases} \Omega_{\mathbf{x}} = \bigcup_{\substack{i=1..n \\ j=1..m}} \Omega_{\mathbf{x}}^{i,j} = \bigcup_{\substack{i=1..n \\ j=1..m}} [x_{i-1/2}, x_{i+1/2}] \times [y_{j-1/2}, y_{j+1/2}] \\ \Delta x = \dfrac{x_{out} - x_{in}}{n}, \ \Delta y = \dfrac{y_{out} - y_{in}}{m} = \Delta x \\ x_{i+1/2} = x_{in} + i\Delta x, \ y_{j+1/2} = y_{in} + j\Delta x \end{cases}$$

(x_i, y_j) are still the coordinates of the center of cell (i, j) and $(x_{i+1/2}, y_j)$ are the coordinates of the center of the interface between cells (i, j) and $(i+1, j)$.

The scheme (II.6) can be simply rewritten as:

$$\frac{\partial f_{i,j}}{\partial t} + \frac{1}{\Delta x}(F_{i+\frac{1}{2},j} - F_{i-\frac{1}{2},j} + F_{i,j+\frac{1}{2}} - F_{i,j-\frac{1}{2}}) = \frac{1}{\tau}(M_{f_{i,j}} - f_{i,j}) \tag{II.8}$$

The flux $F_{i+\frac{1}{2},j}$ is now expressed as (with a similar notation for the other fluxes):

$$F_{i+\frac{1}{2},j} = \max(0, \xi_u) f_{i,j} + \min(0, \xi_u) f_{i+1,j} \tag{II.9}$$

where ξ_u is the first component of the microscopic velocity and has to be replaced by ξ_v, the second component of the microscopic velocity to compute the fluxes along the second direction y.

This scheme assumes that the distribution function is constant on a cell $\Omega_{\mathbf{x}}^{i,j}$ and gives a first order accuracy.

Higher order accuracy can be obtained by reconstructing the distribution function in a cell and considering the value at the numerical interface to compute the fluxes. More generally, the flux $F_{i+\frac{1}{2},j}$ can be expressed as:

$$F_{i+\frac{1}{2},j} = \max(0, \xi_u) f^r_{i,j} + \min(0, \xi_u) f^l_{i+1,j} \tag{II.10}$$

with $f^r_{i,j}$ and $f^l_{i+1,j}$ the values of f on the two sides of the interface. The numerical expression of the distribution functions $f^l_{i,j}$, $f^r_{i+1,j}$ depends on the reconstruction used at the numerical interface.

Let us consider independent reconstructions in each direction. Figure II.2 shows first and second order reconstruction in 1D for a function g.

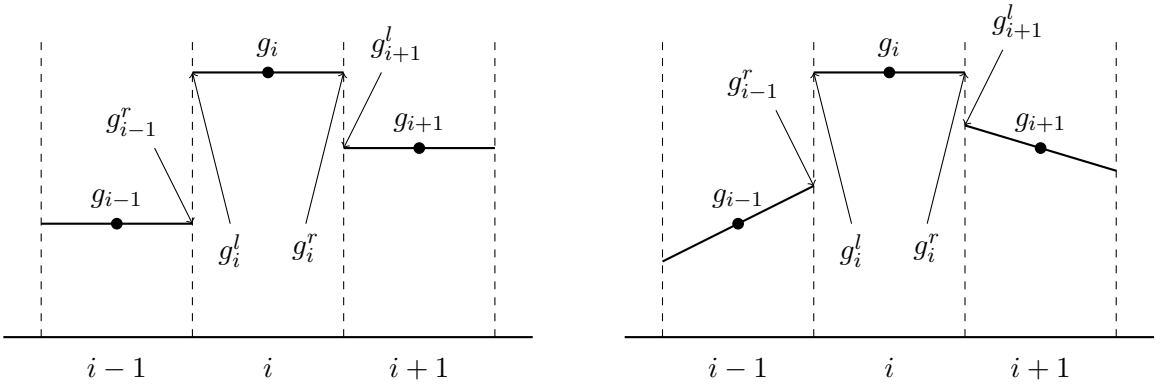

(a) First order reconstruction

(b) Second order reconstruction

Figure II.2: Reconstruction of g in cells $i-1$, i, and $i+1$ at first and second order accuracy

For a first order reconstruction, $g^l_i = g^r_i = g_i$ meaning in our case $f^r_{i,j} = f_{i,j}$ and $f^l_{i+1,j} = f_{i+1,j}$. For second order accuracy, a slope is introduced such that the function is linearly reconstructed in the cell:

$$g^l_i = g_i - \frac{\Delta x}{2} s_i \qquad \text{and} \qquad g^r_i = g_i + \frac{\Delta x}{2} s_i$$

The slope s_i does not modify the mean value of g_i in the cell i and if s_i is set to 0 the first order accuracy is recovered.

The slope s_i has to be defined with a special care. A natural way of defining such a slope could be a centred formulation:

$$s_i = \frac{g_{i+1} - g_{i-1}}{2\Delta x}$$

However, in regions with strong gradients (shocks, discontinuities,...), oscillations would appear. This problem is handled by limiting the slope to ensure the TVD (Total Variation Diminishing)

behaviour of the scheme. In practice, it means that in regions of strong gradients or where local extrema appear, the scheme is reduced to first order. Different limiters exist such as Van Leer limiters [111], Osher limiters [28] or superbee limiters [101]. In our case we use MinMod limiters introduced by Roe [101]:

$$\text{MinMod}(a,b) = \begin{cases} sign(a)\min(|a|,|b|) & \text{if } ab > 0 \\ 0 & \text{otherwise} \end{cases} \tag{II.11}$$

for a and b two real values.

The slope s_i is then defined as:

$$s_i = \frac{1}{\Delta x}\text{MinMod}(g_{i+1} - g_i, g_i - g_{i-1}) \tag{II.12}$$

For a second order accurate scheme, in the case of a 2D distribution function f the values of $f^r_{i,j}$ and $f^l_{i+1,j}$ read:

$$\begin{cases} f^l_{i,j} = f_{i,j} + \dfrac{1}{2}\text{MinMod}(f_{i+1,j} - f_{i,j}, f_{i,j} - f_{i-1,j}) \\ f^r_{i+1,j} = f_{i+1,j} - \dfrac{1}{2}\text{MinMod}(f_{i+1,j} - f_{i,j}, f_{i+2,j} - f_{i+1,j}) \end{cases} \tag{II.13}$$

This type of schemes is known as MUSCL schemes [112].

II.3 The notion of Asymptotic Preserving (AP) scheme

Let $\mathcal{F}^\epsilon$ be a physical model depending on a parameter ϵ which characterizes a microscopic scale, and suppose that, as ϵ goes to zero, the model $\mathcal{F}^\epsilon$ relaxes on a simpler model $\mathcal{F}^0$ (the macroscopic model) which typically depends on smaller number of variables. Let $\mathcal{F}^\epsilon_\delta$ be a discretization of $\mathcal{F}^\epsilon$, where δ characterizes the discretization parameters, so that $\mathcal{F}^\epsilon_\delta \to \mathcal{F}^\epsilon$ as $\delta \to 0$. The idea of Asymptotic Preserving schemes can be illustrated as follows: As ϵ goes to zero, the model

$$\begin{array}{ccc} \mathcal{F}^\epsilon_\delta & \xrightarrow{\epsilon \to 0} & \mathcal{F}^0_\delta \\ \delta \to 0 \downarrow & & \downarrow \delta \to 0 \\ \mathcal{F}^\epsilon & \xrightarrow{\epsilon \to 0} & \mathcal{F}^0 \end{array}$$

Figure II.3: Illustration of an AP scheme [71].

approximates the macroscopic model $\mathcal{F}^0$ which does not depend on ϵ. Similarly, at the discrete level, the asymptotic limit (if exists) of $\mathcal{F}^\epsilon_\delta$ as ϵ goes to zero is $\mathcal{F}^0_\delta$ with δ fixed. Then, if $\mathcal{F}^0_\delta$ is an approximation consistent and stable of $\mathcal{F}^0$, the scheme $\mathcal{F}^\epsilon_\delta$ is said AP [71].

In the case of kinetic models, the microscopic scale is represented by the Knudsen number. For Knudsen numbers going to zero, the hydrodynamic limit is reached at the continuous level. It is necessary to ensure the same property at the discrete level. Hence, the numerical scheme should verify that:

$$\lim_{Kn \to 0} f \longrightarrow M_f$$

The notion of Asymptotic Preserving (AP) schemes applied to kinetic models has been first introduced by Jin in [70]. In [50], two criteria are clearly defined that should be satisfied by a numerical scheme to be AP. First, as the Knudsen number goes to zero, the Euler limit should be recovered on a fixed mesh in space and velocity. In other words, the Chapman-Enskog expansion should be verified also at the discrete level.

The second criteria is about the collision operator. The scheme should allow the resolution of the relaxation term implicitly or faster than a Newton type solver for non linear algebraic systems. This ensures that the time step would not be dramatically decreased as the Knudsen number goes to zero. Additional work on this notion can be found in [72] or in a recent review of Jin [71].

Many schemes have been now proven to be asymptotic preserving. In [95] a deterministic method is presented for the Boltzmann equation. Exponential Runge-Kutta scheme have also successfully been used in [40] with a splitting between free particle transport and collision. Other AP scheme are based on Micro-Macro decomposition [11] or fully implicit schemes [98]. The Unified Gas-Kinetic scheme (UGKS) has also been widely used [115], [32].

II.4 The time discretization

This section presents the numerical integration of the kinetic models in time. Although the algorithm is not strictly identical for the two kinetic models we are interested in (BGK model and ES-BGK model), the general form of the numerical scheme common to the two models is presented for the BGK model case. The distinction of the two models is done at the end of the section.

The time discretization can be performed for all terms explicitly. But in this case, the time step will be determined by the space discretization (Δx), the maximum velocity of the velocity grid and the relaxation time τ. For small Knudsen numbers, the relaxation part becomes very stiff (τ very small) and imposes a very strong restriction on the time step. Asher et al. [6] first presented IMEX schemes to cure this issue. Here, the IMEX scheme [73], [94] is chosen. The relaxation term is treated implicitly while the convective part is non stiff (and non linear for a second order scheme in space with limiters) which means that an explicit scheme is more efficient.

The time integration for a ν-stages IMEX Runge-Kutta scheme reads as follows:

$$\begin{aligned}
f_{i,j}^{n+1} &= f_{i,j}^{n} - \Delta t \sum_{k=1}^{\nu} \tilde{\omega}_k \boldsymbol{\xi} \nabla_{\mathbf{x}} f_{i,j}^{(k)} + \frac{\Delta t}{\tau} \sum_{k=1}^{\nu} \omega_k (M_{f_{i,j}}^{(k)} - f_{i,j}^{(k)}) \\
f_{i,j}^{(k)} &= f_{i,j}^{n} - \Delta t \sum_{l=1}^{k-1} \tilde{A}_{k,l} \boldsymbol{\xi} \nabla_{\mathbf{x}} f_{i,j}^{(l)} + \frac{\Delta t}{\tau} \sum_{l=1}^{k} A_{k,l} (M_{f_{i,j}}^{(l)} - f_{i,j}^{(l)}) \\
f_{i,j}^{(1)} &= f_{i,j}^{n} + \frac{\Delta t}{\tau} A_{1,1} (M_{f_{i,j}}^{(1)} - f_{i,j}^{(1)})
\end{aligned} \tag{II.14}$$

where A and $\tilde{A}$ are $\nu \times \nu$ matrices, with $\tilde{A}_{i,s} = 0$ if $s \geq i$ and $A_{i,s} = 0$ if $s > i$. These coefficients are derived from a double Butcher's tableaux:

$$\begin{array}{c|c} \tilde{A} \\ \hline \tilde{\omega}^T \end{array} \qquad\qquad \begin{array}{c|c} A \\ \hline \omega^T \end{array}$$

All the quantities until stage $k-1$ are known so the equation for stage k becomes:

$$f_{i,j}^{(k)} = \frac{\tau}{A_{k,k}\Delta t + \tau}\Big(f_{i,j}^{n} - \Delta t \sum_{l=1}^{k-1} \tilde{A}_{k,l}\boldsymbol{\xi}\nabla_{\mathbf{x}} f_{i,j}^{(l)} + \frac{\Delta t}{\tau}\sum_{l=1}^{k-1} A_{k,l}(M_{f_{i,j}}^{(l)} - f_{i,j}^{(l)}) + \frac{A_{k,k}\Delta t}{\tau} M_{f_{i,j}}^{(k)}\Big) \tag{II.15}$$

We now need to distinguish the case of the BGK model and the case of the ES-BGK model. In the first one, $f_{i,j}^{(k)}$ can be computed explicitly since all the right hand side is known. Indeed, since the moments of the relaxation term are zero, the macroscopic variables at stage k can be computed integrating in the velocity space the second equation of (II.14), see [97]. Hence, the Maxwellian $M_{f_{i,j}}^{(k)}$ is known.

The case of the ES-BGK model is slightly more complicated. Computing the distribution function at stage k requires the Gaussian distribution $\mathcal{G}_{f_{i,j}}^{(k)}$. For the ES-BGK model, the moments of the Gaussian $\mathcal{G}_{f_{i,j}}^{(k)}$ and the distribution function are not strictly the same. In particular, the third moment does not give the same tensor. The trick used for the BGK model cannot be applied to the ES-BGK model. However, Filbet et al. [51] showed that the IMEX scheme can still be applied to the ES-BGK model. However, density, momentum and energy can still be obtained explicitly, and in particular this yields $\rho_{i,j}^{(k)}$, $\mathbf{U}_{i,j}^{(k)}$, $T_{i,j}^{(k)}$. But to define $\mathcal{G}_{f_{i,j}}^{(k)}$, one also needs $\Theta_{i,j}^{(k)}$. Let us define the tensor $\Sigma_{i,j}^{(k)}$:

$$\Sigma_{i,j}^{(k)} = \int_{\Omega_{\boldsymbol{\xi}}} \boldsymbol{\xi}\otimes\boldsymbol{\xi} f_{i,j}^{(k)} d\boldsymbol{\xi} = \rho_{i,j}^{(k)}(\Theta_{i,j}^{(k)} + \mathbf{U}_{i,j}^{(k)}\otimes\mathbf{U}_{i,j}^{(k)}) \tag{II.16}$$

If (II.15) in the case of the ES-BGK model is multiplied by $\boldsymbol{\xi}\otimes\boldsymbol{\xi}$ and integrated we get:

$$\begin{aligned}\Sigma_{i,j}^{(k)} =& \frac{\tau}{A_{k,k}\Delta t + \tau}\Big(\Sigma_{i,j}^{n} - \Delta t\sum_{l=1}^{k-1}\int_{\Omega_{\boldsymbol{\xi}}}\Big[\tilde{A}_{k,l}\boldsymbol{\xi}\nabla_{\mathbf{x}} f_{i,j}^{(l)} + \frac{1}{\tau}A_{k,l}(\mathcal{G}_{f_{i,j}}^{(l)} - f_{i,j}^{(l)})\Big]d\boldsymbol{\xi} + \\ & \frac{A_{k,k}\Delta t}{\tau}\rho_{i,j}^{(k)}(\mathcal{T}_{i,j}^{(k)} + \mathbf{U}_{i,j}^{(k)}\otimes\mathbf{U}_{i,j}^{(k)})\Big) \\ =& \frac{\tau Pr}{A_{k,k}\Delta t + \tau Pr}\Big(\Sigma_{i,j}^{n} - \Delta t\sum_{l=1}^{k-1}\int_{\Omega_{\boldsymbol{\xi}}}\Big[\tilde{A}_{k,l}\boldsymbol{\xi}\nabla_{\mathbf{x}} f_{i,j}^{(l)} + \frac{1}{\tau}A_{k,l}(\mathcal{G}_{f_{i,j}}^{(l)} - f_{i,j}^{(l)})\Big]d\boldsymbol{\xi} + \\ & \frac{A_{k,k}\Delta t}{A_{k,k}\Delta t + \tau Pr}\rho_{i,j}^{(k)}(T_{i,j}^{(k)} I + \mathbf{U}_{i,j}^{(k)}\otimes\mathbf{U}_{i,j}^{(k)})\Big)\end{aligned}$$

$\Sigma_{i,j}^{(k)}$ can be then calculated explicitly and $\Theta_{i,j}^{(k)}$ is deduced. Thus, $\mathcal{G}_{f_{i,j}}^{(k)}$ and $f_{i,j}^{(k)}$ can be computed solving linear scalar equations.

In the following we will be interested in first and second order schemes, hence we use the IMEX schemes given by the following tableaux:

First-order scheme:

$$\begin{array}{c|c} 0 & \\ \hline 1 & \end{array} \qquad\qquad \begin{array}{c|c} 1 & \\ \hline 1 & \end{array}$$

Explicit scheme Implicit scheme

Second-order scheme:

0	0	0
0	0	0
0	1	0
0	$\frac{1}{2}$	$\frac{1}{2}$

Explicit scheme

$\frac{1}{2}$	0	0
$-\frac{1}{2}$	$\frac{1}{2}$	0
0	$\frac{1}{2}$	$\frac{1}{2}$
0	$\frac{1}{2}$	$\frac{1}{2}$

Implicit scheme

For computational time requirements reasons, steady state calculations will always be done with a first order scheme in time while unsteady state results will be computed with the second order scheme both in space and time.

Thanks to IMEX schemes, the stability of the numerical scheme is dictated only by the convective terms. Thus, in 2D, the CFL condition reads:

$$\Delta t < \min_{i,j}\left(\frac{\Delta x}{\xi_u^i}, \frac{\Delta y}{\xi_v^j}\right) \tag{II.17}$$

where i and j are the indices of the 2D velocity discretization.

II.5 Inlet and outlet boundary conditions

This section introduces three kinds of boundary condition that can be applied on the domain boundaries. We suppose that the gas in the computational domain is immersed in a fluid in the hydrodynamic regime. Wall boundary conditions will be introduce in the next chapter.

For all the boundary conditions, ghost cells are introduced where the distribution function is imposed. The type of boundary condition considered determines the distribution function imposed in the ghost cell. The fluxes are then calculated as usual.

II.5.1 Free flow boundary condition

The simplest condition considers that the fluid at the boundaries of the computational domain and the fluid in the ghost cells have the same state. It means that the flow is entirely determined by what is occurring inside the domain. The boundary condition is then imposed through a distribution function f_{ff} in the ghost cells set equal to the distribution function in the first computational cell. This condition is usually used in outlet.

II.5.2 Inflow or outflow boundary conditions

The name depends on where the condition is imposed. A condition imposed at the inlet (respectively outlet) is called inflow (respectively outflow) boundary condition. It corresponds to imposing a fluid state outside the domain through macroscopic variables. The boundary condition is then imposed through the corresponding Maxwellian (in the case of the BGK model) or Gaussian (in the case of the ES-BGK model) computed with respects to the macroscopic quantities prescribed.

The imposed state can be constant in time or can vary. The case with constant state is usually used for stationary computations where the flow at the boundary is not perturbed. Imposing an unsteady state can be useful when shocks or fan are supposed to pass through the boundary. For example, the simulation of a flow in a pipe can consider that one side of the pipe is linked to a tank filled with the fluid where total pressure P^0 and total temperature T^0 do not vary in time. Hence, the value of the imposed density, velocity and temperature is adapted

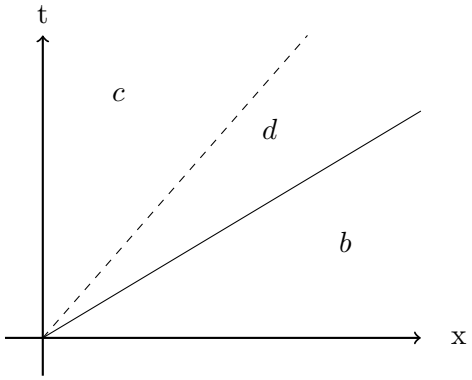

Figure II.4: Representation of the right part of the Riemann problem with the different states (b, c, d). The dash line is the contact discontinuity while the solid line is the fastest wave.

according to the macroscopic values in the first cell of the domain as follows. This procedure is done assuming that the gas outside the computational domain is in equilibrium (this is not necessarily true but the boundary condition is imposed), isentropic and solving the resulting Riemann problem in the normal direction to the boundary.

Let us consider in 1D the case of an inflow boundary condition with imposed total pressure P^0 and total temperature T^0. We are interested in solving the right part of the Riemann problem (see figure II.4).

For each state, we define s the entropy, p the pressure, T the temperature, u the velocity and a the speed of sound. The state b represents the first cell while P^0 and T^0 are imposed in state c.

We have the following relationships:

$$T^0 = T_c\Big(1 + \frac{\gamma-1}{2}\frac{u_c^2}{a_c^2}\Big) \tag{II.18a}$$

$$s_d = s_b = \gamma \log(T_d) - (\gamma-1)\log(p_d) \tag{II.18b}$$

$$s_c = \gamma \log(T_c) - (\gamma-1)\log(p_c) \tag{II.18c}$$

$$R_- = u_b - \frac{2a_b}{\gamma-1} = u_d - \frac{2a_d}{\gamma-1} \tag{II.18d}$$

$$p_d = p_c \tag{II.18e}$$

$$u_d = u_c \tag{II.18f}$$

where R_- is a Riemann invariant. We can deduce from (II.18b), (II.18c) and (II.18e)

$$\Delta s = \frac{a_d}{a_c} = \exp\Big(\frac{s_d - s_c}{2\gamma}\Big) \tag{II.19}$$

From the expression of the total temperature (II.18a) and using (II.18d), (II.18f) and (II.19), it is possible to write an equation verified by a_c:

$$\Big(1 + \frac{2\Delta s}{\gamma-1}\Big)a_c^2 + 2R^-\Delta s a_c + \frac{\gamma-1}{2}R_-^2 - \gamma T^0 = 0 \tag{II.20}$$

It is then possible to find a_c as the positive solution of (II.20) and then deduce the values of u_c and T_c from the expression of the total temperature (II.18a). The equilibrium function imposing the boundary condition can now be built as usual.

II.5.3 Symmetric boundary condition

The symmetric condition considers that the boundary of the domain is an axis of symmetry of the flow. In the ghost cell, the flow has the same properties than in the first cell except for the normal component of the velocity which is the opposite ($u_{ghost} = -u_1$ in 1D). In other words, the particles that have velocity $\boldsymbol{\xi}$ in the first cell, have velocity $\boldsymbol{\xi} - 2\boldsymbol{\xi} \cdot \mathbf{n}_b$ in the ghost cell. $\mathbf{n}_b$ is always a vector of the Cartesian base since it is a normal to the domain boundary considered of the Cartesian grid. The symmetric boundary condition is imposed through the distribution function f_s expressed as:

$$f_s(\boldsymbol{\xi}) = f_1(\boldsymbol{\xi} - 2\boldsymbol{\xi} \cdot \mathbf{n}_b) \tag{II.21}$$

The velocity grid being Cartesian and symmetric with respect to zero, $f_1(\boldsymbol{\xi} - 2\boldsymbol{\xi} \cdot \mathbf{n}_b)$ is always defined, and in particular it is known in the first computational cells.

Chapter III

An accurate asymptotic preserving boundary condition on Cartesian grid

One fundamental property of kinetic models is that they are consistent with the hydrodynamic limit at continuous level. As seen in section I.1.2.3, the Euler limit should be recovered for very small Knudsen numbers. If this problem has been addressed for the numerical scheme (see for example the review [71]), the same attention has not been devoted to the AP enforcement of the boundary condition. Preserving the accuracy up to the boundary is not a trivial task [53]. Moreover, the behaviour of kinetic boundary conditions as the Knudsen number goes to zero has not been clearly investigated yet. In particular, as it will be shown in the following, a classical implementation of the boundary conditions induces spurious effects that pollute the solution.

In this chapter, two contributions are introduced concerning the asymptotic behaviour of the scheme towards the hydrodynamic regime. In particular, the chapter focuses on the boundary conditions with a special care on the preservation of the asymptotic limit towards compressible Euler equations leading to devise a new boundary condition. Moreover, a modification of the numerical scheme is proposed to integrate this idea keeping a second order accuracy up to the possibly moving boundaries. The methods presented here as well as some results have been published in [14] for the BGK model and in [13] for the ES-BGK model.

The first section gives an overview on some techniques to determine the position of a possibly moving body. We then introduce the level set function used to describe an immersed bodies on Cartesian grids. Then, usual wall boundary conditions for kinetic models are presented highlighting the need of devising a new boundary condition to deal with the asymptotic preserving properties. A new boundary condition is proposed and section III.3 is devoted to its enforcement at the desired order of accuracy on a Cartesian grid. Finally, the last section of this chapter illustrates with numerical results the need of such a boundary condition and the accuracy of the proposed method.

III.1 Interface detection methods

In this section we briefly describe some methods used in the literature to detect the position of an immersed body and in particular the interface between the fluid and the solid. As explained in Section II.2, we chose to use Cartesian grids because they are suitable for massive parallel

computations and because there is no need to create a new mesh when the body moves. The cost of this mesh generation step is actually transferred to the enforcement of the boundary condition when the grid is not adapted to the body. Hence, one needs to apply the wall boundary condition on a surface that is arbitrarily crossing the grid. To do so, some geometrical informations are necessary to know the position of the interface.

III.1.1 The volume of fluid method (VOF)

Different methods exists to treat this interface. The method Volume of Fluid (VOF) introduced by Hirt et al. [63] uses a function C (called "*color function*") going from 0 to 1 describing the volume fraction occupied by the fluid. The difficulty is in the reconstruction of the interface with enough precision. A first approximation consist in representing the interface parallel to a grid direction according to the value of the function C. It gives a first order accuracy reconstruction. Higher order reconstruction can be obtained by representing the interface by a discontinuous function [100].

In incompressible flows, the volume conservation at the discrete level (equivalent to the mass conservation for compressible flows) is ensured through the transport of the function C. Since we have:

$$\nabla \cdot \mathbf{U} = 0$$

where $\mathbf{U}$ is the fluid velocity, the transport equation for the function C in conservative form reads as:

$$\partial_t C + \nabla \cdot (C\mathbf{U}) = 0 \tag{III.1}$$

The VOF method has been successfully applied to compressible flows in [103].

III.1.2 The front tracking method

Another method has been developed by Glimm et al. [59] called front tracking method. It is based on Lagrangian markers on the interface. The front is reconstructed linearly between the markers. Two different states are associated to these markers to transport the interface and compute the fluxes for each phase. These states are extrapolation of the states inside each phase to create a ghost state. Thus, the fluxes are computed only with data coming from the same phase. The jump condition coming from the extrapolation on both side of the interface is used to propagate the front and update the states in the cells that change phase.

III.1.3 The level set function

Here, we employ a geometrical description of the interface through a distance function. Introduced by Osher and Sethian [91], the level set function implicitly defines the solid interface Σ in the computational domain by its zero isoline. It gives the signed distance function between a grid point and the immersed body. Its regularity allows the use of efficient transport scheme which is one of its main advantages. We refer the reader to [90] for an overview of the possible applications of the levelset method.

In the solid the values of the physical variables are imposed in each cell since there is no calculation to perform. Such cells are called penalized cells. To decide whether or not a cell is penalized on a Cartesian mesh and to improve accuracy at the boundaries, we use the sign of the levelset function. It is defined by:

$$\phi(\mathbf{x}) = \begin{cases} dist_\Sigma(\mathbf{x}) & \text{outside the solid} \\ -dist_\Sigma(\mathbf{x}) & \text{inside the solid} \end{cases} \tag{III.2}$$

where $dist_\Sigma(\mathbf{x})$ is the minimum distance between the point considered (with coordinates $\mathbf{x}$) and the solid interface Σ.

Thanks to this function it is possible to compute the unit normal of the distance isoline through $\mathbf{x}$, pointing towards the fluid as

$$\mathbf{n}(\mathbf{x}) = \frac{\nabla_\mathbf{x}\phi(\mathbf{x})}{|\nabla_\mathbf{x}\phi(\mathbf{x})|} \tag{III.3}$$

For $\phi = 0$, we have the unit normal to the interface, $\mathbf{n}_w(x)$.

In case of moving geometries, the level set function is convected with the imposed boundary velocity $\mathbf{u}_\phi$:

$$\partial_t\phi + \mathbf{u}_\phi \cdot \nabla_\mathbf{x}\phi = 0 \tag{III.4}$$

For the numerical test cases, when needed, this equation is solved with a WENO5 [69] discretization scheme in space and a standard Runge-Kutta 4 scheme for the integration in time.

Integrating (III.4) in time does not preserve the distance property of ϕ if the velocity field $\mathbf{u}_\phi$ is not uniform (which is usually the case). Therefore, a reinitialisation step is performed after each time integration step to keep this property. This step is based on the resolution of the Eikonal equation:

$$|\nabla_\mathbf{x}\phi| = \frac{1}{\mathbf{v}(\mathbf{x})} \tag{III.5}$$

In our case this equation has to be solved for a velocity $\mathbf{v}(\mathbf{x}) = 1$. A popular method is the Fast Marching algorithm [105]. The Eikonal equation is solved as $|\nabla_\mathbf{x}\phi|^2 = 1$ iterating from one cell to the other starting from a narrow band near the interface ($\phi = 0$).

Now that the interface between the solid and the fluid is defined, we can focus on the boundary condition on the body and how to enforce it. Let us first present the different types of wall boundary conditions for kinetic models.

III.2 Wall boundary conditions

Two kinds of boundary conditions for kinetic models are usually found in the literature: the diffuse boundary condition and the specular reflection.

The diffuse boundary condition model assumes that the solid is in thermodynamic equilibrium with the fluid in contact with the wall. The distribution function for the fluid is therefore described by a wall Maxwellian distribution function, M_w, computed with given temperature and velocity of the wall.

The specular reflection models a wall at which particles are merely reflected. There is no mass and energy fluxes through the wall (impermeability condition). The distribution function f_s, corresponding to this boundary condition is a reflection of the distribution function coming from the fluid.

Both models can be taken into account using an accommodation coefficient $\alpha \in [0, 1]$ to create the boundary (Maxwell,[26]) model:

$$f_b = \alpha f_d + (1 - \alpha) f_s \tag{III.6}$$

where f_b is the distribution function representing the actual wall model.

The coefficient α depends on the gas and the solid considered, through the gas-surface interaction model chosen. A review on gas-surface interactions can be found in [60]. In this work we focus on the asymptotic behaviour of the scheme towards Euler equations with particular

emphasis on the asymptotic behaviour of the boundary condition. Imposing a temperature and a velocity at the wall cannot provide an asymptotic preserving boundary condition, because in Euler equations only the component of the velocity normal to the wall can be prescribed. Hence, the case $\alpha > 0$ cannot provide an asymptotic preserving boundary condition. Thus, to make sure that the boundary condition preserves the Euler limit, it is necessary that $\alpha \to 0$ close to the hydrodynamic regime. However, as our results will show, this is not enough to obtain an AP boundary condition. In the following we will show how to modify specular reflection to preserve the Euler limit. For this reason, in the numerical tests, we will concentrate on the case $\alpha = 0$. However, for completeness, we also present the diffuse boundary condition to include the case of non equilibrium flows, far from the Euler limit.

III.2.1 The diffuse boundary condition

We use this wall model in the formulation of the Euler-AP boundary condition presented later, see section III.2.2.2. The diffuse condition is imposed through a Maxwellian distribution function. Boundary conditions prescribe temperature, velocity and zero mass flux. The wall Maxwellian is first computed with a density of 1, temperature and velocity of the wall. Then by invoking mass conservation through the wall, one can recover the density ρ_w. Indeed, mass conservation near the wall can be written

$$F_{in} + F_{out} = 0$$

with F the mass flux with subscript "in" to denote the flux going towards the wall and "out" the flux going towards the fluid at the physical interface. Then F_{out} corresponds to the quantity of mass going towards the fluid with the wall characteristics (density, temperature, velocity) and with a Maxwellian distribution M_{fw}, called the wall Maxwellian. We have:

$$\int_{(\boldsymbol{\xi}-\mathbf{U}_w)\cdot\mathbf{n}_w<0} (\boldsymbol{\xi}-\mathbf{U}_w)\cdot\mathbf{n}_w f_w d\boldsymbol{\xi} + \int_{(\boldsymbol{\xi}-\mathbf{U}_w)\cdot\mathbf{n}_w>0} (\boldsymbol{\xi}-\mathbf{U}_w)\cdot\mathbf{n}_w M_{fw} d\boldsymbol{\xi} = 0$$

with f_w the distribution function near the wall (for example the one in the closest fluid cell), M_{fw} the wall Maxwellian and $\mathbf{n}_w$ the normal to the wall pointing towards the fluid. This equation can also be expressed in terms of the wall macroscopic quantities (velocity $\mathbf{U}_w$, temperature T_w and density near the wall ρ_w):

$$\int_{(\boldsymbol{\xi}-\mathbf{U}_w)\cdot\mathbf{n}_w<0} (\boldsymbol{\xi}-\mathbf{U}_w)\cdot\mathbf{n}_w f_w d\boldsymbol{\xi} + \rho_w \int_{(\boldsymbol{\xi}-\mathbf{U}_w)\cdot\mathbf{n}_w>0} \frac{(\boldsymbol{\xi}-\mathbf{U}_w)\cdot\mathbf{n}_w}{(2\pi T_w)^{3/2}} \exp\Big(-\frac{|\,\boldsymbol{\xi}-\mathbf{U}_w\,|^2}{2T_w}\Big) d\boldsymbol{\xi} = 0$$

$$\int_{(\boldsymbol{\xi}-\mathbf{U}_w)\cdot\mathbf{n}_w<0} (\boldsymbol{\xi}-\mathbf{U}_w)\cdot\mathbf{n}_w f d\boldsymbol{\xi} + \rho_w \int_{(\boldsymbol{\xi}-\mathbf{U}_w)\cdot\mathbf{n}_w>0} (\boldsymbol{\xi}-\mathbf{U}_w)\cdot\mathbf{n}_w \overline{M_{fw}} d\boldsymbol{\xi} = 0$$

with $\overline{M_{fw}}$ the wall Maxwellian corresponding to a density of 1. Then, $\overline{M_{fw}}$ can be computed with a Newton-Raphson algorithm (discrete Maxwellian).

Then the density ρ_w can be calculated as :

$$\rho_w = -\frac{\int_{(\boldsymbol{\xi}-\mathbf{U}_w)\cdot\mathbf{n}_w<0} (\boldsymbol{\xi}-\mathbf{U}_w)\cdot\mathbf{n}_w f d\boldsymbol{\xi}}{\int_{(\boldsymbol{\xi}-\mathbf{U}_w)\cdot\mathbf{n}_w>0} (\boldsymbol{\xi}-\mathbf{U}_w)\cdot\mathbf{n}_w \overline{M_{fw}} d\boldsymbol{\xi}} \tag{III.7}$$

and

$$M_{fw} = \rho_w \overline{M_{fw}}$$

The diffuse boundary condition is then:

$$f_d = \begin{cases} f_w \quad \text{for} \quad (\boldsymbol{\xi} - \mathbf{U}_w) \cdot \mathbf{n}_w < 0 \\ M_{fw} \quad \text{for} \quad (\boldsymbol{\xi} - \mathbf{U}_w) \cdot \mathbf{n}_w > 0 \end{cases} \tag{III.8}$$

It is worth noting that the same condition holds for both kinetic models considered in this work. It is clear for the BGK model but it is also true for the ES-BGK model. Indeed, this boundary condition consider the fluid at thermodynamic equilibrium with the wall. In this case, we have that $f = \mathcal{G}_f = M_f$ as seen in Section I.4.

III.2.2 Impermeability boundary condition

Here the impermeability condition is considered in the sense of Euler equations. Through the boundary there is no mass flux and no energy flux. We first describe how this boundary condition is typically imposed by specular reflection of the distribution function. Then a novel Euler-AP condition method will be introduced for the inviscid limit.

III.2.2.1 Specular reflection

Each particle hitting the wall is immediately reflected by the wall with the same tangential velocity and the opposite normal velocity :

$$\boldsymbol{\xi}_{refl} = \boldsymbol{\xi} - 2((\boldsymbol{\xi} - \mathbf{U}_w) \cdot \mathbf{n}_w)\mathbf{n}_w$$

with $\boldsymbol{\xi}_{refl}$ the particle velocity after reflection, $\boldsymbol{\xi}$ the particle velocity before reflection, $\mathbf{U}_w$ the wall velocity and $\mathbf{n}_w$ the normal to the wall. This holds true for each particle such that $(\boldsymbol{\xi} - \mathbf{U}_w) \cdot \mathbf{n}_w > 0$. For $(\boldsymbol{\xi} - \mathbf{U}_w) \cdot \mathbf{n}_w < 0$, the distribution function on the boundary is already known and equal to the one in the fluid cell. The distribution function for the boundary condition has to be computed only for $(\boldsymbol{\xi} - \mathbf{U}_w) \cdot \mathbf{n}_w > 0$. The entire distribution function f_s enforcing the boundary condition is then:

$$f_s = \begin{cases} f_w \quad \text{for} \quad (\boldsymbol{\xi} - \mathbf{U}_w) \cdot \mathbf{n}_w < 0 \\ f_w(\boldsymbol{\xi}_{refl}) \quad \text{for} \quad (\boldsymbol{\xi} - \mathbf{U}_w) \cdot \mathbf{n}_w > 0 \end{cases} \tag{III.9}$$

In the reduced model, the same procedure is applied to ϕ and ψ. This guarantees zero mass and energy fluxes (now $\mathbf{U}_w$ is set to zero for simplicity):

$$\begin{aligned} F_{mass} &= \int_{\boldsymbol{\xi}\cdot\mathbf{n}_w<0} \boldsymbol{\xi} \cdot \mathbf{n}_w f_w(\boldsymbol{\xi}) d\boldsymbol{\xi} + \int_{\boldsymbol{\xi}\cdot\mathbf{n}_w>0} \boldsymbol{\xi} \cdot \mathbf{n}_w f_w(\boldsymbol{\xi}_{refl}) d\boldsymbol{\xi} \\ &= \int_{\boldsymbol{\xi}\cdot\mathbf{n}_w<0} \boldsymbol{\xi} \cdot \mathbf{n}_w f_w(\boldsymbol{\xi}) d\boldsymbol{\xi} + \int_{\boldsymbol{\xi}\cdot\mathbf{n}_w<0} -\boldsymbol{\xi} \cdot \mathbf{n}_w f_w(\boldsymbol{\xi}) d\boldsymbol{\xi} \\ &= 0 \end{aligned}$$

$$\begin{aligned} F_{energy} &= \int_{\boldsymbol{\xi}\cdot\mathbf{n}_w<0} |\boldsymbol{\xi}|^2 \boldsymbol{\xi} \cdot \mathbf{n}_w f_w(\boldsymbol{\xi}) d\boldsymbol{\xi} + \int_{\boldsymbol{\xi}\cdot\mathbf{n}_w>0} |\boldsymbol{\xi}|^2 \boldsymbol{\xi} \cdot \mathbf{n}_w f_w(\boldsymbol{\xi}_{refl}) d\boldsymbol{\xi} \\ &= \int_{\boldsymbol{\xi}\cdot\mathbf{n}_w<0} |\boldsymbol{\xi}|^2 \boldsymbol{\xi} \cdot \mathbf{n}_w f_w(\boldsymbol{\xi}) d\boldsymbol{\xi} + \int_{\boldsymbol{\xi}\cdot\mathbf{n}_w<0} -|\boldsymbol{\xi}|^2 \boldsymbol{\xi} \cdot \mathbf{n}_w f_w(\boldsymbol{\xi}) d\boldsymbol{\xi} \\ &= 0 \end{aligned}$$

However, because of the discretization of the velocity space, one needs to compute $f_w(\boldsymbol{\xi}_{refl})$ where in general $\boldsymbol{\xi}_{refl}$ does not correspond to a collocation point. In other words, even though $\boldsymbol{\xi}$

is a grid point, $\boldsymbol{\xi}_{refl}$ is not a velocity grid point except if the wall is parallel to the grid. Therefore $\boldsymbol{\xi}_{refl}$ must be interpolated. The numerical experiments show that the interpolation must be higher-order accurate to guarantee zero mass and energy fluxes at the wall to an acceptable degree of approximation.

In the 1D case, this problem does not arise. It is enough to have a velocity grid symmetric with respect to $\xi_u = 0$. Specular reflection reduces then to choose $f_s(\xi_u) = f_w(-\xi_u)$ in order to build the reflected distribution function.

In 2D, due to interpolation errors, mass and energy fluxes are not identically zero at the walls. This error leads to a boundary layer in the limit of inviscid gas simulations that should not exist. As shown in the numerical illustrations, to remove this spurious effect it is possible to use either a finer velocity grid or a higher-order interpolation, at the price of significantly larger computational costs.

III.2.2.2 A new discrete Euler-AP impermeability condition

A cure is proposed here to remove this spurious effect. It will be describe in the case of the BGK model.

Let us assume that the distribution function is a Maxwellian (Kn number close to 0). Then, imposing the impermeability condition at the wall corresponds to impose a Maxwellian distribution function at the wall exactly as described in section III.2.1. However, in this case the velocity must have the same tangential component of the fluid next to the boundary with zero wall-normal component and the temperature must be the same of the fluid. Therefore, in contrast with what is done in section III.2.1, tangential velocity and temperature are extrapolated from the fluid to the wall. If f_M denote such a boundary condition we have:

$$f_M = \frac{\rho_w^{'}}{(2\pi T_w)^{3/2}} \exp\Big(- \frac{|\boldsymbol{\xi} - \mathbf{U}_w^{'}|^2}{2T_w} \Big) \tag{III.10}$$

where $\rho_w^{'}$ is the density verifying a zero mass flux, T_w is the temperature extrapolated from the fluid and $\mathbf{U}_w^{'}$ is the velocity extrapolated from the fluid $\mathbf{U}_w$ with a zero normal velocity component: $\mathbf{U}_w^{'} = \mathbf{U}_w - (\mathbf{U} \cdot \mathbf{n}_w)\mathbf{n}_w$.

Let us now calculate the fluxes through the wall of unit normal $\mathbf{n}_w$. In the hydrodynamic regime we have at the boundary:

$$f_w(\boldsymbol{\xi}) = \frac{\rho_w}{(2\pi T_w)^{3/2}} \exp\Big(- \frac{|\boldsymbol{\xi} - \mathbf{U}_w|^2}{2T_w} \Big)$$

where ρ_w is the gas density close to the wall.

Then the fluxes through the wall are:

$$\begin{aligned} F_{mass} &= \frac{\rho_w}{(2\pi T_w)^{3/2}} \int_{\boldsymbol{\xi}\cdot\mathbf{n}_w<0} \boldsymbol{\xi} \cdot \mathbf{n}_w \exp\Big(- \frac{|\boldsymbol{\xi} - \mathbf{U}_w|^2}{2T_w} \Big) d\boldsymbol{\xi} \\ &\quad + \frac{\rho_w^{'}}{(2\pi T_w)^{3/2}} \int_{\boldsymbol{\xi}\cdot\mathbf{n}_w>0} \boldsymbol{\xi} \cdot \mathbf{n}_w \exp\Big(- \frac{|\boldsymbol{\xi} - \mathbf{U}_w^{'}|^2}{2T_w} \Big) d\boldsymbol{\xi} \\ &= 0 \end{aligned}$$

The mass fluxes are identically zero because the density $\rho_w^{'}$ is computed such that it is zero.

$$F_{energy} = \frac{\rho_w}{(2\pi T_w)^{3/2}} \int_{\boldsymbol{\xi}\cdot\mathbf{n}_w<0} |\boldsymbol{\xi}|^2 \boldsymbol{\xi}\cdot\mathbf{n}_w \exp\Big(-\frac{|\boldsymbol{\xi}-\mathbf{U}_w|^2}{2T_w}\Big) d\boldsymbol{\xi} + \frac{\rho_w^{'}}{(2\pi T_w)^{3/2}} \int_{\boldsymbol{\xi}\cdot\mathbf{n}_w>0} |\boldsymbol{\xi}|^2 \boldsymbol{\xi}\cdot\mathbf{n}_w \exp\Big(-\frac{|\boldsymbol{\xi}-\mathbf{U}_w^{'}|^2}{2T_w}\Big) d\boldsymbol{\xi}$$

If the velocity at the boundary $\mathbf{U}_w$ has a zero normal velocity component, then the energy flux is zero. If not, the energy flux is not zero because the fluxes are calculated with an upwind scheme and then, the distribution function for $\boldsymbol{\xi}\cdot\mathbf{n}_w < 0$ is taken from the fluid and not the boundary condition. However, since the boundary condition imposes a zero normal velocity, the energy flux goes quickly to zero. At steady state, the mass and energy fluxes are always identically zero. The boundary condition is then expressed as:

$$f_{AP} = \begin{cases} f_w & \text{for} \quad (\boldsymbol{\xi}-\mathbf{U}_w)\cdot\mathbf{n}_w < 0 \\ f_M & \text{for} \quad (\boldsymbol{\xi}-\mathbf{U}_w)\cdot\mathbf{n}_w > 0 \end{cases} \tag{III.11}$$

Eventually, the diluted fluid next to the wall can be considered Maxwellian only in the limit of the continuum regime. To build a fully asymptotic preserving boundary condition valid in more rarefied regimes, this model is included in equation (III.6) with a new coefficient β:

$$f_b = \alpha f_d + (1-\alpha)(\beta f_s + (1-\beta) f_{AP}) \tag{III.12}$$

with $\beta \in [0,1]$ and such that it is close to zero in the inviscid limit for $Kn \to 0$ and f_{AP} is the distribution function built along the lines described above. If Kn is not close to zero, the classic specular reflection ($\beta \to 1$ and $f_b \to \alpha f_d + (1-\alpha) f_s$) correctly takes over.

To set the value of β we emphasize that f_{AP} corresponds to the specular reflection only when the distribution function in the fluid is close to a Maxwellian. If it is not the case, the specular reflection is computed with f_s (in particular in the rarefied regime). Thus, in our model, β is set as follows:

$$\beta = \min\Big(1, \frac{||f - M_f||_{L^2}}{\max(f) tol}\Big) \tag{III.13}$$

with *tol* a tolerance on the distance in L^2 norm between the distribution function in the closest cell immersed in the fluid f and its corresponding Maxwellian. Thus, if $\frac{||f-M_f||_{L^2}}{\max(f)} << tol$, the specular reflection fully corresponds to the Euler-AP boundary condition. Conversely, in the rarefied regime, f is far from the Maxwellian, then $\beta = 1$ and the classical specular reflection correctly takes over. The tolerance *tol* is used to reduce the sensitivity of the algorithm to $||f - M_f||$. To ensure the correct asymptotic behaviour, when f is sufficiently close to the Maxwellian, β must tend to 0. The value of *tol* does not need to be precisely set since if f is far from the Maxwellian, numerical errors are introduced by both the classical specular reflection (due to interpolations) and the new Euler-AP condition since it is not exactly the reflection of f. Thus, a criterion to correctly set *tol*, is that the two sources of error should balance, that is $tol \sim \Delta\xi_u^2$ which is the order of the interpolation error, if the trapezoid rule is used for quadrature.

The general form of this boundary condition is actually the same for both kinetic models (BGK and ES-BGK). The only difference is in the Maxwellian distribution function that has to be replaced by the Gaussian distribution in the case of the ES-BGK model. In the following, it will be refer in both cases as Euler-AP condition keeping in mind this difference.

III.3 Boundary condition enforcement on Cartesian grid

In this section, we present a short overview of the immersed boundary methods usually used to enforce a boundary condition on an interface arbitrarily crossing the grid. Then, a Cartesian scheme is proposed to impose the new Euler-AP boundary condition at the desired order.

III.3.1 Immersed boundary methods

In a recent review by Mittal and Iaccarino [86], different methods to treat immersed boundaries are presented. Most of the methods presented have been successfully applied to Navier-Stokes and Euler equations. However, very few work has been done yet for kinetic models making this contribution of interest. We can distinguish three main classes of methods: the penalization methods, the conservative methods and the interpolation methods. In the penalization methods, the boundary condition is enforced at the continuous level. A term is added in the equation to simulate the presence of the boundary. The pioneer idea comes from Peskin for incompressible blood flows [96]. The membrane of the vessels moves under the action of the viscous blood flows and applies a force on the fluid. This force is integrated in the equation to simulate the presence of the boundaries. However, the impermeability condition was not clearly imposed and leaking of the fluid in the solid has been observed [116]. Another drawback is the accuracy of the method which is only first order. Moreover, the method is hardly applicable to rigid solids since the law for elastic bodies in the rigid limit is not well defined. Some issues were fixed by Leveque et al. [80], especially for the accuracy and the rigid limit, by incorporating jump conditions. Penalization methods are also enforcing the boundary condition at the continuum limit by considering the flow in a porous media with a variable porosity. It has been done successfully for Navier-Stokes equations for incompressible flows [5], [74] by adding a force $F = \frac{1}{K}u$ where K is 0 in the solid and infinity in the fluid. This force drives the velocity of the fluid to 0 in the solid and does not affect the equation for the fluid part. The same idea was applied to compressible flows [17], [81] by penalizing the momentum and the energy equations. However, as the porosity goes to zero, a stong restriction appears on the time step and an implicit scheme for the penalization term should be used.

The second class of immersed boundary methods are the conservative methods. The condition is enforced at the discrete level by modifying the scheme in cells cut by the interface. They are usually referred to as Embedded Boundary methods or Cut-Cell methods [68], [117]. When a cell contains a solid part, it is cut along a straight line approximating the interface. A new numerical interface is created where the boundary condition is imposed through the flux. This method has the advantage of conserving mass, momentum and energy but cut-cells can be very small and thus, impose a strong restriction on the time step to keep stability. Several cures where proposed mostly based on merging the small cut-cell with an entirely fluid neighbour cell [67]. In [38] or in [104], some advantages of such methods are shown with respect to others thanks to the conservation property. However, it becomes particularly complex in 3D to treat all the possible geometrical configurations of a cut-cell.

Another approach has been proved to be efficient for compressible equation. It is based on interpolated states to impose the boundary condition in the vicinity of the boundaries. The pioneer works of Fedkiw [48], [47] introduced the Ghost-Fluid method for multi-materials flows. In [87], the technique is applied to rigid solids. A fictitious state is created in the neighbouring solid cell to compute the fluxes as usual. The state is created by interpolating the macroscopic quantities in the normal direction of the interface and by satisfying the boundary condition. It is locally non-conservative but the order of accuracy can be set *a priori*. This idea has been successfully applied for compressible Euler equations [61] or elliptic equations [34], [54]. In the following, we extend this idea to kinetic models and show how a first and second order accuracy

scheme based on extrapolation is obtained to enforce the boundary condition.

III.3.2 A Cartesian scheme

In this section we describe the scheme to impose the Euler-AP boundary condition of section III.2.2.2 to immersed boundaries on Cartesian grids for the BGK model. The scheme for the ES-BGK model is identical except that instead of using the Maxwellian distribution function M_f we uses the Gaussian distribution function $\mathcal{G}_f$. The diffuse and the specular reflection schemes are similar. Also, it should be noted that this technique can be easily applied to the case of body fitted grids.

In the case of a solid immersed in the flow, a fictitious state has to be created in the solid to compute the transport step numerically between a fluid cell and a cell containing the solid. The idea is first to compute the equivalent distribution function at the solid interface satisfying the imposed boundary condition and then create a fictitious state in the neighbour solid cell called ghost cell that respects the boundary value at a given approximation order. To do so, a few parameters on the boundary are needed. These parameters are presented in figure III.1.

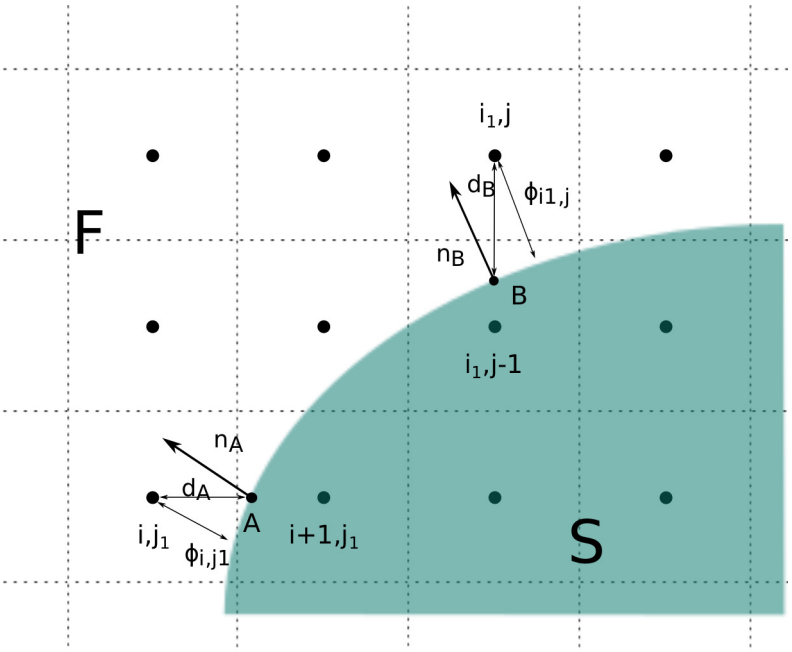

Figure III.1: Immersed interface on a Cartesian mesh.

In each grid point, the shortest distance to the boundary ϕ is known through the levelset function (eq.III.2). One can also compute the normal $\mathbf{n}$ to the boundary in each grid point thanks to (III.3). In the following, we distinguish the interface between two cells and the interface between the fluid and the solid. The first interface will be called numerical interface (where the numerical fluxes are computed) while the latter will be called the physical interface (where the boundary condition is imposed).

The problem reduces to detemine a Maxwellian distribution function on the boundary and extrapolate or interpolate it to the numerical interface.

The point A will be used to compute the interpolation at the interface $i+1/2, j1$. The fluxes at interface $i1, j-1/2$ will be computed by calculating the wall Maxwellian on point B. Since the same scheme is used on points A and B, the method will be explained on point A.

III.3.2.1 First order Euler-AP scheme

To compute the fictitious state at first order, the Maxwellian distribution function at the wall is built as presented previously in III.2.1 with the tangential velocity $\mathbf{U}_A \cdot \boldsymbol{\tau}_{i,j1}$ and temperature T_A taken from the fluid cell and a zero relative normal velocity $(\mathbf{U}_A - \mathbf{U}_w) \cdot \mathbf{n}_{i,j1}$:

$$\begin{cases} T_A = T_{i,j1} \\ (\mathbf{U}_A - \mathbf{U}_w) \cdot \boldsymbol{\tau}_{i,j1} = (\mathbf{U}_{i,j1} - \mathbf{U}_w) \cdot \boldsymbol{\tau}_{i,j1} \\ (\mathbf{U}_A - \mathbf{U}_w) \cdot \mathbf{n}_{i,j1} = 0 \end{cases}$$

The density ρ_A is calculated thanks to the distribution function in cell $(i, j1)$ invoking mass conservation through the wall as in (III.7). The Maxwellian built with ρ_A, $\mathbf{U}_A$, T_A is then simply imposed as the state in the first solid cell $(i + 1, j1)$. The part of the boundary condition f_s corresponding to the specular reflection and f_d corresponding to the diffuse boundary condition can be also easily computed from $f_{i,j1}$ and imposed velocity and temperature. Thus, f_b is fully constructed.

In the case of the ES-BGK model it is necessary to know the opposite stress tensor Θ_A in A. As for the other macroscopic quantities it is set equal to $\Theta_{i+1,j1}$.

III.3.2.2 Second order Euler-AP scheme

The main idea is now to impose the boundary condition on the physical interface and reconstruct the conditions at the numerical interface with second-order accuracy.

The impermeability boundary condition is applied at the physical interface by imposing a Maxwellian distribution function. This distribution function depends on the temperature, the velocity and the distribution function in the fluid. All these information are extrapolated from the fluid. To find the position of the wall, the levelset function is used and the distance d_A between the cell center and the wall is known as:

$$d_A = \frac{\Delta x |\phi_{i,j1}|}{|\phi_{i,j1}| + |\phi_{i+1,j1}|}$$

where $\phi_{i,j1}$ (respectively $\phi_{i+1,j1}$) is the distance between the point $(i, j1)$ (respectively $(i+1, j1)$) and the boundary and Δx is the space grid step. The normal can also be computed by

$$\mathbf{n}_A = \mathbf{n}_{i,j1} + \frac{d_A}{\Delta x}(\mathbf{n}_{i+1,j1} - \mathbf{n}_{i,j1})$$

where $\mathbf{n}_{i,j1}$ (respectively $\mathbf{n}_{i+1,j1}$) is the normal to the boundary in point $(i, j1)$ (respectively $(i + 1, j1)$).

The temperature and the velocity now can be extrapolated with a second order polynomial using $T_{i,j1}$, $T_{i-1,j1}$, $T_{i-2,j1}$ and $\mathbf{U}_{i,j1}$, $\mathbf{U}_{i-1,j1}$, $\mathbf{U}_{i-2,j1}$. The wall temperature T_{ext} is the result of the extrapolation while the wall velocity $\mathbf{U}_{ext}$ is only equal to the tangential part of the extrapolated velocity such that the impermeability condition $((\mathbf{U}_A - \mathbf{U}_w).\mathbf{n}_A = 0)$ is enforced:

$$\begin{cases} T_A = T_{ext} \\ \mathbf{U}_A = \mathbf{U}_{ext} - ((\mathbf{U}_{ext} - \mathbf{U}_w) \cdot \mathbf{n}_A)\, \mathbf{n}_A \end{cases}$$

Again, the opposite stress tensor, Θ_A has to be extrapolated in the same way as the temperature in the case of the ES-BGK model.

To extrapolate the distribution function at the boundary in order to compute the density, an upwind reconstruction is used. For each microscopic velocity $\boldsymbol{\xi}$ such that $(\boldsymbol{\xi} - \mathbf{U}_w) \cdot \mathbf{n}_A < 0$ $f_A(\boldsymbol{\xi})$ is set as:

$$f_A(\boldsymbol{\xi}) = f_{n,m}(\boldsymbol{\xi}) \quad \text{such that} \quad \frac{\mathbf{x}_A - \mathbf{x}_{n,m}}{||\mathbf{x}_A - \mathbf{x}_{n,m}||} \cdot \frac{\boldsymbol{\xi}}{||\boldsymbol{\xi}||} = \max_{(k,l)\in\Upsilon_{i,j1}} \left(\frac{\mathbf{x}_A - \mathbf{x}_{k,l}}{||\mathbf{x}_A - \mathbf{x}_{k,l}||} \cdot \frac{\boldsymbol{\xi}}{||\boldsymbol{\xi}||}\right) \tag{III.14}$$

with $\mathbf{x}_A$ the position of the boundary ($\mathbf{x}_A = \mathbf{x}_{i,j1} + d_A$) and $\Upsilon_{i,j1}$ containing all the fluid neighbours of cell $(i, j1)$. A graphic illustration is given in figure III.2. In this example, the velocity grid has 8 grid points in 2D. The third dimension in velocity is eliminated with the reduced model, which, we recall, is exact (see section **??**). The distribution function is required in A for $\boldsymbol{\xi}_1$, $\boldsymbol{\xi}_6$, $\boldsymbol{\xi}_7$, $\boldsymbol{\xi}_8$. Here $\Upsilon_{i,j}$ is represented in blue. One can create f_A for $(\boldsymbol{\xi} - \mathbf{U}_w) \cdot \mathbf{n}_A < 0$ as :

$$\begin{cases} f_A(\boldsymbol{\xi}_1) = f_{i,j}(\boldsymbol{\xi}_1) \\ f_A(\boldsymbol{\xi}_6) = f_{i+1,j+1}(\boldsymbol{\xi}_6) \\ f_A(\boldsymbol{\xi}_7) = f_{i+1,j+1}(\boldsymbol{\xi}_7) \\ f_A(\boldsymbol{\xi}_8) = f_{i,j+1}(\boldsymbol{\xi}_8) \end{cases}$$

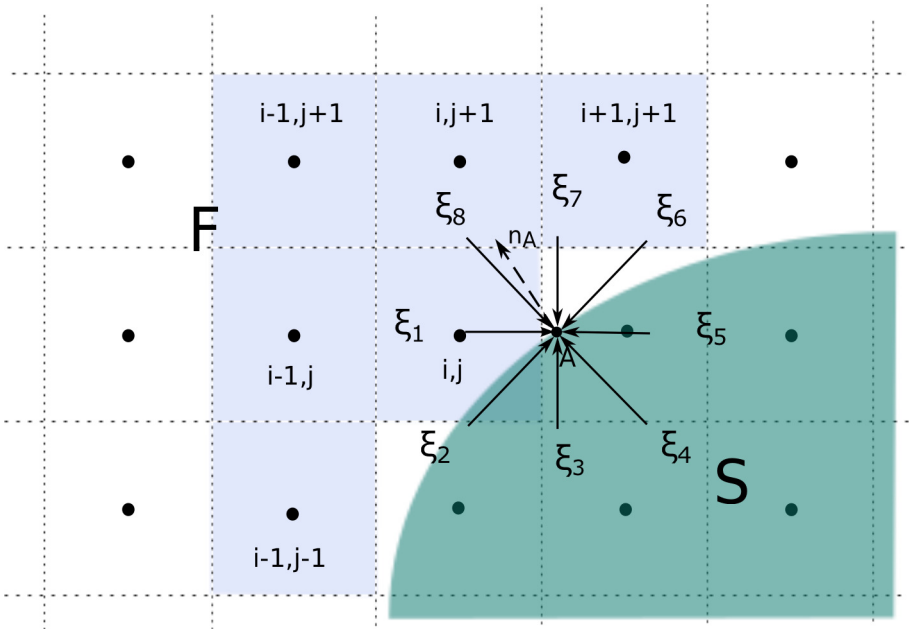

Figure III.2: Graphic illustration of the reconstruction for a 8 velocities grid.

It is worth to remark that this reconstruction avoids interpolation but is not formally second-order accurate. A MUSCL-type reconstruction could be applied instead but an upwind reconstruction has the advantage of taking into account the main direction of the flux. Indeed, a reconstruction with slopes chosen as in (II.13) does not prevent the possibility of selecting a downwind reconstruction which might lead to high extrapolation errors.

The part of f for $(\boldsymbol{\xi} - \mathbf{U}_w) \cdot \mathbf{n}_A > 0$ corresponds to microscopic velocities coming from the wall and is not required for the computation of the wall Maxwellian f_{M_A}.

Finally, the distribution function used as boundary condition can be computed as follows:

$$f_{AP} = \begin{cases} f_A \quad \text{for} \quad (\boldsymbol{\xi} - \mathbf{U}_w) \cdot \mathbf{n}_A < 0 \\ f_{M_A} \quad \text{for} \quad (\boldsymbol{\xi} - \mathbf{U}_w) \cdot \mathbf{n}_A > 0 \end{cases} \tag{III.15}$$

Similarly, f_s and f_d can be built in A from the reconstructed distribution function f_A. Thus, the boundary condition f_b is known in A.

Once the distribution for the boundary condition is known at the wall, it has to be interpolated or extrapolated to the numerical interface with a linear reconstruction to preserve second order. One can use the same slope as in the fluid cell and the exact distance between the numerical (between cells) and physical interface (d_A on figure III.1):

$$f_{i+1/2,j1,r} = f_{AP} + \frac{d_A}{\Delta x}\text{MinMod}(f_{i,j1} - f_{i-1,j1}, f_{i-1,j1} - f_{i-2,j1}) \tag{III.16}$$

The fluxes at the numerical interface can be now computed as usual.

III.4 Numerical results

The accuracy of the Euler-AP boundary condition is initially tested in 1D for cases where the reference solution is exact, section III.4.1. In 2D, we consider well known test cases both on a body fitted mesh (section III.4.2) and on a Cartesian mesh (section III.4.3), in the continuum regime. Second-order accuracy of the method is illustrated on the Ringleb flow (section III.4.4) for the BGK model and on a cylindrical Couette flow for the ES-BGK model (section III.4.5). Furthermore, we compare the Euler-AP wall model to numerical results in the literature in the rarefied regime (section III.4.6). Finally, we simulate a nozzle plume with coexisting continuum and rarefied regime to qualitatively validate the Euler-AP boundary condition against experimental data.

The parameter *tol* is always $tol = 10^{-2}$ according to the criteria described in section III.2.2.2. If the velocity space step is such that $\Delta\xi_u^2$ is not of the order of 10^{-2} the tolerance has to be modified ensuring that $tol \simeq \Delta\xi_u^2$. In order to focus on the spurious effects due to a treatment of the boundary condition which is not AP, and on the improvement we can obtain, in most cases the reference Knudsen numbers tested are very small.

III.4.1 Reflection of a rarefaction wave and a shock wave

Here, we will test the precision of the new Euler-AP method with $\alpha = 0$ for typical 1D problems for which the exact solution is known. In particular, we consider the reflection of a rarefaction wave and a shock wave on a solid wall for a monoatomic gas at equilibrium. The model used is the BGK model. The boundary condition applied at the wall is the impermeability condition with the Euler-AP method. One can note that the classical way to implement it (specular reflection) perfectly works here since there is no need to interpolate in the velocity space. For the rarefaction wave, the exact solution is computed using Riemann invariants with a velocity $v = -0.35$ assigned to the left of the rarefaction wave (see Figure III.3, left). To the right, where the gas is steady, the pressure is 1 and the speed of sound is 1. For the shock, the Rankine-Hugoniot conditions and an exact Riemann problem at the wall are used (see Figure III.3, right). The shock wave propagates at Mach 1.2. Kn_∞ is set to 10^{-10}.

The domain goes from 0 to 3 and the wave is generated at $t = 0$ in 0. The wall position is set to $x = 3$. In order to compute the error of our scheme with respect to the analytical solution, the grid points (center of each cell) are shifted with respect to the wall position as follows:

$$x_i = x_i + \psi\Delta x$$

with Δx the space step and ψ a coefficient varying from 0 to 1. When $\psi = 0.5$, the position of the wall exactly corresponds to a numerical interface. In this case, the error with respect to the analytical solution is optimal.

Numerical simulations are performed with 100 space grid points and 50 grid points in velocity, with an initial data ($t_s = 0$) computed analytically (for Euler equations) at t=1.8 for the rarefaction wave and t=1 for the shock wave. The simulation is stopped at $t_s = 3$ and $t_s = 2$ respectively, when the wave is completely reflected by the wall. This is equivalent to the analytical solution at $t = 4.8$ for the rarefaction wave and $t = 3$ for the shock wave.

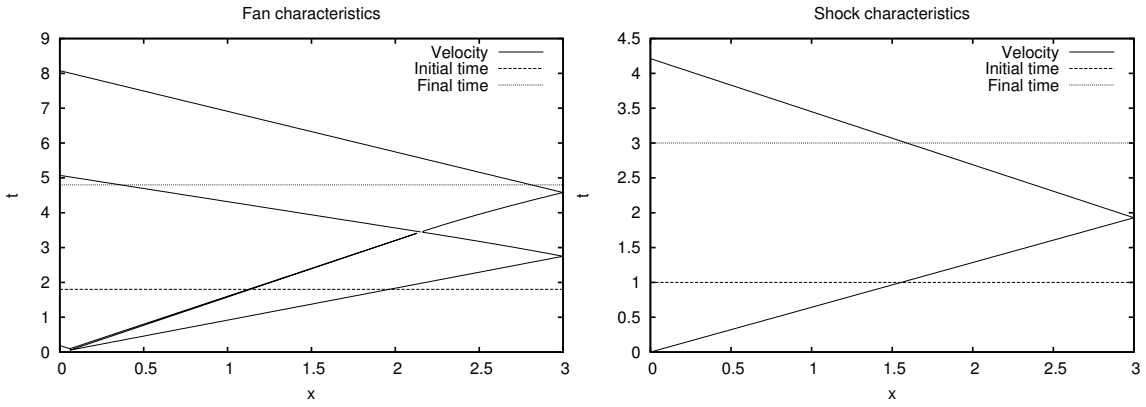

(a) Rarefaction wave (b) Shock wave

Figure III.3: Characteristics for the reflection of a rarefaction wave and a shock wave.

Errors in L_1, L_2 and L_∞-norm for the velocity as a function of ψ (the position of the wall), have been computed and shown on Figure III.4.

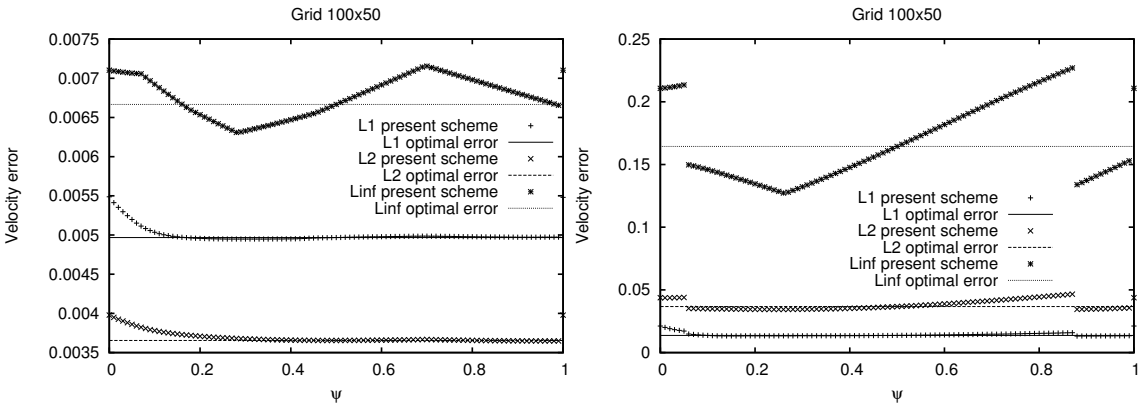

(a) Rarefaction wave (b) Shock wave

Figure III.4: Velocity error for the reflection of a rarefaction wave and a shock wave.

We observe that the errors in L_1 and L_2 norms increase as ψ goes to 0 because the macroscopic quantities are extrapolated over larger distances. However, they remain close to the optimal error. For the three norms, the error for $\psi = 0$ and $\psi = 1$ is the same because it represents the same configuration.

III.4.2 The oblique shock

Here, we will compare the specular reflection described in sect.III.2.2.1 with the new Euler-AP method with $\alpha = 0$ on a 2D exact test case, using a body-fitted grid. A wedge reflect an incoming horizontal flux at $M = 2.324$. The grid is body fitted to deal with the single issue of the boundary condition without the influence of the Cartesian grid scheme. The angle of the wall is 10 degrees. The initial condition is $u = 3$, $v = 0$, $p = 1$, $T = 1$ in dimensionless form and $Kn_\infty = 10^{-8}$. The same condition is imposed at inlet and the impermeability condition is applied on the body. A shock is created on the body and moves in the fluid. The analytical solution for the angle of the shock (δ), Mach number, density, pressure and temperature after the shock is known:

$$\begin{cases} \delta = 35.2326 \\ M = 1.818 \\ \rho = 1.4987 \\ P = 1.9969 \\ T = 1.3324 \end{cases}$$

Two specular reflections schemes have been tested with different interpolation methods and compared to the new Euler-AP method. The first one uses a bilinear interpolation. The second one uses a bicubic interpolation. Results are shown for a grid 100×100 in space and 21×21 in velocity space (and 81×81 for the bilinear interpolation).

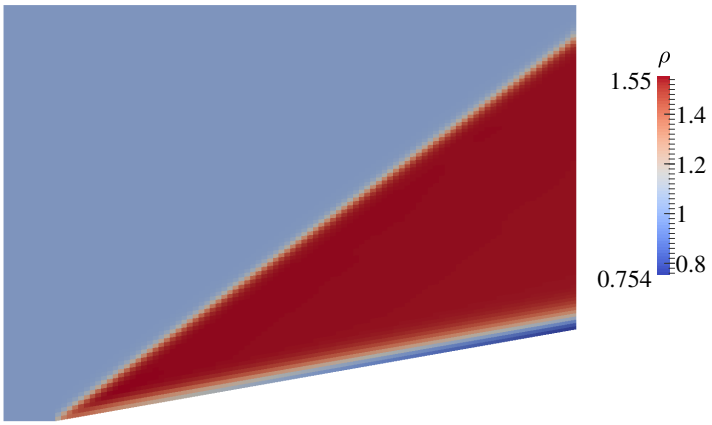

Figure III.5: Density solution for the oblique shock with bilinear interpolation on 21×21 grid points.

The layer developing close to the wall with the bilinear interpolation (see figure III.5) is due to a spurious energy flux across the wall (100 times larger than for the present method, see figure III.8). This energy flux is caused by interpolation errors. In fact, when the velocity grid is refined, the spurious layer tends to decrease as we can see using 81×81 points on the velocity grid (see figure III.6).

The layer is much smaller in the case of a bicubic interpolation (see figure III.7) because the spurious energy flux across the wall is much lower and gives results in better accordance with the theory. Again, it shows that this spurious layer is only a numerical artefact.

The Euler-AP method does not show this kind of layer on the boundary (see figure III.8). The solution is uniform after the shock.

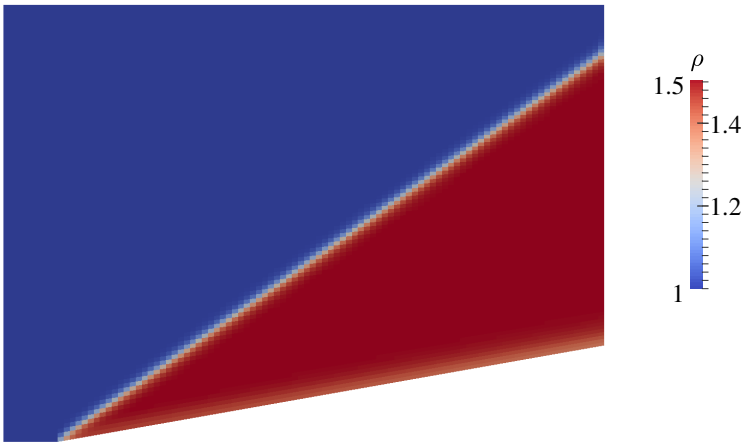

Figure III.6: Density solution for the oblique shock with bilinear interpolation on 81×81 grid points.

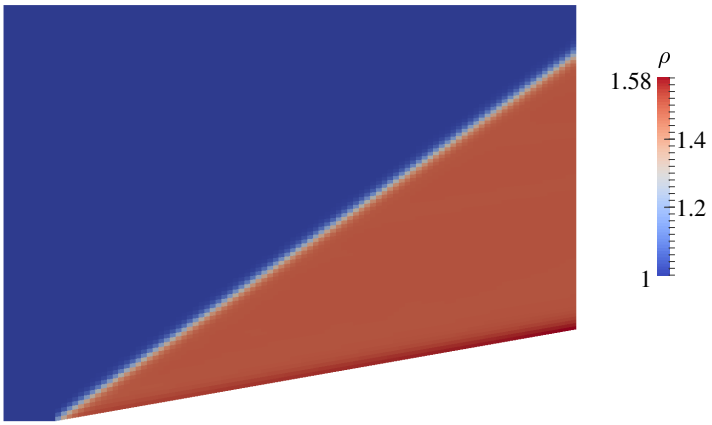

Figure III.7: Density solution for the oblique shock with a bicubic interpolation with 21×21 velocity grid points.

On a horizontal line ($y = 0.3$), one can compare the different results with respect to the analytical solution. Figure III.9 shows the comparison of the solutions for the pressure and the temperature given by each method with 21×21 points in velocity. The exact solution (for Euler equations) is represented with a solid line.

For all methods, the position of the shock is correct but the values for the pressure and the temperature after the shock are different. The Euler-AP method and the specular reflection with a bicubic interpolation are clearly more accurate. Zooming on these pictures (see figure III.10) we can see that the results obtained by the Euler-AP method are even more accurate than the ones obtained with the bicubic interpolation.

Note that these spurious overestimated post-shock values arise from the error in the boundary condition and propagate in the bulk of the fluid affecting the whole solution.

The same phenomenon is observed for the ES-BGK model (see figure III.11a). As in the

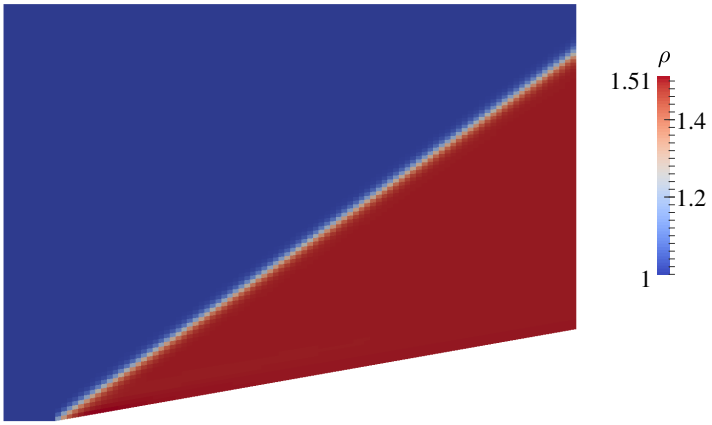

Figure III.8: Density for the oblique shock with the present method (21×21).

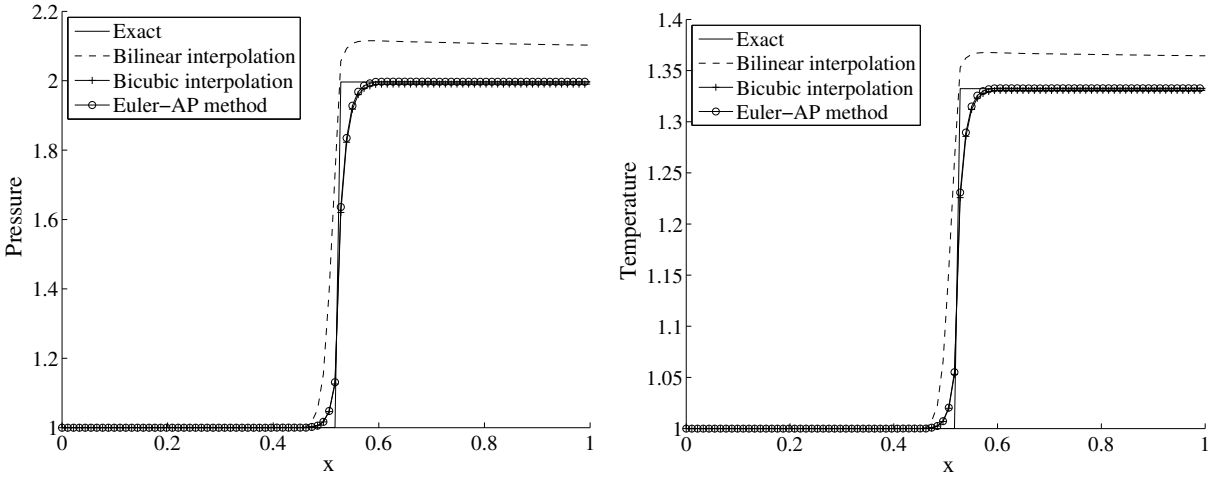

(a) Pressure profile.

(b) Temperature profile.

Figure III.9: Comparison of the specular and Euler-AP conditions for the pressure and the temperature.

case of the BGK model, the new Euler-AP boundary condition proposed corrects the spurious fluxes. The solution obtained is uniform after the shock. No boundary layer is observed (see figure III.11b).

The comparison with the exact solution along the horizontal line $y = 3$ is shown on figure III.12 with a zoom around the shock on figure III.13a. We compare it also with the solution given by the BGK model with the new Euler-AP boundary condition. Once again it is shown that without particular care, the solution is polluted by the spurious fluxes at the boundary. Moreover, the accuracy of the ES-BGK model is the same as the accuracy of the BGK solution. This was expected since we are in the hydrodynamic regime and the two models should behave identically.

On the same test case, we also tested the sensibility of the solution with respect to the value of *tol* in the case of the BGK model. We now impose the boundary condition still through formula (III.12) but with β set as in (III.13). We recall that to get the correct asymptotic behaviour towards the hydrodynamic regime, we still impose $\alpha = 0$. The error on the temperature in

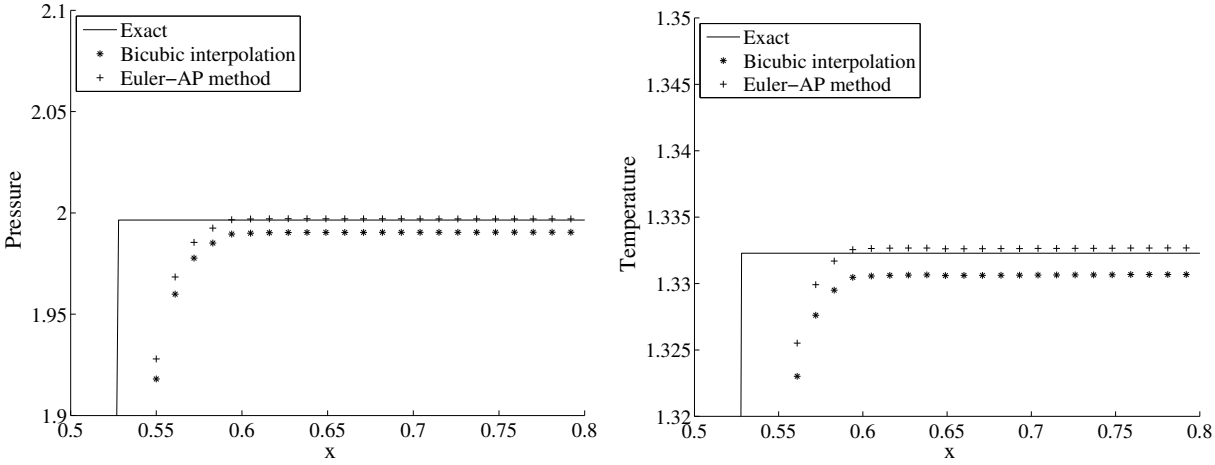

(a) Pressure profile.

(b) Temperature profile.

Figure III.10: Zoom on post-shock values for the pressure and the temperature for the BGK model.

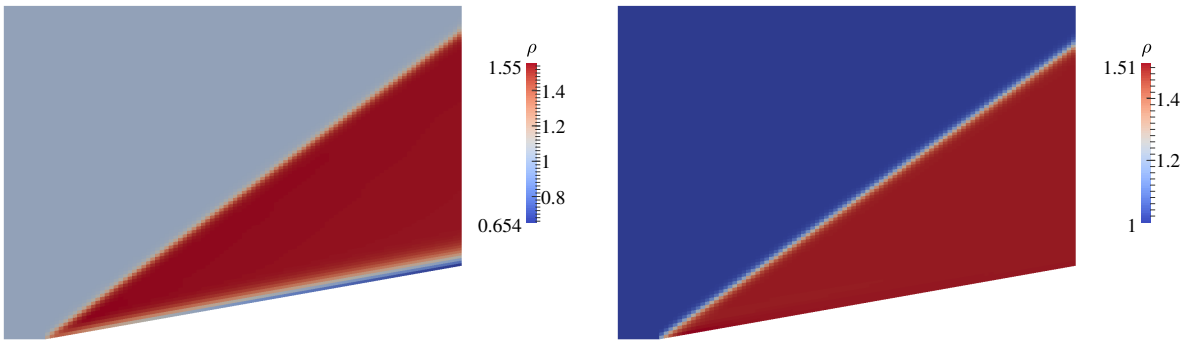

(a) Classical specular reflection.

(b) Euler-AP boundary condition.

Figure III.11: Oblique shock solution for the ES-BGK model.

L_1 norm is shown on figure III.14. It shows that for small values of the parameter tol, the relative error on the temperature in L_1 norm is larger. It means that for small values of tol, the classical specular reflection takes over in the boundary condition ($\beta \simeq 1$) and induces the spurious layer. Conversely, for larger values of tol, we get the correct solution at the boundary (only the discretization error is left). For the first velocity grid tested (21×21), we have $\Delta\xi_u^2 \simeq 1$ and the correct solution is obtained for $tol > 10^{-1}$. The second velocity grid corresponds to $\Delta\xi_u^2 \simeq 10^{-1}$ and the correct solution is obtained for $tol > 10^{-2}$. Thus, setting the parameter tol as $\Delta\xi_u^2$ gives the correct behaviour of the boundary condition. Moreover, the solution has a low sensibility to the value of the parameter tol as long as it is not too small meaning not lower than, approximatively, $\Delta\xi_u^2/10$.

In figure III.14, one can also note that the error on the temperature decreases, regardless of the value of tol, when $\Delta\xi_u$ is reduced. This is due of course to the fact that the interpolation error decreases.

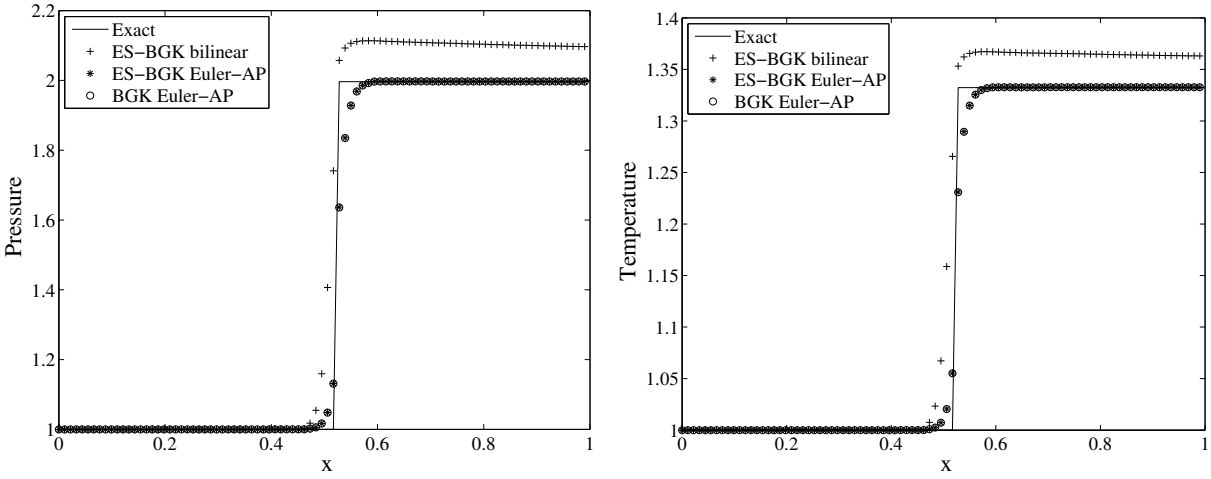

(a) Pressure profile. (b) Temperature profile.

Figure III.12: Comparison of the specular (for ES-BGK) and Euler-AP conditions (for BGK and ES-BGK) for the pressure and the temperature.

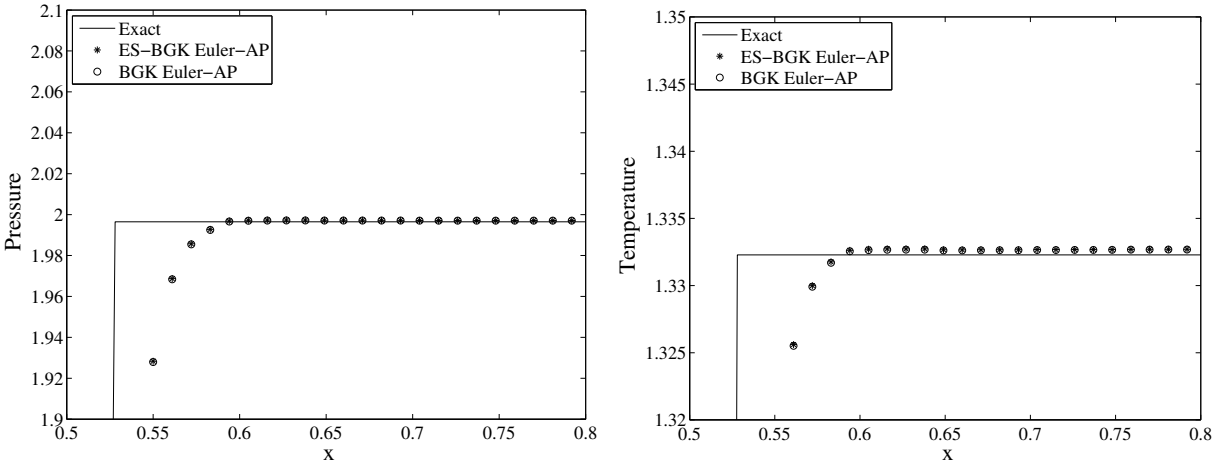

(a) Pressure profile. (b) Temperature profile.

Figure III.13: Zoom on post-shock values for the BGK and ES-BGK model.

III.4.3 The blunt body problem with the BGK model

The Euler-AP boundary condition has been validated on the oblique shock test case for a body fitted grid. In this section accuracy of the specular reflection with bicubic interpolation and Euler-AP method are compared on a Cartesian grid for the BGK model. Once again, the accommodation coefficient α is set to 0. A cylinder is immersed in a flow at $M = 3.09$ ($u = 4$, $v = 0$, $p = 1$, $T = 1$ in dimensionless form). The domain is [-0.3,0]×[0,0.45] and the cylinder radius is 0.1 centred in [0,0].

The impermeability condition is first computed with a purely specular reflection. The velocity grid goes from -10 to 10 in each direction and $Kn_\infty = 10^{-8}$. The boundary conditions at the border of the domain are free flow on north and east, inlet with the initial condition on west and specular reflection on south. Since the velocity grid is Cartesian, imposing the specular reflection on south can be done exactly. The impermeability condition is applied on the body.

The present method and the specular reflection with a bicubic interpolation are tested on a

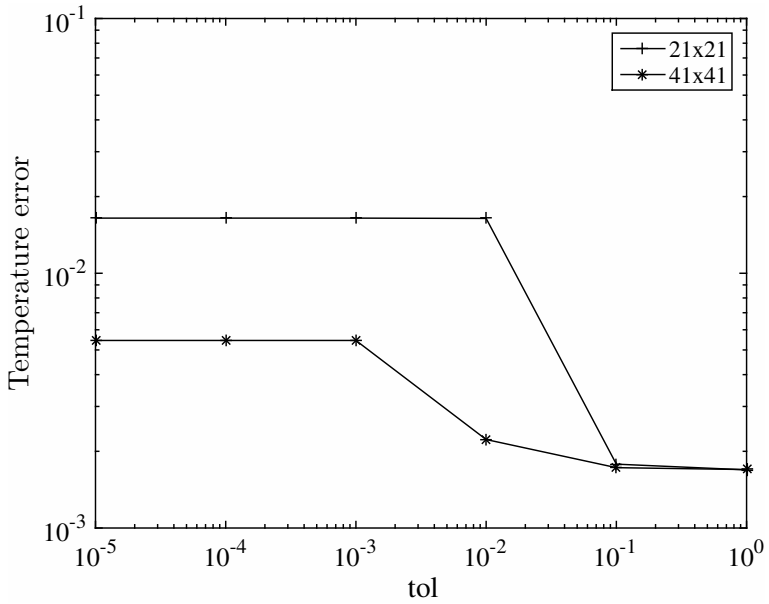

Figure III.14: Temperature error in L_1 norm for two different velocity grids.

spatial grid 80×120 and a velocity grid 31×31. Figure III.15 shows the solution with the Euler-AP method on the left and the normalized difference in the density between the two methods on the right.

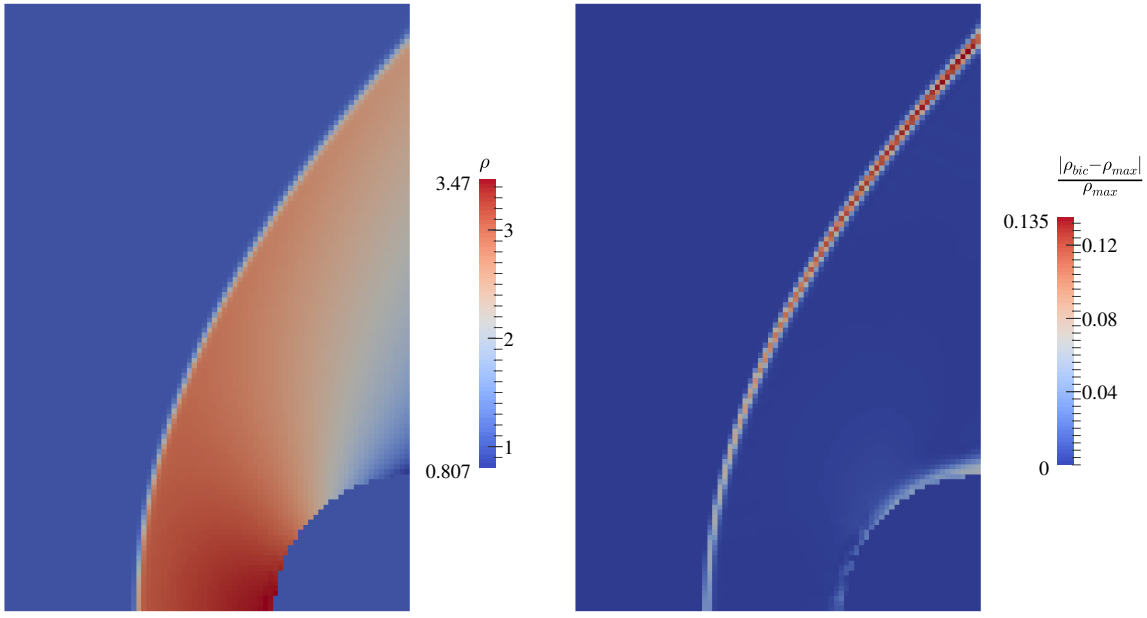

(a) Density solution.

(b) Difference between Euler AP and specular conditions.

Figure III.15: Density solution with the Euler-AP method and map of the difference between the two methods.

One can observe that the difference is mostly located on the shock and on the body. The relative error is about 10% of the solution.

The same test case is solved with Euler equations. BGK simulations are compared to this Euler solution with emphasis on the boundary. The structure of the error is very close in the two cases. The largest difference is located on the shock because the solution of the BGK equation is more diffusive than the one calculated with Euler equations. Thus, the shock is less sharp. On the cylinder, the error is much smaller. For the bicubic interpolation, the biggest difference is about 10% while for the present method it is less than 5% of the Euler solution. As in the oblique shock case, the Euler-AP method is more accurate on the boundary (see top of the cylinder in fig. III.16). It correctly preserves the asymptotic properties towards Euler equations even on Cartesian grid with immersed boundaries.

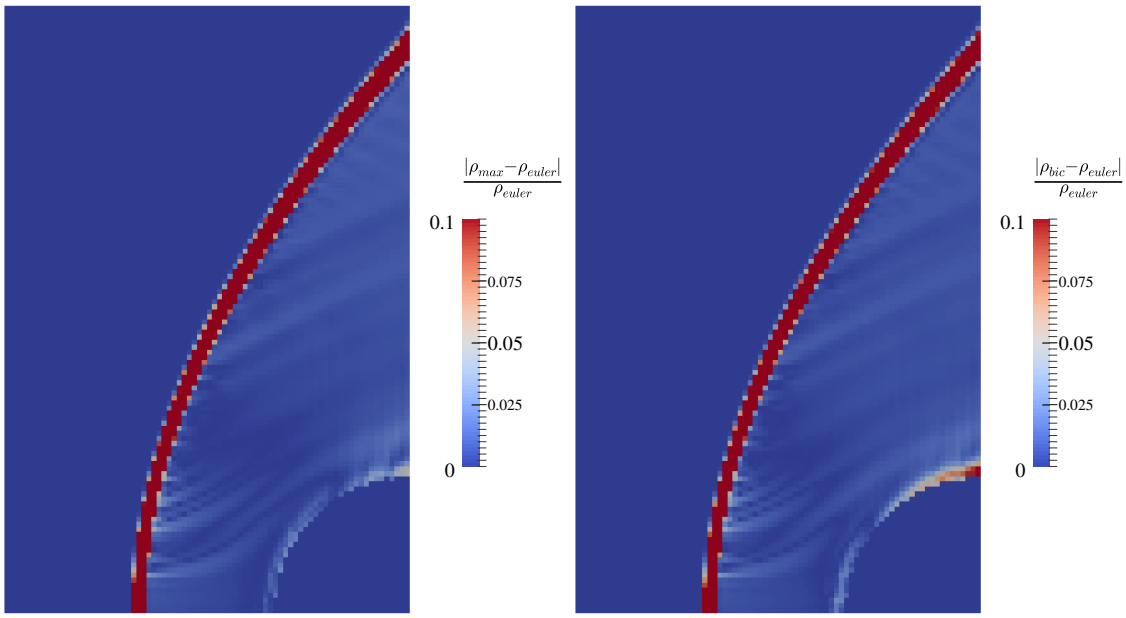

(a) Euler AP. (b) Bicubic interpolation

Figure III.16: Error with respect to Euler solution for the Euler-AP method and the bicubic interpolation.

Moreover the computational time is dramatically different (9 hours for the Euler-AP method and 19 hours for the bicubic interpolation with 128 processors).

A quantitative comparison of the computational time for the two methods is performed on 64 processors and is shown in figure III.17 for the BGK model. The Euler-AP method is clearly faster than the specular reflection with a bicubic interpolation. Also, the computational time increases faster for the bicubic interpolation as the number of velocity grid points increases (linear regression of the two curves: 1.73 against 1.55 for the present method).

III.4.4 Ringleb flow with the BGK model

Now that we have validated the boundary condition on body fitted grids and Cartesian grids, we show that our Cartesian method with this boundary condition is second-order accurate for the BGK model. Ringleb flow is a 2D steady state test case where the analytical solution can be calculated for Euler equations and will be used as a reference solution. This is a potential

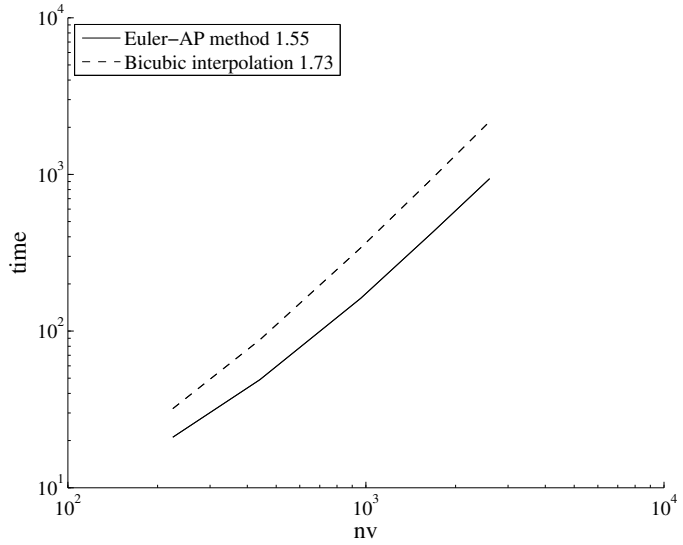

Figure III.17: Computational time for the two methods with respect to the number of velocity grid points.

flow and the exact solution is obtained with the hodograph method [107].

Setting (θ,V) such that $u = V\cos\theta$ and $v = V\sin\theta$, the stream function is given by $\Psi = \dfrac{sin\theta}{V}$.

The streamline equations are:

$$x = \frac{1}{2\rho}(\frac{1}{V^2} - 2\Psi^2) + \frac{L}{2} \quad \text{and} \quad y = \frac{sin\theta cos\theta}{\rho V^2}$$

with (for $\gamma = 5/3$, monoatomic gas):

$$L = ln\Big(\frac{3V}{6 + 2\sqrt{9 - 3V^2}}\Big) - \frac{\sqrt{9 - 3V^2}(V^2 - 4)}{V^2 - 3}, \quad c^2 = 1 - \frac{\gamma - 1}{2}V^2, \quad \rho = c^{\frac{2}{\gamma - 1}}$$

The computational domain is [-0.5,-0.1]×[-0.6,0] and the flow is solved between 2 streamlines: Ψ_1=0.8 and Ψ_2=0.9. Since $\mathbf{u}\cdot\mathbf{n} = 0$ on a streamline (with $\mathbf{n}$ the normal to the streamline), any streamline can be considered as a solid boundary where the Euler impermeability condition is enforced with $\alpha = 0$. The boundary conditions in inlet (y=-0.6) and outlet (y=0) are supersonic and exactly imposed.

The finest grid used is 128×192 in space and 241×241 in velocity. To compute the space order of convergence, the solution is calculated on five different grids in space (8×12, 16×24, 32×48, 64×96) but the velocity grid is kept 241×241. Thus, the result is not perturbed by convergence in velocity space.

Figure III.18 shows the solution for the pressure on the left and the error map for the density on the right. The solid black lines are the two streamlines between which the BGK equation is solved. Outside, the exact Euler solution is shown. The flow is not perturbed by the boundary condition along the streamlines and the error map on the right shows that the error with respect to the analytical solution is less than 1%.

Figure III.19 shows the error with respect to the analytical solution for L_1 and L_∞ norms (see also tables III.1 and III.2). Second order is obtained in L_1norm. However, on the finest grid, it is possible to notice a slight deterioration in accuracy with respect to previous grids which

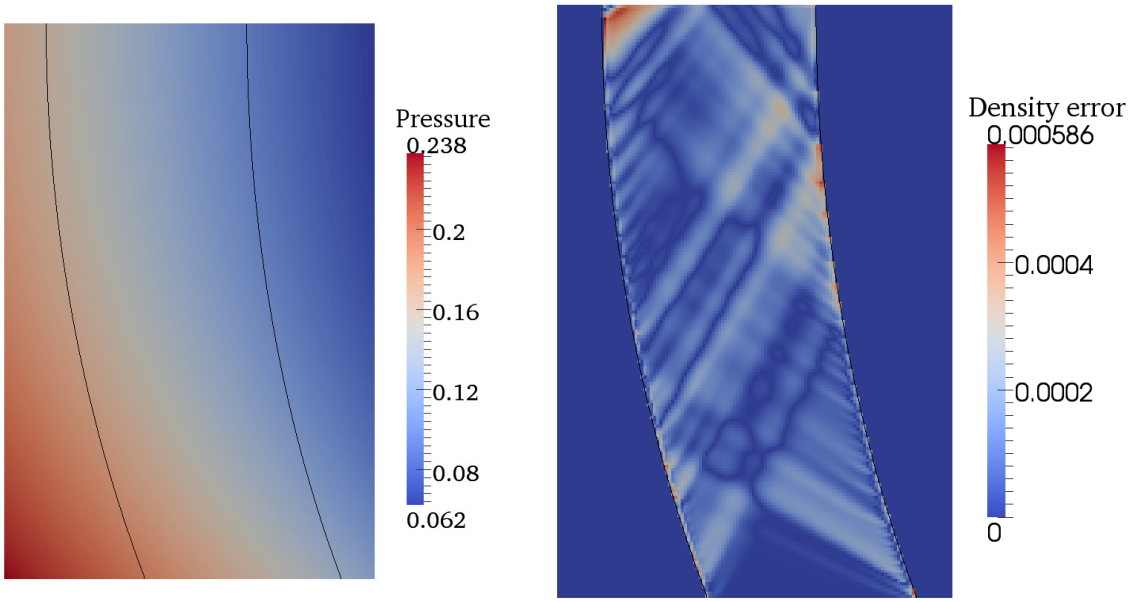

(a) Pressure solution (space grid 128×192).

(b) Density error (space grid 128×192).

Figure III.18: Pressure solution and error map for the density.

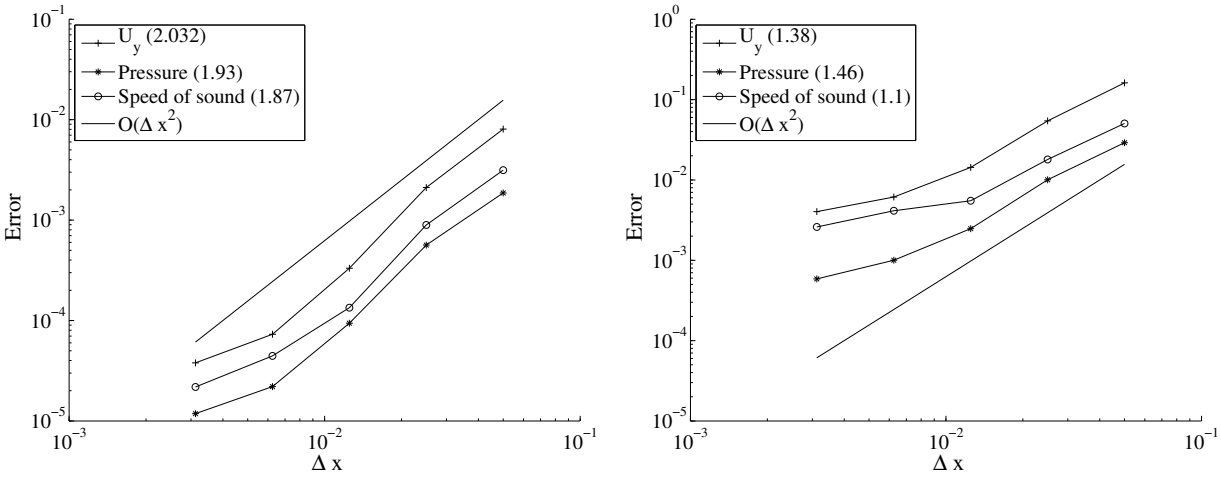

(a) L_1 norm

(b) L_∞ norm

Figure III.19: Error in L_1 and L_∞ norm.

actually show a convergence order bigger than 2. This phenomenon is probably due to the fact that at this degree of refinement the space error is of the same order of magnitude of the error in velocity space, where the reconstruction of the distribution function at the boundary is indeed carried out with first order accuracy. In L_∞ norm the order is smaller (1.5 for the pressure) but it occurs on a tiny subdomain and it does not spoil the L_1 norm order of convergence.

Finally, figure III.20 (see also table III.3) shows the relative error on the pressure as the velocity grid is refined with respect to the solution on the finest velocity grid used (241×241

N_x	U_y	order	P	order	Speed of sound	order
8	8.1×10^{-3}		1.9×10^{-3}		3.1×10^{-3}	
16	2.1×10^{-3}	1.93	5.64×10^{-4}	1.725	8.94×10^{-4}	1.81
32	3.32×10^{-4}	2.67	9.39×10^{-5}	2.59	1.34×10^{-4}	2.73
64	7.29×10^{-5}	2.19	2.2×10^{-5}	2.1	4.45×10^{-5}	1.59
128	3.78×10^{-5}	0.94	1.18×10^{-5}	0.895	2.18×10^{-5}	1.03

Table III.1: Error in L_1 norm.

N_x	U_y	order	P	order	Speed of sound	order
8	0.16		2.9×10^{-2}		5.04×10^{-2}	
16	5.43×10^{-2}	1.57	1×10^{-2}	1.53	1.79×10^{-2}	1.49
32	1.43×10^{-2}	1.93	2.5×10^{-3}	2.02	5.5×10^{-3}	1.7
64	6.1×10^{-3}	1.22	1×10^{-3}	1.3	4.1×10^{-3}	0.41
128	4×10^{-3}	0.6	5.86×10^{-4}	0.77	2.6×10^{-3}	0.67

Table III.2: Error in L_∞ norm.

for a space grid 64×96). It shows that for large $\Delta\xi_u = \Delta\xi_v$ the error decreases fast and then the solution converges with a second order accuracy even in L_∞ norm (which is the accuracy of the quadrature rule).

N_{vx}	L_1	order	L_∞	order
15	0.05		0.0604	
31	3.46×10^{-6}	10.01	9.35×10^{-5}	8.91
61	1.82×10^{-6}	0.9491	2.32×10^{-5}	2.06
121	4.3×10^{-7}	2.1065	5.1×10^{-6}	2.21

Table III.3: L_1 and L_∞ norm of the pressure error for the Ringleb flow on the 64×96 space grid.

III.4.5 Cylindrical Couette flow with the ES-BGK model

We propose here a test case to compute the convergence order of our Cartesian method for the BGK model. Since, the hydrodynamic limit of the ES-BGK is the same as the one of the BGK model, testing the convergence order on the Ringleb flow is not presented here and is expected. The order of convergence is then tested on a cylindrical Couette flow at $Kn = 0.01$. The diameter of the inner cylinder is 0.4 while the outer cylinder has a diameter of 0.8. The temperature imposed on both cylinder is 1 and the inner cylinder is rotating at a constant surface speed of 1. The outer cylinder is at rest. The fully asymptotic preserving boundary condition is used (III.12) with $\alpha = 0.5$. The flow is initialised with $\rho = 0$, $\mathbf{U} = 0$, $T = 1$. The velocity grid discretization is kept constant and goes from -6 to 6 with 61 points in each direction. The space domain is [-1,1]×[-1,1] and six different space grids are tested (10×10, 20×20, 40×40, 80×80, 160×160 and 320×320). Figure III.21a shows the density solution for the finest grid (320×320 in space, 61×61 in velocity). Since no analytical solution is known, the convergence order is computed from the density integrated along on horizontal line at $y = 0$ between $x = -0.8$ and $x = -0.4$. We then calculate the absolute value of the difference between this integrated density on two consecutive grids (with a grid step two times smaller). The convergence of this difference is shown in figure III.21b. Using six different grids gives five points for the convergence curve.

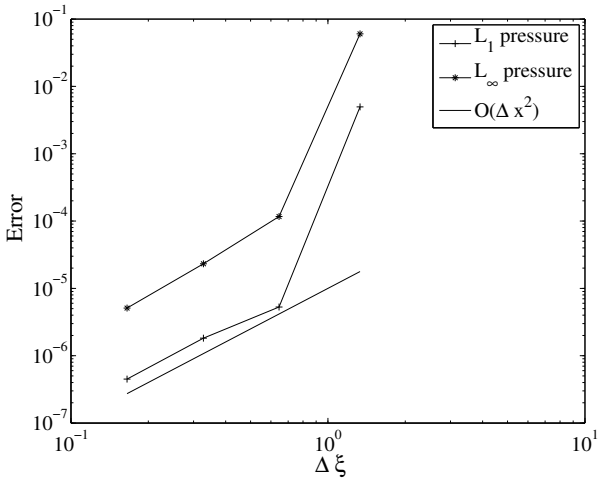

Figure III.20: L_1 and L_∞ norm of the pressure error for the ringleb flow on the 64×96 space grid.

A second order convergence is observed.

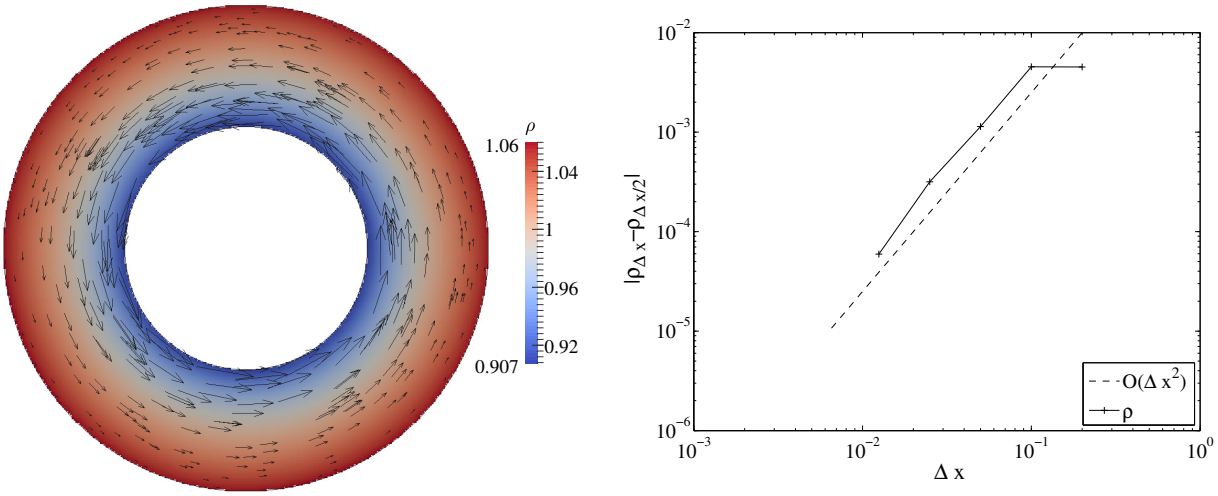

(a) Density solution and velocity vectors.

(b) Error.

Figure III.21: Steady state solution and error for the Couette flow.

III.4.6 Flow past a vertical plate

Several test cases have been so far presented to show the accuracy of the Euler-AP boundary condition in the continuum regime, for body-fitted and Cartesian meshes. We now validate the Euler-AP wall condition in the rarefied regime with the BGK model.

The flow past a vertical plate was first introduced by Bird [16] to study the formation of vortices at different Knudsen numbers. This case highlights the rarefied effects for a simple geometry, with a specular boundary condition applied on the vertical plate. Our results are compared to the numerical ones obtained by Bird [16] with DSMC and by Chen et al. [32] with AUGKS.

A vertical plate is immersed in a flow at Mach 0.53 of Argon. The undisturbed initial flow is imposed at inlet ($x = -4/3$), outlet ($x = 2$), at the upper boundary ($y = 2$), $U_\infty = 0.6881$ and a temperature of 1 (in dimensionless values). At $y = 0$, a symmetric boundary condition is enforced corresponding to the specular reflection. The plate is placed at $x = 0$ and goes from $y = 0$ to $y = 1$ (height $h = 1$). It has zero thickness and is situated exactly at the interface between two cells. The Euler-AP condition is imposed on both sides of the plate with our second order scheme. The physical space is discretized with 100×60 cells. The velocity space is [-10,10]×[-10,10] and is discretized with 41 cells in each directions. The solution is shown for 4 different Knudsen numbers in III.22. We note that for this test case, the results are presented with the value of the Knudsen number in Bird's sense (Kn_B). To fit with our model, we actually take $Kn_\infty = Kn_B \dfrac{5\sqrt{2\pi}}{16}$.

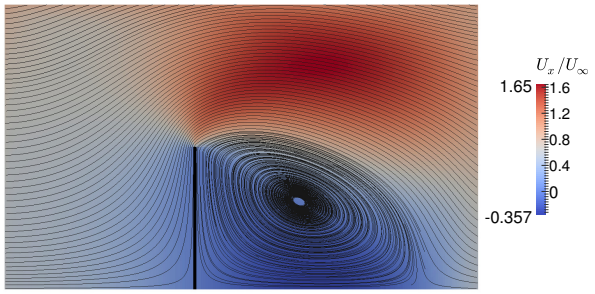

(a) $Kn_B = 0.044$.

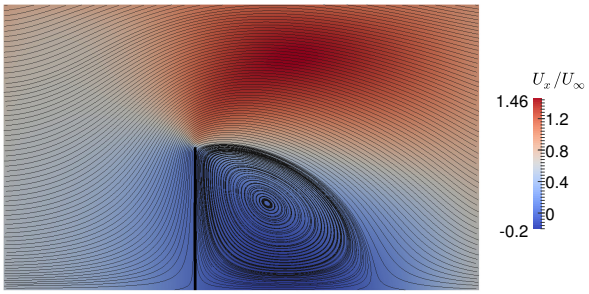

(b) $Kn_B = 0.088$.

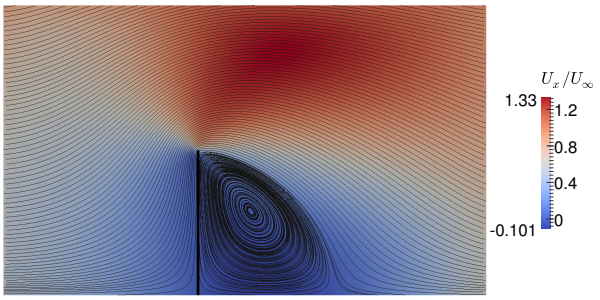

(c) $Kn_B = 0.147$.

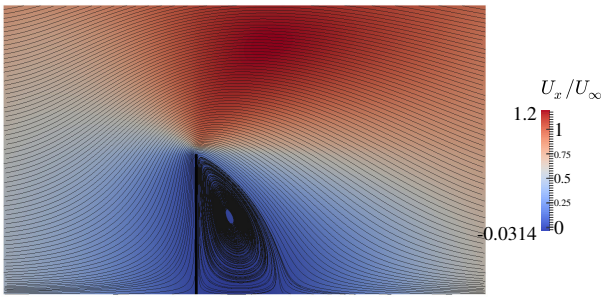

(d) $Kn_B = 0.293$.

Figure III.22: Horizontal velocity and streamlines at $Kn_B = 0.044$, $Kn_B = 0.088$, $Kn_B = 0.147$ and $Kn_B = 0.293$.

The steady state of this problem shows a vortex behind the plate. As mentioned by Bird, the solution strongly depends on the boundaries of the domain. However, for the same computational domain and boundary conditions, comparisons can be made with the results obtained by Bird on the velocity profile along a vertical axis passing through the center of the vortex for different Knudsen numbers.

Figures III.23 shows that the velocity profiles obtained with the Euler-AP boundary condition and a second-order scheme for BGK and ES-BGK model are in good agreement with Bird's results for different Knudsen numbers. The results show that the vortex becomes stronger as the Knudsen number decreases. Small variations of the position of the vortex center definition induce large variations of the velocity at $y = 0$ and can explain the difference between the solutions. The solutions of the BGK model and the ES-BGK model are similar for this test

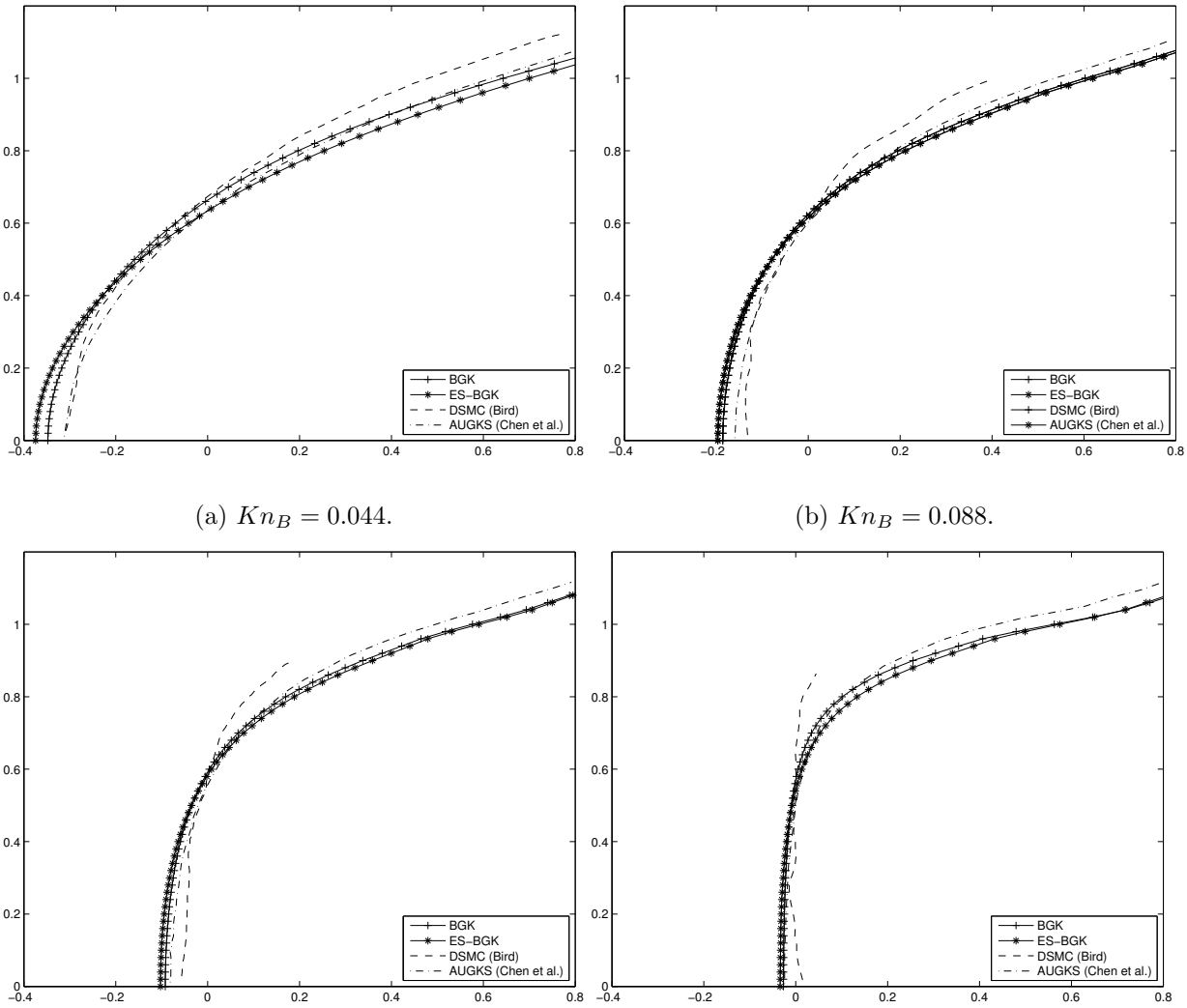

(a) $Kn_B = 0.044$.

(b) $Kn_B = 0.088$.

(c) $Kn_B = 0.147$.

(d) $Kn_B = 0.293$.

Figure III.23: Horizontal velocity solution at $Kn_B = 0.044$, $Kn_B = 0.088$, $Kn_B = 0.147$ and $Kn_B = 0.293$.

case. The comparison with respect to the two reference solutions provides a validation of the method in the rarefied regime for both models. In this case, the value of the parameter β is 0 at the initial state but goes quickly towards 1 for all boundary points since the Knudsen number is large.

III.4.7 A nozzle plume

We consider a final qualitative validation against experimental results. A flow expands at the outlet of a nozzle in a low pressure atmosphere. The spreading jet has been studied for example by Latvala et al. in [78] and [79]. Experiments were performed for different ambient pressures to determine the angle and the shape of the jet at the outlet of the nozzle.

The area ratio between the throat and the outlet of the nozzle is 4.8. Here, we impose the total pressure ($P_{tot} = 1$) and the total temperature ($T_{tot} = 0.6$) at the inlet of the nozzle. Considering that Mach 1 is reached at the throat, one can determine the Mach number, the

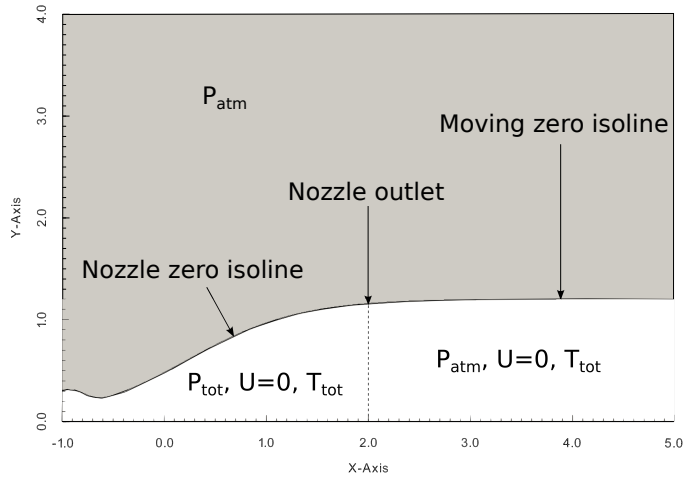

Figure III.24: Computational domain at t=0.

pressure and the temperature at the outlet under the assumption of a one dimensional isentropic flow. In our case, this gives M=3.7763, T=0.1738 and p=0.0126. This pressure is called the adaptation pressure P_c. If the ambient pressure P_{atm} is lower than P_c the flow inside the nozzle is independent of P_{atm}.

We obtain the jet angle by tracking the contact discontinuity between the gas coming from the nozzle and the gas initially outside the nozzle with a level set function keeping fixed the point at the extremity of the nozzle ($x = 2$). At each time step, the level set function is transported according to the velocity of the fluid with the procedure described in section III.1.3 for moving boundaries. In the cells initially outside the fluid domain and freshly appeared (determined by the cell center) in the jet, the computed boundary condition is imposed. All the viscous effects (mixing layer) are supposed to be concentrated across the contact discontinuity represented by the isoline zero of the level set function. The velocity of the contact discontinuity is computed thanks to a Riemann problem where only the ambient pressure P_{atm} is imposed.

At initial state, the nozzle is filled with a gas at rest with $p = 1$ and $T = 0.6$. Outside of the nozzle, the gas is also at rest, with $p = P_{atm}$ and $T = 0.6$. The initial configuration with the zero isoline of the level set function is shown on figure III.24. The dark area above the nozzle is penalized, no computations are performed unless the level set evolves and includes this region. The computational domain is [-1,5]×[0,4] and is discretized with 120×80 cells. The velocity space [-10,10]×[-10,10] is discretized with 101 points in each directions.

The solution for $P_c/P_{atm} = 2000$ is shown on figures III.25, III.26, III.27 and III.28 for different times. First, the flow goes out of the nozzle and turns back because of the abrupt expansion ($t = 1.2$ and $t = 5$). Then, when the flows stabilizes in the nozzle, a shock propagates from the inlet towards the outlet. On figure III.27, at $t = 11.1$ the shock is at $x = 2.7$ and establishes the angle of the jet with the nozzle outlet.

Figure III.29 shows the angle δ of the jet at the outlet for different pressure ratio P_c/P_{atm} and for BGK and compressible Euler models. When this ratio is equal to 1, the angle of the flux at the outlet should be the same as the angle of the nozzle outlet. The figure shows that in this configuration, δ is actually larger. This is due to the calculation of P_c through 1D relations. Thus, the pressure at the boundary of the nozzle at the outlet is not equal to P_c but it is larger. If this pressure is imposed outside the nozzle, we obtain an angle δ equal to the one of the nozzle exit (first point on figure III.29). These results can be qualitatively compared with the experimental results obtained by Latvala et al. in [78] where it is shown, for $\gamma = 7/5$, that the

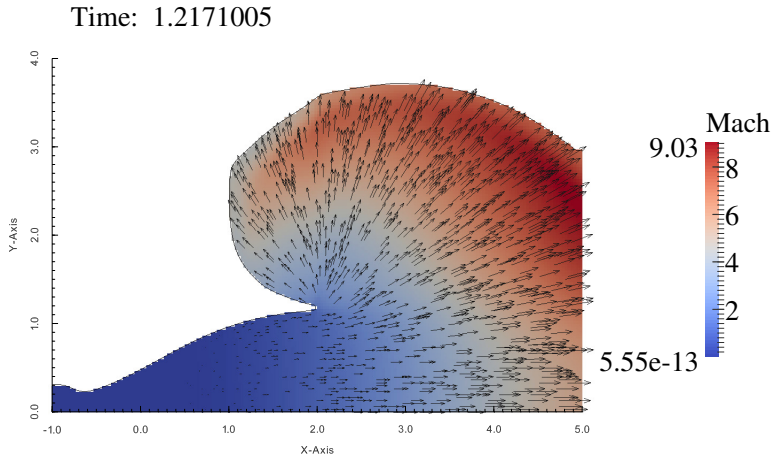

Figure III.25: Mach number and velocity vectors at t=1.2 for $P_c/P_{atm} = 2000$.

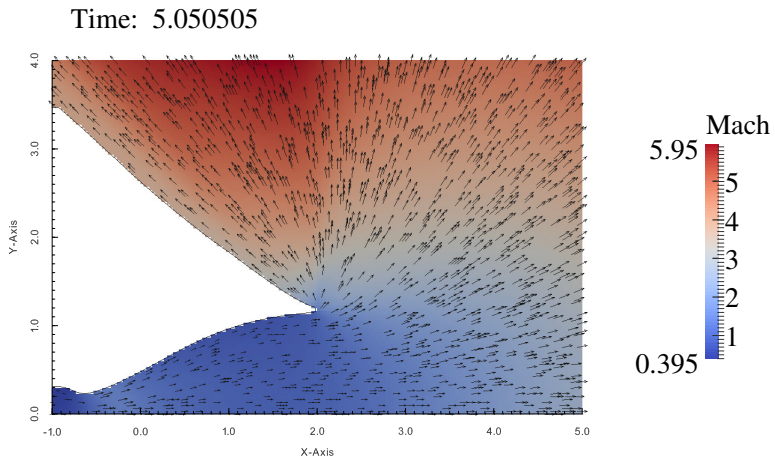

Figure III.26: Mach number and velocity vectors at t=5 for $P_c/P_{atm} = 2000$.

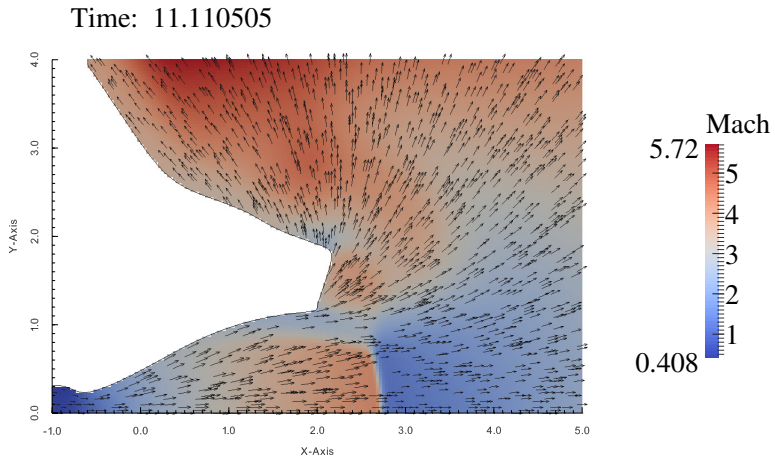

Figure III.27: Mach number and velocity vectors at t=11 for $P_c/P_{atm} = 2000$.

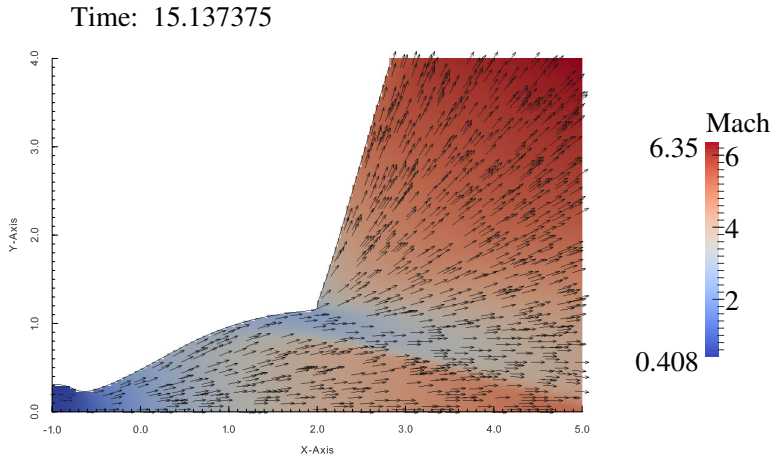

Figure III.28: Mach number and velocity vectors at steady state for $P_c/P_{atm} = 2000$.

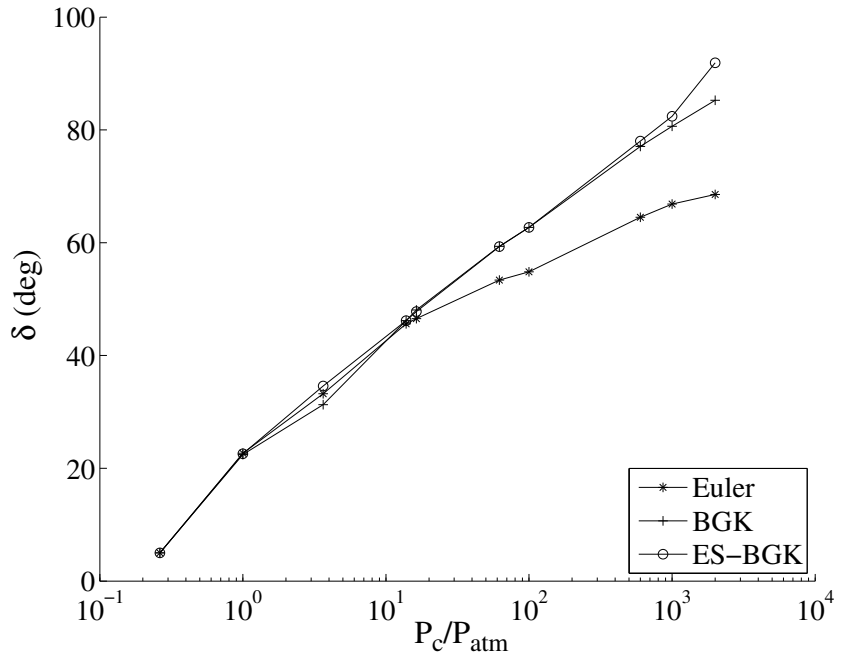

Figure III.29: Angle for different pressure ratios calculated with Euler, BGK and ES-BGK models.

evolution of the jet angle is linear with the logarithm of the pressure ratio. The same behaviour is observed in figure III.29 for the BGK and ES-BGK model. The compressible Euler model progressively detaches from a straight line as the rarefaction increases. The quantitative results cannot be directly compared to experiments since in our case, $\gamma = 5/3$.

For small pressure ratios (< 10) the BGK, ES-BGK and compressible Euler models give the same angle. When the ratio increases, the difference becomes larger and the kinetic models stay very close to a straight line. For this kind of pressure ratio, the local relaxation time increases outside the nozzle and becomes too large to consider the fluid at equilibrium. Thus, the continuum model tends to give a different solution. This emphasizes the necessity of using a kinetic model with an AP boundary condition since this problem cannot be solved with a continuum model for high pressure ratio. Also, a solution computed with a specular reflection wall condition in the nozzle would significantly pollute the simulation because of a net reduction of the efficient section of the nozzle.

At high pressure ratios, the two kinetic models give similar angles. Actually, we could expect a difference since the ES-BGK model should handle differently high Knudsen number ($> 10^{-1}$). It is not possible to see this difference on this test because the angle becomes very complicated to estimate when the flow turns back. It corresponds to pressure ratios higher than 10^4.

III.5 Preliminary conclusion

In this chapter, we showed that without a particular treatment, standard methods are not AP in presence of interior boundaries, because they exhibit spurious energy fluxes through the boundaries, when the hydrodynamic limit is approached. These artefacts are purely numerical, and a possible cure relies on a more accurate treatment of the boundary condition, at the price of costly higher order interpolations in velocity space. Here we proposed an efficient boundary condition which ensures that an AP scheme remains AP up to the wall boundary. We illustrated this result by comparing several numerical schemes to model the impermeability condition for the BGK and ES-BGK models with emphasis on asymptotic preserving properties in the Euler limit. Rarefied flow test cases have been also investigated. Moreover, we also proposed a technique to impose the boundary conditions on Cartesian grids, specializing the method of immersed boundaries to the case of kinetic fluid flows. We have also shown how to recover second order accuracy on Cartesian meshes (see Ringleb flow test case) using this new wall condition and simulated non-trivial rarefied regime test cases. In particular, the last test case highlights the necessity of a kinetic model with the correct asymptotic behaviour. Such cases cannot be correctly simulated with a continuous model.

One other issue due to kinetic models is the cost due to the high dimensionality of the problem. In the following, we address this problem and present some techniques improving the computational time.

Chapter IV

Computational time optimization techniques

This chapter is devoted the optimization of the computational time. It has been already mentioned several times that kinetic models are very slow to compute. They also require a large amount of memory with respect to macroscopic models because of the velocity discretization in each spatial cell.

The first solution to improve the computational time required is to parallelize the code. In the first section, we present the tools used and describe the algorithm to go from a sequential code to a parallel code for both BGK and ES-BGK model. In the second section, a new local velocity approach is proposed. Performances of the new algorithm are investigated through different test cases in 1D and 2D for different regimes.

IV.1 Code parallelization

A natural way to reduce the computational time is the parallelization. It is also useful for memory requirement. A sequential code is executed by one thread only and can use at most the memory of one node while a parallel code is executed by several threads and the memory available depends on the number of nodes used. In other words, a parallel code gives access to more memory and the work is divided through the number of threads used. For the resolution of kinetic equations it becomes rapidly necessary since it is slow to compute and requires a large amount of memory, in particular in 3D.

There are two main libraries to do computations in parallel: OpenMP and MPI. The first one is very easy to set up. The parts of the code that should be parallelized (usually independent loops) are specified and the parallelization is done during the compilation. The memory is shared between the threads and there is no need to communicate data. The main drawback is that it can only be used with one node. Hence, the number of thread is limited by the node as well as the memory. MPI is a more powerful library but there is more work to write the code. Each threads are treated independently and executes the same code without knowing what the other threads are doing. The memory is divided and each thread can only access to its part of the memory. Thus, threads need to communicate data especially at the boundary of their respective domains but there is no limitation on the number of threads (and nodes) that can be used. For this reason, although it is not as simple as OpenMP to implement, the MPI library has been used in this work.

The parallelization is very efficient on Cartesian grids and it is one of the reason we use this type of grid. The computational domain can be easily divided in equal square (or rectangular)

sub-domains without taking a particular care about the problem solved. Each thread is assigned to one sub-domain and executes the code. This first step is called "partitioning". On a Cartesian grid, with a domain entirely fluid, it also respects the "load balancing" since all sub-domains are identical and so is the work to solve the equation. Figure IV.1 shows the partitioning of a rectangular domain with four threads.

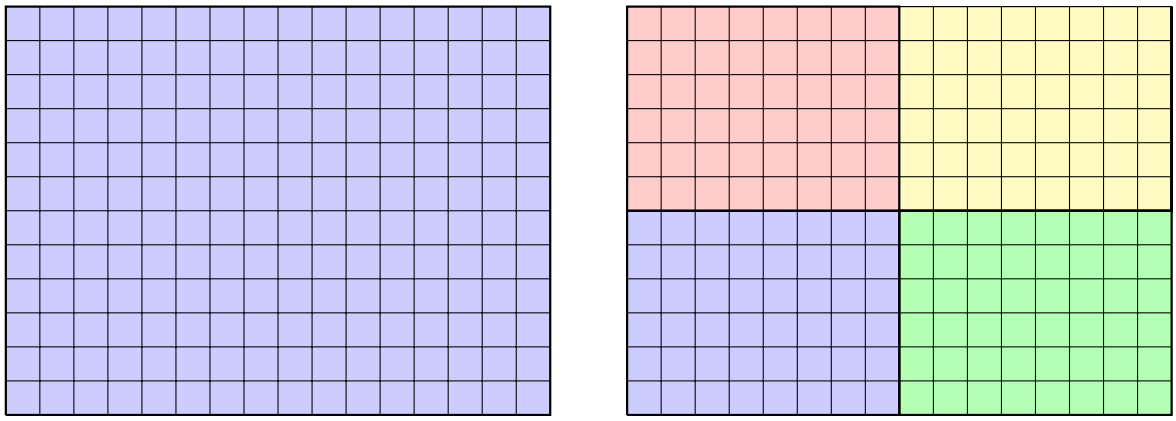

(a) Domain with 1 thread

(b) Domain with 4 threads

Figure IV.1: Partitioning of a rectangular domain. Each color correspond to a sub-domain of 1 thread.

Each thread executes the code in their sub-domain but do not know what is happening in the neighbouring sub-domain. To compute the fluxes at a numerical interface that match with an interface between two sub-domains, it is then necessary to communicate the data between threads and to know exactly which data are required. This is determined by the numerical scheme.

Let us consider a fluid cell (i, j). Computing the relaxation term does not require the knowledge of any data in the neighbouring cells but the transport does. In particular, the scheme (II.8) with the fluxes expressed as in (II.10) and (II.13) requires the knowledge of the distribution function in the first neighbouring cells with the slopes to get second order. To compute the slopes one needs two cells on each side of the cell (i, j) in each direction. The stencil is represented in figure IV.2a. Close to a wall, we still need two cells in the opposite direction to the wall. To reconstruct the fluxes at the wall, one needs to extrapolate the macroscopic variables to build the boundary condition (see(III.12)) at the desired order. Also, to reconstruct the distribution function at the boundary with (III.14), diagonal cells are involved $(i \pm 1, j \pm 1)$. Since we restrict ourselves to second order, in the worst case (angle of a domain) two cells are still enough (see stencil of figure IV.2b) but we need to communicate the distribution function and the macroscopic variables (velocity, temperature and stress tensor).

Each thread will have four more cells (two on each side) in each direction than the actual computational domains. These extra cells are called "ghost cells". The neighbouring threads compute the solution in these cells that are part of their computational domain and communicate it at each time step to update the ghost cells.

Once the code is parallelized, it is important to measure the performance or scalability to know its efficiency. The tests are performed on the blunt body test case at $M = 3$ as presented in section III.4.3 but with a square domain to have the best performance.

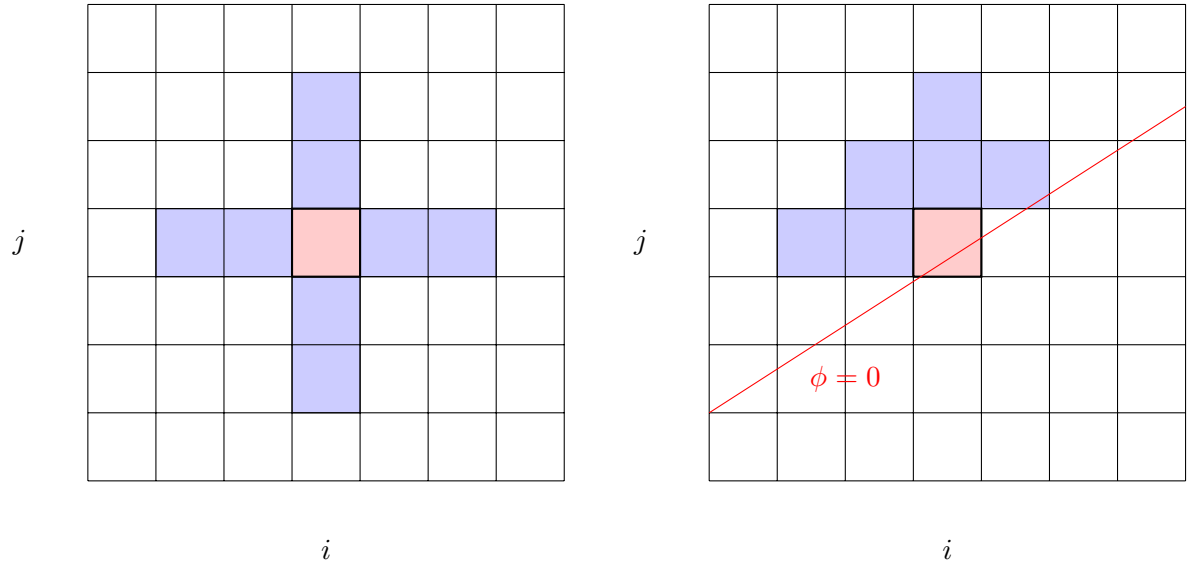

(a) Stencil used far from the wall.

(b) Stencil used close to a wall.

Figure IV.2: Largest stencil used to compute the fluxes far from the wall and close to the wall.

IV.1.1 Weak scalability

The first test is the weak scalability. It measures how the code behaves as we increase simultaneously the number of degrees of freedom and the number of threads such that the number of degrees of freedom stays constant for each thread. If the problem on one thread is of size S, we compare the execution time with a problem of size $N_{threads}S$ on $N_{threads}$ threads. Ideally, the computational time for a given number of iterations should stay constant. We run the simulation for 500 iterations with an initial space grid 50^2 on one thread. The velocity grid is 21×21 for all tests. The scalability is then tested on 4 threads on a 100^2 grid, 16 threads on a 200^2 grid, 64 threads on a 400^2 grid, 256 threads on a 800^2 grid.

The weak scalability test is shown on figure IV.3. It shows a good scalability even if there is a small loss of performance as the number of thread increases. It can be explained by the penalized part of the domain where there are no calculations to perform. This induces an unbalance of the load on the threads and then a loss in scalability. Also, the increasing number of threads makes the time devoted to communications more important and leads to a higher computational time.

IV.1.2 Strong scalability

The strong scalability is another test to evaluate the performance of a parallel code. Here, the grid is kept constant and the number of thread is increased. The ratio between the amount of data to communicate and the size of the problem solved on each thread increases with the number of thread used. If the grid is initially too coarse, the computational time will then suffer from the time due to the communications. Eventually this problem will always happen for a large number of threads. The same test case as for the weak scalability is used with the same grid in velocity (21×21) but with a space grid 800×800. The speed up s is calculated as:

$$s_i = T_0/T_N$$

where T_0 is the computational time on one thread and T_N the computational time on N threads.

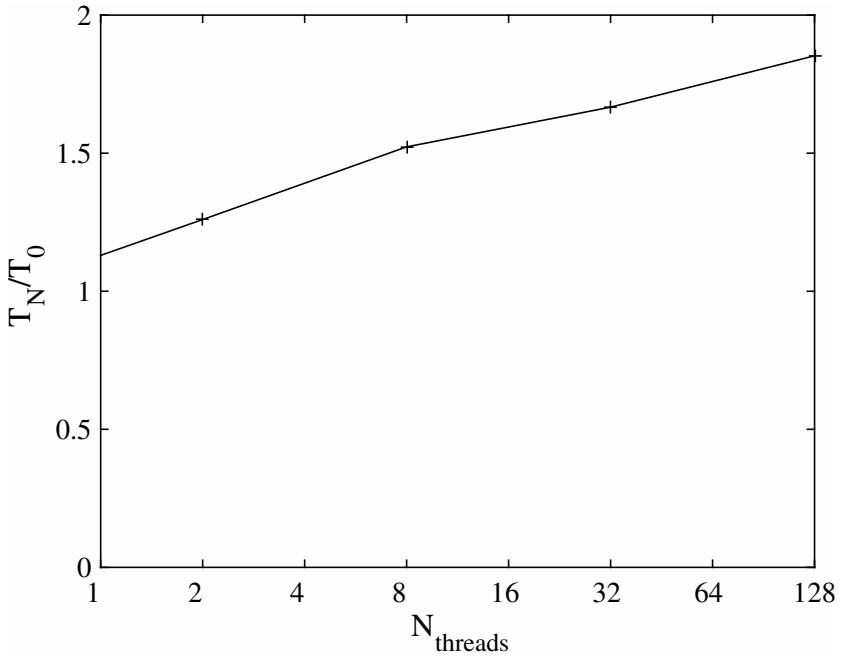

Figure IV.3: Weak scalability. The computational time is normalized with respect to the computational time on one thread (T_0).

The strong scalability has been tested until 1024 threads. For such a number of threads, we observed large differences according to how the computational time is calculated. It has been calculated in three different ways. The first one correspond to the wall time $t - Wt$ used for the whole calculation (which corresponds also to the CPU time since all the nodes are used exclusively). The second way is the wall time without the MPI initialization Wt. Finally we also calculated the wall time $it - Wt$ used for a single time step (as the mean of 500 iterations). All the results represent the mean of three computations.

Figure IV.4 shows that the scalability is better than the theoretical expectations for 4 and 16 threads. This is due to memory access time for the 1 thread computation. To have enough memory, several nodes are required and then the time to access to the data stored in an other node slow down the code. When 4 or 16 threads are used, they are distributed on different nodes and then each thread has enough memory on its node. The time required to access to the data is decreased. A linear regression of the scalability curve from $N_{threads} = 4$ to $N_{threads} = 1024$ would give a scalability of 0.7 which is a satisfying result. Even for 1024 threads, the scalability is very good. However, the case of the total wall time loose performance on 1024 threads while the two other keeps a good scalability. This is probably due to the architecture of the cluster that can be slow to initialize a parallel set-up. The difference between the two other results is the initialization of the computation (partitioning, creation of the computational domain, initial condition). Its effect decreases as we increase the duration of the computation. In all cases a loss of performance is observed for high number of threads. It is expected since the communications represent a larger part of the computation as the number of thread increases. This is also due to the penalized part in the domain where the thread have less work to do as for the weak scalability. The partitioning being independent of the penalization, the load on each threads is no more balanced. A solution would be to also paralellize the code in velocity space to keep a good scalability on more threads.

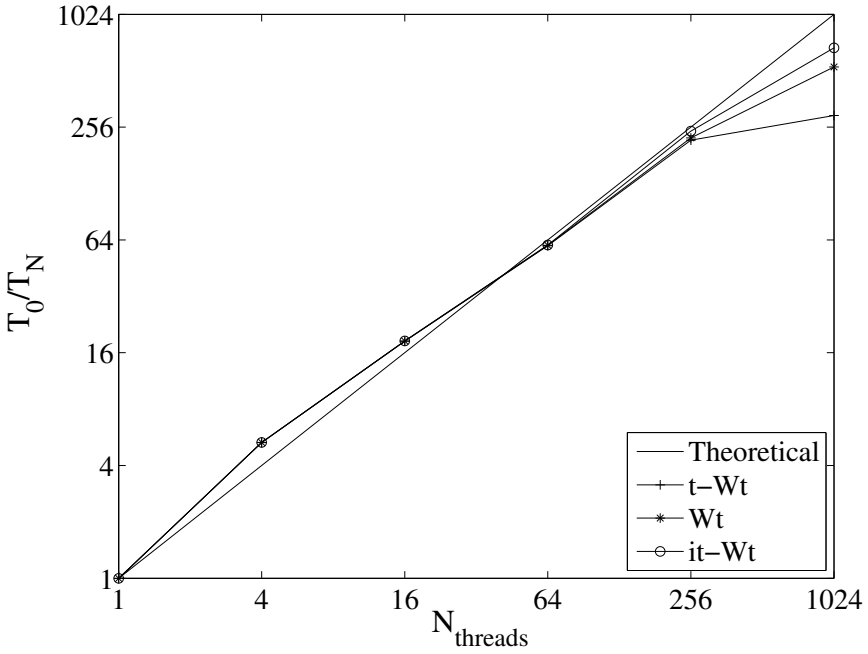

Figure IV.4: Strong scalability.

IV.2 A local velocity grid approach

This section is devoted to another important contribution of this work to the improvement of the resolution of kinetic models in terms of computational cost. The results have been published in [12].

The discrete velocity method (DVM) is a deterministic method for solving kinetic models. It is based on a discretization of the velocity space. It has the advantage of not suffering from numerical noise (like with DSMC, [16]) and the cost depends on the velocity grid. However, the size of the velocity grid can increase rapidly as strong gradients of temperature or velocity appear in the field since the same velocity grid is used for the whole computation. For realistic test cases like hypersonic atmosphere re-entries or satellite engines, the velocity grid needs to be large and fine inducing very large computational requirements in time and memory. Computations in 3D become even more complicated.

This problem has already been addressed in several works. In [32], an AMR technique has been developed for the gas-kinetic scheme [115]. The resulting method is accurate but there is no relation between velocity grids in different space cell. Thus, interpolations are required to compute the transport step leading to approximation errors and possible increasing computational time. An other AMR technique has been presented in [9] for steady flow. The method is based on a Cartesian velocity grid that is refined or coarsened according to a criteria. It has been proven accurate but at each time step, grid adaptation and interpolations are still required not only for the transport step but also between successive velocity grids. The problem of defining *a priori* the boundaries of the velocity as been dealt with by Brull and Mieussens in [23]. At each time step an entire velocity grid is generated in each space cell according to the macroscopic values. Once again interpolations are needed between neighbouring space cells and between time steps possibly causing some overhead in CPU time.

The idea presented in the following aims to reduce the computational time with a very simple algorithm and without causing CPU time overhead. Interpolations and refinement steps are avoided and a significant gain is observed in computational time without loss of accuracy.

In a first part, the algorithm will be described in 1D. Then the approach will be extended to a multidimensional space.

IV.2.1 The 1D algorithm

We start describing the construction of the local velocity grid in 1D. For test cases with strong shocks or with high temperature or velocity differences, the boundaries of the velocity grid have to be very extended with a fine grid spacing. We recall (see Section II.1 and (II.4)) that usually the grid is defined with the following conditions:

$$\mathcal{G} = (\xi_u^i)_{i=-n_v..n_v} \quad \text{such that} \begin{cases} \xi_u^{max} = |u|_{max} + 5\sqrt{T_{max}} \\ \xi_u^{min} = -\xi_u^{max} \\ \Delta\xi_u \leq \sqrt{T_{min}} \end{cases} \tag{IV.1}$$

with $|u|_{max}$ the maximum absolute value of the macroscopic velocity and T_{max} the maximum temperature over space and time. In spatial cells, the distribution function will be concentrated on a sub-part of the global velocity grid and will be zero (or negligible) elsewhere.

The idea of the present work is to avoid the computation of the distribution function where it is negligible and more specifically, where the convective fluxes will be zero or negligible.

Local grids in velocity are chosen for each space cell based on the macroscopic quantities. Each local grid is a sub-set of the global velocity grid which would be the one chosen thanks to (II.4).

In particular, considering a global velocity grid with a set of N_v velocity points $(\xi_u^k)_{k=1,N_v}$, the local grid on a cell i is set as follows:

$$\begin{aligned} \hat{\xi}_{u_{min}}^{\ i} = \xi_u^l \quad \text{such that} \quad \xi_u^l = \max_{k\in[1,N_v]}(\xi_u^k \leq u_i - \alpha\sqrt{T_i}) \\ \hat{\xi}_{u_{max}}^{\ i} = \xi_u^l \quad \text{such that} \quad \xi_u^l = \min_{k\in[1,N_v]}(\xi_u^k \geq u_i + \alpha\sqrt{T_i}) \end{aligned} \tag{IV.2}$$

where u_i and T_i are the macroscopic velocity and temperature in cell i. $\hat{\xi}_{u_{min}}^{\ i}$ and $\hat{\xi}_{u_{max}}^{\ i}$ are respectively the minimum and maximum velocity node contained in the local grid for the space cell i. Note that in this way, the interfaces of velocity cells belonging to different local grids are aligned. Then, no interpolation is needed to compute the numerical fluxes in the transport step. Indeed, all the local grids are based on the global grid. Thus, if ξ_u is outside the local grid at t^n, $f(x, \xi_u, t^n)$ is set to zero.

Defining in such a way the local velocity grids is not enough as the gas evolves. Let us consider the case where a velocity point ξ_u^k exists in the velocity grid of a given space cell i but not in the velocity grid of the neighbour cell $i+1$. Even small, the value of the distribution function $f_{i,k}$ is not zero in the first cell while $f_{i+1,k} = 0$. Thus a small flux is created and it must contribute to update $f_{i,k}$ and $f_{i+1,k}$. But for the cell that does not contain this microscopic velocity, the value of the distribution function cannot be updated unless that point is included in the local grid and the value of f in that cell may become non negligible in long time. Hence, at the beginning of the time step, the local grids will be set as the union of the local grids contained in the stencil of the numerical flux (see Figure IV.5). For a first-order scheme based on a three points stencil:

$$\begin{cases} \xi_{u_{min}}^{\ i} = \min(\hat{\xi}_{u_{min}}^{\ i-1}, \hat{\xi}_{u_{min}}^{\ i}, \hat{\xi}_{u_{min}}^{\ i+1}) \\ \xi_{u_{max}}^{\ i} = \max(\hat{\xi}_{u_{max}}^{\ i-1}, \hat{\xi}_{u_{max}}^{\ i}, \hat{\xi}_{u_{max}}^{\ i+1}) \end{cases} \tag{IV.3}$$

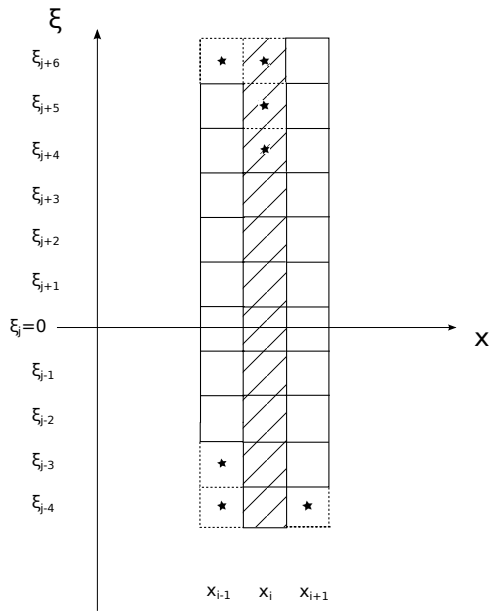

Figure IV.5: Representation of velocity-space cells in phase space in 1D. Local grids defined in cell $i-1$, i, $i+1$ before the union are in solid lines and stencil used for the transport in space cell i after the union is in dashed lines. Cells in the local grid for space cell i are hatched. Cells with marker ★ are cells added after the union.

$\xi_{u_{min}}^{\ i}$ and $\xi_{u_{max}}^{\ i}$ are respectively the new minimum and maximum velocity contained in the local grid for cell i. This step ensures that not only the distribution function is zero outside the local grid but the numerical fluxes at the grid interfaces are also zero outside $(\xi_{u_{min}}^{\ i}, \xi_{u_{max}}^{\ i})$.

For a second-order scheme in space, there are actually two more cells involved in the stencil of the transport step for each cell. Indeed, to calculate the flux between cell i and cell $i+1$, one needs the slopes in cell i and in cell $i+1$. In the cell $i+1$ the slopes are calculated with (II.13) which involves the distribution function in cell $i+2$. Thus, the union is performed as follows:

$$\begin{cases} \xi_{u_{min}}^{\ i} = \min(\hat{\xi}_{u_{min}}^{\ i-2}, \hat{\xi}_{u_{min}}^{\ i-1}, \hat{\xi}_{u_{min}}^{\ i}, \hat{\xi}_{u_{min}}^{\ i+1}, \hat{\xi}_{u_{min}}^{\ i+2}) \\ \xi_{u_{max}}^{\ i} = \max(\hat{\xi}_{u_{max}}^{\ i-2} \hat{\xi}_{u_{max}}^{\ i-1}, \hat{\xi}_{u_{max}}^{\ i}, \hat{\xi}_{u_{max}}^{\ i+1}, \hat{\xi}_{u_{max}}^{\ i+2}) \end{cases} \tag{IV.4}$$

With this approach, the maximum microscopic velocity used for the computation of the transport step is not necessarily the maximum velocity of the global grid $\mathcal{G}$. It may also vary in time but it remains at most the maximum velocity of the global grid. To improve the computational time, at each time step a new Δt can be computed considering the maximum velocity $\xi_{u_{max}}$ of all the local velocity grids. This modification may reduce the CPU time in all cases where the maximum velocity of the global grid is not contained in any local grid.

This approach ensures that for a Maxwellian distribution function and $\alpha \geq 5$ the density error is less than 10^{-6}. However, the error can be larger for high Knudsen numbers, when the distribution function is not Maxwellian. In order to account for these cases, the local grid at the new time step is chosen as follows. First, in a space cell i at time t^n, the local grid $\mathcal{G}_i^n$ is estimated as in (IV.2). Then a test is performed on the distribution function to check that the new local grid contains a significant part (set with a tolerance) of the distribution function

stored in the old grid $\mathcal{G}_i^{n-1}$. This condition reads as follows:

$$\frac{|\int_{\mathcal{G}_i^n} f_i^n d\xi_u - \int_{\mathcal{G}_i^{n-1}} f_i^n d\xi_u|}{\int_{\mathcal{G}_i^{n-1}} f_i^n d\xi_u} < tol \tag{IV.5}$$

where *tol* is a tolerance (set to 10^{-5} in all numerical test cases). If (IV.5) does not hold, $\mathcal{G}_i^n = \mathcal{G}_i^{n-1}$. Finally, the union of the neighbour velocity grids is performed as in (IV.4).

Defining the local velocity grids in such a way ensures that if all the distribution function is contained in the local grids at the first time step, the convective fluxes outside the local grids are zero even if the distribution function is not a Maxwellian. A similar criteria could be imagined on the energy for instance. That is why in the case of the reduced model, we also added the same criteria on the second distribution function to ensure at each time step the conservation of mass and energy.

Let us summarize the algorithm to define the local grid in the space cell i at the beginning of each time step for a 1D case. Let $\mathcal{G}_i^{n-1}$ be the grid used in the previous time step:

1. Compute the maximum and minimum velocity required with respect to the parameter α, the macroscopic velocity and the temperature as in (IV.2).

2. Check if the distribution function f_i^n is contained in the new local grid $\mathcal{G}_i^n$ with respect to a tolerance as in (IV.5). Otherwise set $\mathcal{G}_i^n = \mathcal{G}_i^{n-1}$.

3. Perform the union with the neighbour local velocity grids with (IV.4).

4. Compute the numerical fluxes using the new grid and evolve f_i^{n+1}.

Note that step 2 is not performed at t=0 because the distribution function at t=0 is initialized with the local Maxwellian in each space cell. Thus the criteria on the standard deviation is enough to initialize the local velocity grids with good accuracy.

IV.2.2 The multidimensional space algorithm

The extension to multidimensional space is quite straightforward. The same approach is used along all dimensions independently. By considering the local macroscopic velocity and local temperature, criteria (IV.2) is applied to construct the local grid in each space direction with the corresponding component of the macroscopic velocity. The maximum and minimum microscopic velocity ($\hat{\boldsymbol{\xi}}_{max} = (\hat{\xi_u}_{max}, \hat{\xi_v}_{max}, \hat{\xi_w}_{max})$ and $\hat{\boldsymbol{\xi}}_{min} = (\hat{\xi_u}_{min}, \hat{\xi_v}_{min}, \hat{\xi_w}_{min})$ in 3D) are then computed along each space direction independently. To make sure of including all non zero flux on non-existing velocities (as described in 1D), a union of the neighbour velocity grids has to be performed. In multidimensional cases, the fluxes are calculated with a directional splitting. Each local grid has to include all the local grids involved in the transport step. For example, in 2D, in a space cell (i, j) and for a second-order scheme in space:

$$\boldsymbol{\xi}_{min}^{i,j} = \min_{k=-2,..,2}(\hat{\boldsymbol{\xi}}_{min}^{i+k,j}, \hat{\boldsymbol{\xi}}_{min}^{i,j+k}) \qquad \text{and} \qquad \boldsymbol{\xi}_{max}^{i,j} = \max_{k=-2,..,2}(\hat{\boldsymbol{\xi}}_{max}^{i+k,j}, \hat{\boldsymbol{\xi}}_{max}^{i,j+k}) \tag{IV.6}$$

As in the 1D case, this kind of approach might not be accurate away from the hydrodynamic regime. Therefore, the same correction of the local velocity grid is applied based on the integral of the distribution function (Eq.(IV.5)).

The local grids are then a sub-rectangle of the global grid in 2D and a brick in 3D.

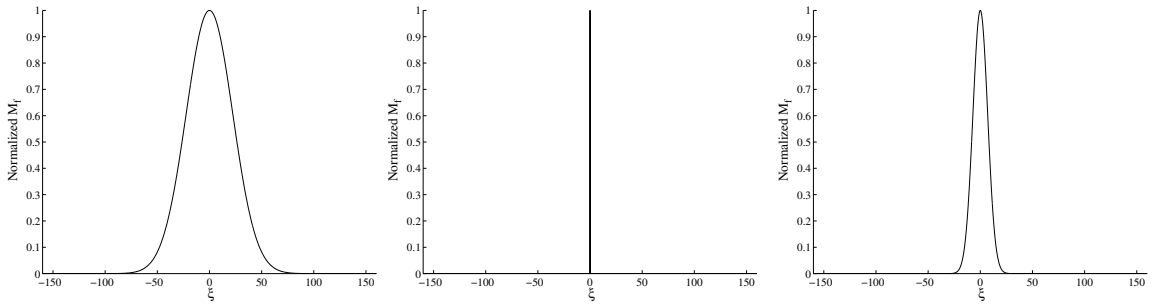

(a) Region A (b) Region B (c) Region C

Figure IV.6: Test case 1: Normalized Maxwellian distribution functions.

IV.3 Numerical results

In this section numerical results will be presented in 1D and 2D for both hydrodynamic and rarefied regimes. Three test cases are presented for the BGK model. In the second test case, we also show the results for the ES-BGK model in both hydrodynamic and rarefied regime. The computations for the 2D test cases are performed in parallel.

IV.3.1 Test case 1: Two interacting blast waves

IV.3.1.1 Hydrodynamic regime

This test case was initially introduced by Woodward and Colella [114]. It is a popular test case that shows the ability of a scheme to correctly capture very strong shock waves in the continuum regime. Initially, the domain [0,1] is decomposed in three sub-domains:

$$\begin{cases} \rho = 1, \quad u = 0, \quad p = 1000 \quad \text{in [0,0.1]} \quad \text{(region A)} \\ \rho = 1, \quad u = 0, \quad p = 0.01 \quad \text{in [0.1,0.9]} \quad \text{(region B)} \\ \rho = 1, \quad u = 0, \quad p = 100 \quad \text{in [0.9,1]} \quad \text{(region C)} \end{cases}$$

In each subdomain, the distribution function is initialized as a Maxwellian. Due to the large temperature differences, the support of each Maxwellian is very different as shown on Figure IV.6.

At the boundaries of the domain, solid walls reflect the waves. The classic specular reflection is applied. The Knudsen number is set to 10^{-5} and the simulation is stopped at t=0.01. Second-order schemes in space and time are used. The global velocity grid is computed as in (II.4). In this case, the velocity space is [-160,160] and is discretized uniformly with 3200 grid points for the global grid. The solution is shown on Figure IV.7 for the temperature and the density. The solid line corresponds to the solution of the BGK equation on the global grid, the dashed line corresponds to the solution of compressible Euler equations while the solution for the BGK equation with the local grid method and $\alpha = 6$ is represented with + signs.

The local velocity grids are defined as in (IV.2), and we investigate the performance of the scheme as a function of the parameter α. Note that increasing α means that the local grid boundaries are enlarged. Figure IV.8 shows the boundaries of the local grids as a function of space when only criteria (IV.2) is used with $\alpha = 6$. Taking into account the second criteria enlarges the local grid around shocks (see figure IV.9). Comparing it with the global grid (in solid lines) highlights that the local grid includes only a fraction of the global grid points.

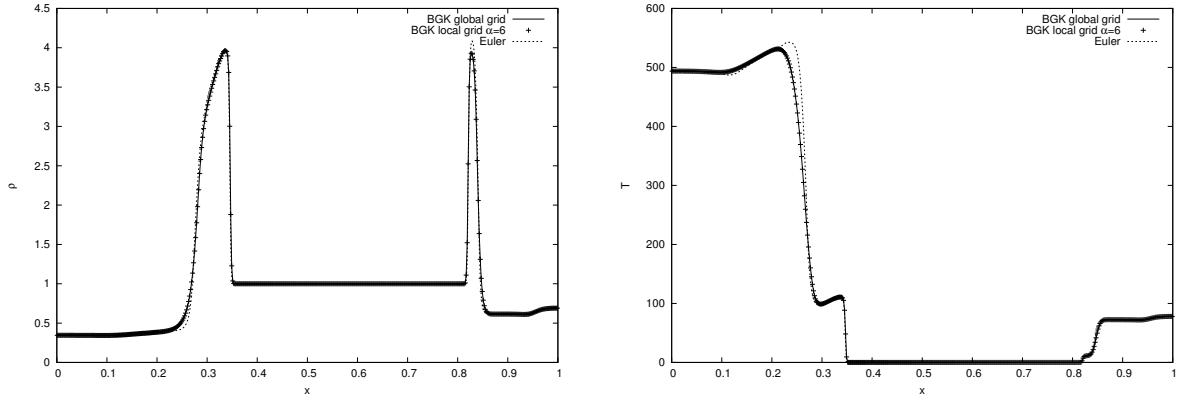

(a) Density (b) Temperature

Figure IV.7: Test case 1, $Kn_\infty = 10^{-5}$: Density and temperature solution with 500 grid points in space.

Figures IV.10 and IV.11 show the normalized errors in L_1, L_2 and L_∞ norm for the density, velocity and energy for several values of α. The behaviour for large values of α is also presented in L_∞norm on Figure IV.11. Defining $\underline{\rho} = (\rho, \mathbf{U}, E)$, the different norms are normalized as follows:

$$L_{p,normalized}(\underline{\rho}) = \frac{||\underline{\rho}_{\mathcal{G}} - \underline{\rho}_{\mathcal{G}_v}||_{L_p}}{||\underline{\rho}_{\mathcal{G}}||_{L_p}} \tag{IV.7}$$

where L_p is the standard $L_p$norm, $\underline{\rho}_{\mathcal{G}}$ is the solution for $\underline{\rho}$ on the global velocity grid, $\underline{\rho}_{\mathcal{G}_v}$ is the solution for $\underline{\rho}$ with the local velocity grid method.

It is observed that the error decreases fast and for $\alpha \geq 6$ the error is already lower than 10^{-6} in all norms. It remains stable for large values of α.

One can also compute the conservation error on mass and energy normalized by the initial value of mass and energy respectively (Figure IV.12) as a function of α. This error has a similar behaviour and reaches quickly machine precision (which corresponds to the conservation error on the global grid) since the scheme is conservative.

Results on Figure IV.13a show the fractions of the computational time and of the total number of velocity grid points used with respect to the global grid calculation as function of α. These results are obtained with a constant time step defined with the maximum velocity of the global grid. Even for $\alpha = 600$ the velocity grid does not coincide with the global grid because of the presence of regions where the temperature is small. Indeed, in such areas the standard deviation of the Maxwellian is small (~ 0.1) and a large value of α is required to get the whole grid ($\alpha \sim 1600$). If the time step is defined at each iteration with the maximum velocity contained in the local grids (but still constant in space), the computational time can be significantly reduced when the maximum velocity of the global grid is not contained in any local grid. Figure IV.13b shows the comparison of the computational time obtained with a constant time step and a variable time step defined as above.

The largest gain is obtained for small values of α. But even with higher values, there is still a gain. For instance, for $\alpha = 6$, the error is below 10^{-6} with a conservation error below 10^{-5} while the gain in CPU time is around 50% using less than 75% of the global grid.

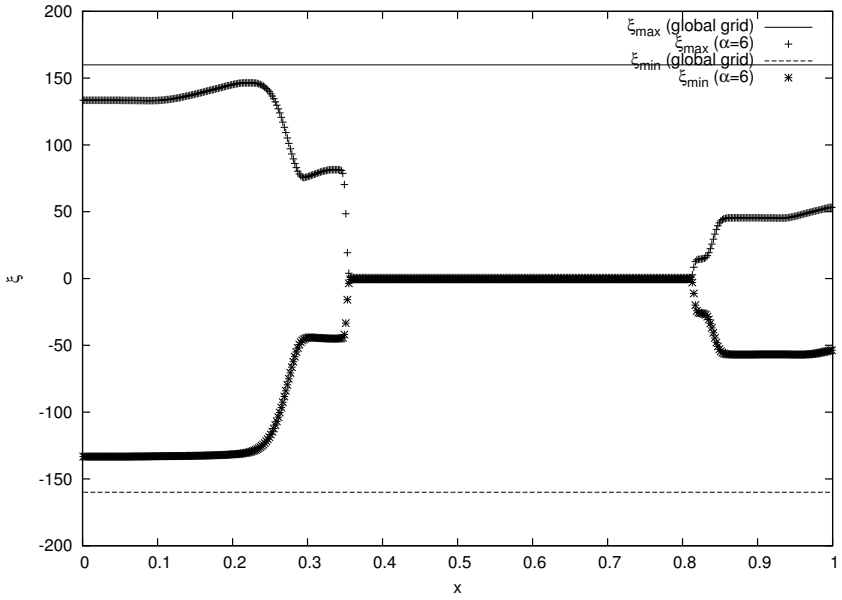

Figure IV.8: Test case 1, $Kn_\infty = 10^{-5}$: Maximum and minimum velocity in the local grids for $\alpha = 6$ (first criteria).

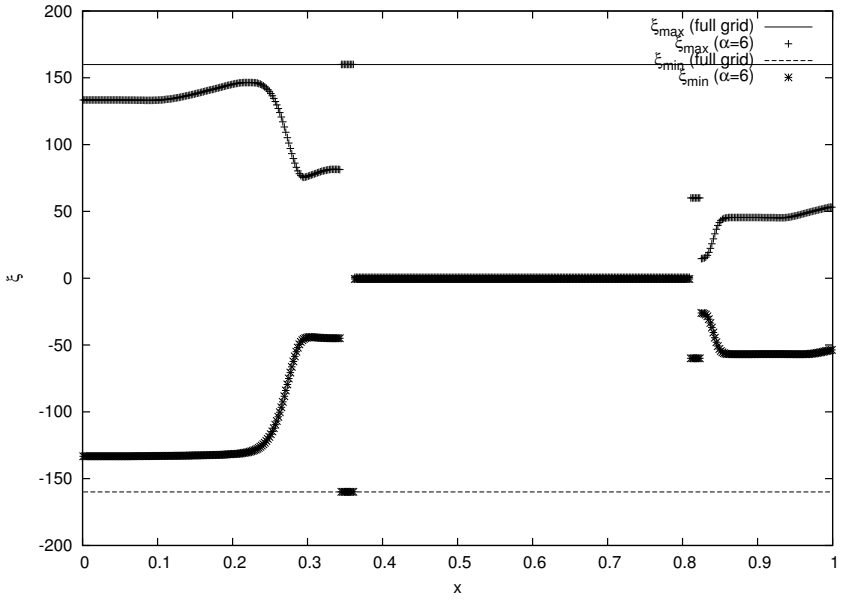

Figure IV.9: Test case 1, $Kn_\infty = 10^{-5}$: Maximum and minimum velocity in the local grids for $\alpha = 6$ (both criteria).

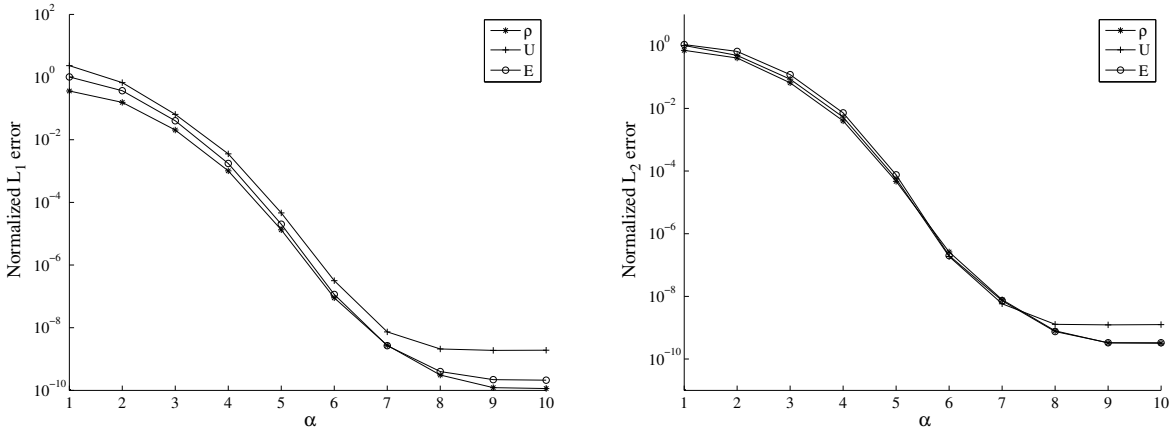

(a) L_1 errors (b) L_2 errors

Figure IV.10: Test case 1, $Kn_\infty = 10^{-5}$: L_1 and L_2 error on density, velocity and energy.

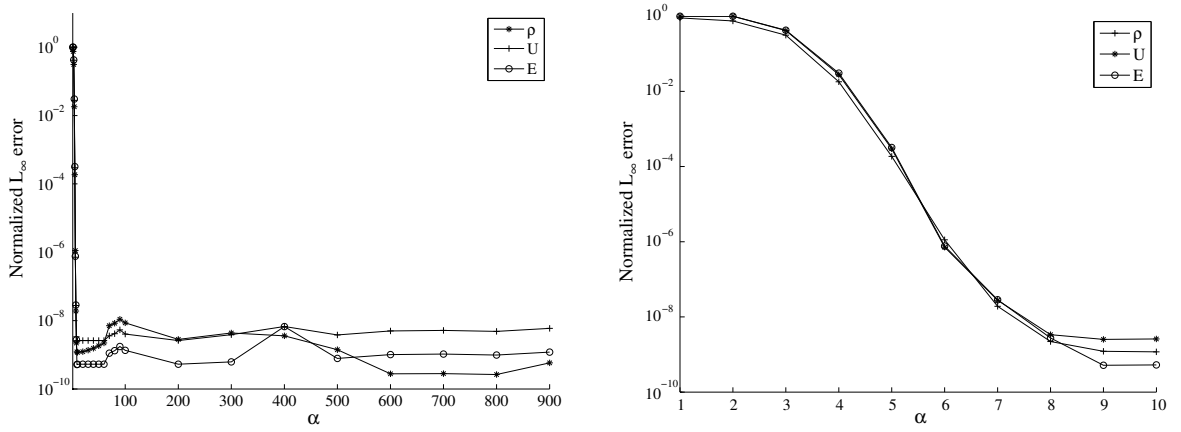

Figure IV.11: Test case 1, $Kn_\infty = 10^{-5}$: L_∞ error on density, velocity and energy.

IV.3.1.2 Rarefied regime

Here the method is tested on the same test case but with a higher Knudsen number. In particular, we consider $Kn_\infty = 10^{-2}$ as an intermediate regime, and $Kn_\infty = 1$ for the fully kinetic regime. The local grids are now defined with (IV.2) and (IV.5).

In these cases, the error of the method is larger with respect to the case at low Knudsen number because the distribution function may be more diffusive than the Maxwellian and thus the conservation error may increase as Kn_∞ grows. Since the shape of the distribution function is not close to a Maxwellian distribution function, criteria (IV.5) on the integral of the distribution function has to be used. Hence, the error still goes towards zero for reasonable values of α. We show the results on the error in L_∞ on Figures IV.15. In other norms, the errors behave similarly. These results also show that for α around 5, there is a kink in the error. This occurs when the conservation criteria (IV.5) becomes less restrictive than the criteria on α. Typically, for these values of α (around 5) the more restrictive criteria switches from one to another during the calculation. The same behaviour can be observed in the following error curves relative to 2D hydrodynamic or kinetic regime.

The gain in the computational time (see Figure IV.16) is much smaller than for $Kn_\infty = 10^{-5}$ because the relaxation time is too high to redistribute the particles as a Maxwellian distribution

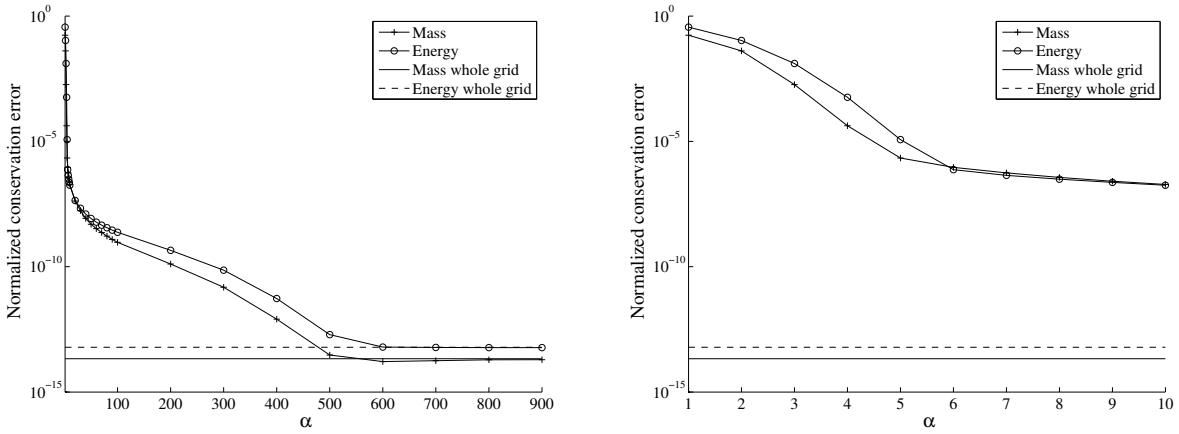

Figure IV.12: Test case 1, $Kn_\infty = 10^{-5}$: Conservation error.

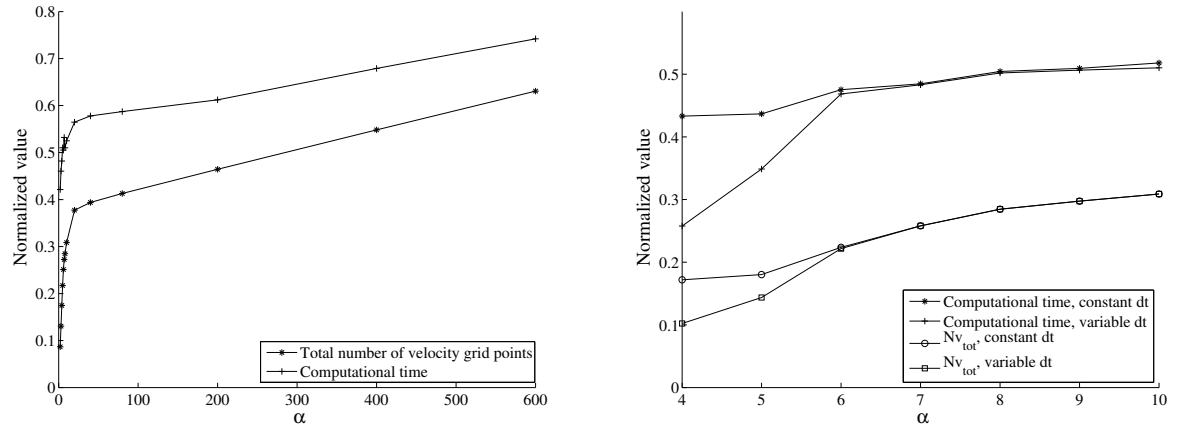

(a) Constant time step.

(b) Constant and variable time step.

Figure IV.13: Test case 1, $Kn_\infty = 10^{-5}$: Normalized number of velocity grid points used and computational time with respect to the global grid calculation.

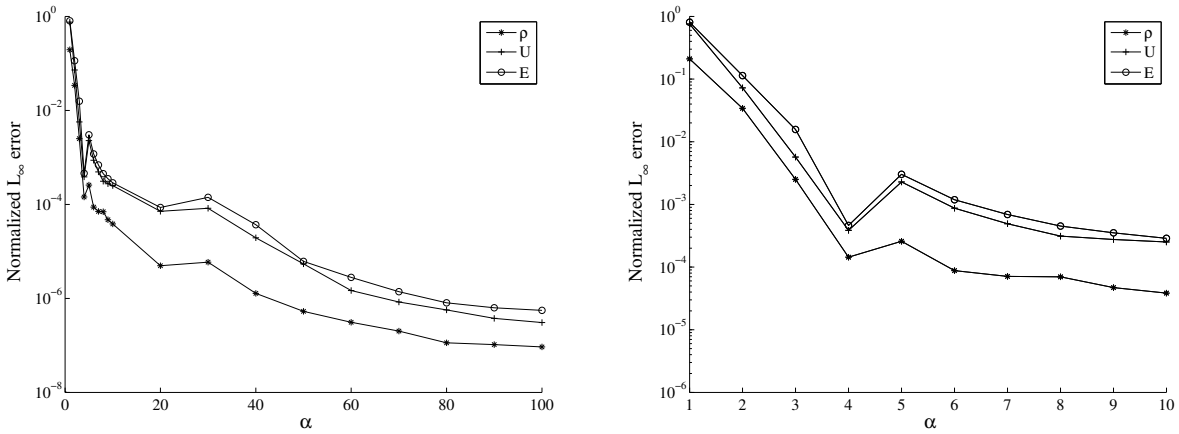

Figure IV.14: Test case 1, $Kn_\infty = 10^{-2}$: L_∞ error on density, velocity and energy (left) with a zoom on small values of α (right).

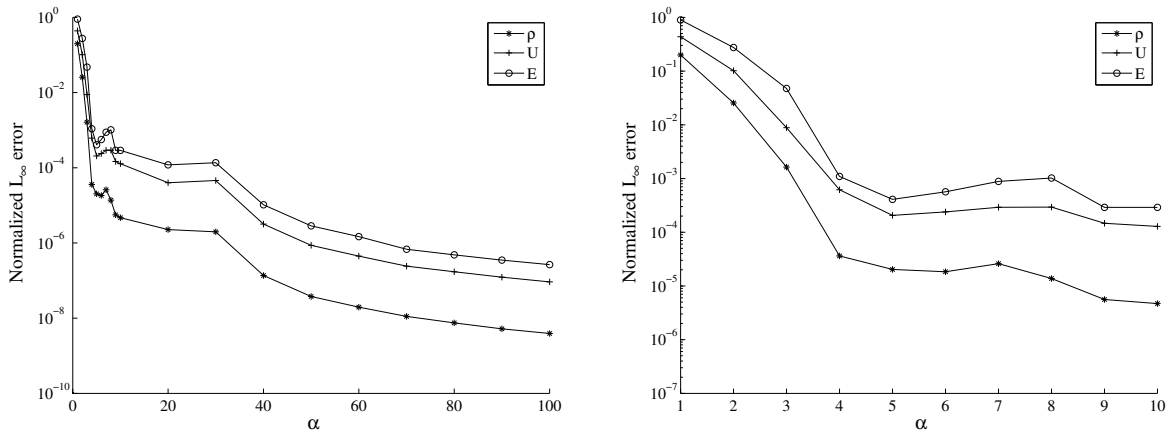

Figure IV.15: Test case 1, $Kn_\infty = 1$: L_∞ error on density, velocity and energy (left) with a zoom on small values of α (right).

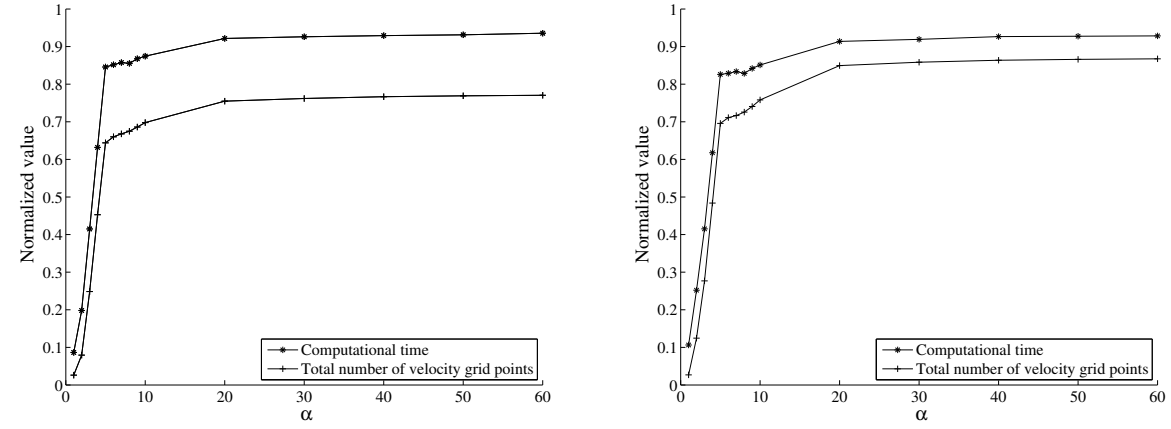

(a) $Kn_\infty = 10^{-2}$ (b) $Kn_\infty = 1$

Figure IV.16: Test case 1: Computational time and total number of velocity grid points used for different values of Kn_∞.

function after the convective step. Then, after several time steps, the distribution function lies on a large part of the velocity grid in all cells. But even in this case a gain of about 15% can be obtained for a relative error of 10^{-4}, which is obtained at $\alpha = 6$.

IV.3.2 Test case 2: A Mach 3 wind tunnel with a step

As in the first test case, the rarefied and hydrodynamic regimes are investigated in the case of a wind tunnel with a step. We also present the results obtained with the ES-BGK model for two different Knudsen numbers: $Kn_\infty = 10^{-5}$ and $Kn_\infty = 0.01$.

IV.3.2.1 The hydrodynamic regime with the BGK model

Here, the local grid method is tested on a 2D case. A flow at $M = 3$ propagates in a tunnel with a step. A shock is created on the step and then is reflected on the top of the tunnel. Strong shocks propagate and interact with themselves and with the boundaries. This is also a difficult test case for the discrete velocity model because of the step geometry. The temperature profile obtained with the BGK model at $Kn_\infty = 10^{-5}$ is shown in Figure IV.17.

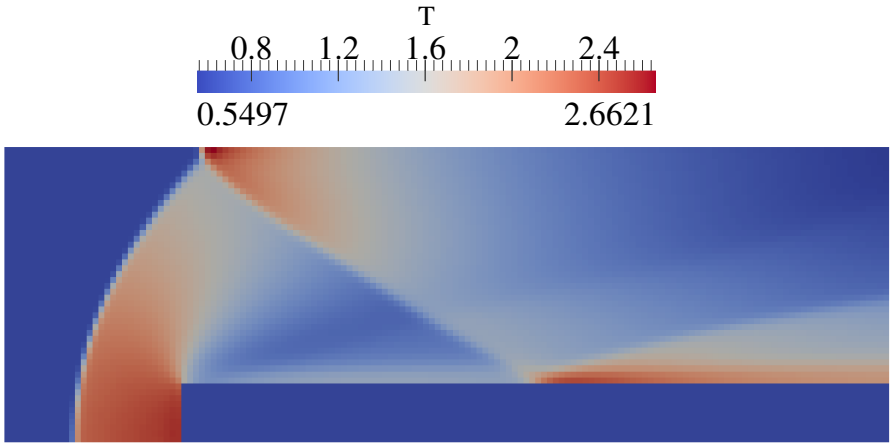

Figure IV.17: Test case 2, $Kn_\infty = 10^{-5}$: Solution for the temperature (BGK model).

The domain is [0,3]×[0,1]. The step lies from $x = 0.6$ to $x = 3$ and goes from $y = 0$ to $y = 0.2$. The spatial domain is discretized with 150×50 cells. The Knudsen number is set to 10^{-5}. The global velocity space is [-20,20]×[-20,20] discretized on a Cartesian grid with 61 grid points in each direction. It is built to satisfy conditions (II.4). We look at the solution at $t = 1.2$.

The error is calculated with respect to the BGK solution on the whole velocity grid for different values of α for density, velocity and temperature. The L_∞ norm of this error is plotted on Figures IV.18. Other norms behave similarly.

As for the 1D case, the error on macroscopic variables goes quickly towards zero as α grows. For values of α between 5 and 10, the error is lower than 10^{-4} in all norms.

Figure IV.19 shows the computational time and the total number of velocity grid points used for one iteration on one processor. It shows a good scalability of the method with respect to the number of velocity grid points. For small values of α (≤ 5) the computational time becomes less sensitive to the number of velocity grid points used because the execution time of some parts of the code is independent or almost independent of the number of velocity grid points. For example, the time required to compute the Maxwellian distribution function is mostly due to the solution of the non-linear system in (II.3) and the number of space cells.

The computational time to get the solution at t=1.2 has also been compared for constant and variable time steps, as well as the total number of velocity grid points used for the whole calculation (see Figure IV.20). It shows that the method is efficient because the computational time scales well with the number of velocity grid points. With $\alpha = 10$, less than 30% of the whole grid is used and the computational time is reduced by more than 50% with a good accuracy (the L_∞norm is lower than 10^{-4} for all variables).

We also display the number of velocity grid points used in each cell at the final time (Figure IV.21). More detail is needed in the regions where there are sharp gradients, and where the gas is far from equilibrium. The width of the grid is determined by the temperature and thus it follows the temperature profile (compare Figure IV.17 and IV.21).

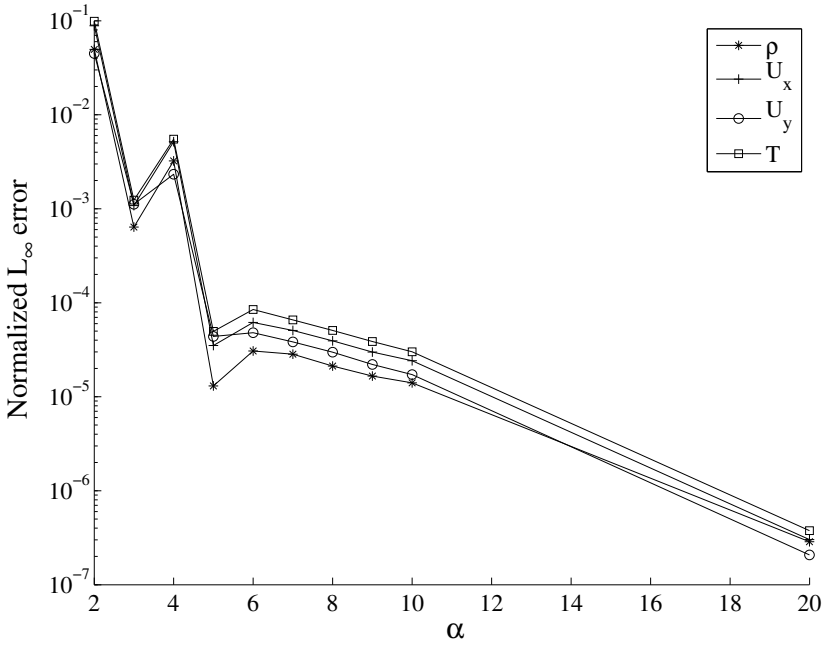

Figure IV.18: Test case 2, $Kn_\infty = 10^{-5}$: L_∞ error on density, velocity and temperature (BGK model).

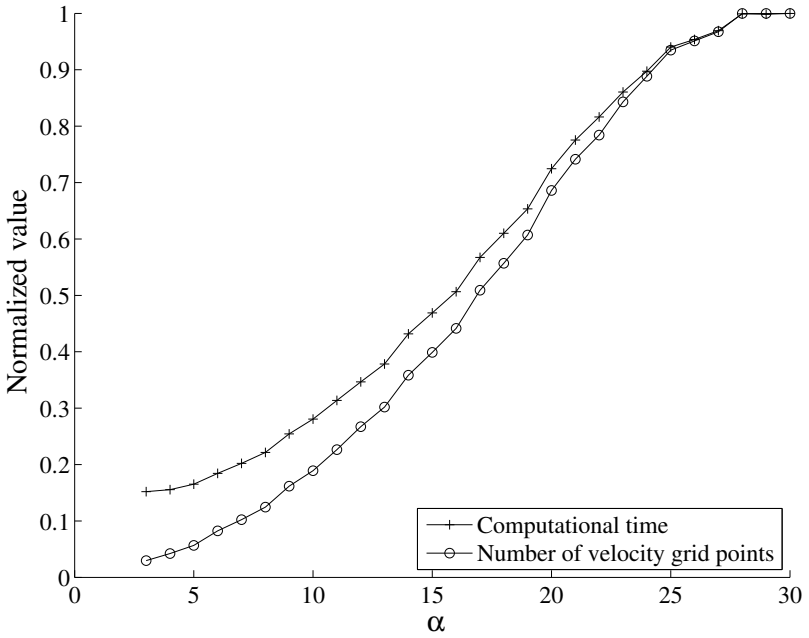

Figure IV.19: Test case 2, $Kn_\infty = 10^{-5}$: Normalized number of velocity grid point used and computational time with respect to the full grid calculation for one iteration on one processor with the BGK model.

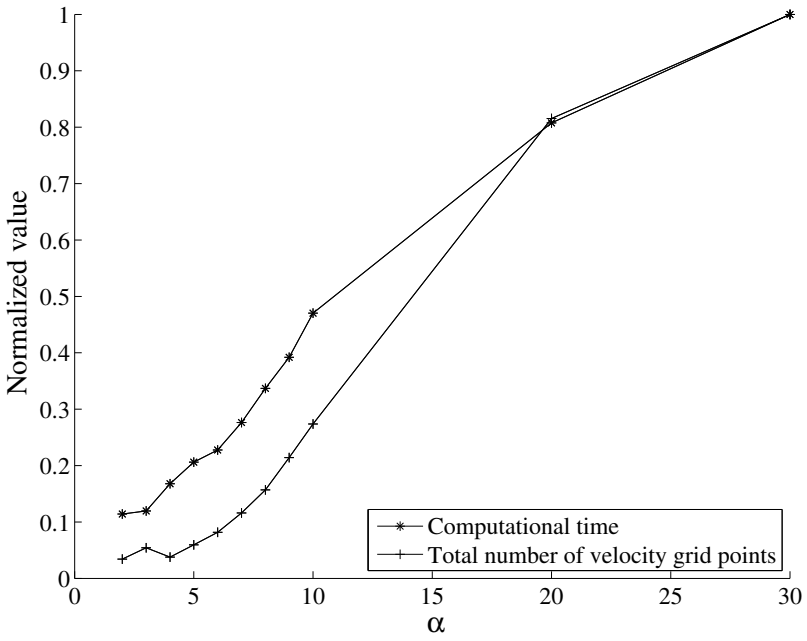

Figure IV.20: Test case 2, $Kn_\infty = 10^{-5}$: Normalized number of velocity grid point used and computational time with respect to the full grid calculation (BGK model).

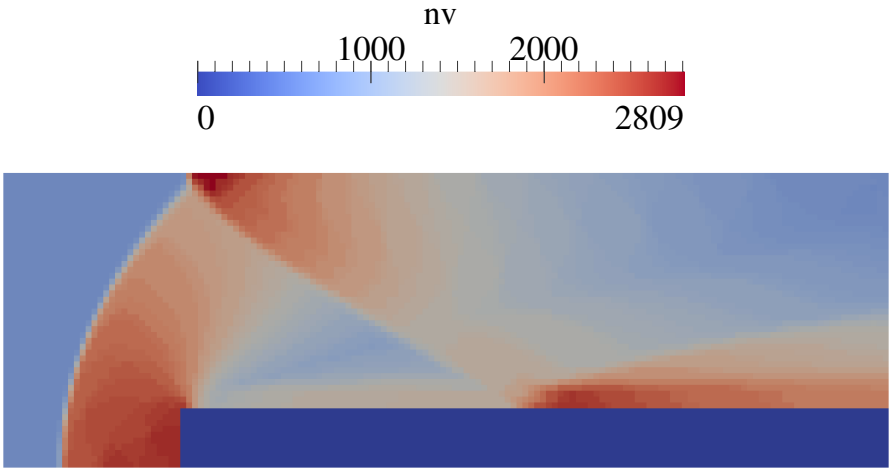

Figure IV.21: Test case 2, $Kn_\infty = 10^{-5}$: Number of velocity grid points used in each cell at t=1.2 for $\alpha = 10$ (BGK model).

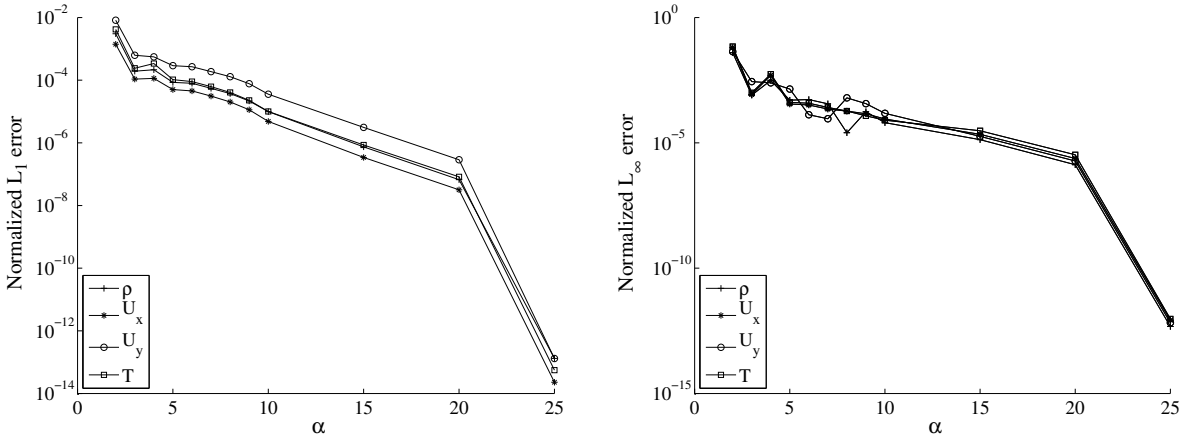

(a) Normalized L_1-norm of the error (b) Normalized L_∞-norm of the error

Figure IV.22: Test case 2, $Kn_\infty = 10^{-5}$: L_1 and L_∞ norm of the error with the ES-BGK model.

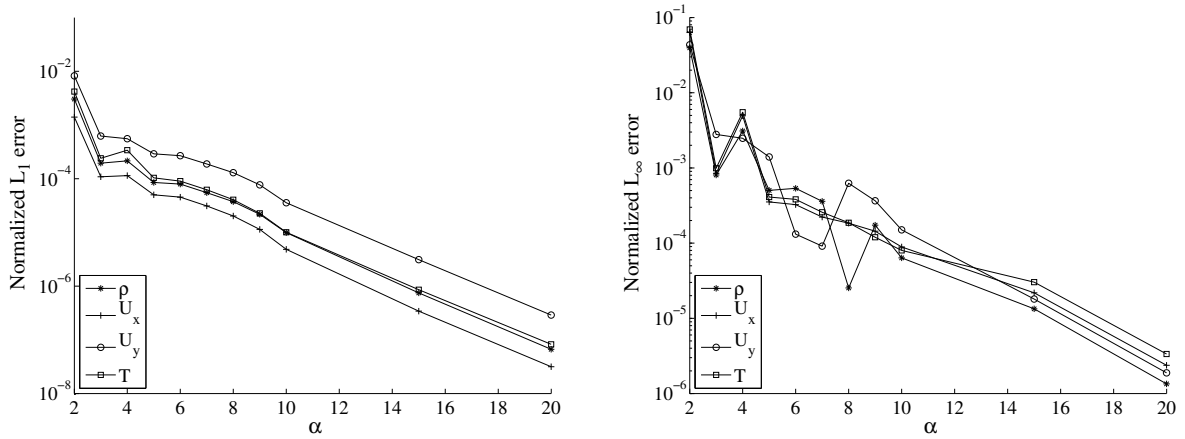

(a) Normalized L_1-norm of the error (b) Normalized L_∞-norm of the error

Figure IV.23: Test case 2, $Kn_\infty = 10^{-5}$: L_1 and L_∞ norm of the error with the ES-BGK model.

IV.3.2.2 The hydrodynamic regime with the ES-BGK model

The same test case is now simulated with the ES-BGK model. The Knudsen number is still 10^{-5} and the exact same method is applied as for the BGK model. We show the error in L_1 and L_∞ normalized error (figure IV.22) for the density, velocity and temperature with respect to the full grid calculation (obtained with $\alpha = 30$).

For $\alpha > 20$ the error goes quickly to zero in all norms. Figure IV.23 is a zoom on values of α between 2 and 20. As for the BGK model, the error is of the order of 10^{-4} for values of α around 4 and higher.

If we now compare the computational time, good reductions are obtained (see figure IV.24). For normalized errors below 10^{-4} in all norms ($\alpha > 10$), a gain of more than 50% is obtained using around 30% of the grid. These results are comparable to the ones obtain with the BGK model. It was expected since for this kind of regime, there should be no difference between the anisotropic Gaussian of the ES-BGK model and the Maxwellian distribution function of the BGK model. Thus, the local grid algorithm behaves similarly.

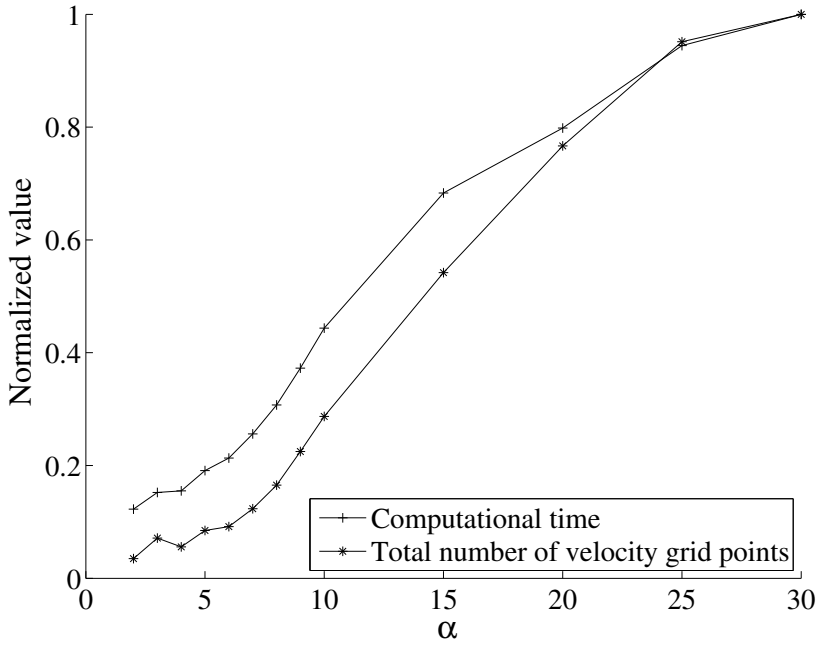

Figure IV.24: Test case 2, $Kn_\infty = 10^{-5}$: Normalized number of velocity grid point used and computational time with respect to the full grid calculation (ES-BGK model).

IV.3.2.3 The rarefied regime with the BGK model

The same test case is presented but with a Knudsen number set to 10^{-2} for the BGK model. Here, the distribution function will no longer be close to a Maxwellian. The criteria (IV.5) on the integral of the distribution function is more restrictive than the criteria involving α especially for small values of α. The results on the error in L_∞norm are shown in Figure IV.25a while the computational gains appear in Figure IV.25b. For $\alpha = 10$, the error is of the order of 10^{-5} and the CPU time is again reduced by more than 50%.

IV.3.2.4 The rarefied regime with the ES-BGK model

We now show the results obtained for the wind tunnel with a step in rarefied regime with the ES-BGK model. The results on the normalized error in L_∞ norm and on the computational gain are presented on figure IV.26.

Once again it shows that error decreases rapidly as α increases. For α larger than five, the normalized L_∞ error is already lower than 10^{-5} for the density, the velocity and the temperature. The computational time is about 80% lower than with the full velocity grid. Compared to the results in the rarefied regime of the BGK model, it is similar. However, we observe an increasing of the number of velocity grid points used for $\alpha = 9$ with respect to the case $\alpha = 10$. It is probably due to the the most restrictive criteria used to build the local grids that changes. In the rarefied regime, even for values of α around eight, the most restrictive criteria can be the one on the conservation. Indeed, the Gaussian being anisotropic, defining the width of the local grids only with a criteria based on the temperature is not always a good approximation. The constraints should also be considered. Thus, the criteria for the width of the local grids could be modified by considering the symmetric tensor $\mathcal{T}$ instead of the temperature. One could consider

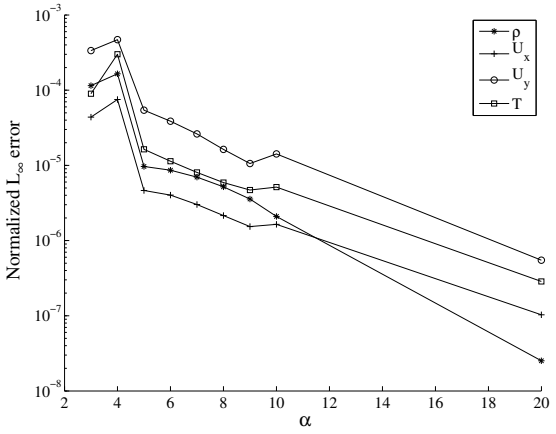

(a) L_∞ error on density, velocity and temperature.

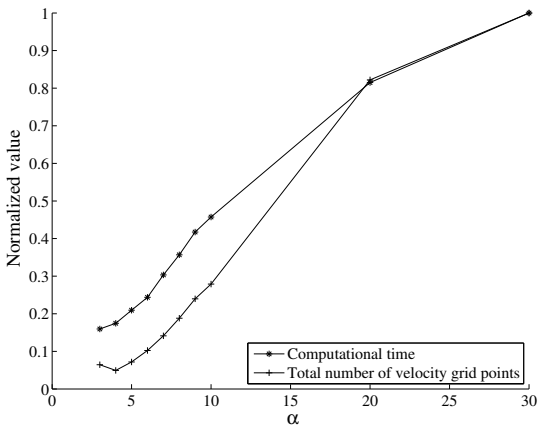

(b) Normalized number of velocity grid points used and computational time with respect to the full grid calculation.

Figure IV.25: Test case 2, $Kn_\infty = 10^{-2}$: Error, number of velocity grid points used and computational time for the BGK model.

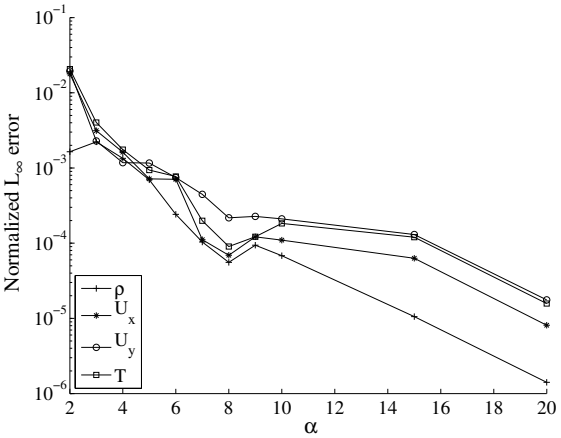

(a) L_∞ error on density, velocity and temperature.

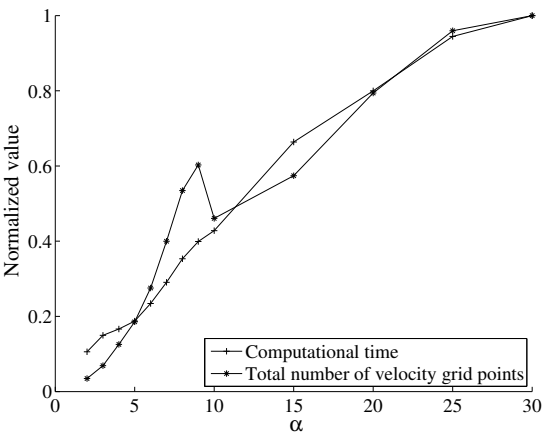

(b) Normalized number of velocity grid points used and computational time with respect to the full grid calculation.

Figure IV.26: Test case 2, $Kn_\infty = 10^{-2}$: Error, number of velocity grid points used and computational time for the ES-BGK model.

to set the grids in 1D as:

$$\hat{\xi_{u}}^{i}_{min} = \xi^l_u \quad \text{such that} \quad \xi^l_u = \max_{k\in[1,N_v]}(\xi^k_u \leq u_i - \alpha\sqrt{\max|\mathcal{T}_i|})$$
$$\hat{\xi_{u}}^{i}_{max} = \xi^l_u \quad \text{such that} \quad \xi^l_u = \min_{k\in[1,N_v]}(\xi^k_u \geq u_i + \alpha\sqrt{\max|\mathcal{T}_i|})$$

where $\max|\mathcal{T}_i|$ is the absolute maximum value of the tensor $\mathcal{T}$ in the cell i (its abolute value in 1D since it is a scalar).

Although considering the same algorithm for both BGK and ES-BGK model has induced this bump in the number of velocity grid points used in the case of the ES-BGK mode, the computational time has not been affected by this phenomenon. Hence, we decide to not modified the algorithm for the ES-BGK model. In the worst cases, the criteria on the conservation would increase automatically the size of the velocity grid.

IV.3.3 Test case 3: the blunt body at Mach 10

Another 2D test case is presented to show the efficiency of the method on a Cartesian grid with immersed boundaries. A cylinder is immersed in a flow at Mach 10. A shock develops on the body and very strong differences of temperature and velocity will appear in the field. We consider $Kn = 10^{-5}$ and therefore we impose the Euler-AP boundary condition on the cylinder.

This test requires a very large and fine velocity grid to capture all the phenomena. The domain is [-2,0]$\times$ [0,4] and is discretized with 50$\times$ 100 cells in space. The global velocity space is discretized with 101$\times$101 cells in [-50,50]$\times$[-50,50].

Figure IV.27 shows the solution for the temperature and the number of velocity grid points in each cell at steady state for $\alpha = 6$. As expected and observed in the case of the wind tunnel, the grid is enlarged around the shock and contains more velocity grid points in high temperature areas.

The error obtained with the local grids is calculated with respect to the solution on the global velocity grid (Figure IV.28).

Taking an error of the order of 10^{-6} (see Figures IV.28) corresponds to $\alpha = 6$ and gives a gain about 70% of the computational time (see Figure IV.29).

In Figure IV.29, one can note that for the smallest value of α ($\alpha = 2$), the number of grid points used is actually larger than for $\alpha = 3$. This is due to the criteria on the integral (IV.5) which is more restrictive and imposes to enlarge the grid to include all points where f cannot be disregarded. This occurs also in the case of the wind tunnel (see Figure IV.25b).

IV.4 Preliminary conclusion

In this chapter, we presented two solutions to improve the computational time requirement of the resolution of the BGK and ES-BGK model. The first natural way to reduce the computaional time is to parallelize the code. The use of Cartesian grids has been fully exploited making the partitioning of the computational domain easier. The scalability results showed a good behaviour of the code as the number of thread increases. A strong scalability of 0.7 is obtained until using more than a thousand of threads.

We then proposed a simple algorithm to avoid computations on the velocity grid where the distribution function is almost zero. This algorithm can be rapidly implemented for both BGK and ES-BGK model and gives very satisfying results. It has been successfully tested on 1D and

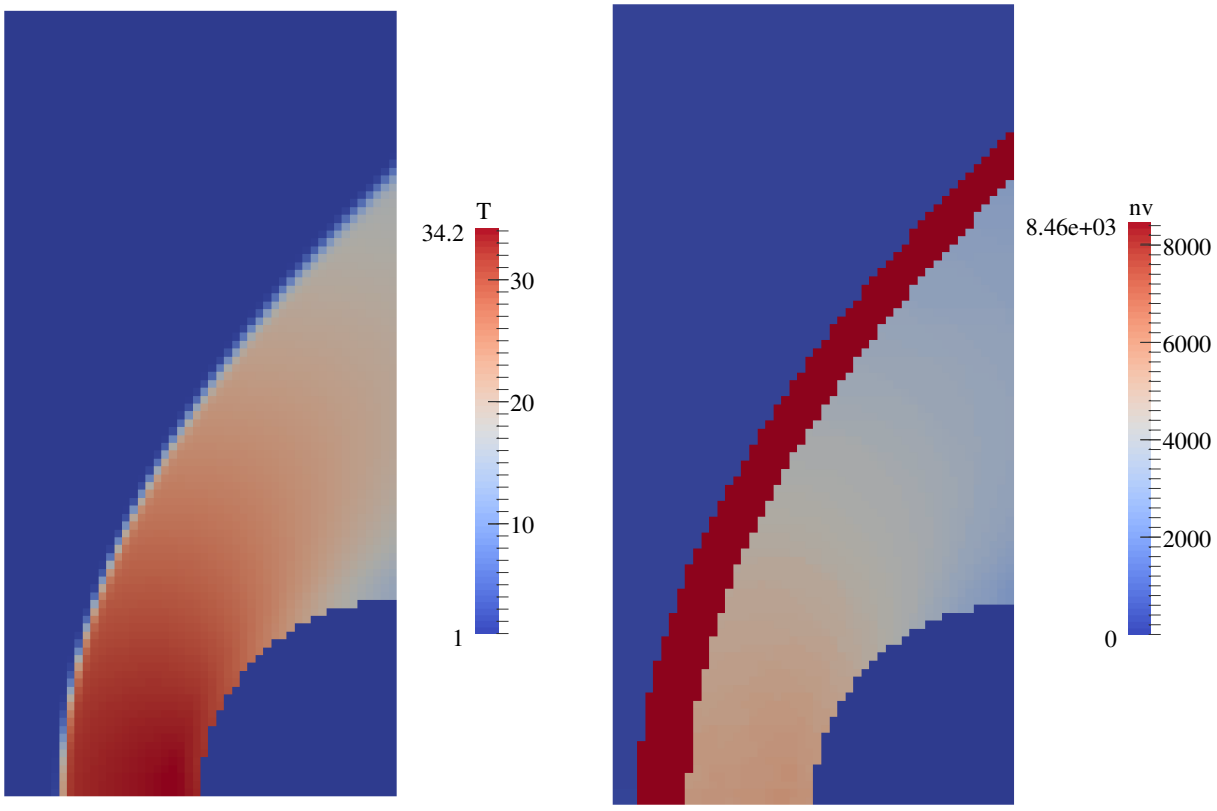

(a) Temperature.

(b) Number of velocity grid points.

Figure IV.27: Test case 3, $Kn_\infty = 10^{-5}$: Blunt body solution for the temperature and number of velocity grid points in each cell at steady state.

2D test cases in rarefied and hydrodynamic regimes. We reached a gain on the computational time higher than 50% in most cases for a relative error lower than 10^{-4}. However, it is important to keep in mind that such methods as well as more sophisticated methods proposed in the literature are case dependent. But with the proposed method, the cost of the worst case is the cost of the classical DVM method.

Let us now exploit all the improvements done for the boundary conditions and the local velocity discretization on 3D computations that would be almost computationally prohibitive without including the previous work.

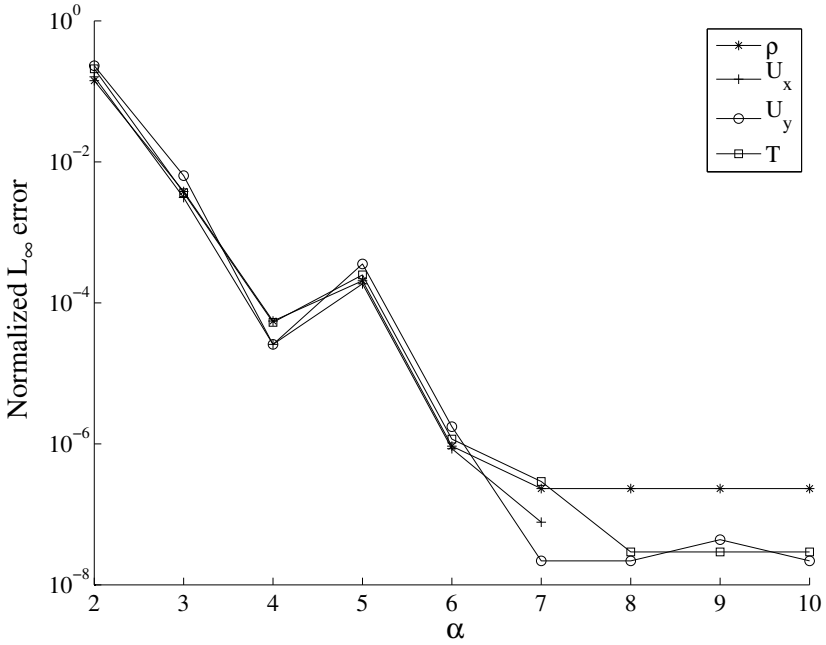

Figure IV.28: Test case 3, $Kn_\infty = 10^{-5}$: L_∞ error on density, velocity and temperature.

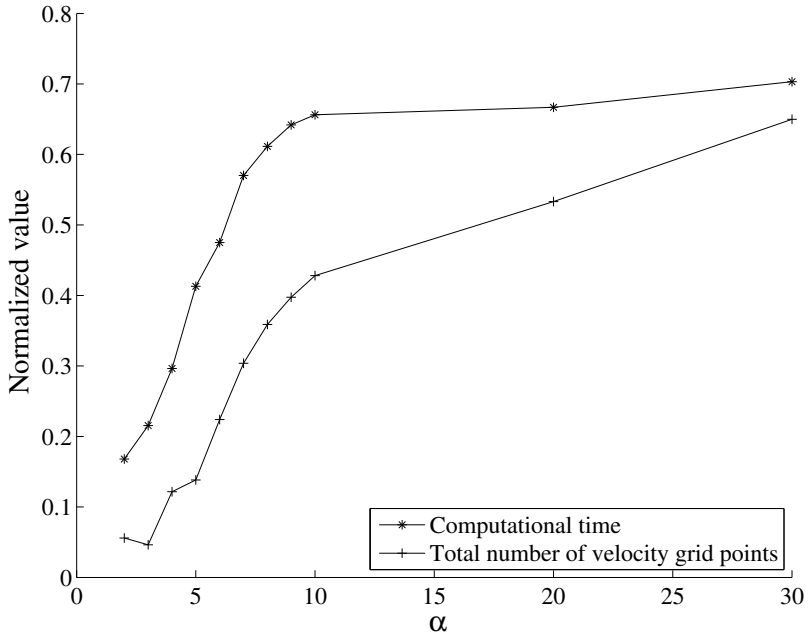

Figure IV.29: Test case 3, $Kn_\infty = 10^{-5}$: Normalized number of velocity grid points used and computational time with respect to the full grid calculation.

Chapter V

Simulations in 3D

Chapter III and IV were devoted to new methods used to impose efficiently the boundary conditions and to reduce the computational time required to solve the kinetic models. We now apply all these techniques to the BGK model in 3D to solve new test cases that could have been computationally prohibitive before this work.

An advantage of the methods previously presented is that their extension in 3D is straightforward. Thus, in this chapter, we show the viability of the methods in 3D through numerical results.

V.1 The Blunt body at Mach 3

The Blunt body test case is now considered in 3D. The parameters are the same as the ones used in 2D but with the third dimension. The initial state as the following properties in dimensionless variables: $u = 4$, $v = 0$, $w = 0$, $p = 1$ and $T = 1$. The Mach number is actually 3.16. We first consider the Blunt body as a cylinder to compare the results to the 2D case such that there are no effect due to the third dimension. The cylinder has the z-axis as revolution axis and its radius is 0.1. The computational domain is [-0.3,0]×[0,0.45]×[0,0.05] discretized with 60×90×10 cells in space. In velocity, the domain is [-10,10]×[-10,10]×[-5,5] and is discretized with 21×21×11 cells.

Figure V.1a shows ten density isolines between 0.8 and 3. The upper part is the solution of the 3D code projected on a $x - y$ plane. This solution is compared to the 2D code solution and the same isolines. It shows a very good accordance between the two codes.

The Blunt body is now a sphere of radius of 0.1 and its center is in (0,0,0). Thanks to symmetrical considerations, the computational domain is reduced to [-0.2,0]×[0,0.3]×[0,0.3] and is discretized with 60×90×90 cells. The velocity space is [-10,10]×[-10,10]×[-10,10] and is discretized with 21×21×21 cells. The density contours on a slice are shown on figure V.1b.

V.2 An hypersonic re-entry of Apollo capsule in rarefied conditions

The hypersonic re-entry of Apollo capsule has been widely studied in [58] in different regimes and with different models. The geometry used is axisymmetric around the x-axis and is presented in figure V.2. α is the incidence angle of the capsule and V_∞ is the free stream velocity.

In the following, the initial flow is along the x-axis and a rotation is applied to the capsule to impose the desired angle θ. c_m is the center of mass and its position can be chosen. A second

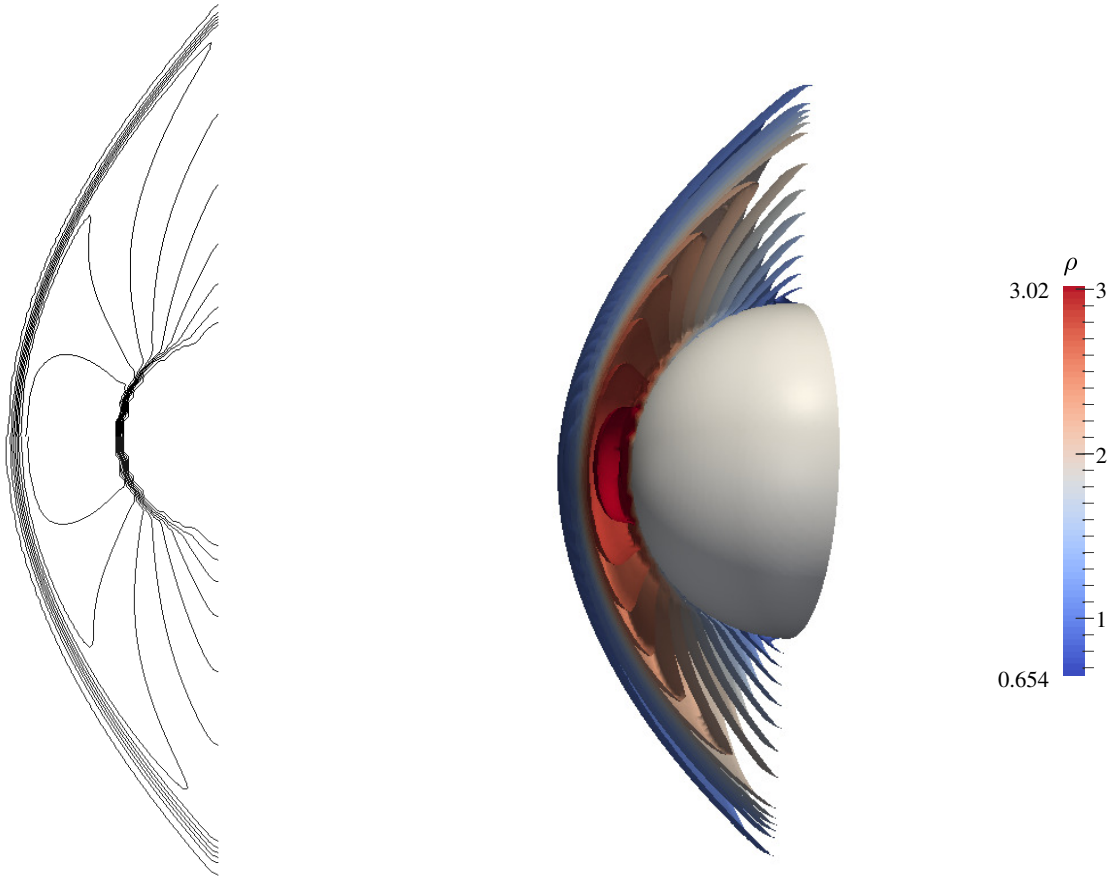

(a) 10 density isolines between 0.8 and 3. The upper part is the 3D code solution, the lower part is the 2D code solution.

(b) Density contours for the 3D Blunt body.

Figure V.1: Comparison on a plane for the cylinder in 3D with the Blunt body in 2D (left) and Blunt body in 3D (right).

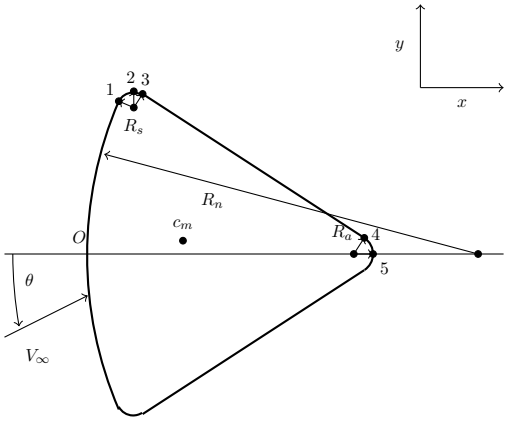

(a) Apollo capsule slice in the (x,y) plane, form 1.

	x	y
1	0.3743	1.8368
2	0.5543	1.9558
3	0.6608	1.9242
4	3.3254	0.1938
5	3.4306	0
O	0	0

R_a=0.2311
R_s=0.1956
R_n=4.6939

(b) Apollo capsule geometrical parameters.

Figure V.2: Apollo capsule geometry, form 1.

geometry is also used. It is the same geometry as in figure V.2 but the capsule is cut by a $y-z$ plan in $x=2$. It is referred as form 2 in the following and all the coordinate given are expressed with respect to the coordinate system of figure V.2.

The point c_m is the center of mass. If the aerodynamic forces acting on the capsule are calculated, it is possible to express the torque associated with respect to this center of mass. Let $\mathbf{F}$ denote the sum of the aerodynamic forces acting on the capsule (drag and lift):

$$\mathbf{F} = \int_{\delta\Gamma} \rho\Theta\mathbf{n}_{\delta\Gamma} d\sigma \tag{V.1}$$

where $d\sigma$ is a surface element used as the integration variable over $\delta\Gamma$ which is the surface of the capsule. $\mathbf{n}_{\delta\Gamma}$ is the unit normal to the capsule surface pointing towards the capsule and $\rho\Theta$ is the stress tensor calculated as follows:

$$\rho\Theta = \int_{\mathbf{c}\cdot\mathbf{n}_{\delta\Gamma}>0} \mathbf{c}\otimes\mathbf{c} f d\boldsymbol{\xi} + \int_{\mathbf{c}\cdot\mathbf{n}_{\delta\Gamma}<0} \mathbf{c}\otimes\mathbf{c} f_b d\boldsymbol{\xi} \tag{V.2}$$

where $\mathbf{c}$ is defined as $\mathbf{c} = \boldsymbol{\xi} - \mathbf{U}_w$ with $\mathbf{U}_w$ the velocity of the boundary $\delta\Gamma$ (that is not necessarily constant in space) and f_b the boundary condition imposed on $\delta\Gamma$.

From this expression one can deduce the value of the drag and lift coefficient C_D and C_L as:

$$\begin{cases} C_D = \dfrac{F_x}{0.5\rho_\infty V_\infty^2 A_{ref}} \\ C_L = \dfrac{F_y}{0.5\rho_\infty V_\infty^2 A_{ref}} \end{cases} \tag{V.3}$$

where F_x (respectively F_y) is the x-component (respectively y-component) of $\mathbf{F}$, ρ_∞ is the free stream density and A_{ref} is the reference area which is in this case: $A_{ref} = \frac{\pi D_b^2}{4} = 12.0171$ ($D_b = 3.9116$ being the maximal diameter of the capsule).

V.2.1 Fixed capsule

In [58] data are given on the drag and lift coefficients at different altitudes with different temperatures. The numerical simulations are performed with a Navier-Stokes code for low Knudsen numbers ($< 10^{-1}$) and with a DSMC code for higher Knudsen numbers. We propose to solve this test case with our methods and schemes for all range of Knudsen numbers. The re-entry

velocity is 9600 m/s. The boundary conditions are purely diffuse on the capsule with a prescribed temperature of 1. At the domain boundary, the free flow condition is applied except in front of the capsule where the free stream conditions are imposed through a Maxwellian distribution function. Since no informations are given on the computational domain in [58], we take a domain [-4,4]×[-4,4]×[-4,4] in space. The incidence angle of the capsule is $\theta = -25$ degrees. We focus on two different altitudes: 110 and 130 km. The free stream conditions are given in table V.1 where m_w is the molecular weight in atomic mass unit.

alt (km)	Kn_∞	T_∞(K)	m_w(u)	T_w(K)
130	2.07	500	25.441	524
110	0.19	247	27.232	920

Table V.1: Free stream conditions for two different altitudes.

From these free stream conditions it is possible to get the dimensionless variables:

$$R = \frac{\mathcal{N}_A k_b}{m_w}$$
$$\hat{T} = \frac{T}{T_\infty}$$
$$\hat{\mathbf{U}} = \frac{\mathbf{U}}{\sqrt{RT_\infty}}$$

alt (km)	C_{DGlass}	C_D	C_{LGlass}	C_L
130	1.812	1.8	0.089	0.058
110	1.655	1.79	0.245	0.140

Table V.2: Drag and Lift coefficients

In table V.2, preliminary results are given for 2 different altitudes. The comparison with the data by Glass et al. in [58] shows a reasonable accordance of the computed drag and lift coefficient. Two different altitudes are few to have reliable conclusions but it seems that the behaviour of the coefficient is similar. The drag coefficient tends to decrease with the altitude while the lift coefficient increases. Data in [58] are for gas mixture of mono-atomic and polyatomic gases so quantitative comparisons are not appropriate. However, the values obtained seem closer to the ones of Glass et al. at the higher altitudes. It is probably because at these altitudes the gas is mostly oxygen and then mono atomic (more than 50%). For such a problem, accuracy is also an issue especially at low altitude. In particular no informations are given in [58] about the size of the computational domain as well as the size of the mesh. This crucial informations impact the comparisons especially for the drag coefficient. With the given parameters, in dimensionless variables, the velocity grid has to be large and fine ($M \sim 30$ and $T \sim 1$). It then requires a very large number of grid points in velocity. To have also a good resolution in space, the number of grid points (in the phase space) becomes prohibitive.

V.2.2 Moving capsule

By choosing the position of the center of mass c_m one can compute the torque acting on the capsule:

$$\boldsymbol{\tau} = \int_{\delta\Gamma} (\mathbf{x} - \mathbf{x}_{c_m}) \wedge \mathbf{F} d\sigma \tag{V.4}$$

If we consider the rotation of the capsule due to this torque around the z-axis passing by the center of mass (and considered fixed in space) the angle velocity is linked to the torque by the relation:

$$\tau_z = I_z \frac{d\omega}{dt} = I_z \frac{d^2\alpha}{dt^2} \tag{V.5}$$

where ω is the angular velocity, τ_z is the third component of the torque (along the z-axis) and I_z is the moment of inertia of the capsule around the z-axis. Considering that the capsule rotates only around the z-axis is actually a valid approximation in our case due to the symmetry of the problem. It can also be verified numerically that the other component of the torque are negligible. Then the evolution of the incidence angle is computed through the system:

$$\begin{cases} \dfrac{d\alpha}{dt} = \omega \\ \dfrac{d\omega}{dt} = \dfrac{\tau_z}{I_z} \end{cases} \tag{V.6}$$

with ω_0 and α_0 the given initial condition for the angular velocity and the incidence angle.

Now that the angular velocity is known, it is possible to recover the velocity $\mathbf{U}_w$ used to compute the aerodynamic forces and to impose the boundary condition. By considering the center of mass fixed in space and time, the velocity $\mathbf{U}_w$ reads:

$$\mathbf{U}_w(\mathbf{x}) = -|\mathbf{x} - \mathbf{x}_{c_m}|\omega \mathbf{n}_{\delta\Gamma} \tag{V.7}$$

In the following cases, the flow is initialised at $M = 4$ with initial temperature $T = 0.6$ and initial density $\rho = 1$. The flow is along the x-axis. Free flow boundary conditions are applied on the sides of the domain except in front of the capsule where the flow is imposed with the initial conditions. The boundary conditions on the capsule are purely diffuse with $T_w = 1$ and $\mathbf{U}_w$ as in (V.7). The domain is [-4,4]×[-4,4]×[-4,4] discretized with 60 cells in each directions. In velocity, we have 21 cells in each directions and the domain is [-10,10]×[-10,10]×[-10,10]. A translation is applied on the geometry such that the center of mass is always in (0,0,0). During the computations, we then only consider the rotation of the capsule around the z-axis due to the torque. The moment of inertia I_z is set to 1.

Two cases are presented. The first one consider the geometry in V.2. The initial angle is $\theta_0 = -25$. The center of mass is in (2,0,0) or (1,0,0) in the coordinate system of figure V.2 and the Knudsen number is set to 10^{-5}. The second case consider the modified geometry (initial geometry cut with a plan in $x = 2$ perpendicular to the x-axis). The flow is identical but the center of mass is in (0.5,0.2,0). The Knudsen number is 10^{-5}. The steady state solutions are given in figure V.3. The evolution of the angle θ is shown in figure V.4.

In the first case, the center of mass is on the symmetric axis of the capsule. The point where the aerodynamic forces apply is on this symmetric axis (due to the symmetry of the capsule). In the equilibrium position, the point where the aerodynamic forces apply and the center of mass are aligned with the direction of the flow. Thus, the steady state solution is symmetric with respect to the x-axis. Indeed, the evolution of the incidence angle shows that the steady state incidence angle is -180 (see figure V.4a) degrees meaning that the capsule has turned over. This is due to the position of the center of mass which is behind the point where apply the aerodynamic forces. If the center of mass is in (1,0,0), the incidence angle goes to zero V.4a.

If now, the position of the center of mass is not on the symmetric axis of the capsule, the equilibrium position gives an angle of 18 degrees for $Kn = 10^{-5}$ and 14.7 degrees for $Kn = 0.1$.

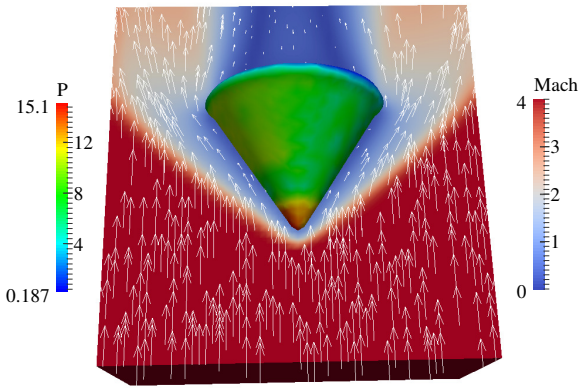

(a) Form 1, $Kn = 10^{-5}$, $c_m = (2, 0, 0)$.

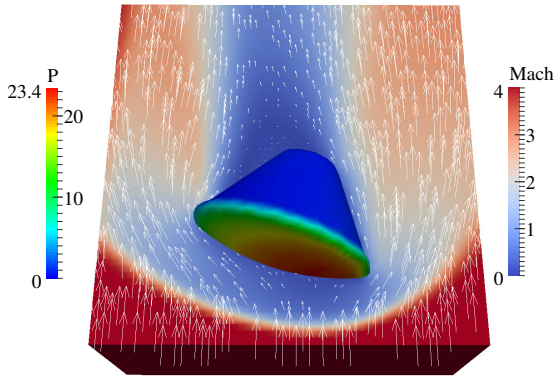

(b) Form 2, $Kn = 10^{-5}$, $c_m = (0.5, 0.16, 0)$.

Figure V.3: Steady state solution for different capsule forms and positions of the center of mass.

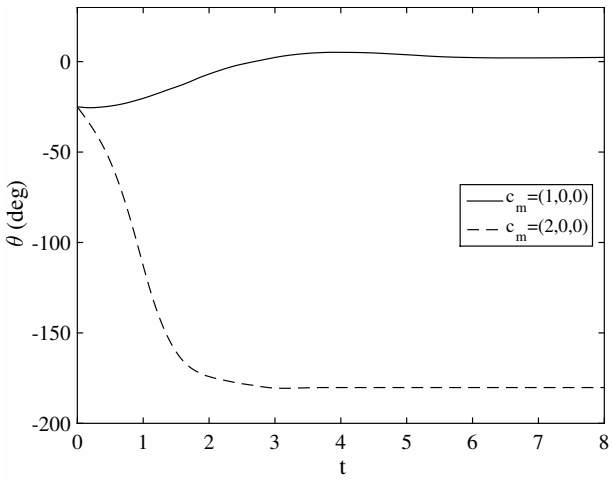

(a) Form 1, $Kn = 10^{-5}$.

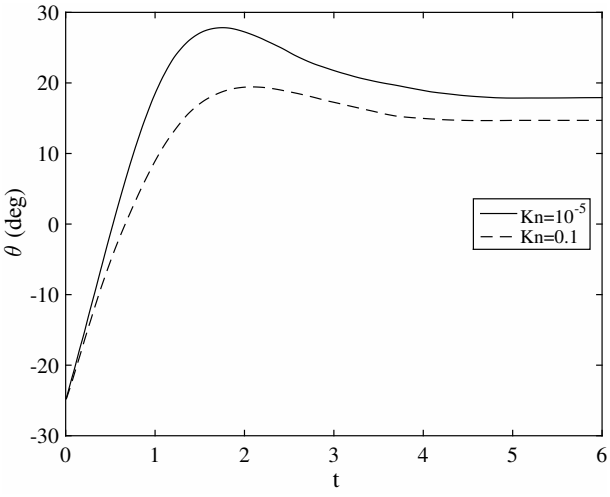

(b) Form 2, $c_m = (0.5, 0.16, 0)$.

Figure V.4: Evolution of the incidence angle of the capsule for different forms, position of the center of mass and Knudsen numbers.

V.3 Preliminary conclusion

We presented in this chapter, preliminary results in 3D. The extension to the third dimension has been validated on a cylinder with respect to the 2D code. We also show the ability of the code to deal with moving geometry. Quantifications on the gain obtained with the local grids method has to be performed. On the test cases presented, we estimated that the computational time is reduced by 10 times based on the gain on 1 iteration. It is just an estimation since it is almost impossible to run these tests with a full DVM method with the computational resources at our disposal. More validations are needed but these first simulations illustrate that the method is adaptable in 3D and seems efficient.

Chapter VI

A numerical method for particle transport in rarefied flows

In many complex applications, the fluid flows can contain solid particles, bubbles or droplets. These applications go from combustion in engines [41] to transport of particle pollutants in atmosphere or rivers [66]. Other applications can be found in biology for biospray in upper airways [8]. Different models and methods have been developed to address this problem. We firstly summarize the different approaches present in the literature as well as the particle methods used to solve these models. Then, a model is proposed to solve the particle transport. A fully Lagrangian method and a remeshing method are then presented and compared to solve the model for 2D test cases. Finally, we investigate the test case of a nozzle plume ejecting particles in a rarefied field.

VI.1 A short review on some particle transport model and particle methods

The models presented in this section are mostly developed for biospray where droplets are in suspension in a gas flows or for engines where particles of combustion are present in the flow. They are based on a coupling of the gas phase dynamics and the particle phase dynamics.

We then present some popular particle methods used to solve these kind of models.

VI.1.1 Particle transport model

We present here an overview on transport particle models existing in the literature. Depending on the cases considered, the gas flow and the particle flow can be considered in hydrodynamic regime as well as in rarefied regime.

VI.1.1.1 Fluid/Fluid model

A first approach consist in considering two hydrodynamic equations to describe the fluid flow and the particle flow. It has been used in the case of a gas deflagration-to-detonation reaction with dust [55], [7]. A volume fraction α is introduced in the equations to consider the two phases and a source term, to simulate the interactions. For example, under the assumption that the particles are solids incompressible and that the pressure is negligible in the particle phase, the following set of equation can be obtained (index g denoting the gas phase and index p denoting

the particle phase):

$$\begin{aligned}
&\frac{\partial \alpha_g \rho_g}{\partial t} + \nabla_{\mathbf{x}} \cdot (\alpha_g \rho_g \mathbf{U}_g) = 0 \\
&\frac{\partial \alpha_g \rho_g \mathbf{U}_g}{\partial t} + \nabla_{\mathbf{x}} (\alpha_g \rho_g \mathbf{U}_g \otimes \mathbf{U}_g + \alpha_g p \mathbf{I}) = p \nabla \alpha_g + \alpha_g \rho_g \mathbf{g} - \mathbf{F} \\
&\frac{\partial \alpha_g \rho_g E_g}{\partial t} + \nabla_{\mathbf{x}} (\alpha_g \rho_g \mathbf{U}_g H_g) = -p \frac{\partial \alpha_g}{\partial t} + \alpha_g \rho_g \mathbf{U}_g \cdot \mathbf{g} - \mathbf{F} \cdot \mathbf{U}_g \\
&\frac{\partial \alpha_p \rho_p}{\partial t} + \nabla_{\mathbf{x}} \cdot (\alpha_p \rho_p \mathbf{U}_p) = 0 \\
&\frac{\partial \alpha_p \rho_p \mathbf{U}_p}{\partial t} + \nabla_{\mathbf{x}} (\alpha_p \rho_p \mathbf{U}_p \otimes \mathbf{U}_p) = \alpha_p \rho_p \mathbf{g} + \mathbf{F} \\
&\frac{\partial \alpha_p \rho_p E_p}{\partial t} + \nabla_{\mathbf{x}} (\alpha_p \rho_p \mathbf{U}_p E_p) = \alpha_p \rho_p \mathbf{U}_p \cdot \mathbf{g} + \mathbf{F} \cdot \mathbf{U}_p
\end{aligned}$$

where $\mathbf{I}$ is the identity matrix, p is the gas pressure, $\mathbf{g}$ is the gravity force, $\mathbf{F}$ is the drag force of the gas acting on the particles H is the total enthalpy and E is the total energy. The drag force is usually set from empirical formula [21]. One could choose:

$$\mathbf{F} = \frac{\alpha_g \rho_g}{m_p} \frac{\pi d_p}{8} C_D (\mathbf{U}_g - \mathbf{U}_p) |\mathbf{U}_g - \mathbf{U}_p|$$

VI.1.1.2 Fluid/Kinetic models

A second approach considers a fluid/kinetic model. Numerical methods have been developed in the 70s and 80s in this sense by coupling a macroscopic model for the fluid flow with a transport equation with possible source terms for the second phase usually called spray [42], [62], [25]. In the case of thin sprays, the particle flow is so diluted that the particle volume fraction is negligible with respect to the one of the gas. The gas-particle interaction is modeled through a Stokes drag force: $\mathbf{F}(\mathbf{x}, \boldsymbol{\xi}', r) = \frac{D}{m'(r)} (\mathbf{U}_g(\mathbf{x}) - \boldsymbol{\xi}')$. D is the drag coefficient, $m'(r)$ is the mass of a particle of radius r, $\boldsymbol{\xi}'$ is the particle velocity and $\mathbf{U}_g$ is the velocity of the gas. The following equations are obtained:

$$\begin{aligned}
&\frac{\partial \rho_g}{\partial t} + \nabla_{\mathbf{x}} \cdot (\rho_g \mathbf{U}_g) = 0 \\
&\frac{\partial \rho_g \mathbf{U}_g}{\partial t} + \nabla_{\mathbf{x}} (\rho_g \mathbf{U}_g \otimes \mathbf{U}_g) + \nabla_{\mathbf{x}} p = \int_{\mathbb{R}^3} \int_{\mathbb{R}} m'(r) f_p(\mathbf{x}, \boldsymbol{\xi}, t, r) \mathbf{F}(\mathbf{x}, \boldsymbol{\xi}', r) dv dr \\
&\frac{\partial f_p}{\partial t} + \boldsymbol{\xi}' \cdot \nabla_{\mathbf{x}} f_p + \nabla_{\boldsymbol{\xi}'} \cdot (\mathbf{F} f_p) = 0
\end{aligned}$$

where ρ_g is the gas density, p is the gas pressure and f_p is the distribution function associated to the gas flows that depends on $\mathbf{x}$, $\boldsymbol{\xi}'$, t and the radius r of the particles.

In the case of thick sprays, a collision term is added in the particle flow equation to consider the interaction between particles [84].

VI.1.1.3 Kinetic/Kinetic models

Finally, another approach has been proposed by Ferrari and Pareschi [49] for the simulation of sprays in rarefied regime. It is closed to a granular flow model and represent the flow of impurities through a Boltzmann equation while the gas flow is considered at thermodynamic equilibrium and is represented by a Maxwellian distribution function. In [92], the gas flow is described by a Boltzmann equation and the particle flow is governed by a Vlasov equation. The

coupling Boltzmann/Boltzmann and Boltzmann/Vlasov has also been studied in details in [30] for applied test cases.

VI.1.2 Particle methods

Particle methods were introduced to make easy calculations of simple flows [102]. Their main advantage with respect to finite volume methods or finite difference methods is that calculations are performed only where there are particles. We distinguish three main methods to solve particle motion all based on Lagrangian or semi-Lagrangian schemes: the Particle-In-Cell method, the Smooth Particle Hydrodynamice method and the vortex methods.

VI.1.2.1 The Particle-In-Cell method (PIC)

Particle-In-Cell method [45] is the most popular to solve Vlasov equation:

$$\frac{\partial f_p}{\partial t} + \boldsymbol{\xi'} \cdot \nabla_{\mathbf{x}} f_p + \nabla_{\boldsymbol{\xi'}} \cdot \mathbf{F} f_p = 0$$

This method uses a grid and computational particles that represent a fixed number of real particles N_p. These computational particles are moved according to the equations of motion:

$$\begin{aligned}
\frac{dN_p}{dt} &= 0 \\
\frac{d\mathbf{x}_p}{dt} &= \mathbf{v}_p \\
\frac{d\mathbf{v}_p}{dt} &= \mathbf{F}_p
\end{aligned}$$

where $\mathbf{F}_p$ is the force define in the Vlasov equation acting on the computational particle p. In the case of an electromagnetic field for example, this force depends on the other computational particles. It is then necessary to project each computational particles on a fixed grid to recover charge density or particle electric field. In the case of fluid dynamics equations, it is the density or the pressure that one wants to recover. This is done through an interpolation kernel $W(\mathbf{x}_i - \mathbf{x}_p)$ where i is the cell multi-index. For instance, the density in cell i is obtained as:

$$\rho_i = \sum_p \frac{m'_p N_p}{|\Omega_i|} W(\mathbf{x}_i - \mathbf{x}_p)$$

where $|\Omega_i|$ is the volume of cell i. It is now possible to compute the force in cell i. But since the computational particles do not coincide with the cell center of the cells, it is necessary to reconstruct the continuous field of $\mathbf{F}$ and in particular its value at the particles position:

$$\mathbf{F}_p = \sum_i \mathbf{F}_i W(\mathbf{x}_i - \mathbf{x}_p)$$

This sequence of operation has to be performed at each time step.

Usually the interpolation kernels are low order b-splines (see figure VI.1) and give a satisfactory accuracy.

However, although the method is considered robust and that a small number of particles yields to satisfactory results, it generates a lot of numerical noises that could pollute the solution. Moreover, storing particles and a grid increases the memory requirement and could be prohibitive with a kinetic model.

Figure VI.1: Two first b-spline for a length scale of H.

VI.1.2.2 The Smooth Particle Hydrodynamic method (SPH)

An other kind of particle methods also considers regularization of the particles with an interpolation kernel. The pioneering idea has been developed almost simultaneously by Gingold and Monaghan in [56] and by Lucy in [82]. They are called Smooth Particle Hydrodynamic (SPH) methods. A more recent review is found in [88]. Each particle has a position, a velocity, a mass and an internal energy. The representation of the flow is given by interpolating the quantities carried by each particle with an interpolation kernel W. A general quantity A carried by a particle is expressed as the sum of the same quantity carried by all the particles interpolated in $\mathbf{x}_p$:

$$A_p = \sum_i m_i' \frac{A_i}{\rho_i} W(\mathbf{x}_p - \mathbf{x}_i, h)$$

For example, the SPH representation of the density of a particle p is:

$$\rho_p = \sum_i m_i' W(\mathbf{x}_p - \mathbf{x}_i, h)$$

where i is an index on all the particles and h is a regularization parameter of the support of W that depends on the distance between the particles.

The SPH formulation is then obtained by replacing each quantities in the equation by their SPH representation. In the case of Euler equations:

$$\begin{aligned}
\frac{d\mathbf{x}_p}{dt} &= \mathbf{U}_p \\
\frac{d\mathbf{U}_p}{dt} &= -\sum_i m_i' (\frac{p_i}{\rho_i^2} + \frac{p_p}{\rho_p^2}) \nabla_i W(\mathbf{x}_p - \mathbf{x}_i, h) \\
\frac{d\mathbf{e}_p}{dt} &= \frac{p_p}{\rho_p} \sum_i m_i' (\mathbf{U}_i - \mathbf{U}_p) \nabla_i W(\mathbf{x}_p - \mathbf{x}_i, h)
\end{aligned}$$

where p is the particle pressure and e its internal energy.

Instead of PIC method, no grids are considered and usually, the interpolation kernel used are more accurate. SPH methods are very efficient for front tracking and free surface motion [36], [44] or for large deformation due to the Lagrangian method. However, recovering macroscopic quantities induces a lot of errors due to interpolation kernels. In addition, the advantage of this method is the use of high order interpolation kernels that could lead to negative values of the distribution function which we cannot afford.

VI.1.2.3 Vortex method

Finally, the last kind of methods are vortex methods. These methods are based on a vorticity formulation of the equation [75], [35], [99]. It is particularly used for incompressible flows.

The drawback of these methods is that singularity in the flow can lead to non accurate or non physical solutions [10],[35]. We also refer to [52] where other Lagrangian methods are presented but do not appear to be clearly an efficient solution. Remeshing techniques have been developed for vortex methods to avoid that singular solutions occur when particles overlap or get too close [46], [31], [37] by redistributing them on a grid. In our case, we need the preservation of the positivity of the distribution function (as in PIC methods) and on a Cartesian mesh in phase space. This allows also an easy integration of the distribution function to recover the number and density of the particles.

VI.2 A particles transport model in rarefied flows

In this work, we are interested in particle transport in rarefied flows. Then, the model used is closed to the one of Ostmo et al. [92] but the rarefied flow is described by the BGK or ES-BGK model. These models are preferred to the Boltzmann equation for computational requirement reasons. Even if we consider that the particle flow is diluted, computing the motion of each particles would be computationally prohibitive. A statistical approach is then more suitable solved with a particle method. Thus, the particle flow is described by a Vlasov equation.

The idea is to introduce a model representing a spray of particles in the diluted gas flow. Let's consider that a set of particles represented by the distribution function f_p with microscopic velocities $\boldsymbol{\xi'}$ is passively transported by the fluid. We assume that the flow of these particles is so diluted that they do not collide between each other. Each particles moves with its own velocity. This velocity is biased by the gas that can be traduced by a force acting on the particles and yet an acceleration. It is then governed by the Vlasov type equation:

$$\frac{\partial f_p}{\partial t} + \nabla_{\mathbf{x}} \cdot \boldsymbol{\xi'} f_p + \nabla_{\boldsymbol{\xi'}} \cdot \mathbf{a} f_p = 0 \tag{VI.1}$$

The acceleration is due to a drag force [93]. Here we choose to model it as $\mathbf{a} = D(\mathbf{U}_g - \boldsymbol{\xi'})$. This force correspond to the Stokes drag force and has also been validated experimentally in the case of granular flows [22]. We do not consider other forces acting on the particles such as gravity for example. $\mathbf{U}_g$ is the velocity field given by the solution of the kinetic model (BGK or ES-BGK model):

$$\mathbf{U}_g = \frac{\int_{\mathbb{R}^3} \boldsymbol{\xi} f d\boldsymbol{\xi}}{\int_{\mathbb{R}^3} f d\boldsymbol{\xi}}$$

The number of particles N_p in a domain Ω can be easily recovered:

$$N_p = \int_\Omega \rho_p dx = \int_\Omega \int_{\mathbb{R}^3} f_p d\boldsymbol{\xi'} dx \tag{VI.2}$$

where ρ_p is the particle density.

The system of equations we are studying is then the following:

$$\begin{cases} \dfrac{\partial f}{\partial t} + \boldsymbol{\xi} \cdot \nabla_{\mathbf{x}} f = Q(f,f) \\ \dfrac{\partial f_p}{\partial t} + \nabla_{\mathbf{x}} \cdot \boldsymbol{\xi'} f_p + \nabla_{\boldsymbol{\xi'}} \cdot D(\mathbf{U}_g - \boldsymbol{\xi'}) f_p = 0 \end{cases} \tag{VI.3}$$

where the first equation is the kinetic model giving the gas flow with:

$$Q(f,f) = \begin{cases} \dfrac{1}{\tau}(M_f - f) & \text{for the BGK model} \\ \dfrac{1}{\tau}(\mathcal{G}_f - f) & \text{for the ES-BGK model} \end{cases}$$

In the proposed model, the influence of the particles on the gas flow is neglected. We consider that the particle flow is so diluted with respect to the gas flow that it does not bias it. Thus, no feedback on the kinetic equation for the gas (through a source term for example, see [30]) is present in this model. We also disregard particle collisions.

VI.3 Numerical scheme

In this section, two methods to solve the Vlasov equation for the particle transport are presented. The first way to treat the transport of the particles is fully Lagrangian. In a second part we present an other method consisting in remapping the particles on a fixed mesh.

VI.3.1 Lagrangian scheme

The first approach considers a Lagrangian scheme to solve (VI.1). Each particle has its own trajectory, does not depend on the other particles and is considered as a dirac:

$$f_p(\mathbf{x}, \boldsymbol{\xi}', t) = \sum_p m'_p \delta_{\mathbf{x}}(\mathbf{x} - \mathbf{x}_p(t)) \delta_{\boldsymbol{\xi}'}(\boldsymbol{\xi}' - \boldsymbol{\xi}'_p(t)) \tag{VI.4}$$

where m'_p is the mass of particle p and $\delta_{\mathbf{x}}$ (respectively $\delta_{\boldsymbol{\xi}'}$) is the dirac function in the physical space (respectively the velocity space).

The method is particularly efficient for passive transport and is easily parallelizable. A splitting is performed to solve first the transport in physical space and then the transport in velocity space. Eq.(VI.1) becomes:

$$\begin{cases} \dfrac{\partial f_p}{\partial t} + \nabla_x \cdot \boldsymbol{\xi}' f_p = 0 \\ \dfrac{\partial f_p}{\partial t} + \nabla_{\boldsymbol{\xi}'} \cdot \mathbf{a} f_p = 0 \end{cases} \tag{VI.5}$$

This equation is solved by tracking the position of the set of particles initially defined by the distribution function in phase space:

$$\begin{cases} f_p(\mathbf{x}, \boldsymbol{\xi}', t) = f_p(\mathbf{x}_0, \boldsymbol{\xi}'_0, t = 0) & \text{(VI.6a)} \\ \dfrac{d\mathbf{x}}{dt} = \boldsymbol{\xi}' & \text{(VI.6b)} \\ \dfrac{d\boldsymbol{\xi}'}{dt} = D(\mathbf{U}_g - \boldsymbol{\xi}') & \text{(VI.6c)} \end{cases}$$

If the velocity $\mathbf{U}_g$ is not known analytically (which is usually the case if it comes from the resolution of another equation), it has to be interpolated at the particle position.

One drawback of this model is that no informations are exchanged between the particles. Then particles can overlap and lead to a degradation of accuracy or non-physical phenomena [76]. Moreover, the structure of the grid is lost and it is almost impossible to imagine a feedback from the particles to the kinetic models. Indeed, this feedback would be imposed through the kinetic equation in each cell. A grid structure (identical as in the kinetic equation if possible) is then required for the particle transport to recover the Eulerian field.

In the following we propose another technique based on methods widely used in fluid dynamics.

VI.3.2 A particle method with remeshing

The underlying idea of the particle method using a remeshing step is to keep all flow information on the initial mesh, in our case Cartesian. The scheme is the following. A Lagrangian step is performed at each time step. Then the particles are redistributed in phase space, in each Cartesian cell, according to an interpolation kernel. New equivalent particles are created in the center of each cell while the old ones are suppressed. Hence, at each time step, all data is known on the initial mesh, in the Cartesian cells. In other words, at the beginning of each time step, $\mathbf{x}_i = \mathbf{x}_p$ and $\boldsymbol{\xi'}_i = \boldsymbol{\xi'}_p$ where i is the cell index and p denote the particle itself. To avoid a remeshing step in 6D (3D×3D) a splitting is performed between physical space and velocity space. The particles are first transported in the physical space at velocity $\boldsymbol{\xi'}$ and remeshed in the same space. Then, the transport in velocity space if realized according to the acceleration term. Finally, the particles are redistributed in velocity space. At each time step, the equations to solve are:

$$\begin{cases} \dfrac{d\mathbf{x}_p}{dt} = \boldsymbol{\xi'}_i \\ \tilde{f}_p(\mathbf{x}_i, \boldsymbol{\xi'}_i) = R_{\mathbf{x}}(f_p^n(\mathbf{x}_p, \boldsymbol{\xi'}_i)) \\ \dfrac{d\boldsymbol{\xi'}_p}{dt} = \mathbf{a}_p \\ f_p^{n+1}(\mathbf{x}_i, \boldsymbol{\xi'}_i) = R_{\boldsymbol{\xi'}}(\tilde{f}_p(\mathbf{x}_i, \boldsymbol{\xi'}_p)) \end{cases} \tag{VI.7}$$

where R_x and $R_{\boldsymbol{\xi'}}$ are respectively the remeshing operator in space and in velocity.

(a) Case $\xi'_u > 0$ (b) Case $\xi'_u < 0$

Figure VI.2: 1D configuration after a transport step in physical space (same behaviour in velocity space with $\xi'_u \equiv a_u$)

Figure VI.2 shows the two different cases for a 1D configuration of the transport of a particle p initially in $x = x_i$. The particle moves to the position $x = x_p$ and is remeshed on the two closest grid points (in the case of a two point interpolation kernel). α_p and β_p are the weights associated to these two grid points for the remeshing of the particle p.

For the remeshing step, different kernel are present in the literature preserving the moments of the distribution function up to a certain order (see for example [77], [83]). However, in our case positivity and diffusivity properties of the kernel are a real issue. In particular, we need the distribution function of the particles to stay positive after the remeshing step. Moreover, the remeshing stencil has to be as compact as possible to avoid the spreading of the particles due to a wide stencil. Finally, if the position of the particle does not change, the weight associated to the collocated grid point has to be one such that it does not induce numerical diffusion. The best compromise is found with the Λ_1 kernel:

$$\Lambda_1 = \begin{cases} \alpha = 1 - y \\ \beta = y \end{cases} \tag{VI.8}$$

where y is defined from figure VI.2 as:

$$\begin{cases} y = \dfrac{x_p - x_i}{\Delta x} & \text{if} \quad \xi'_u > 0 \\ y = \dfrac{x_p - x_{i-1}}{\Delta x} & \text{if} \quad \xi'_u \leq 0 \end{cases}$$

Then, the distribution function after remeshing (still in a general 1D case) is:

$$f_{p_i} = \sum_n \omega_{ni} f_{p_n} \tag{VI.9}$$

where f_{p_i} is the particle distribution function after the remeshing step in $x = x_i$, f_{p_n} is the particle distribution function after the transport in $x = x_n$ and ω_{ni} are the remeshing weights in $x = x_i$ for the particle n. They are defined as:

$$\omega_{ni} = \begin{cases} \alpha & \text{if} \quad x_p > x_i \\ \beta & \text{if} \quad x_p < x_i \end{cases}$$

One can note that the remeshing preserves the positivity since the weights ω_n defined from α and β are always positive.

In 2D, the weights are computed with a tensor product. If α_1 and α_2 (respectively β_1 and β_2) are the 1D weights (as in (VI.8)) in the first direction (respectively in the second direction), the weights associated to the 2×2 stencil (see Figure VI.3) are computed as:

$$\omega_n{}^{i,j} = \alpha_i \beta_j \tag{VI.10}$$

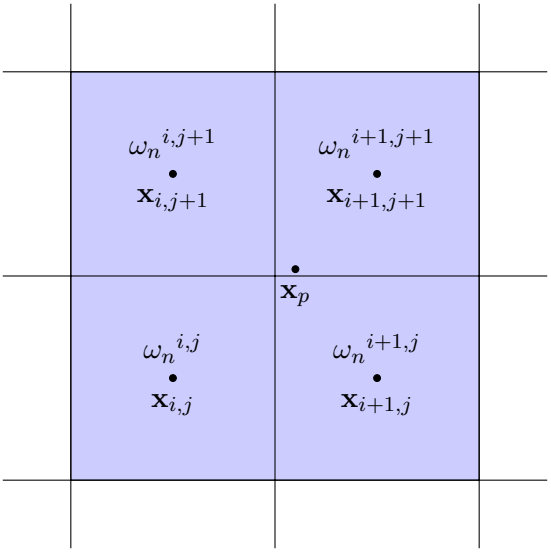

Figure VI.3: Stencil with interpolation weights associated to the cells for the remeshing of a particle in $\mathbf{x}_p$.

The particle distribution function in cell (i, j) is then computed similarly to the 1D case as:

$$f_{p_{i,j}} = \sum_n \omega_n{}^{i,j} f_{p_n} \tag{VI.11}$$

VI.3.3 Time integration

In both methods, two Lagrangian steps are performed. The first one is a transport in the physical space:

$$\frac{d\mathbf{x}_p}{dt} = \boldsymbol{\xi}' \tag{VI.12}$$

The integration is done with a first order Euler scheme.

The second equation is:

$$\frac{d\boldsymbol{\xi'}}{dt} = \mathbf{a} = D(\mathbf{U}_g - \boldsymbol{\xi'}) \tag{VI.13}$$

Here the acceleration depends on the particle velocity. The solution would benefit from a high order integration scheme. But since the splitting is of first order and the first equation is solved with a first order Euler scheme, we use, here also, a first order Euler scheme.

One can note that in equation (VI.12) $\boldsymbol{\xi'}$ depends on the position of the particle through (VI.13) and on the velocity field $\mathbf{U}_g$. In this case, a higher order splitting method (for example a Strang splitting, [109]) can be used for eq.(VI.12). In the case of the remeshing method, a higher order splitting would imply several remeshing steps and a dramatic increase of the computational time required.

VI.4 Numerical results

In the three first test cases, the particle methods are tested with a given velocity field, where the analytical solution can be computed. The domain is [-5,5]×[-5,5] in space and velocity. These test cases are used to validate the numerical methods (Lagrangian scheme and remeshing).

The last example is the passive transport of particles in a nozzle plume. The velocity field is given from the resolution of a kinetic model. In all test cases, the mass of the particles is constant.

VI.4.1 Test 1

The domain is [-5,5]×[-5,5] in space and velocity. We consider a zero velocity field, constant in time. All the particles are initially concentrated in (0,0) and have a gaussian distribution in the velocity space. The analytical solution can be easily computed in this case for a given mesh in space and velocity:

$$\begin{cases} x = \dfrac{\xi'_u(t=0)}{D}(1-\exp(-Dt)) \\ y = \dfrac{\xi'_v(t=0)}{D}(1-\exp(-Dt)) \end{cases} \tag{VI.14}$$

The steady state solution for different drag coefficients is shown on Figure VI.4 and VI.5.

As expected, the larger is the drag coefficient D, the closer to the initial condition the solution is.

The solution is first computed with the Lagrangian method. At steady state, in each cell, the density of particles at the cell center is interpolated. The error with respect to the analytical solution does not depend on the space discretization. For the numerical test, the space grid is kept constant (51×51) and the velocity grid is refined from 11×11 to 401×401.

For the remeshing method, the comparison is also done on the number of particles in each cell. The initial distribution function is given by:

$$f_p(0, \boldsymbol{\xi'}, t=0) = \frac{100}{2\pi|\Omega_{x_0}|}\exp(-\frac{|\boldsymbol{\xi'}|^2}{2})$$

where Ω_{x_0} is the cell where all the particles are initially situated. In this case, the center of this cell is $(x_0, y_0) = (0, 0)$. The total number of particles initially in this cell (also in the field) is $N_{p_0} = \int_{\Omega_{x_0}} \int_{\mathbb{R}^2} f_p(0, \boldsymbol{\xi'}, 0) d\boldsymbol{\xi'} d\mathbf{x} = 100$. The analytical solution can be easily computed in this

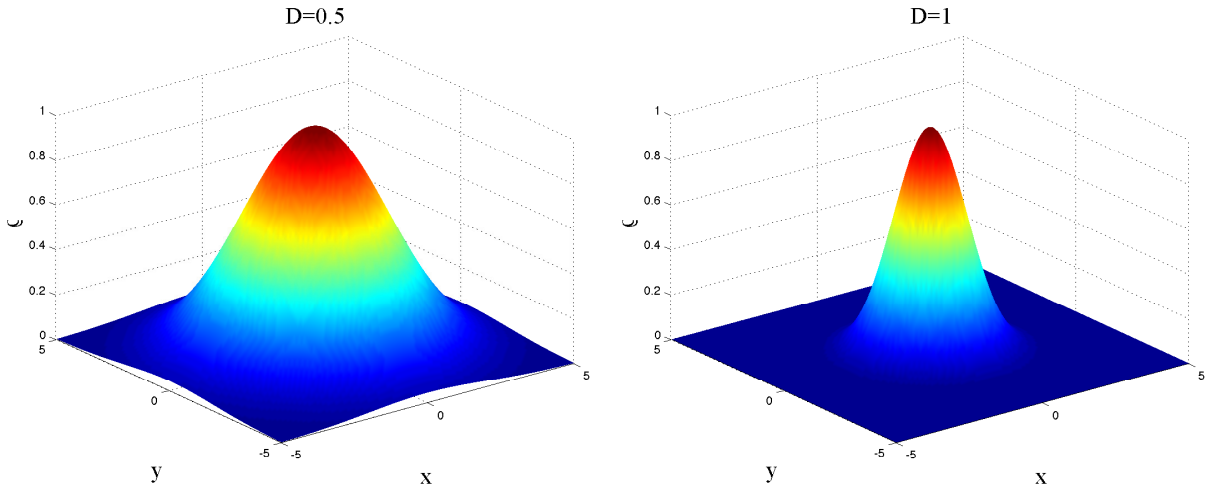

(a) D=0.5 (b) D=1

Figure VI.4: Density distribution at steady state for D=0.5,1

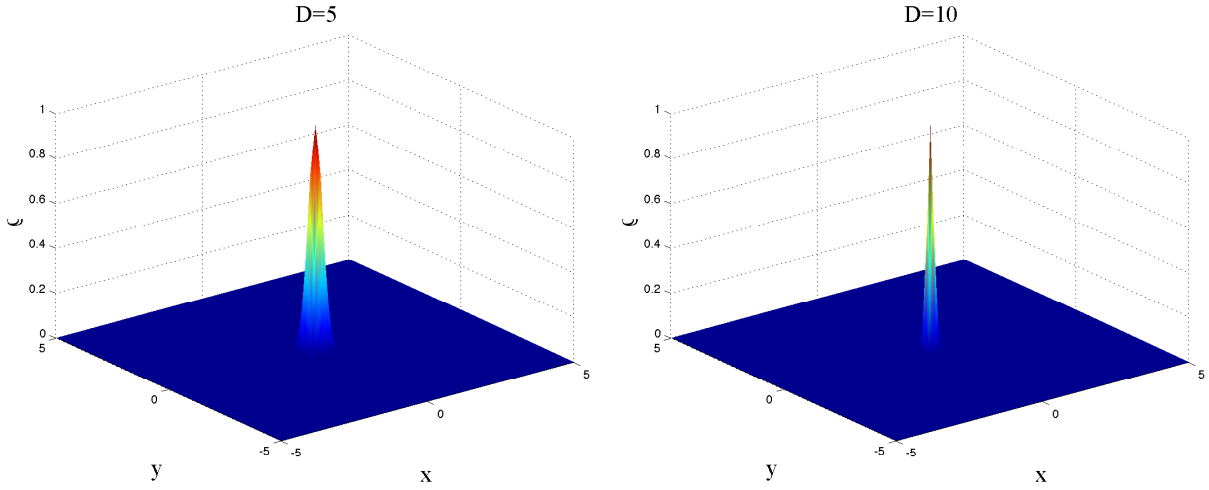

(a) D=5 (b) D=10

Figure VI.5: Density distribution at steady state for D=5,10

case with the error function. In a cell $\Omega_{i,j} = [x_{i-1/2}, x_{i+1/2}] \times [y_{j-1/2}, y_{j+1/2}]$:

$$N_{i,j} = \int_{\Omega_{i,j}} \int_{\mathbb{R}^2} f_p(\mathbf{x}, \boldsymbol{\xi}', t) d\boldsymbol{\xi}' d\mathbf{x} \tag{VI.15}$$

The analytical solution of the problem gives the number of particles in a position $\mathbf{x}$ is determined by the initial microscopic velocity corresponding to that position. In other words, for a set of particles to be in $\mathbf{x} = (x, y)$ at steady state with $U = 0$, one needs (see (VI.14)):

$$\begin{cases} \xi'_u(t=0) = Dx \\ \xi'_v(t=0) = Dy \end{cases}$$

Then,

$$N_{i,j} = D^2 |\Omega_{x_0}| \int_{Dx_{i-1/2}}^{Dx_{i+1/2}} \int_{Dy_{j-1/2}}^{Dy_{j+1/2}} f_p(0, \boldsymbol{\xi}', 0) d\boldsymbol{\xi}' \tag{VI.16}$$

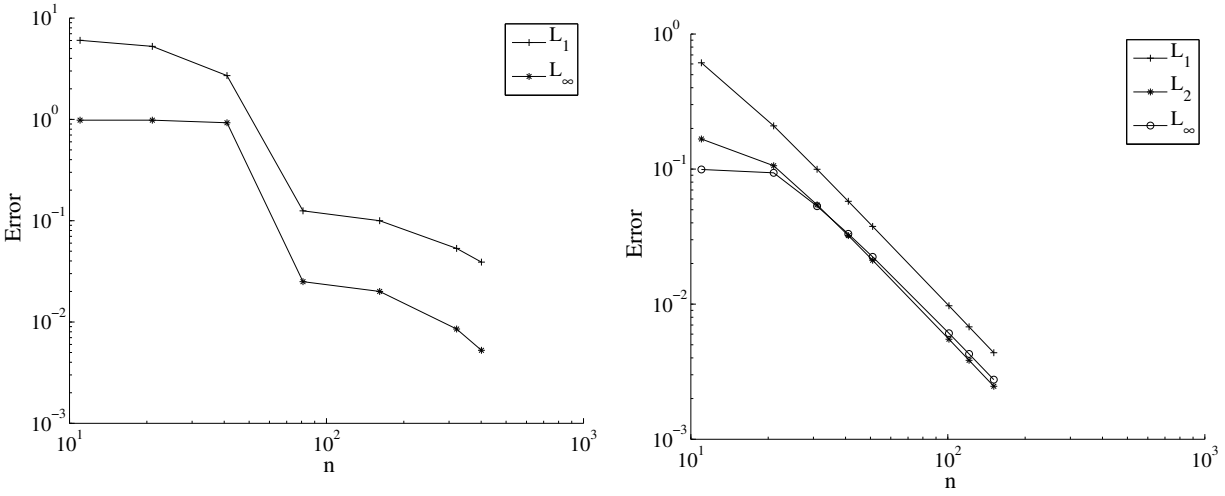

(a) L_1 and L_∞ norm of the error with the Lagrangian scheme.

(b) L_1, L_2 and L_∞ norm of the error with remeshing.

Figure VI.6: Test 1: Errors for the Lagrangian scheme and the remeshing method with respect to the analytical solution ($D = 1$).

By introducing the error function erf with the initial distribution function:

$$N_{i,j} = 25D^2\Big(\mathrm{erf}(Dx_{i+1/2}) - \mathrm{erf}(Dx_{i-1/2})\Big)\Big(\mathrm{erf}(Dy_{j+1/2}) - \mathrm{erf}(Dy_{j-1/2})\Big) \tag{VI.17}$$

The simulations are run on different grids going from 11×11 to 151×151 in space and velocity.

The error with respect to the number of velocity grid points in each direction is shown in figure VI.6a in L_1 and L_∞ norm for the Lagrangian method while the error of the remeshing method is shown on figure VI.6b.

This first test shows that both methods converge towards the analytical solution but with different behaviour. The Lagrangian method convergence is noisier (see figure VI.7a). This is due to the way in which the local number of particles is calculated. In each cell the number of particles is interpolated to find the value at the cell center. Then, the results closely depends on how much information is present in the cell. However, the problem tends to disappear as the number of velocity grid points increases, in particular, when $\Delta\mathbf{x} \simeq \Delta\boldsymbol{\xi}$ (see figure VI.7b). It explains why the error decreases suddenly around 51 points in each direction in velocity space. This is a very well known problem of Lagrangian method when one wants to recover an Eulerian field and can be prohibitive in our case if a fine grid is used in space.

For the remeshing method, the convergence results are more stable. This method gives a smooth second order convergence. At steady state, only the phase space error is observed. The transport in physical space and velocity space is done exactly so the error of the numerical solution is only due to the remeshing process. A second order interpolation kernel is used to redistribute the particles. As expected, the convergence rates observed on figure VI.6b show a second order convergence. In contrast with the Lagrangian method, the solution is not noisy even for large $\Delta\boldsymbol{\xi}$ since the particles are redistributed at each time step. However, the stencil being compact (2 points in each directions), for large $\Delta\boldsymbol{\xi}$ the particles are remeshed in priority along the grid axis and a bias along the coordinate directions may appear.

VI.4.2 Test 2

The data are the same as in the first test, except that a non zero velocity field is imposed. In particular, we consider $\mathbf{U}_g = (1, 1)$. The solutions are compared at $t = 2$ for $D = 1$.

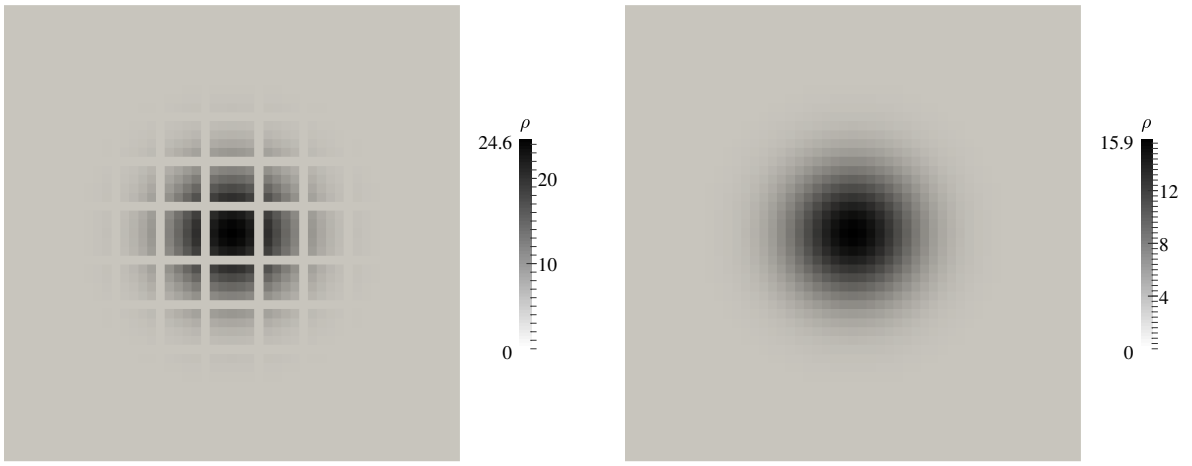

(a) Grid 51×51 in space, 41×41 in velocity.

(b) Grid 51×51 in space, 41×41 in velocity.

Figure VI.7: Test 1: Steady state solution by the Lagrangian method with two different velocity grids ($D = 1$).

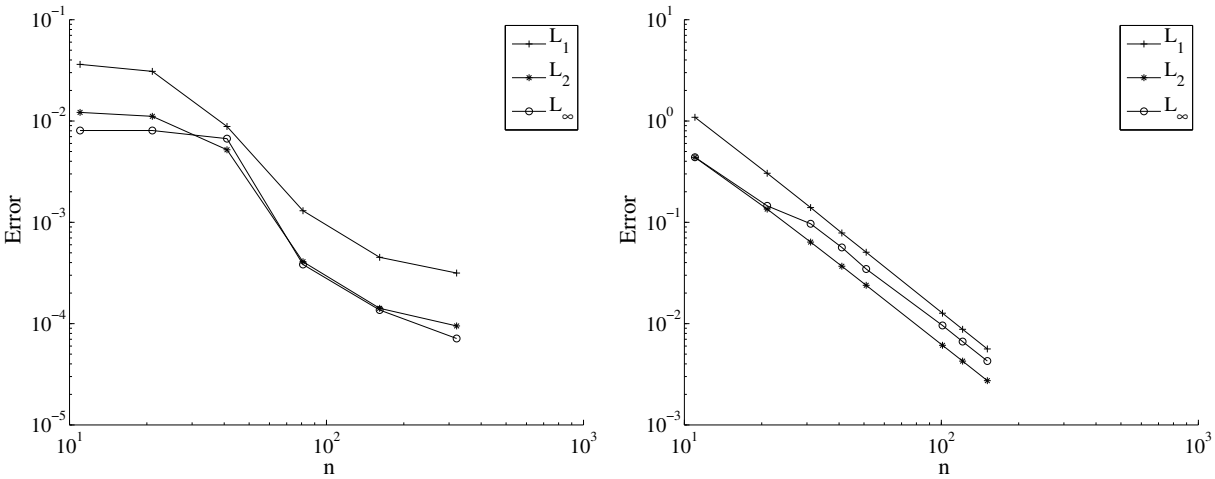

(a) Lagrangian method

(b) Remeshing method

Figure VI.8: Test 2: L_1, L_2 and L_∞ norm of the error.

As expected, the same conclusions hold for this velocity field (see figure VI.8). The remeshing method gives a second order convergence. Even if the splitting is first order, it does not impact the accuracy of the solution since the equation for the acceleration is at steady state and the velocity field is constant. Then, the integration in time is exact and only the error in space is observed.

VI.4.3 Test 3

We now consider in this test the velocity field expressed as $\mathbf{U}_g = (-y, x)$ and with $D = 5$. The trajectory of a single particle is computed with the Lagrangian scheme. The analytical solution

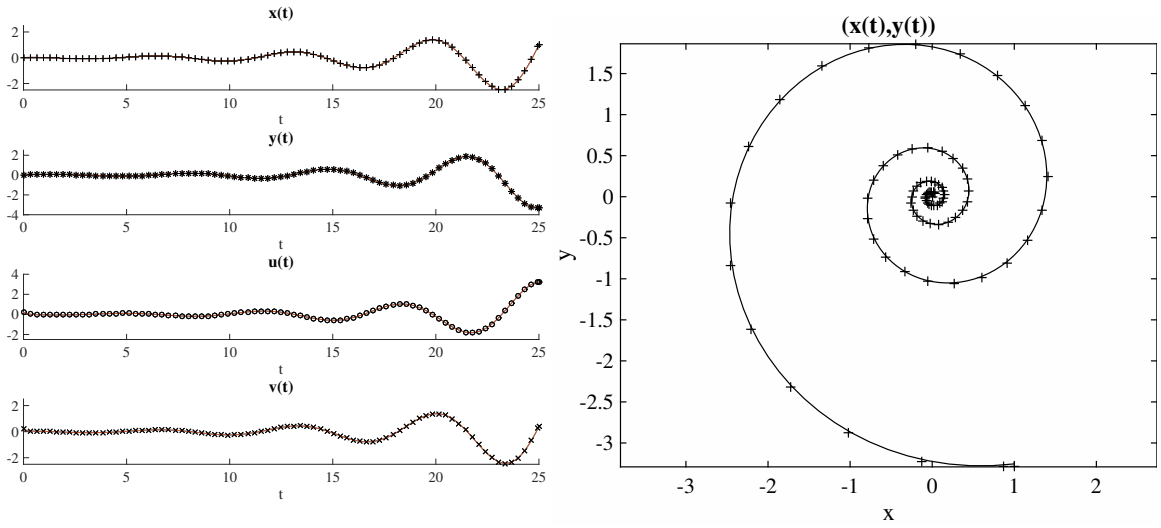

(a) Position and velocity.

(b) Particle trajectory.

Figure VI.9: Test 3: Particle position and velocity over time solved with the Lagrangian scheme. Analytical solution in solid line. Particle initially in (0,0) with (u,v)=(0.2,0.2).

is computed solving the system of four first order differential equations:

$$\begin{cases} \dfrac{dx}{dt} = \xi'_u \\ \dfrac{dy}{dt} = \xi'_v \\ \dfrac{d\xi'_u}{dt} = -D(y + \xi'_u) \\ \dfrac{d\xi'_v}{dt} = D(x - \xi'_v) \end{cases} \tag{VI.18}$$

In this test, we compare the analytical solution with $x(0) = 0$, $y(0) = 0$, $\xi'_u(0) = 0.2$ and $\xi'_v(0) = 0.2$ at $t = 25$ with the Lagrangian scheme.

This velocity field is not constant in space any more. The solution computed with the Lagrangian method follows correctly the analytical trajectory for different particles (see figures VI.9 and VI.10).

We also consider a cluster of particles that are initially in the cell containing the point (1,0). For these particles, the problem is solved with both the Lagrangian method and the remeshing method, and compared to the analytical solution at $t = 5$. Figures VI.11-VI.13 shows the particle density computed with the remeshing method for a grid 121×121 in space and velocity. At $t = 5$, one can observe that the position of non zero particle density is not clearly concentrated in a point. This is due to the initial particle distribution that allows a diffusion of the particles in the neighbouring cells before their velocities converge towards the given velocity field. This diffusion is also biased by the interpolation kernel used during the remeshing step and tends to spread the particles even when their microscopic velocities have converged to the velocity field.

Figure VI.14 shows the error with respect to the analytical solution for the remeshing method. Also in this case, a second order convergence is observed.

Now that the two methods have been validated on several test cases where the analytical solution was known, we focus on a test case where the velocity field is computed from the kinetic model.

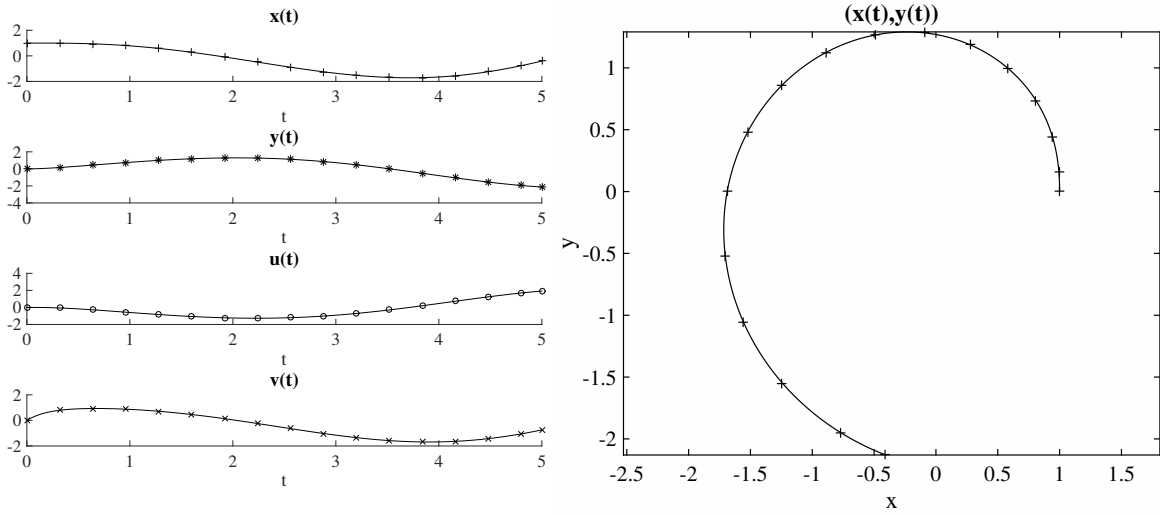

(a) Position and velocity.

(b) Particle trajectory.

Figure VI.10: Test 3: Particle position and velocity over time solved with the Lagrangian scheme. Analytical solution in solid line. Particle in (1,0) with (u,v)=(0,0) at $t = 0$.

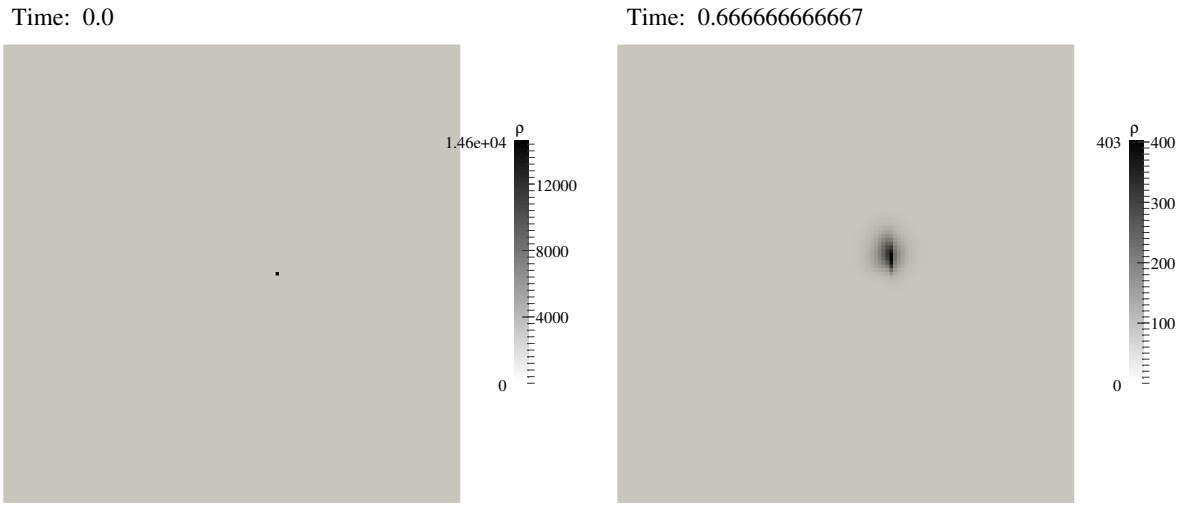

(a) $t = 0$

(b) $t = 0.666$

Figure VI.11: Test 3: Particle density at $t = 0$ and $t = 0.666$ with the remeshing method.

VI.4.4 A nozzle plume

The coupling between the kinetic model and the particle method is investigated through a nozzle plume. The firing of satellite thrusters in space can induce a contamination of surrounding parts (that might be optical disposals) by incompletely burnt particles for instance. Thus, lenses, mirror or solar panel situated near the thruster become inefficient. Usually, a collar is added just behind the thruster. It is then important to quantify how much particles come and stick on this collar and to evaluate the resulting opacity after the firing of the thruster. This evaluation requires the ability of simulating a nozzle plume in highly rarefied environment (space) and the transport of particles in this flow.

In chapter III, the ability of our numerical scheme to simulate such a phenomenon with

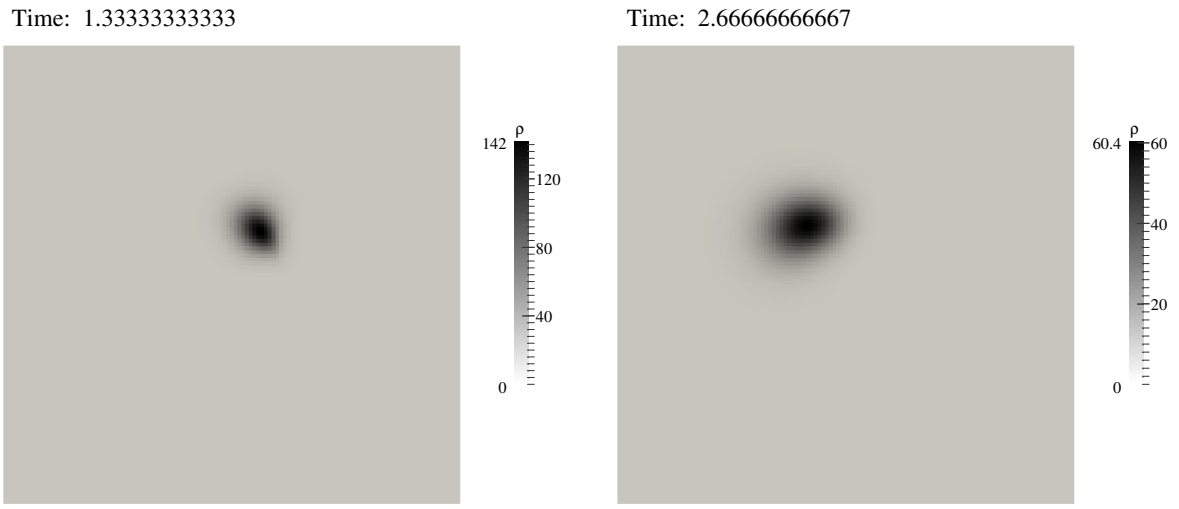

(a) $t = 1.333$ (b) $t = 2.666$

Figure VI.12: Test 3: Particle density at $t = 1.333$ and $t = 2.666$ with the remeshing method.

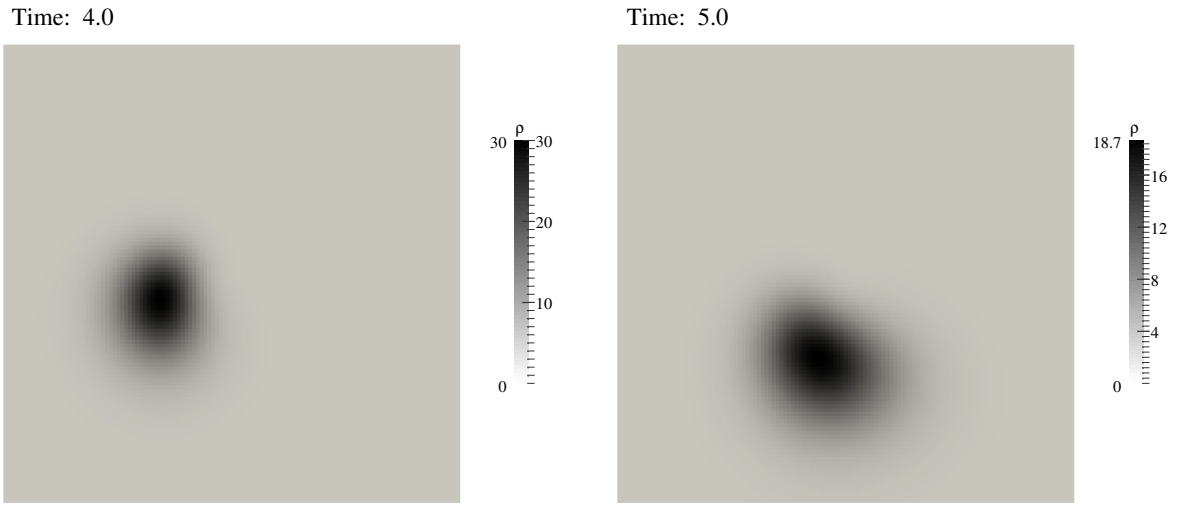

(a) $t = 4$ (b) $t = 5$

Figure VI.13: Test 3: Particle density at $t = 4$ and $t = 5$ with the remeshing method.

BGK and ES-BGK model and proper boundary conditions has been shown. We know add the transport model to simulate the ejection of particles. The Knudsen number Kn_∞ is set to 10^{-5} corresponding to the conditions in the nozzle where the hydrodynamic regime is expected.

When a particle hits the nozzle, we assume that it sticks to the solid boundary. Outside the nozzle, if a particle reaches the jet boundary its velocity is set to the minimum between its own velocity and the jet boundary velocity. Thus, it cannot cross the zero-isoline of the levelset and go in the surrounding domain.

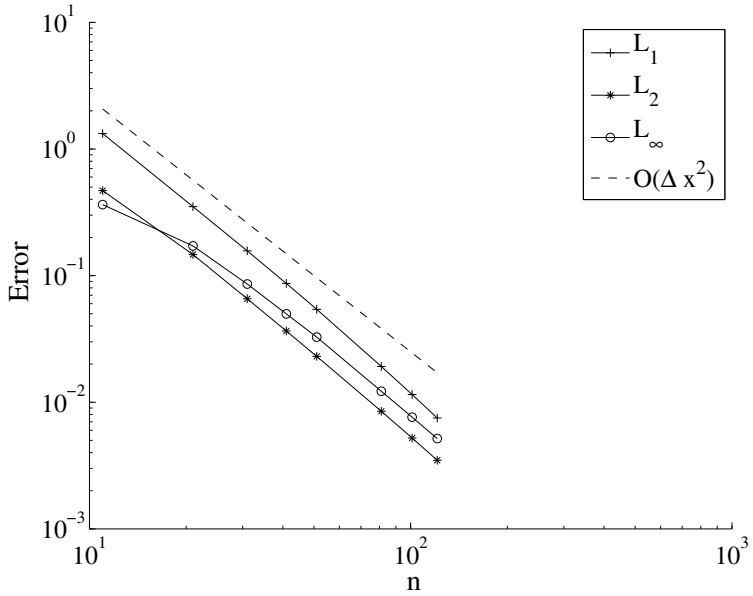

Figure VI.14: Test 3: L_1, L_2 and L_∞ norm of the error with the remeshing method ($t = 5$, $D = 5$).

VI.4.4.1 Constant velocity field

In this first step, both particle methods are compared. The gas flow is taken at steady state for a pressure ratio $P_c/P_{out} = 200000$. Particles of mass $m' = 2.56 \times 10^{-6}$ are injected at the inlet of the nozzle at $t = 0$ through the same distribution function as in test case 1.

Figure VI.15 shows the particles trajectory computed with the Lagrangian method (grey dot) and the associated density field computed with the remeshing method (in color). We mention that the lower value of the density field is 0 but for convenience, we set it to 0.0001 to see the field in logarithmic scale. We can observe from the figure a good accordance between the two methods. Also, the remeshing method gives a higher density near the symmetric axe of the nozzle. This is due to the remeshing process that remeshes the particles that went out of the domain partly inside of it. Conversely, the Lagrangian method lets the particle where it left the domain. No particles are turning back at the outlet of the nozzle even if the angle of the jet does. This is mostly due to the inertia of the particles when they arrive at the outlet but also to the numerical discontinuity of the velocity at the outlet boundary of the nozzle (in the first cell outside the nozzle, the horizontal velocity is positive while in the jet immediately above the nozzle, it is negative). A very fine grid in space and velocity is required to observe the particle turning back, something that we cannot afford. However, using a larger stencil for the remeshing step could be a solution to make the particles go through this discontinuity. But such stencils introduce too much numerical diffusion for our needs. Another solution is to add a diffusion term in the velocity divergence that physically corresponds to the Brownian motion of the particles due to the temperature for example [20], [22], [43]. Here, we choose to add a perturbation in the velocity space. After the transport in velocity, a white noise is added to each microscopic velocity such that:

$$\boldsymbol{\xi'}^{n+1} = \boldsymbol{\xi'}^{n} + D(\mathbf{U}_g - \boldsymbol{\xi'}^{n}) + \mathrm{rand}(-1,1)\Delta\boldsymbol{\xi'}$$

with $\mathrm{rand}(-1,1)$ a random number between -1 and 1.

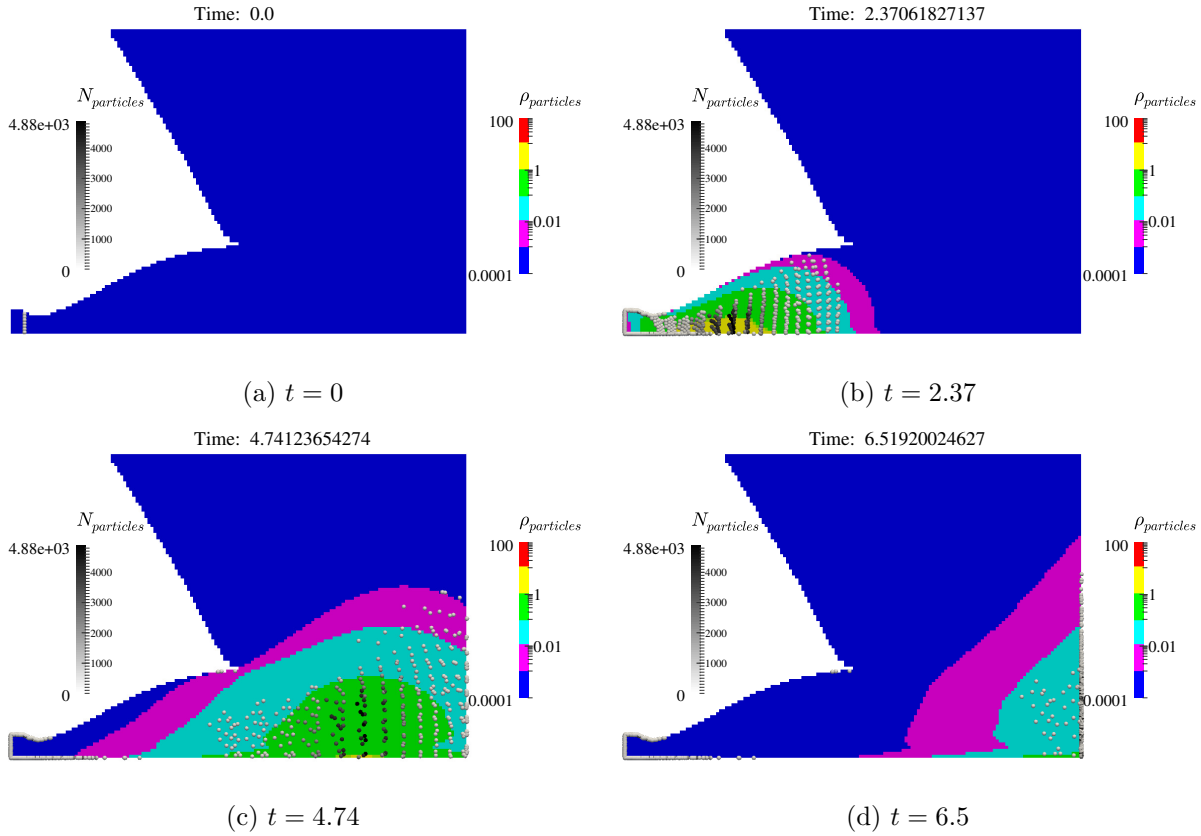

(a) $t = 0$ (b) $t = 2.37$

(c) $t = 4.74$ (d) $t = 6.5$

Figure VI.15: Comparison of the two methods for $D = 1$.

VI.4.4.2 Time dependant particles flow

We are now interested in the realistic test case of the ejection of particles during the firing of the thrusters. The firing of thrusters in rarefied conditions induces a pollution of optical devices (mirror, lenses) that are usually present on satellites especially during the transitional state. We want to quantify how many particles go towards the optical devices placed on a satellite. These devices are usually located above the inlet of the nozzle perpendicularly to its symmetric axis.

In initial conditions, the nozzle is filled with gas and particles. At the inlet, particles are injected continuously. This boundary condition is imposed through a constant distribution function in the ghost cell equal to the initial state. We recall the initial conditions on figure VI.16. We specified here a surface Γ that goes from above the inlet of the nozzle and until the upper boundary of the domain. It represents the position of optical devices placed on the satellites. In the following, we compute the particle flux through Γ, to understand whether the particle flow can contaminate (or damage) the devices.

Figure VI.17 shows that the particles go out of the domain (through the surface Γ on figure VI.16) sooner for higher pressure ratios. The jet reaches faster the inlet of the nozzle because the velocity of the jet boundary increases with the pressure ratio. On the same figure, one can note that even for large pressure ratios, the particles flux through Γ goes to zero at steady state. Indeed, at steady state, the expanded jet turns back but not until the left boundary of the domain. Thus, no particles are ejected in this direction at steady state.

On figure VI.17 one can remark that there is a peak in the flux when the particles start to go out of the domain. This bump is actually higher for $P_c/P_{atm} = 10000$ than for $P_c/P_{atm} = 10^6$.

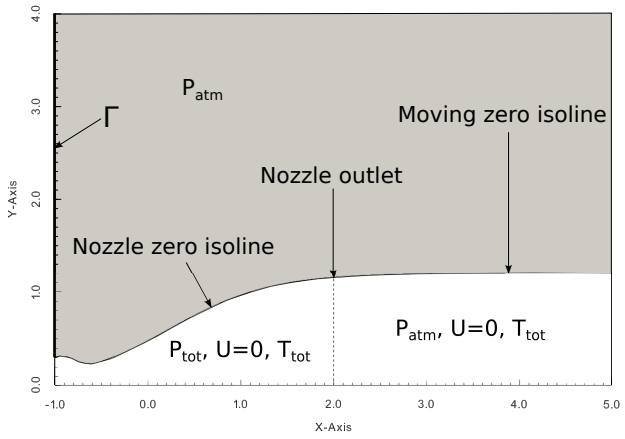

Figure VI.16: Initial configuration of the computational domain for the simulation of the particle flow in a nozzle plume.

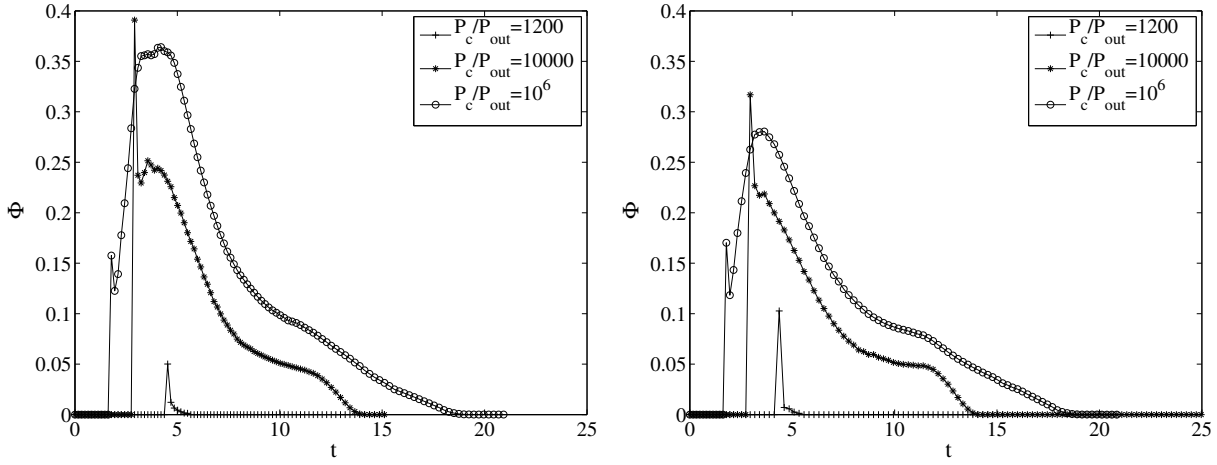

(a) BGK model

(b) ES-BGK model

Figure VI.17: Particles flux for three pressure ratios (1200, 10000, 10^6).

It is due to the particles that have initially a higher microscopic velocity than the boundary of the jet. Since the particles are not allowed to cross the boundary (due to the boundary condition we chose) they artificially stick to the jet contour. As the pressure ratio increases, the jet boundary velocity increases and less particles have a microscopic velocity higher than the jet boundary velocity. Thus, less particles stick to the jet boundary making the peak lower.

Comparing figures VI.17a and VI.17b one can deduce that the difference between the BGK model and the ES-BGK model increases with the pressure ratio $r = P_c/P_{atm}$. A more precise comparison is shown on figure VI.18 for two other pressure ratios ($r = 10^4$, $r = 4.10^5$). The general behaviour is the same, the particles start to go out of the domain at the same time and a peak is observed.Also, we can see that the fluxes for the ES-BGK are lower. As the pressure ratio increases, the local Knudsen number in the jet increases too (order $Kn_\infty r$) and explains the differences between the two models.

From these fluxes, we can deduce the number of particles that went out by the side of the domain. Figure VI.19 shows this number for different pressure ratios.

For pressure ratios lower than 10^3, the expanded jet does not go back until the inlet of the

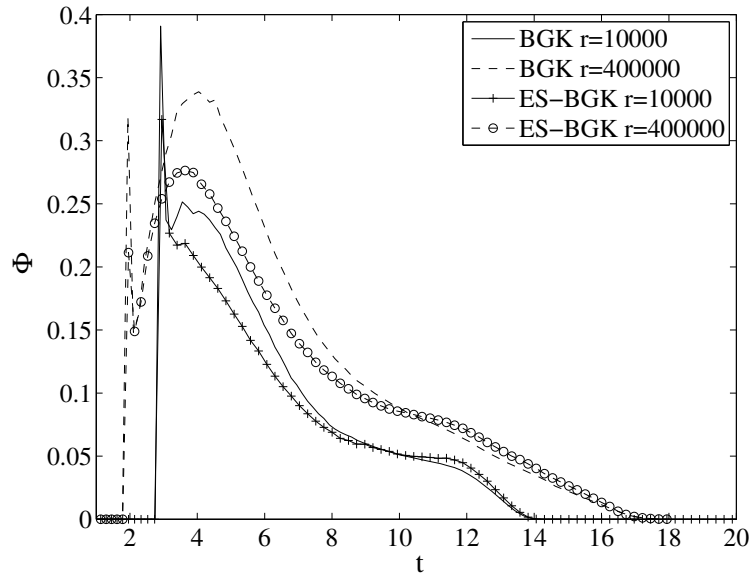

Figure VI.18: Particle flux for the BGK model and the ES-BGK model for two different pressure ratios (10^4, 4.10^5).

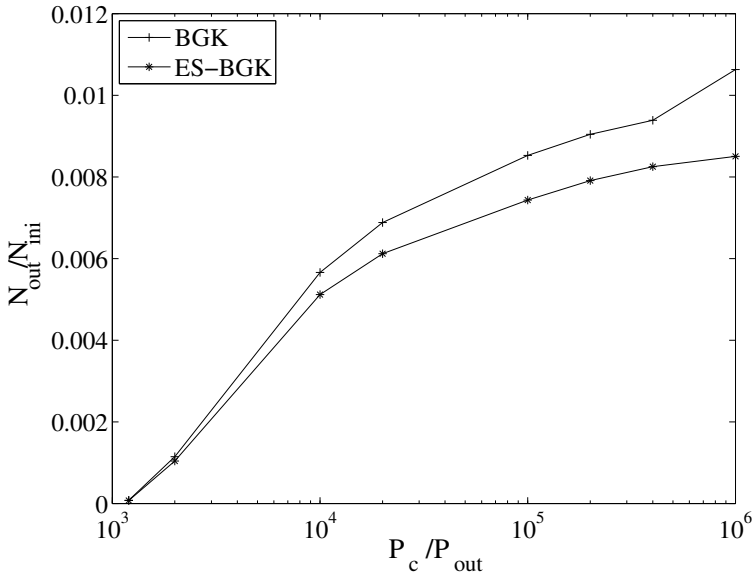

Figure VI.19: Normalized number of particles exiting the domain above the nozzle inlet.

nozzle so no particles are ejected in front of it.For very high pressure ratios, the number of particles going through Γ tends to stabilize because no particles are going through Γ during steady state. The ejection of particles on optical devices is a purely transitional phenomenon. This observation is in accordance with

Comparing the results given by the two models, we can note that the BGK model seems to overestimate the number of ejected particles with respect to the ES-BGK model. For very high pressure ratios, the Knudsen number becomes of order 1. In this regime we can expect that the ES-BGK model is more reliable since it simulates the correct Prandtl number.

VI.5 Preliminary conclusion

In this chapter, we proposed a numerical method to solve applied problems dealing with particle dynamics in rarefied flows. A Vlasov equation with a drag force has been used to simulate the particle flow while the gas flow has been modelled with a kinetic equation. We applied a Lagrangian scheme with a remeshing technique to the Vlasov equation. The advantage of this method with respect to finite volume or finite difference schemes is that the equation is solved only where there are particles. It is also easy to recover an Eulerian field with this method. The method has been validated on different 2D test cases with respect to analytical solutions. We also added a Brownian motion in the particle transport model through a perturbation in the velocity space. A nozzle flow has been presented where the two kinetic models have been solved to compute the particle dynamics interacting with the gas velocity field. On this test case, we reproduced the contamination phenomenon observed experimentally [39]. Moreover, based on the results, it was possible to show that the pollution is due to the transitional regime. At steady state, no particles are ejected in front of the nozzle. However, the lack of data on such phenomenon in the literature does not allow a quantitative validation.

Conclusion

In this PhD thesis, we focused on complex flows where both rarefied and hydrodynamic regimes are coexisting. In particular, one objective was to apply the methods developed here to the case of a nozzle plume in rarefied environment to explain the contaminations of optical devices around satellite thrusters. As already said, this phenomenon has been observed experimentally in [39] but has never been clearly explained and reproduced from a numerical point of view.

Two deterministic models are presented, the BGK model and the ES-BGK model solved with a Discrete Velocity method (DVM). In space, we chose a Cartesian discretization with a finite volume scheme to exploit the simplicity of Cartesian meshes for massive parallel computations. In time, the integration scheme is a so-called IMEX scheme that allows an implicit treatment of the collision term. This is particularly important in hydrodynamic regime where the term becomes stiff. Thus, the time step is only governed by the convective part of the equation independently of the regime.

The first contribution focused on the wall condition asymptotic behaviour of the numerical methods towards the hydrodynamic regime. It is necessary to ensure this behaviour when both regimes are present but also for domain decomposition methods [2]. In this case, it is mandatory to have a smooth transition between the solution of the macroscopic model near the boundary and the solution from the kinetic model.

Since we use Cartesian grids, considering an immersed solid in a flow implies that the grid is not necessarily fitted with the body. Enforcing the boundary condition is then done with an immersed boundary method. We chose to create a ghost state in the solid cells such that the boundary condition is correctly imposed without modification of the numerical scheme computing the fluxes at the interface between two cells. It has been shown on numerical examples (oblique shock, Blunt body) that the standard way to enforce the specular boundary condition on a surface arbitrarily crossing the grid is not satisfying from a computational point of view (large errors, necessity of a very fine velocity grid or high order interpolations). Although theoretically asymptotic preserving at the continuous level, this boundary condition cannot allow in practice to recover the correct solution for a general flow around an immersed without a high computational cost. In this sense, a novel method has been proposed to preserve the correct asymptotic behaviour towards the continuous regime by imposing an equilibrium distribution function as boundary condition satisfying the impermeability requirements. We prove the efficiency of this method in the continuous regime for different test cases (reflection of rarefaction waves and shock waves, oblique shock, Blunt body). Moreover, we extended the method of Gorsse et al. [61] to kinetic models in order to recover second-order accuracy up to the boundary with the immersed boundary method. This result is shown on the Ringleb flow for the BGK model and on a cylindrical Couette flow in rarefied regime for the ES-BGK model. To deal with more general regimes, the term corresponding to the specular reflection is modeled by a convex combination between the standard specular reflection and the new impermeability condition. This new condition is integrated into the classical Maxwell boundary condition.

In the rarefied regime, the method has been applied and compared to results in the literature on the flow past a vertical plate test case. A good accordance with the results of Bird [16] and Chen [32] has been observed for several Knudsen numbers. Finally, the proposed method and AP boundary condition has been applied to moving geometry. In particular, the test case of the nozzle plume has been investigated, qualitatively and compared to the experimental results of Latvala et al. [79]. We also highlighted the need for these cases of kinetic models with the asymptotic preserving boundary condition while continuous models such as compressible Euler equations cannot describe the correct dynamics. Moreover, without a proper treatment of the boundary condition (AP boundary condition), especially inside the nozzle, the solution would be dramatically polluted due to large errors at the nozzle boundaries.

A considerable effort have also been devoted to the computational performances of the code. Because of the discretization in velocity, kinetic models are heavy to compute. In this sense, the code has been parallelized and good performances have been observed (strong scalability of 0.7). A novel local grid approach in velocity has also been proposed. The idea is to avoid computations for microscopic velocities corresponding to a negligible distribution function. A simple algorithm has been proposed to solve with a better efficiency the kinetic model with the discrete velocity method. The same drawback are observed than with the full discrete velocity methods: the velocity grid has to be set *a priori* for the whole calculation. However, the computational time has been dramatically reduced for several test cases in 1D, 2D and in hydrodynamic regime as well as in rarefied regime. Moreover, no overhead in computational time are observed meaning that the cost of the method is at most the cost of the standard method. Indeed, reduction up to 80% have been obtained keeping a relative error with respect to the full grid calculation lower than 10^{-4}.

Thanks to these development, numerical simulations have been run in 3D with reasonable computational requirements for the BGK model. The code has been validated with respect to the 2D code on the Blunt body test case. Apollo re-entries have also been simulated in different regimes to recover aerodynamic coefficient. The code developed allows a rotation of the capsule around the center of mass according to the torque due to the aerodynamic forces. Evolutions over time have been shown for different capsule shapes, different regimes and position of the center of mass.

Finally, in the last chapter, we added a one way coupling between the kinetic model and a particle transport model to simulate the case of the contamination of optical devices around satellite thrusters. The particle transport model is based on a Vlasov type equation. The coupling is done through the acceleration term due to the drag force. This drag force is here linear with the difference between the gas velocity and the particle velocity. This representation has been validated experimentally for granular flows for example in [21]. We also added a perturbation in the velocity space through a white noise corresponding to the Brownian motion of the particles [43]. To solve this model, we introduce a method based on a remeshing process. The particles are transported with a Lagrangian step with a splitting in phase space (between the transport in physical space and in velocity space) and then, redistributed on the initial Cartesian meshes. With respect to Smooth Particles Hydrodynamic (SPH) method or Particle-in-Cell methods, the proposed method has the advantage of conserving the positivity of the particle distribution function, being defined on the Cartesian mesh for every time step and not being sensitive to clustering of particles. The method has been validated with respect to analytical solutions and then applied to the transport of particles ejected in a nozzle plume.

Based on the observation in [39] and on the results obtained with the coupled model with

BGK and ES-BGK model, we gave a first explanation to the phenomenon of contamination. In rarefied environment, the nozzle jet turns back towards the nozzle inlet during the transitional state. In this case, particles initially in the nozzle are also ejected backwards and depose on the optical devices. However, at steady state, if we consider that the optical devices are placed above the inlet of the nozzle, the jet does not turn back enough to contaminate them. There is a pollution only during the transitional state (at least for pressure ratios until 10^6). Unfortunately, the lack of data, cannot allow a quantitative comparison of our results.

All the developments made in this work allow simulations of complex flows, independently of the regime at a reasonable accuracy, with moving geometries and in 3D, which is very challenging for kinetic models. The methods presented have been applied to BGK and ES-BGK model. A one way coupling with a particle transport model has been proposed to try to explain the peculiar phenomenon of the contamination of optical devices on satellites due to the firing of thrusters. This work is a step towards the simulations of more complex gases in real conditions at a reasonable computational cost and could have an impact on different industrial fields. In this sense, it should be interesting to furthermore validate the 3D code and try to improve the local velocity grid approach technique to reduce even more the computational time or to avoid the main drawback of DVM techniques of setting *a priori* the velocity grid. It could be fruitful to investigate for instance how the idea of Brull and Mieussens in [23] or AMR techniques such as in [9] could be efficiently applied with our method. Also, a reduction of the cost from a memory point of view should be studied.

More work on the coupling between the kinetic models and the particle transport model is needed. Firstly, the diffusion term could be improved to better simulate the Brownian motion of the particles. We added a perturbation in velocity space but more complex models could be developed by modeling this perturbation with a gradient of the distribution function and a parameter that could depend on the temperature similarly to what has been done in [25]. Moreover, source terms could be added in the particle transport model as well as in the kinetic model like in [30]. The first one could represent the collisions between the particles in the case of a less rarefied flow. The source term in the kinetic model is the feedback from the particle flow to the gas flow. Such a model would allow the simulation of sprays where the particles influence the gas flow.

Finally, maybe the most important improvement that could be done is the extension to more complex gases. In particular, to compare the numerical results to experimental data, the model should be extended to polyatomic gases. Extensions of the BGK and ES-BGK models exist by integrating a variable for the internal energy. The methods proposed here should probably be easily applied to such models. Thus, quantitative comparisons could be made on the jet angle and on the plume shape for the nozzle test case since experimental data are available in [78] and [79]. The 3D test case of the Apollo capsule could also be quantitatively validated in different regimes. However, for this last test case, gas mixtures could also be considered with chemical reactions between different species and radiation.

Appendix A

Reduced model for the BGK model

We present here the details of the calculation to obtain the reduced model in 1D and in a general case for the BGK model in dimensionless form with d degrees of freedom. In section I.2.2, the idea of the reduced model has been introduced following the work of Chu [33].

A.1 The 1D case

Let us consider two distribution function ϕ and ψ independent of the reduced dimensions y and z:

$$\begin{aligned} \phi(x,\xi_u,t) &= \int_{\mathbb{R}^2} f d\xi_v d\xi_w \\ \psi(x,\xi_u,t) &= \int_{\mathbb{R}^2} \frac{1}{2}(\xi_v^2+\xi_w^2) f d\xi_v d\xi_w \end{aligned} \tag{A.1}$$

Defining the second distribution function ψ is necessary to recover the expression of the energy, yet, building the Maxwellian distribution function. The two distribution functions verify in 1D:

$$\begin{aligned} \partial_t \phi + \xi_u \partial_x \phi &= \frac{1}{\tau}(M_\phi - \phi) \\ \partial_t \psi + \xi_u \partial_x \psi &= \frac{1}{\tau}(M_\psi - \psi) \end{aligned} \tag{A.2}$$

The macroscopic quantities are recovered as follows:

$$\int_{\mathbb{R}^d} f(\boldsymbol{\xi}) \mathbf{m}_1(\boldsymbol{\xi}) d\boldsymbol{\xi} = \begin{pmatrix} \int_{\mathbb{R}} \phi(\xi_u) d\xi_u \\ \int_{\mathbb{R}} \xi_u \phi(\xi_u) d\xi_u \\ \int_{\mathbb{R}} \frac{1}{2}\xi_u^2 \phi(\xi_u) d\xi_u + \int_{\mathbb{R}} \psi(\xi_u) d\xi_u \end{pmatrix} = \begin{pmatrix} \rho \\ \rho u \\ E \end{pmatrix} \tag{A.3}$$

Let us now detail the calculation of the Maxwellian distribution function M_ϕ and M_ψ. They are defined as:

$$\begin{aligned} M_\phi(x,\xi_u,t) &= \int_{\mathbb{R}^2} M_f d\xi_v d\xi_w \\ M_\psi(x,\xi_u,t) &= \int_{\mathbb{R}^2} \frac{1}{2}(\xi_v^2+\xi_w^2) M_f d\xi_v d\xi_w \end{aligned} \tag{A.4}$$

where M_f is the Maxwellian distribution function depending on the macroscopic density, velocity and temperature (we now drop the dependencies for clarity):

$$M_f = \frac{\rho}{(2\pi T)^{d/2}} \exp\Big(- \frac{|\boldsymbol{\xi} - \mathbf{U}|^2}{2T} \Big)$$

Thus, since ξ_u, ξ_v, ξ_w are independent variables:

$$\begin{aligned} M_\phi &= \int_{\mathbb{R}^2} M_f d\xi_u d\xi_v \\ &= \frac{\rho}{(2\pi T)^{d/2}} \exp\Big(- \frac{(\xi_u - u)^2}{2T}\Big) \int_{\mathbb{R}^2} \exp\Big(- \frac{(\xi_v - v)^2}{2T}\Big) \exp\Big(- \frac{(\xi_w - w)^2}{2T}\Big) d\xi_u d\xi_v \\ &= \frac{\rho}{(2\pi T)^{d/2}} \exp\Big(- \frac{(\xi_u - u)^2}{2T}\Big) \int_{\mathbb{R}} \sqrt{2T} \exp(-\alpha^2) d\alpha \int_{\mathbb{R}} \sqrt{2T} \exp(-\beta^2) d\beta \end{aligned}$$

where α (respectively β) comes from the changing of variable $\alpha = \frac{\xi_v - v}{\sqrt{2T}}$ (respectively $\beta = \frac{\xi_w - w}{\sqrt{2T}}$). We now use the result on the integration of a Gaussian:

$$\int_{\mathbb{R}} \exp(-x^2) dx = \sqrt{\pi} \tag{A.5}$$

Finally we get the expression of the first equilibrium distribution function with:

$$M_\phi = \frac{\rho}{(2\pi T)^{d/2-1}} \exp\Big(- \frac{(\xi_u - u)^2}{2T}\Big) \tag{A.6}$$

A.2 General case

In a more general case with d degrees of freedom and D dimensions in space, to reduce the dimensions from $D+1$ to d, one can write:

$$\begin{aligned} \phi &= \int_{\mathbb{R}^{d-D}} f \prod_{k=D+1,d} d\xi_k \\ \psi &= \int_{\mathbb{R}^{d-D}} \frac{1}{2} \sum_{l=D+1,d} \xi_l^2 f \prod_{k=D+1,d} d\xi_k \end{aligned} \tag{A.7}$$

and

$$\begin{aligned} M_\phi &= \int_{\mathbb{R}^{d-D}} M_f \prod_{k=D+1,d} d\xi_k \\ &= \frac{\rho}{(2\pi T)^{d/2}} \prod_{l=1,D} \exp\Big(- \frac{(\xi_l - U_l)^2}{2T}\Big) \int_{\mathbb{R}^{d-D}} \prod_{k=D+1,d} \exp\Big(- \frac{(\xi_k - U_k)^2}{2T}\Big) d\xi_k \\ &= \frac{\rho}{(2\pi T)^{d/2}} \prod_{l=1,D} \exp\Big(- \frac{(\xi_l - U_l)^2}{2T}\Big) \prod_{k=D+1,d} \int_{\mathbb{R}} \exp\Big(- \frac{(\xi_k - U_k)^2}{2T}\Big) d\xi_k \\ &= \frac{\rho}{(2\pi T)^{d/2}} \prod_{l=1,D} \exp\Big(- \frac{(\xi_l - U_l)^2}{2T}\Big) (2\pi T)^{\frac{d-D}{2}} \end{aligned}$$

Then, a general expression for the equilibrium distribution function M_ϕ is:

$$M_\phi = \frac{\rho}{(2\pi T)^{D/2}} \prod_{l=1,D} \exp\Big(- \frac{(\xi_l - U_l)^2}{2T}\Big) \tag{A.8}$$

where ξ_k and U_k denote the k-th component of the vectors $\boldsymbol{\xi}$ and $\mathbf{U}$ respectively.

We now detail the calculation of the second equilibrium distribution function M_ψ in the general case:

$$M_\psi = \int_{\mathbb{R}^{d-D}} \frac{1}{2} \sum_{k=D+1,d} \xi_k^2 \frac{\rho}{(2\pi T)^{d/2}} \prod_{l=1,d} \exp\Big(- \frac{(\xi_l - U_l)^2}{2T} \Big) \prod_{k=D+1,d} d\xi_k$$

assuming that the dimensions we want to reduce are indexed from $D+1$ to d. With the changing of variable $\alpha_k = \frac{\xi_k - U_k}{\sqrt{2T}}$:

$$\begin{aligned}
M_\psi =& \frac{\rho(2T)^{\frac{d-D}{2}}}{2(2\pi T)^{d/2}} \prod_{l=1,D} \exp\Big(- \alpha_l^2 \Big) \int_{\mathbb{R}^{d-D}} \sum_{k=D+1,d} (\sqrt{2T}\alpha_k + U_k)^2 \prod_{l=D+1,d} \exp\Big(- \alpha_l^2 \Big) d\alpha_l \\
=& \frac{\rho(2T)^{\frac{d-D}{2}}}{2(2\pi T)^{d/2}} \prod_{l=1,D} \exp\Big(- \alpha_l^2 \Big) \sum_{k=D+1,d} \int_{\mathbb{R}^{d-D}} (\sqrt{2T}\alpha_k + U_k)^2 \prod_{\substack{l=D+1,d \\ l\neq k}} \exp\Big(- \alpha_l^2 \Big) d\alpha_l \\
=& \frac{\rho(2T)^{\frac{d-D}{2}}}{2(2\pi T)^{d/2}} \prod_{l=1,D} \exp\Big(- \alpha_l^2 \Big) \sum_{k=D+1,d} \prod_{\substack{l=D+1,d \\ l\neq k}} \int_{\mathbb{R}} \exp\Big(- \alpha_l^2 \Big) d\alpha_l \\
& \times \int_{\mathbb{R}} (\sqrt{2T}\alpha_k + U_k)^2 \exp\Big(- \alpha_k^2 \Big) d\alpha_k \\
=& \frac{\rho(2T)^{\frac{d-D}{2}}}{2(2\pi T)^{d/2}} \prod_{l=1,D} \exp\Big(- \alpha_l^2 \Big) \sum_{k=D+1,d} \pi^{\frac{d-D-1}{2}} \\
& \times \int_{\mathbb{R}} (\sqrt{2T}\alpha_k + U_k)^2 \exp\Big(- \alpha_k^2 \Big) d\alpha_k
\end{aligned}$$

Let us now develop the last term:

$$\begin{aligned}
\int_{\mathbb{R}} (\sqrt{2T}\alpha_k + U_k)^2 \exp\Big(- \alpha_k^2 \Big) d\alpha_k =& 2T \int_{\mathbb{R}} \alpha_k^2 \exp(-\alpha_k^2) d\alpha_k + \cancel{2\sqrt{2T}U_k \int_{\mathbb{R}} \alpha_k \exp(-\alpha_k^2) d\alpha_k} \\
& + U_k^2 \int_{\mathbb{R}} \exp(-\alpha_k^2) d\alpha_k
\end{aligned} \tag{A.9}$$

If we consider that the flow is independent of the second and third direction, it also coherent to consider that U_k is constant in the reduced directions. In particular, with a Galilean transformation it is always possible to reduce the problem to $U_k = 0$. Then,

$$\begin{aligned}
M_\psi =& \frac{\rho(2T)^{\frac{d-D}{2}}}{2(2\pi T)^{d/2}} \prod_{l=1,D} \exp(-\alpha_l^2) \sum_{k=D+1,d} \pi^{\frac{d-D-1}{2}} 2T \int_{\mathbb{R}} \alpha_k^2 \exp\Big(- \alpha_k^2 \Big) d\alpha_k \\
=& \frac{\rho(2T)^{\frac{d-D}{2}}}{2(2\pi T)^{d/2}} \prod_{l=1,D} \exp(-\alpha_l^2) \sum_{k=D+1,d} \pi^{\frac{d-D-1}{2}} T\sqrt{\pi} \\
=& \frac{(d-D)T\rho(2\pi T)^{\frac{d-D}{2}}}{2(2\pi T)^{d/2}} \prod_{l=1,D} \exp(-\alpha_l^2) \\
=& \frac{(d-D)T\rho}{2(2\pi T)^{D/2}} \prod_{l=1,D} \exp(-\alpha_l^2)
\end{aligned}$$

Finally,

$$M_\psi = \frac{d-D}{2} T M_\phi \tag{A.10}$$

Appendix B

Discrete Maxwellian algorithm for the BGK model

We present the Newton-Raphson algorithm to compute the discrete Maxwellian distribution function. The algorithm used for the BGK model is first presented. Details are also given for the case of the reduced model and, in particular, how the Jacobian is calculated. In the second part, we present the algorithm used in the case of the ES-BGK model.

The first three moments of the distribution functions are known and we define the collision invariant $\mathbf{m}(\boldsymbol{\xi}) = (1, \boldsymbol{\xi}, \frac{1}{2}|\boldsymbol{\xi}|^2)^T$. The Maxwellian distribution function M_f is computed such that, with the given quadrature rule:

$$\langle M_f, \mathbf{m}(\boldsymbol{\xi})\rangle = \begin{pmatrix} \rho \\ \rho\mathbf{U} \\ E \end{pmatrix}$$

where $(\rho, \rho\mathbf{U}, E) = \langle f, \mathbf{m}(f)\rangle$, that is the moments are computed from f approximately, using the given quadrature rule.

We are looking for M_f under the form: $M_f = \exp(\boldsymbol{\alpha}\cdot\mathbf{m}(\boldsymbol{\xi}))$. Let us define the function:

$$\mathbf{F}(\boldsymbol{\alpha}) = \langle \exp(\boldsymbol{\alpha}\cdot\mathbf{m}(\boldsymbol{\xi})), \mathbf{m}(\boldsymbol{\xi})\rangle - \underline{\boldsymbol{\rho}}$$

with $\underline{\boldsymbol{\rho}} = (\rho, \rho\mathbf{U}, E)^T$, the macroscopic variables computed from the moments of f. The discrete Maxwellian verifies $\mathbf{F}(\boldsymbol{\alpha}) = 0$. Thus, the problem of computing the discrete Maxwellian reduces to find $\boldsymbol{\alpha}$ such that $\mathbf{F}(\boldsymbol{\alpha}) = 0$. This is done with a Newton-Raphson algorithm. The initial value of $\boldsymbol{\alpha}$ corresponds to the continuous Maxwellian (in dimensionless form):

$$\boldsymbol{\alpha}_c = \Big(\ln(\frac{\rho}{(2\pi T)^{N/2}}) - \frac{|\mathbf{U}|^2}{2T}, \frac{\mathbf{U}}{T}, -\frac{1}{T}\Big)$$

The algorithm is summarized as follows:

tol is a tolerance on the convergence of the algorithm that basically corresponds to the conservation error allowed.

In the case of the reduced models, the algorithm is identical but the function $\mathbf{F}$ is defined as:

$$\begin{aligned} \mathbf{F}(\boldsymbol{\alpha}) &= \langle \widetilde{M_\phi}, \mathbf{m}_1(\boldsymbol{\xi})\rangle + \langle \widetilde{M_\psi}, \mathbf{e}_3\rangle - \langle f, \mathbf{m}_1(\boldsymbol{\xi})\rangle \quad \text{in 1D} \\ \mathbf{F}(\boldsymbol{\alpha}) &= \langle \widetilde{M_\phi}, \mathbf{m}_2(\boldsymbol{\xi})\rangle + \langle \widetilde{M_\psi}, \mathbf{e}_4\rangle - \langle f, \mathbf{m}_2(\boldsymbol{\xi})\rangle \quad \text{in 2D} \end{aligned} \tag{B.1}$$

Algorithm 1 Algorithm to compute the discrete Maxwellian

$\boldsymbol{\alpha} \leftarrow \boldsymbol{\alpha}_c$
while $\mathbf{F}(\boldsymbol{\alpha}) < tol$ **do**
  Compute $\mathrm{Jac}(\mathbf{F}) = \dfrac{\partial F_i}{\partial \alpha_j}$ $for\ i, j = 1, ...D+2$
  Compute $\mathbf{F}(\boldsymbol{\alpha})$

  $\boldsymbol{\alpha} \leftarrow \boldsymbol{\alpha} - \mathrm{Jac}(\mathbf{F}) \cdot \mathbf{F}(\boldsymbol{\alpha})$
end while
$M_f \leftarrow \exp(\boldsymbol{\alpha} \cdot \mathbf{m}(\boldsymbol{\xi}))$

where $\mathbf{e}_3 = (0,0,1)^T$, $\mathbf{e}_4 = (0,0,0,1)^T$, $\mathbf{m}_1(\boldsymbol{\xi}) = (1, \xi_u, \frac{1}{2}|\xi_u|^2)^T$, $\mathbf{m}_2(\boldsymbol{\xi}) = (1, \xi_u, \xi_v, \frac{1}{2}(\xi_u^2+\xi_v^2))^T$. And:

$$\boldsymbol{\alpha}_c = \left(\ln(\frac{\rho}{\sqrt{2\pi T}}) - \frac{u^2}{2T}, \frac{u}{T}, -\frac{1}{T}\right)^T \quad \text{in 1D}$$
$$\boldsymbol{\alpha}_c = \left(\ln(\frac{\rho}{2\pi T}) - \frac{u^2+v^2}{2T}, \frac{u}{T}, \frac{v}{T}, -\frac{1}{T}\right)^T \quad \text{in 2D}$$

The Newton-Raphson algorithm give the expression of $\widetilde{M_\phi}$. $\widetilde{M_\psi}$ is then easily computed with the formula:

$$\widetilde{M_\psi} = \frac{(d-D)T}{2}\widetilde{M_\phi} = -\frac{d-D}{2\alpha_{D+2}}\widetilde{M_\phi} \tag{B.2}$$

Let us detail the expression of the Jacobian $\mathrm{Jac}(\mathbf{F})$ in the case of the reduced model (in D dimensions):

$$\frac{\partial F_i}{\partial \alpha_j} = \frac{\partial}{\partial \alpha_j}(\langle \widetilde{M_\phi}, \mathbf{m}_{D,i}(\boldsymbol{\xi})\rangle + \delta_{D+2,i}\langle \widetilde{M_\psi}, \mathbf{e}_{D+2}\rangle - \langle f, \mathbf{m}_{D,i}(\boldsymbol{\xi})) \tag{B.3}$$

where $\mathbf{m}_{D,i}$ is the i-th component of the collision invariant $\mathbf{m}_D$ and $\delta_{D+2,i}$ is the Kronecker symbol.

We now have to set a quadrature rule, meaning how $\langle \cdot, \cdot \rangle$ is expressed. In this work we have chosen the trapezoidal quadrature rule (see II.1). Thus

$$\frac{\partial F_i}{\partial \alpha_j} = \frac{\partial}{\partial \alpha_j}(\sum_{\boldsymbol{\xi}} \widetilde{M_\phi}\mathbf{m}_{D,i}(\boldsymbol{\xi})\Delta\boldsymbol{\xi} + \sum_{\boldsymbol{\xi}} \widetilde{M_\psi}\mathbf{e}_{D+2}\delta_{D+2,i}\Delta\boldsymbol{\xi} - \sum_{\boldsymbol{\xi}} f\mathbf{m}_{D,i}(\boldsymbol{\xi})\Delta\boldsymbol{\xi}) \tag{B.4}$$

where $\Delta\boldsymbol{\xi}$ is the cell volume in the velocity space.

One can note that

$$\frac{\partial}{\partial \alpha_j}\sum_{\boldsymbol{\xi}} f\mathbf{m}_D(\boldsymbol{\xi})\Delta\boldsymbol{\xi} = 0 \tag{B.5}$$

Then

$$\frac{\partial F_i}{\partial \alpha_j} = \frac{\partial}{\partial \alpha_j}(\sum_{\boldsymbol{\xi}} \widetilde{M_\phi}\mathbf{m}_{D,i}(\boldsymbol{\xi})\Delta\boldsymbol{\xi} + \delta_{D+2,i}\sum_{\boldsymbol{\xi}} \widetilde{M_\psi}\mathbf{e}_{D+2}\Delta\boldsymbol{\xi}) \tag{B.6}$$

Using (B.2)

$$\begin{aligned}\frac{\partial F_i}{\partial \alpha_j} =& \frac{\partial}{\partial \alpha_j}\Big(\sum_{\boldsymbol{\xi}} \widetilde{M_\phi}\mathbf{m}_{D,i}(\boldsymbol{\xi})\Delta\boldsymbol{\xi} - \delta_{D+2,i}\sum_{\boldsymbol{\xi}}\frac{d-D}{2\alpha_{D+2}}\widetilde{M_\phi}\mathbf{e}_{D+2}\Delta\boldsymbol{\xi}\Big)\\ =& \sum_{\boldsymbol{\xi}}\mathbf{m}_{D,i}\mathbf{m}_{D,j}\exp(\boldsymbol{\alpha}\cdot\mathbf{m}_D)\Delta\boldsymbol{\xi}\\ & - \delta_{D+2,i}\frac{d-D}{2\alpha_{D+2}}\Big(\sum_{\boldsymbol{\xi}}\mathbf{m}_{D,j}\exp(\boldsymbol{\alpha}\cdot\mathbf{m}_D)\Delta\boldsymbol{\xi}\\ & - \delta_{D+2,j}\frac{1}{\alpha_{D+2}}\sum_{\boldsymbol{\xi}}\exp(\boldsymbol{\alpha}\cdot\mathbf{m}_D)\Delta\boldsymbol{\xi}\Big)\end{aligned} \tag{B.7}$$

Appendix C

Reduced model for the ES-BGK model

This annexe is devoted to the details of the calculation of the ES-BGK reduced model. We follow the same idea as for the BGK model with similar notations. We consider a general case with d translationnal degrees of freedom and D dimensions in space. We look for the expression of the reduced model with the two functions ϕ and ψ. They are defined as:

$$\begin{aligned}\phi &= \int_{\mathbb{R}^{d-D}} f \prod_{k=D+1,d} d\xi_k \\ \psi &= \int_{\mathbb{R}^{d-D}} \frac{1}{2} \sum_{l=D+1,d} \xi_l^2 f \prod_{k=D+1,d} d\xi_k\end{aligned} \tag{C.1}$$

The macroscopic quantities are recovered as follows:

$$\int_{\mathbb{R}^d} f(\boldsymbol{\xi}_D)\mathbf{m}_D(\boldsymbol{\xi})d\boldsymbol{\xi} = \begin{pmatrix} \int_{\mathbb{R}^D} \phi(\boldsymbol{\xi}_D)d\boldsymbol{\xi}_D \\ \int_{\mathbb{R}^D} \boldsymbol{\xi}\phi(\boldsymbol{\xi}_D)d\boldsymbol{\xi}_D \\ \int_{\mathbb{R}^D} \frac{1}{2}|\boldsymbol{\xi}_D|^2\phi(\boldsymbol{\xi}_D)d\boldsymbol{\xi}_D + \int_{\mathbb{R}^{d-D}} \psi(\boldsymbol{\xi}_D)d\boldsymbol{\xi}_D \\ \int_{\mathbb{R}^D} \mathbf{c}_D \otimes \mathbf{c}_D\phi(\boldsymbol{\xi}_D)d\boldsymbol{\xi}_D \end{pmatrix} = \begin{pmatrix} \rho \\ \rho\mathbf{U}_D \\ E \\ \rho\Theta_D \end{pmatrix} \tag{C.2}$$

In this equation we consider that $\boldsymbol{\xi}_D$ and $\mathbf{c}_D$ have the dimension of the reduced velocity space ($= D$), Θ_D is the reduced pressure tensor of dimension $D\times D$ and that $\mathbf{m}_D(\boldsymbol{\xi}) = (1, \boldsymbol{\xi}_D, \frac{1}{2}|\boldsymbol{\xi}_D|^2, \mathbf{c}_D\otimes \mathbf{c}_D)^T$. Dimensions omitted are the reduced dimensions.

Let us find the expression of the corresponding equilibrium distribution functions $\mathcal{G}_\phi$ and $\mathcal{G}_{gred}$ defined as:

$$\begin{aligned}\mathcal{G}_\phi &= \int_{\mathbb{R}^{d-D}} \mathcal{G}_f \prod_{k=D+1,d} d\xi_k \\ \mathcal{G}_\psi &= \int_{\mathbb{R}^{d-D}} \frac{1}{2} \sum_{l=D+1,d} \xi_l^2 \mathcal{G}_f \prod_{k=D+1,d} d\xi_k\end{aligned} \tag{C.3}$$

We first rewrite the equilibrium distribution function as a product:

$$\mathcal{G}_f = \frac{\rho}{\sqrt{\det(2\pi\mathcal{T})}} \prod_{i,j=1}^{d} \exp\Big(- \frac{(\xi_i - U_i)(\xi_j - U_j)\mathcal{T}_{i,j}^{-1}}{2}\Big) \tag{C.4}$$

where ξ_k and U_k are the k-th component of the vectors $\boldsymbol{\xi}$ and $\mathbf{U}$ respectively. $\mathcal{T}^{-1}_{i,j}$ is the component (i,j) of the tensor $\mathcal{T}^{-1}$. Then the equilibrium distribution function $\mathcal{G}_\phi$ is:

$$\begin{aligned}\mathcal{G}_\phi =& \frac{\rho}{\sqrt{\det(2\pi\mathcal{T})}} \int_{\mathbb{R}^{d-D}} \prod_{i,j=1}^{d} \exp\Big(-\frac{(\xi_i - U_i)(\xi_j - U_j)\mathcal{T}^{-1}_{i,j}}{2}\Big) \prod_{k=D+1,d} d\xi_k \\ =& \frac{\rho}{\sqrt{\det(2\pi\mathcal{T})}} \prod_{i,j=1}^{D} \exp\Big(-\frac{(\xi_i - U_i)(\xi_j - U_j)\mathcal{T}^{-1}_{i,j}}{2}\Big) \\ & \times \int_{\mathbb{R}^{d-D}} \prod_{i,j=D+1}^{d} \exp\Big(-\frac{(\xi_i - U_i)(\xi_j - U_j)\mathcal{T}^{-1}_{i,j}}{2}\Big) \prod_{k=D+1,d} d\xi_k\end{aligned}$$

One important hypothesis in the reduced model for ES-BGK is that the constraints in the cross directions including a reduced dimensions are identically zero, meaning that for the tensor $\mathcal{T}$:

$$\mathcal{T}_{i,j} = \mathcal{T}_{i,j}\delta_{i,j} \qquad \text{for } i,j > D$$

In other words, the product under the integral is actually:

$$\prod_{i,j=D+1}^{d} \exp\Big(-\frac{(\xi_i - U_i)(\xi_j - U_j)\mathcal{T}^{-1}_{i,j}}{2}\Big) = \prod_{i=D+1}^{d} \exp\Big(-\frac{(\xi_i - U_i)^2}{2\mathcal{T}_{i,i}}\Big) \tag{C.5}$$

Then,

$$\begin{aligned}\mathcal{G}_\phi =& \frac{\rho}{\sqrt{\det(2\pi\mathcal{T})}} \prod_{i,j=1}^{D} \exp\Big(-\frac{(\xi_i - U_i)(\xi_j - U_j)\mathcal{T}^{-1}_{i,j}}{2}\Big) \prod_{k=D+1,d} \int_{\mathbb{R}} \exp\Big(-\frac{(\xi_k - U_k)^2}{2\mathcal{T}_{k,k}}\Big) d\xi_k \\ =& \frac{\rho}{\sqrt{\det(2\pi\mathcal{T})}} \prod_{k=D+1,d} \sqrt{2\pi\mathcal{T}_{k,k}} \prod_{i,j=1}^{D} \exp\Big(-\frac{(\xi_i - U_i)(\xi_j - U_j)\mathcal{T}^{-1}_{i,j}}{2}\Big)\end{aligned}$$

Let us denote by $\mathcal{T}_D$ the reduced tensor defined by $(\mathcal{T}_D)_{i,j} = \mathcal{T}_{i,j}$ for $i,j = 1,..,D$. Finally,

$$\mathcal{G}_\phi = \frac{\rho}{\sqrt{\det(2\pi\mathcal{T}_D)}} \prod_{i,j=1}^{D} \exp\Big(-\frac{(\xi_i - U_i)(\xi_j - U_j)\mathcal{T}^{-1}_{i,j}}{2}\Big) \tag{C.6}$$

Similarly to te BGK model, we can express the second equilibrium distribution function $\mathcal{G}_\psi$ with $\mathcal{G}_\phi$:

$$\mathcal{G}_\psi = \int_{\mathbb{R}^{d-D}} \frac{1}{2} \sum_{k=D+1,d} \xi_k^2 \mathcal{G}_f \prod_{l=D+1,d} d\xi_l$$

Using (C.4) and (C.5) we easily obtained that:

$$\begin{aligned}
\mathcal{G}_\psi =& \frac{\rho}{2\sqrt{\det(2\pi\mathcal{T})}} \prod_{i,j=1}^{D} \exp\Big(- \frac{(\xi_i - U_i)(\xi_j - U_j)\mathcal{T}^{-1}_{i,j}}{2}\Big) \\
& \times \sum_{k=D+1,d} \int_{\mathbb{R}^{d-D}} \xi_k^2 \prod_{l=D+1,d} \exp\Big(- \frac{(\xi_l - U_l)^2}{2\mathcal{T}_{l,l}}\Big) d\xi_l \\
=& \frac{\rho}{2\sqrt{\det(2\pi\mathcal{T})}} \prod_{i,j=1}^{D} \exp\Big(- \frac{(\xi_i - U_i)(\xi_j - U_j)\mathcal{T}^{-1}_{i,j}}{2}\Big) \sum_{k=D+1,d} \int_{\mathbb{R}} \xi_k^2 \exp\Big(- \frac{(\xi_k - U_k)^2}{2\mathcal{T}_{k,k}}\Big) d\xi_k \\
& \times \prod_{\substack{l=D+1,d \\ l\neq k}} \int_{\mathbb{R}} \exp\Big(- \frac{(\xi_l - U_l)^2}{2\mathcal{T}_{l,l}}\Big) d\xi_l \\
=& \frac{\rho}{2\sqrt{\det(2\pi\mathcal{T})}} \prod_{i,j=1}^{D} \exp\Big(- \frac{(\xi_i - U_i)(\xi_j - U_j)\mathcal{T}^{-1}_{i,j}}{2}\Big) \\
& \times \sum_{k=D+1,d} \sqrt{2\mathcal{T}_{k,k}} \int_{\mathbb{R}} (\sqrt{2\mathcal{T}_{k,k}}\alpha_k + U_k)^2 \exp(-\alpha_k^2) d\alpha_k \prod_{\substack{l=D+1 \\ l\neq k}}^{d} \sqrt{2\pi\mathcal{T}_{l,l}}
\end{aligned}$$

The same assumptions as in (A.9) can be done for the ES-BGK model (with $U_k = 0$):

$$\begin{aligned}
\int_{\mathbb{R}} (\sqrt{2\mathcal{T}_{k,k}}\alpha_k + U_k)^2 \exp\Big(- \alpha_k^2\Big) d\alpha_k =& 2\mathcal{T}_{k,k} \int_{\mathbb{R}} \alpha_k^2 \exp(-\alpha_k^2) d\alpha_k + \cancel{2\sqrt{2\mathcal{T}_{k,k}} U_k \int_{\mathbb{R}} \alpha_k \exp(-\alpha_k^2) d\alpha_k} \\
& + U_k^2 \cancel{\int_{\mathbb{R}} \exp(-\alpha_k^2) d\alpha_k} \\
=& \mathcal{T}_{k,k}\sqrt{\pi}
\end{aligned} \tag{C.7}$$

Finally we get the expression of $\mathcal{G}_\psi$:

$$\mathcal{G}_\psi = \frac{\sum_{k=D+1,d} \mathcal{T}_{k,k}}{2} \mathcal{G}_\phi \tag{C.8}$$

To compute $\sum_{k=D+1,d} \mathcal{T}_{k,k}$ in 2D, only $\mathcal{T}_{3,3}$ is necessary. With the definition of ψ and the assumption that $w = 0$ one can note that the pressure tensor is obtained as:

$$\begin{aligned}
\Theta_{3,3} &= \frac{1}{\rho} \int_{\mathbb{R}} (\xi_w - w)^2 f d\xi_w \\
&= \frac{1}{\rho} \int_{\mathbb{R}} \xi_w^2 f d\xi_w \\
&= \frac{1}{\rho} \int_{\mathbb{R}} 2\psi d\xi_w
\end{aligned} \tag{C.9}$$

$\mathcal{T}_{3,3}$ can be then computed as $\mathcal{T}_{3,3} = \frac{1}{Pr} T + (1 - \frac{1}{Pr})\Theta_{3,3}$

In 1D, one needs also $\mathcal{T}_{2,2}$ and (C.9) is no longer valid. However, only the sum $\mathcal{T}_{2,2} + \mathcal{T}_{3,3}$ is required. And we have:

$$\mathcal{T}_{2,2} + \mathcal{T}_{3,3} = \frac{2}{Pr} T + (1 - \frac{1}{Pr})(\Theta_{2,2} + \Theta_{3,3})$$

It is enough to compute $\Theta_{2,2} + \Theta_{3,3}$. In particular:

$$\begin{aligned}\Theta_{2,2} + \Theta_{3,3} &= \frac{1}{\rho}\Big(\int_{\mathbb{R}}((\xi_v - v)^2 + (\xi_w - w)^2) f d\xi_v d\xi_w\Big) \\ &= \frac{1}{\rho}\Big(\int_{\mathbb{R}}(\xi_v^2 + \xi_w^2) f d\xi_v d\xi_w\Big) \\ &= \frac{1}{\rho}\Big(\int_{\mathbb{R}} 2\psi d\xi_v d\xi_w\Big)\end{aligned} \tag{C.10}$$

The reduced Gaussian distribution functions can be computed exactly in 1D and 2D but in the first case, only the sum $\mathcal{T}_{2,2} + \mathcal{T}_{3,3}$ is known. Hence, it is impossible, with this reduced model to get the correct component $\Theta_{2,2}$ and $\Theta_{3,3}$ individually. A possible cure is the introduction of a third distribution function:

$$\begin{aligned}\phi_1 &= \int_{\mathbb{R}^2} f d\xi_v d\xi_w \\ \phi_2 &= \int_{\mathbb{R}^2} \frac{1}{2}\xi_v^2 f d\xi_v d\xi_w \\ \phi_3 &= \int_{\mathbb{R}^2} \frac{1}{2}\xi_w^2 f d\xi_v d\xi_w\end{aligned}$$

Appendix D

Discrete Gaussian Algorithm for the ES-BGK model

The algorithm to compute the discrete equilibrium distribution function is similar for the ES-BGK model but equations are added to conserve the pressure tensor. The collision invariant that we consider now is $\mathbf{m}(\boldsymbol{\xi}) = (1, \boldsymbol{\xi}, \frac{1}{2}|\boldsymbol{\xi}|^2, \mathbf{c} \otimes \mathbf{c})$.

We still look for a Gaussian distribution function under the form:

$$\mathcal{G}(\boldsymbol{\xi}) = \exp(\boldsymbol{\alpha} \cdot \mathbf{m}(\boldsymbol{\xi})) \tag{D.1}$$

Conserving the four first moments of the distribution function means that we are looking for $\boldsymbol{\alpha}$ such that:

$$\mathbf{F}(\boldsymbol{\alpha}) = \langle \exp(\boldsymbol{\alpha} \cdot \mathbf{m}(\boldsymbol{\xi})), \mathbf{m}(\boldsymbol{\xi}) \rangle - \underline{\boldsymbol{\rho}} = 0 \tag{D.2}$$

where now $\underline{\boldsymbol{\rho}} = (\rho, \rho\mathbf{U}, E, \rho\mathcal{T})^T$ obtained from

$$\langle f(\boldsymbol{\xi}), \mathbf{m}(\boldsymbol{\xi}) \rangle = \begin{pmatrix} \rho \\ \rho\mathbf{U} \\ E \\ \rho\Theta \end{pmatrix} \tag{D.3}$$

We recall that $\mathcal{T} = \frac{1}{Pr} TI + (1 - \frac{1}{Pr})\Theta$ in dimensionless form.

The energy being linked to the trace of the stress tensor, the system to solve in D.2 is not linearly independent. Thus, the equation on the energy is removed and for computational convenience, the system is rewritten with $\mathbf{m}(\boldsymbol{\xi}) = (1, \mathbf{c}, \mathbf{c} \otimes \mathbf{c})^T$ and then $\underline{\boldsymbol{\rho}} = (\rho, \mathbf{0}, \rho\mathcal{T})^T$.

In the continuous case, the vector $\boldsymbol{\alpha}_c$ verifying the conservation reads:

$$\boldsymbol{\alpha}_c = (\ln(\frac{\rho}{\sqrt{\det(2\pi\mathcal{T})}}), \mathbf{0}, -\frac{\mathcal{T}^{-1}_{i,j}}{1 + \delta_{i,j}}) \tag{D.4}$$

where $\mathcal{T}^{-1}_{i,j}$ is the term i, j of the symmetric tensor $\mathcal{T}^{-1}$.

For the reduced model, $\mathcal{T}_{3,3}$ is linearly independent on the other equations in 2D (respectively $\mathcal{T}_{2,2}$ and $\mathcal{T}_{3,3}$ in 1D) and it is assumed that the extra diagonal terms of the tensor $\mathcal{T}$ are zeros. Hence, the system to solve has three equations in 1D, six in 2D. There is no reduced model in 3D and the number of equations to solve is ten. The vector $\boldsymbol{\alpha}$ satisfying the conservation for

the reduced models are:

$$\boldsymbol{\alpha}_c = \Big(\ln(\frac{2\pi\rho\sqrt{\mathcal{T}_{2,2}\mathcal{T}_{3,3}}}{\sqrt{\det(2\pi\mathcal{T})}}), 0, -\frac{\mathcal{T}_{1,1}^{-1}}{2}\Big)^T \quad \text{in 1D}$$
$$\boldsymbol{\alpha}_c = \Big(\ln(\frac{\rho\sqrt{2\pi\mathcal{T}_{3,3}}}{\sqrt{\det(2\pi\mathcal{T})}}), \mathbf{0}, -\frac{\mathcal{T}_{i,j}^{-1}}{1+\delta_{i,j}}\Big)^T \quad \text{in 2D, for i,j=1,2}$$

These vectors are used as initial solution for the Newton-Raphson algorithm (algorithm 1).

For the reduced model with a trapezoidal quadrature rule, the Jacobian is computed as follows:

$$\begin{aligned}\frac{\partial F_i}{\partial \alpha_j} =& \frac{\partial}{\partial \alpha_j}\Big(\sum_{\boldsymbol{\xi}} \tilde{\mathcal{G}}_\phi \mathbf{m}_{D,i}(\boldsymbol{\xi})\Delta\boldsymbol{\xi} - \sum_{\boldsymbol{\xi}} f\mathbf{m}_{D,i}(\boldsymbol{\xi})\Delta\boldsymbol{\xi}\Big) \\ =& \sum_{\boldsymbol{\xi}} \mathbf{m}_{D,i}(\boldsymbol{\xi})\Delta\boldsymbol{\xi}\frac{\partial}{\partial\alpha_j}\tilde{\mathcal{G}}_\phi \\ =& \sum_{\boldsymbol{\xi}} \mathbf{m}_{D,i}(\boldsymbol{\xi})\Delta\boldsymbol{\xi}\mathbf{m}_{D,j}\exp(\boldsymbol{\alpha}\cdot\mathbf{m}_D(\boldsymbol{\xi}))\end{aligned} \tag{D.5}$$

with similar notations than for the BGK algorithm. $\mathbf{m}_D$ is the collision invariant of the reduced model in dimension D, meaning

$$\mathbf{m}_D = (1, (\xi_u - u), (\xi_v - v), (\xi_u - u)^2, (\xi_v - v)^2, (\xi_u - u)(\xi_v - v))^T$$

$\mathbf{m}_{D,i}$ is its i-th component. $\tilde{\mathcal{G}}_\phi$ is the discrete equilibrium distribution function for the first equation of the reduced model. The second discrete equilibrium distribution function $\tilde{\mathcal{G}}_\psi$ is recovered as:

$$\begin{aligned}\tilde{\mathcal{G}}_\psi &= \frac{\mathcal{T}_{2,2}+\mathcal{T}_{3,3}}{2}\tilde{\mathcal{G}}_\phi \qquad \text{in 1D} \\ \tilde{\mathcal{G}}_\psi &= \frac{1}{2}\mathcal{T}_{3,3}\tilde{\mathcal{G}}_\phi \qquad \text{in 2D}\end{aligned} \tag{D.6}$$

Bibliography

[1] Alaia, A. *A Time Dependent Domain Decomposition Method for a Multi-scale Hydrodynamic-Kinetic System of Equations.* PhD thesis, Politecnico di Torino, 2011. (Cited on pages 11, 13, and 16.)

[2] Alaia, A., and Puppo, G. A hybrid method for hydrodynamic-kinetic flow - Part II - Coupling of hydrodynamic and kinetic models. *Journal of Computational Physics 231*, 16 (June 2012), 5217–5242. (Cited on page 121.)

[3] Andries, P., Bourgat, J.-F., Le Tallec, P., and Perthame, B. Numerical comparison between the Boltzmann and ES-BGK models for rarefied gases. *Computer Methods in Applied Mechanics and Engineering 191*, 31 (May 2002), 3369–3390. (Cited on pages 23, 156, and 170.)

[4] Andries, P., and Perthame, B. The ES-BGK model equation with correct Prandtl number. *22nd International Symposium on Rarefied Gas Dynamics. AIP Conference Proceeding 585* (2001), 30. (Cited on page 23.)

[5] Angot, P., Bruneau, C.-H., and Fabrie, P. A penalization method to take into account obstacles in incompressible viscous flows. *Numerische Mathematik 81*, 4 (1999), 497–520. (Cited on page 46.)

[6] Ascher, U. M., Ruuth, S. J., and Spiteri, R. J. Implicit-explicit Runge-Kutta methods for time-dependent partial differential equations. *Applied Numerical Mathematics. An IMACS Journal 25*, 2-3 (1997), 151–167. (Cited on pages 34, 157, and 171.)

[7] Baer, M., and Nunziato, J. A two-phase mixture theory for the deflagration-to-detonation transition (DDT) in reactive granular materials. *International Journal of Multiphase Flow 12*, 6 (1986), 861–889. (Cited on page 101.)

[8] Baranger, C., Boudin, L., Jabin, P.-E., and Mancini, S. A modeling of biospray for the upper airways. *ESAIM: Proceedings 14* (2005), 41–47. (Cited on page 101.)

[9] Baranger, C., Claudel, J., Hérouard, N., and Mieussens, L. Locally Refined Discrete Velocity Grid for Deterministic Rarefied Flow Simulations. In *AIP Conference Proceedings* (2014), AIP, pp. 389–396. (Cited on pages 73 and 123.)

[10] Beale, J. T., and Majda, A. Vortex methods. I. Convergence in three dimensions. *Mathematics of Computation 39*, 159 (1982), 1–27. (Cited on page 105.)

[11] Bennoune, M., Lemou, M., and Mieussens, L. Uniformly stable numerical schemes for the Boltzmann equation preserving the compressible Navier–Stokes asymptotics. *Journal of Computational Physics 227*, 8 (Apr. 2008), 3781–3803. (Cited on page 34.)

[12] Bernard, F., Iollo, A., and Puppo, G. A Local Velocity Grid Approach for BGK Equation. *Communications in Computational Physics 16*, 4 (2014), 956–982. (Cited on page 73.)

[13] Bernard, F., Iollo, A., and Puppo, G. Simulation of Diluted Flow Regimes in Presence of Unsteady Boundaries. In *Finite Volumes for Complex Applications VII-Elliptic, Parabolic and Hyperbolic Problems*. Springer, 2014, pp. 801–808. (Cited on page 39.)

[14] Bernard, F., Iollo, A., and Puppo, G. Accurate Asymptotic Preserving Boundary Conditions for Kinetic Equations on Cartesian Grids. *Journal of Scientific Computing* (Jan. 2015). (Cited on page 39.)

[15] Bhatnagar, P. L., Gross, E. P., and Krook, M. A Model for Collision Processes in Gases. I. Small Amplitude Processes in Charged and Neutral One-Component Systems. *Phys. Rev. 94* (May 1954), 511–525. (Cited on pages 9, 19, 154, 156, 168, and 169.)

[16] Bird, G. A. *Molecular Gas Dynamics and the Direct Simulation of Gas Flows*. Oxford engineering science series. Clarendon Press, 1994. (Cited on pages 8, 11, 19, 25, 62, 73, 122, 154, and 168.)

[17] Boiron, O., Chiavassa, G., and Donat, R. A high-resolution penalization method for large Mach number flows in the presence of obstacles. *Computers and Fluids 38*, 3 (Mar. 2009), 703–714. (Cited on page 46.)

[18] Borgnakke, C., and Larsen, P. S. Statistical collision model for Monte Carlo simulation of polyatomic gas mixture. *Journal of Computational Physics 18* (Aug. 1975), 405–420. (Cited on page 18.)

[19] Bouchut, F., and Perthame, B. A BGK model for small Prandtl number in the Navier-Stokes approximation. *Journal of Statistical Physics 71*, 1-2 (1993), 191–207. (Cited on page 22.)

[20] Boudet, J. F., Amarouchene, Y., and Kellay, H. Shock Front Width and Structure in Supersonic Granular Flows. *Physical Review Letters 101*, 25 (Dec. 2008). (Cited on page 116.)

[21] Boudet, J. F., and Kellay, H. Drag Coefficient for a Circular Obstacle in a Quasi-Two-Dimensional Dilute Supersonic Granular Flow. *Physical Review Letters 105*, 10 (Aug. 2010). (Cited on pages 102 and 122.)

[22] Boudin, L., Boutin, B., Fornet, B., Goudon, T., Lafitte, P., Lagoutière, F., and Merlet, B. Fluid-particles flows: a thin spray model with energy exchanges, 2009. (Cited on pages 105 and 116.)

[23] Brull, S., and Mieussens, L. Local discrete velocity grids for deterministic rarefied flow simulations. *Journal of Computational Physics 266*, C (June 2014), 22–46. (Cited on pages 73 and 123.)

[24] Cabannes, H., Gatignol, R., and Luol, L.-S. The discrete Boltzmann equation. *Lecture Notes at University of California, Berkley* (Jan. 1980), 1–65. (Cited on page 28.)

[25] Carrillo, J.-A., Goudon, T., and Lafitte, P. Simulation of fluid and particles flows: Asymptotic preserving schemes for bubbling and flowing regimes. *Journal of Computational Physics 227*, 16 (Aug. 2008), 7929–7951. (Cited on pages 102 and 123.)

[26] Cercignani, C. *The Boltzmann Equation and Its Applications*. Springer-Verlag GmbH, 1988. (Cited on pages 11, 13, 15, 17, and 41.)

[27] Cercignani, C., Illner, R., and Pulvirenti, M. *The Mathematical Theory of Dilute Gases*. No. v. 106 in Applied Mathematical Sciences Series. Springer-Verlag GmbH, 1994. (Cited on pages 11 and 14.)

[28] Chakravarthy, S., and Osher, S. High resolution applications of the Osher upwind scheme for the Euler equations. In *Fluid Dynamics and Co-located Conferences*. American Institute of Aeronautics and Astronautics, Jan. 2014. (Cited on page 33.)

[29] Chapman, S., and Cowling, T. *The Mathematical Theory of Non-uniform Gases: An Account of the Kinetic Theory of Viscosity, Thermal Conduction and Diffusion in Gases*. Cambridge Mathematical Library. Cambridge University Press, 1970. (Cited on pages 17, 19, 156, and 170.)

[30] Charles, F. *Modélisation mathématique et étude numérique d'un aérosol. Application à la simulation du transport de particules de poussière en cas d'accident de perte de vide dans ITER.* PhD thesis, École Normale Supérieure de Cachan - ENS Cachan, 2009. (Cited on pages 103, 106, and 123.)

[31] Chatelain, P., Curioni, A., Bergdorf, M., Rossinelli, D., Andreoni, W., and Koumoutsakos, P. Billion vortex particle direct numerical simulations of aircraft wakes. *Computer Methods in Applied Mechanics and Engineering 197*, 13-16 (Feb. 2008), 1296–1304. (Cited on page 105.)

[32] Chen, S., Xu, K., Lee, C., and Cai, Q. A unified gas kinetic scheme with moving mesh and velocity space adaptation. *Journal of Computational Physics 231*, 20 (Aug. 2012), 6643–6664. (Cited on pages 34, 62, 73, and 122.)

[33] Chu, C. K. Kinetic-theoretic description of the formation of a shock wave. *Phys. Fluids 8* (1965), 12–22. (Cited on pages 21 and 125.)

[34] Cisternino, M., and Weynans, L. A Parallel Second Order Cartesian Method for Elliptic Interface Problems. *Communications in Computational Physics 12*, 5 (NOV 2012), 1562–1587. (Cited on page 46.)

[35] Cottet, G., and Koumoutsakos, P. *Vortex Methods: Theory and Practice*. Cambridge University Press, 2000. (Cited on pages 104 and 105.)

[36] Cottet, G.-H., and Maitre, E. A level set method for fluid-structure interactions with immersed surfaces. *Mathematical models and methods in applied sciences 16*, 03 (2006), 415–438. (Cited on page 104.)

[37] Cottet, G.-H., and Weynans, L. Particle methods revisited: a class of high order finite-difference methods. *Comptes Rendus Mathematique 343*, 1 (July 2006), 51–56. (Cited on page 105.)

[38] Dechriste, G., and Mieussens, L. AIP Conference Proceedings. In *PROCEEDINGS OF THE 29TH INTERNATIONAL SYMPOSIUM ON RAREFIED GAS DYNAMICS* (2014), AIP Publishing LLC, pp. 988–994. (Cited on page 46.)

[39] Dettleff, G., and Grabe, M. Basics of Plume Impingement Analysis for Small Chemical and Cold Gas Thrusters. *Models and Computational Methods for Rarefied Flows, AVT- 194 RTO AVT/VKI, Rhode St. Genese, Belgium* (2011). (Cited on pages 7, 8, 120, 121, 122, and 149.)

[40] Dimarco, G., and Pareschi, L. Exponential Runge-Kutta methods for stiff kinetic equations. *SIAM Journal on Numerical Analysis 49*, 5 (2011), 2057–2077. (Cited on page 34.)

[41] Doisneau, F., Laurent, F., Murrone, A., Dupays, J., and Massot, M. Eulerian multi-fluid models for the simulation of dynamics and coalescence of particles in solid propellant combustion. *Journal of Computational Physics 234*, C (Feb. 2013), 230–262. (Cited on page 101.)

[42] Dukowicz, J. K. A particle-fluid numerical model for liquid sprays. *Journal of Computational Physics 35*, 2 (1980), 229–253. (Cited on page 102.)

[43] Einstein, A. On the movement of small particles suspended in stationary liquids required by the molecular-kinetic theory of heat. *Annalen der Physik 17*, 549-560 (1905), 16. (Cited on pages 116 and 122.)

[44] Enright, D., Fedkiw, R., Ferziger, J., and Mitchell, I. A Hybrid Particle Level Set Method for Improved Interface Capturing. *Journal of Computational Physics 183*, 1 (Nov. 2002), 83–116. (Cited on page 104.)

[45] Evans, M. W., Harlow, F. H., and Bromberg, E. The Particle-in-cell Method for Hydrodynamic Calculatons. Tech. rep., Los Alamos Scientific Laboratory, 1957. (Cited on page 103.)

[46] Farjoun, Y., and Seibold, B. An exactly conservative particle method for one dimensional scalar conservation laws. *Journal of Computational Physics 228*, 14 (Aug. 2009), 5298–5315. (Cited on page 105.)

[47] Fedkiw, R. P. Coupling an Eulerian fluid calculation to a Lagrangian solid calculation with the ghost fluid method. *Journal of Computational Physics 175*, 1 (2002), 200–224. (Cited on page 46.)

[48] Fedkiw, R. P., Aslam, T., Merriman, B., and Osher, S. A non-oscillatory Eulerian approach to interfaces in multimaterial flows (the ghost fluid method). *Journal of Computational Physics 152*, 2 (1999), 457–492. (Cited on page 46.)

[49] Ferrari, E., and Pareschi, L. Modelling and numerical methods for the dynamics of impurities in a gas. *International Journal for Numerical Methods in Fluids 57*, 6 (2006), 693–713. (Cited on page 102.)

[50] Filbet, F., and Jin, S. A class of asymptotic-preserving schemes for kinetic equations and related problems with stiff sources. *Journal of Computational Physics 229*, 20 (Oct. 2010), 7625–7648. (Cited on page 34.)

[51] Filbet, F., and Jin, S. An Asymptotic Preserving Scheme for the ES-BGK Model of the Boltzmann Equation. *Journal of Scientific Computing 46*, 2 (June 2010), 204–224. (Cited on page 35.)

[52] Filbet, F., and Sonnendrücker, E. Comparison Of Eulerian Vlasov Solvers. *Comput. Phys. Commun. 150*, IRMA-2001-035. 3 (2001), 247–266. (Cited on page 105.)

[53] Filbet, F., and Yang, C. An inverse Lax-Wendroff method for boundary conditions applied to Boltzmann type models. *Journal of Computational Physics 245*, C (July 2013), 43–61. (Cited on page 39.)

[54] Gibou, F., Fedkiw, R. P., Cheng, L.-T., and Kang, M. A second-order-accurate symmetric discretization of the Poisson equation on irregular domains. *Journal of Computational Physics 176*, 1 (2002), 205–227. (Cited on page 46.)

[55] Gidaspow, D. Hydrodynamics of fiuidizatlon and heat transfer: Supercomputer modeling. *Applied Mechanics Reviews 39*, 1 (1986), 1–23. (Cited on page 101.)

[56] Gingold, R. A., and Monaghan, J. J. Smoothed particle hydrodynamics - Theory and application to non-spherical stars. *Monthly Notices of the Royal Astronomical Society 181* (Nov. 1977), 375–389. (Cited on page 104.)

[57] Giovangigli, V. *Multicomponent Flow Modeling*. Modeling and Simulation in Science, Engineering and Technology. Birkhäuser Boston, 1999. (Cited on page 18.)

[58] Glass, J. N. M. C. E., and Greenez, F. A. DSMC simulations of Apollo capsule aerodynamics for hypersonic rarefied conditions. *AIAA paper* (2006). (Cited on pages 93, 95, and 96.)

[59] Glimm, J., Grove, J. W., Li, X., and Tan, D. C. Robust computational algorithms for dynamic interface tracking in three dimensions. *SIAM Journal on Scientific Computing 21*, 6 (2000), 2240–2256. (Cited on page 40.)

[60] Goodman, F. *Dynamics of Gas-Surface Scattering*. Elsevier Science, 2012. (Cited on page 41.)

[61] Gorsse, Y., Iollo, A., Telib, H., and Weynans, L. A simple second order cartesian scheme for compressible Euler flows. *Journal of Computational Physics 231*, 23 (Oct. 2012), 7780–7794. (Cited on pages 46 and 121.)

[62] Harlow, F. H., and Amsden, A. A. Numerical calculation of multiphase fluid flow. *Journal of Computational Physics 17* (Jan. 1975), 19–52. (Cited on page 102.)

[63] Hirt, C. W., and Nichols, B. D. Volume of fluid (VOF) method for the dynamics of free boundaries. *Journal of Computational Physics 39* (Jan. 1981), 201–225. (Cited on page 40.)

[64] Holway, L. H. Kinetic Theory of Shock Structure Using an Ellipsoidal Distribution Function. In *Rarefied Gas Dynamics, Volume 1* (1965), J. H. D. Leeuw, Ed., pp. 193+. (Cited on pages 9, 23, 154, 156, 168, and 170.)

[65] Holway, L. H. New Statistical Models for Kinetic Theory: Methods of Construction. *Physics of Fluids 9*, 9 (1966), 1658. (Cited on pages 9, 23, 154, 156, 168, and 170.)

[66] Hotchkiss, R., and Hirt, C. Particulate transport in highly distorted three-dimensional flow fields. Tech. rep., Los Alamos Scientific Lab., Oct 1972. (Cited on page 101.)

[67] Hu, X. Y., Khoo, B. C., Adams, N. A., and Huang, F. L. A conservative interface method for compressible flows. *Journal of Computational Physics 219*, 2 (Dec. 2006), 553–578. (Cited on page 46.)

[68] Ingram, D. M., Causon, D. M., and Mingham, C. G. Developments in Cartesian cut cell methods. *Mathematics and Computers in Simulation 61*, 3-6 (2003), 561–572. (Cited on page 46.)

[69] Jiang, G.-S., and Shu, C.-W. Efficient Implementation of Weighted ENO Schemes. *Journal of Computational Physics 126*, 1 (June 1996), 202–228. (Cited on page 41.)

[70] Jin, S. Efficient asymptotic-preserving (AP) schemes for some multiscale kinetic equations. *SIAM Journal on Scientific Computing 21*, 2 (1999), 441–454. (Cited on page 34.)

[71] Jin, S. Asymptotic preserving (AP) schemes for multiscale kinetic and hyperbolic equations: a review. *Rivista di Matematica della Università di Parma. Serie 7 3*, 2 (2012), 177–216. (Cited on pages 33, 34, 39, and 149.)

[72] Jin, S., Pareschi, L., and Toscani, G. Diffusive relaxation schemes for multiscale discrete-velocity kinetic equations. *SIAM Journal on Numerical Analysis 35*, 6 (1998), 2405–2439. (Cited on page 34.)

[73] Kennedy, C. A., and Carpenter, M. H. Additive Runge-Kutta schemes for convection-diffusion-reaction equations. *Applied Numerical Mathematics 44*, 1-2 (Jan. 2003), 139–141. (Cited on page 34.)

[74] Khadra, K., Angot, P., Parneix, S., and Caltagirone, J.-P. Fictitious domain approach for numerical modelling of Navier-Stokes equations. *International Journal of Numerical Methods in Fluids 34*, 8 (Dec. 2000), 651–684. (Cited on page 46.)

[75] Koumoutsakos, P., and Leonard, A. High-resolution simulations of the flow around an impulsively started cylinder using vortex methods. *Journal of Fluid Mechanics 296* (1995), 1–38. (Cited on page 104.)

[76] Krasny, R. A study of singularity formation in a vortex sheet by the point-vortex approximation. *Journal of Fluid Mechanics 167* (1986), 65–93. (Cited on page 106.)

[77] Lagaert, J.-B., Balarac, G., Cottet, G.-H., and Bégou, P. Particle method: an efficient tool for direct numerical simulations of a high Schmidt number passive scalar in turbulent flow. *Proceedings of the Summer Program 2012* (2012), 167–176. (Cited on page 107.)

[78] Latvala, E. K., and Anderson, T. P. Experimental Determination of Jet Spreading From Supersonic Nozzles at High Altitudes. Tech. rep., Arnold Engineering Development Center, 1959. (Cited on pages 64, 65, and 123.)

[79] Latvala, E. K., and Anderson, T. P. Studies of the Spreading of Rocket Exhaust Jets at High Altitudes. *Planetary and Space Science 4* (Jan. 1961), 77–91. (Cited on pages 64, 122, and 123.)

[80] Leveque, R. J., and Li, Z. The immersed interface method for elliptic equations with discontinuous coefficients and singular sources. *SIAM Journal on Numerical Analysis 31*, 4 (1994), 1019–1044. (Cited on page 46.)

[81] Liu, Q., and Vasilyev, O. V. A Brinkman penalization method for compressible flows in complex geometries. *Journal of Computational Physics 227*, 2 (Dec. 2007), 946–966. (Cited on page 46.)

[82] Lucy, L. B. A numerical approach to the testing of the fission hypothesis. *Astronomical Journal 82* (Dec. 1977), 1013–1024. (Cited on page 104.)

[83] Magni, A. *Méthodes particulaires avec remaillage: analyse numérique nouveaux schémas et applications pour la simulation d'équations de transport.* PhD thesis, Université de Grenoble, 2011. (Cited on page 107.)

[84] Mathiaud, J. *Étude de systèmes de type gaz-particules.* PhD thesis, École Normale Superieure de Cachan - ENS Cachan, 2006. (Cited on page 102.)

[85] Mieussens, L. Discrete-Velocity Models and Numerical Schemes for the Boltzmann-BGK Equation in Plane and Axisymmetric Geometries. *Journal of Computational Physics 162*, 2 (Aug. 2000), 429–466. (Cited on pages 20 and 28.)

[86] Mittal, R., and Iaccarino, G. Immersed Boundary Methods. *Annual review of fluid mechanics 37*, 1 (Jan. 2005), 239–261. (Cited on page 46.)

[87] Mohd-Yusof, J. Combined immersed-boundary/B-spline methods for simulations of fow in complex geometries. *Center for Turbulence Research Annual Research Briefs* (1997). (Cited on page 46.)

[88] Monaghan, J. J. Smoothed particle hydrodynamics. *Reports on Progress in Physics 68*, 8 (July 2005), 1703–1759. (Cited on page 104.)

[89] Nordsieck, A., and Hicks, B. L. Monte Carlo evaluation of the Boltzmann collision integral. In *Rarefied Gas Dynamics, Volume 1* (1967), p. 695. (Cited on page 8.)

[90] Osher, S., and Fedkiw, R. P. Level Set Methods: An Overview and Some Recent Results. *Journal of Computational Physics 169*, 2 (May 2001), 463–502. (Cited on page 40.)

[91] Osher, S., and Sethian, J. A. Fronts propagating with curvature-dependent speed : Algorithms based on hamilton jacobi formulations. *Journal of Computational Physics 79*, 12 (1988), 12–49. (Cited on page 40.)

[92] Østmo, S., Frezzotti, A., and Ytrehus, T. Kinetic theory study of steady evaporation from a spherical condensed phase containing inert solid particles. *Physics of Fluids 9*, 1 (1997), 211. (Cited on pages 102 and 105.)

[93] Owen, J. P., and Ryu, W. S. The effects of linear and quadratic drag on falling spheres: an undergraduate laboratory. *European Journal of Physics 26*, 6 (Sept. 2005), 1085–1091. (Cited on page 105.)

[94] Pareschi, L., and Russo, G. Implicit–Explicit Runge–Kutta Schemes and Applications to Hyperbolic Systems with Relaxation. *Journal of Scientific Computing 25*, 1 (Oct. 2005), 129–155. (Cited on page 34.)

[95] Pareschi, L., and Russo, G. Efficient asymptotic preserving deterministic methods for the Boltzmann equation. *Models and Computational Methods for Rarefied Flows, AVT-194 RTO AVT/VKI, Rhode St. Genese, Belgium* (2011). (Cited on page 34.)

[96] Peskin, C. S. Flow patterns around heart valves: A numerical method. *Journal of Computational Physics 10*, 2 (1972), 252 – 271. (Cited on page 46.)

[97] Pieraccini, S., and Puppo, G. Implicit–Explicit schemes for BGK kinetic equations. *Journal of Scientific Computing 32*, 1 (2007), 1–28. (Cited on page 35.)

[98] Pieraccini, S., and Puppo, G. Microscopically implicit-macroscopically explicit schemes for the BGK equation. *Journal of Computational Physics* (2011). (Cited on page 34.)

[99] Ploumhans, P., Daeninck, G., and Winckelmans, G. Simulation of three-dimensional bluff-body flows using the vortex particle and boundary element methods. *Flow, turbulence and combustion 73*, 2 (2004), 117–131. (Cited on page 104.)

[100] Rider, W. J., and Kothe, D. B. Reconstructing Volume Tracking. *Journal of Computational Physics 141*, 2 (Apr. 1998), 112–152. (Cited on page 40.)

[101] Roe, P. L. Characteristic-based schemes for the Euler equations. *Annual review of fluid mechanics 18* (Sept. 1986), 337–365. (Cited on page 33.)

[102] Rosenhead, L. The Formation of Vortices from a Surface of Discontinuity. In *Proceedings of the Royal Society of London. Series A* (Nov. 1931), pp. 170–192. (Cited on page 103.)

[103] Saurel, R., and Abgrall, R. A simple method for compressible multifluid flows. *SIAM Journal on Scientific Computing 21*, 3 (1999), 1115–1145 (electronic). (Cited on page 40.)

[104] Seo, J. H., and Mittal, R. A sharp-interface immersed boundary method with improved mass conservation and reduced spurious pressure oscillations. *Journal of Computational Physics 230*, 19 (Aug. 2011), 7347–7363. (Cited on page 46.)

[105] Sethian, J. A. Fast Marching Methods. *SIAM Review 41* (Jan. 1999), 199–235. (Cited on page 41.)

[106] Shakhov, E. Generalization of the Krook kinetic relaxation equation. *Fluid Dynamics 3*, 5 (1968), 95–96. (Cited on page 22.)

[107] Shapiro, A. *The Dynamics and Thermodynamics of Compressible Fluid Flow*. Ronald Press, 1953. (Cited on page 59.)

[108] Sone, Y. *Kinetic Theory and Fluid Dynamics*. Modeling and Simulation in Science, Engineering and Technology. Birkhäuser Boston, 2002. (Cited on page 11.)

[109] Strang, G. On the construction and comparison of difference schemes. *SIAM Journal on Numerical Analysis 5*, 3 (1968), 506–517. (Cited on page 109.)

[110] Struchtrup, H. The BGK-model with velocity-dependent collision frequency. *Continuum Mechanics and Thermodynamics 9*, 1 (1997), 23–31. (Cited on page 22.)

[111] Van Leer, B. Towards the ultimate conservative difference scheme. II. Monotonicity and conservation combined in a second-order scheme. *Journal of Computational Physics 14*, 4 (1974), 361–370. (Cited on page 33.)

[112] Van Leer, B. Towards the ultimate conservative difference scheme. V. A second-order sequel to Godunov's method. *Journal of Computational Physics 32*, 1 (1979), 101–136. (Cited on page 33.)

[113] Villani, C. Mathematics of Granular Materials. *Journal of Statistical Physics 124*, 2 (Aug. 2006), 781–822. (Cited on page 18.)

[114] Woodward, P., and Colella, P. The numerical simulation of two-dimensional fluid flow with strong shocks. *Journal of Computational Physics (ISSN 0021-9991) 54* (Apr. 1984), 115–173. (Cited on page 77.)

[115] Xu, K., and Huang, J.-C. A unified gas-kinetic scheme for continuum and rarefied flows. *Journal of Computational Physics 229*, 20 (Oct. 2010), 7747–7764. (Cited on pages 34 and 73.)

[116] Xu, S., and Wang, Z. J. An immersed interface method for simulating the interaction of a fluid with moving boundaries. *Journal of Computational Physics 216*, 2 (Aug. 2006), 454–493. (Cited on page 46.)

[117] Yang, G., Causon, D., Ingram, D., Saunders, R., and Batten, P. A cartesian cut cell method for compressible flows. part a. static body problems. *Aeronaut. J. 101* (1997), 47–56. (Cited on page 46.)

List of Figures

Schémas préservant la limite asymptotique pour les modèles BGK et ES-BGK sur grilles cartésiennes

Contents

Introduction

Une particularité des écoulements complexes, comme par exemple dans le cas de pompes à vide ou de rentrées hypersonique de véhicules dans l'atmosphère, est la coexistence de deux types de régimes : le régime raréfié et le régime hydrodynamique. Le régime raréfié se caractérise par une distance importante entre les molécules de gaz comparée à une distance caractéristique de l'écoulement. On trouve aussi ce genre de régime dans des microsystèmes électromécaniques où la longueur caractéristique du système est très faible. Le comportement microscopique des molécules peut alors largement différer du comportement moyen (macroscopique) de l'écoulement. Dans le cas contraire, le régime est qualifié d'hydrodynamique ou continue.

L'objectif de cette thèse est de simuler des écoulements pouvant mêler ces deux types de régime. La réalisation d'expériences dans des cas industriels tels que les rentrées atmosphériques

de capsules étant très difficile en conditions réelles due aux très haute vitesses et faible pression mises en jeu, la simulation numérique revêt une importance particulière. Il est alors crucial que la modélisation numérique de ces phénomènes assurent une transition correcte de la solution d'un régime à l'autre. Cette propriété de préservation de l'asymptotique doit être également respectée en présence de solides immergés. Dans cette thèse, nous allons considérer différent type de géométries allant d'objets fixes (marche, Blunt body) à des objets mobiles ou déformables (capsule, jet de tuyère). Les méthodes et schémas développés devront également être adaptable à un environnement HPC (High Parallel Computing) afin de réduire au maximum le coût de calcul.

Deux cas test réalistes vont être étudiés plus particulièrement : le transport de particules dans un jet de tuyère de satellite en milieu raréfié et la rentrée atmosphérique d'une capsule. Le premier cas test est inspiré d'expériences révélant qu'après l'allumage d'un moteur en milieu raréfié, des poussières viennent polluer un bouclier placé à l'avant du moteur. En conditions réelles, ce bouclier est remplacé par des dispositifs optiques qui sont alors endommagés ou rendus inutilisables.

Du point de vue de la modélisation numérique, les équations classiques de la mécanique des fluides comme les équations de Navier-Stokes ou d'Euler compressible ne décrivent pas correctement la dynamique d'un écoulement en régime raréfié à cause de leur approche macroscopique. Une approche statistique est alors plus appropriée en considérant l'état thermodynamique des molécules de gaz à travers une fonction de distribution. Cette fonction de distribution représente la densité de molécules de gaz en un point de l'espace de dimension D et ayant une certaine vitesse microscopique à un temps donné. Un espace des vitesses microscopiques de dimension d est introduit. L'évolution temporelle de cette fonction de distribution est régie par l'équation de Boltzmann. Deux phénomènes physiques sont considérés : la conservation de la masse dans l'espace des phases et les collisions entre les molécules de gaz. Le grand nombre de variables indépendantes rend l'équation très couteuse à résoudre (En 3D, trois variables d'espace, trois variables de vitesse plus le temps). Une méthode très répandue pour résoudre cette équation utilise une approche Monte Carlo sur un nombre choisi de molécules et considérant les collisions d'un certain nombre de molécules. Cette méthode connue sous le nom de "Direct Simulation Monte Carlo" (DSMC, [16]) est très efficace en régime très raréfié mais est difficilement applicable pour des gaz denses car elle est basée sur l'hypothèse de chaos moléculaires. Du fait de l'approche probabiliste elle génère également du bruit stochastique.

La résolution de l'équation de Boltzmann en utilisant des modèles déterministes ne souffre pas de ces inconvénients. Nous allons ici nous concentrer sur deux de ces modèles : le modèle BGK [15] et le modèle ES-BGK [64], [65]. Ils sont résolus avec une méthode aux vitesses discrètes ("Discrete Velocity Method", DVM) introduisant une discrétisation de l'espace des vitesses microscopiques. Après une brève présentation de ces modèles et des schémas numériques utilisés, nous nous intéresserons à la préservation de la limite asymptotique vers les équations d'Euler et, en particulier, nous proposerons une condition de paroi permettant une transition continue entre le régime raréfié et le régime hydrodynamique dans le cas de solides immergés. Nous proposerons ensuite différentes techniques réduisant le coût de calcul afin de permettre des simulations d'écoulements 3D avec des géométries mobiles. Les schémas sur grilles cartésiennes étant particulièrement adaptés au calcul parallèle, nous opterons pour ce type de grille. Enfin, nous introduirons un modèle de transport de particules ainsi qu'une méthode de résolution afin de traiter le cas du jet d'un tuyère en milieu raréfié et de la pollution des dispositifs optiques.

I Les modèles cinétiques

Dans cette section, nous allons introduire l'équation de Boltzmann qui permet la résolution d'écoulements dans le régime hydrodynamique mais aussi dans le régime raréfié. Ensuite, deux modèles utilisés dans ce travail vont être présenter.

I.1 L'équation de Boltzmann

Un indicateur pour définir si un écoulement peut être qualifié de raréfié ou non est le nombre de Knudsen Kn. Il est défini comme le rapport entre le libre parcours moyen entre les molécules de gaz λ et une longueur caractéristique de l'écoulement L :

$$Kn = \frac{\lambda}{L} \tag{I.1}$$

Si le nombre de Knudsen est petit ($< 10^{-2}$), le régime est dit hydrodynamique et les équations classiques de la mécanique des fluides (Euler, Navier-Stokes) peuvent être utilisées. Si il est grand, ces équations ne sont plus valables. L'équation valide pour tout les types de régimes est l'équation de Boltzmann :

$$\frac{\partial f}{\partial t} + \boldsymbol{\xi} \cdot \nabla_{\mathbf{x}} f + \mathbf{a} \cdot \nabla_{\boldsymbol{\xi}} f = Q(f, f) \tag{I.2}$$

où f est la fonction de distribution de densité dépendant du temps t, de la position $\mathbf{x} = (x, y, z)^T$, et de la vitesse microscopique $\boldsymbol{\xi} = (\xi_u, \xi_v, \xi_w)^T$. Q est l'opérateur de collision.

Les quantités macroscopiques caractérisant l'écoulement telles que la densité ρ, la vitesse $\mathbf{U} = (u, v, w)^T$ et l'énergie E sont calculées à partir des moments de la fonction de distribution f :

$$\begin{pmatrix} \rho(\mathbf{x},t) \\ \rho(\mathbf{x},t)\mathbf{U}(\mathbf{x},t) \\ E(\mathbf{x},t) \end{pmatrix} = \int_{\mathbb{R}^d} f(\mathbf{x},\boldsymbol{\xi},t)\mathbf{m}(\boldsymbol{\xi})d\boldsymbol{\xi} \quad \text{avec} \quad \mathbf{m}(\boldsymbol{\xi}) = \begin{pmatrix} 1 \\ \boldsymbol{\xi} \\ \frac{1}{2} \mid \boldsymbol{\xi} \mid^2 \end{pmatrix} \tag{I.3}$$

L'énergie totale E peut également être calculée à partir de la température T :

$$E(\mathbf{x},t) = \frac{d}{2}\rho(\mathbf{x},t)RT(\mathbf{x},t) + \frac{1}{2}\rho(\mathbf{x},t) \mid \mathbf{U}(\mathbf{x},t) \mid^2 \tag{I.4}$$

R est la constante spécifique du gaz qui peut s'exprimer en fonction de la constant universel des gaz $\mathcal{R}$ et de la masse molaire $\mathcal{M}$ du gaz :

$$R = \frac{\mathcal{R}}{\mathcal{M}}$$

Ici nous considérons également un gaz monoatomique pour lequel $d = 3$ et dont le ratio de chaleur spécifique est :

$$\gamma = 1 + \frac{2}{d} = \frac{5}{3}$$

Les moments d'ordre supérieur donnent le tenseur des contraintes Θ et le flux de chaleur $\mathbf{q}$:

$$\begin{aligned} \Theta(\mathbf{x},t) &= \frac{1}{\rho(\mathbf{x},t)} \int_{\mathbb{R}^d} \mathbf{c} \cdot \mathbf{c}^T f(\mathbf{x},\boldsymbol{\xi},t)d\boldsymbol{\xi} \\ \mathbf{q}(\mathbf{x},t) &= \int_{\mathbb{R}^d} \frac{1}{2}\mathbf{c} \cdot |\mathbf{c}|^2 f(\mathbf{x},\boldsymbol{\xi},t)d\boldsymbol{\xi} \end{aligned} \tag{I.5}$$

où $\mathbf{c} = \boldsymbol{\xi} - \mathbf{U}(\mathbf{x},t)$.

I.2 Le modèle BGK

Le modèle BGK de Bhatnagar, Gross et Krook [15] est une approximation de l'équation de Boltzmann où le terme de collision est linéarisé autour d'une fonction d'équilibre maxwellienne :

$$\frac{\partial f}{\partial t}(\mathbf{x},\boldsymbol{\xi},t)+\boldsymbol{\xi}\cdot\nabla_{\mathbf{x}}f(\mathbf{x},\boldsymbol{\xi},t)=\frac{1}{\tau}(M_f(\mathbf{x},\boldsymbol{\xi},t)-f(\mathbf{x},\boldsymbol{\xi},t)) \tag{I.6}$$

où τ est le temps de relaxation et M_f est la fonction de distribution maxwellienne telle que :

$$M_f(\mathbf{x},\boldsymbol{\xi},t)=\frac{\rho(\mathbf{x},t)}{(2\pi T(\mathbf{x},t))^{d/2}}\exp\Big(-\frac{|\,\boldsymbol{\xi}-\mathbf{U}(\mathbf{x},t)\,|^2}{2T(\mathbf{x},t)}\Big) \tag{I.7}$$

dans sa forme adimensionnée. Le temps de relaxation est lié aux quantités macroscopiques et au nombre de Knudsen à l'infinie définie à partir des grandeurs de références :

$$\frac{1}{\tau}=\frac{1}{Kn_{local}}=\frac{1}{Kn_\infty}\rho T^{1-\delta}\quad\text{où}\quad Kn_\infty=\frac{\mu_0}{\sqrt{RT_0}\rho_0 L}$$

μ_0 étant la viscosité de référence du gaz à la température de référence T_0, ρ_0 est la densité de référence et δ est l'exposant de la loi de viscosité du gaz.

Le principal désavantage de ce modèle est qu'il ne respecte pas les coefficients de transport pour un gaz monoatomique. Par un développement de Chapman-Enskog [29] permettant de retrouver les équations de la limite hydrodynamique du modèle, le nombre de Prantdl obtenu et de 1 au lieu de 2/3 pour un gaz monoatomique. Rappelons que le nombre de Prantdl est définie par :

$$Pr=\frac{\mu c_p}{\kappa}=\frac{2}{3} \tag{I.8}$$

où κ est la conductivité thermique et c_p est la chaleur spécifique à pression constante.

I.3 Le modèle ES-BGK

Le modèles ES-BGK [64, 65, 3], est basé sur une opérateur de collision similaire à celui du modèle BGK mais donne un numéro de Prandtl correct égal à 2/3 pour un gas monoatomique. La fonction d'équilibre est maintenant une gaussienne isotrope. L'équation du modèle est la suivante :

$$\frac{\partial f}{\partial t}+\boldsymbol{\xi}\cdot\nabla_{\mathbf{x}}f=\frac{1}{\tau}\Big(\mathcal{G}_f-f\Big) \tag{I.9}$$

Le temps de relaxation τ s'exprime maintenant :

$$\frac{1}{\tau}=\frac{Pr}{Kn_{local}}=\frac{Pr}{Kn_\infty}\rho T^{1-\delta}\quad\text{où}\quad Kn_\infty=\frac{\mu_0}{\sqrt{RT_0}\rho_0 L}$$

Et la fonction d'équilibre s'exprime de manière adimensionnée par :

$$\mathcal{G}_f(\mathbf{x},\boldsymbol{\xi},t)=\frac{\rho(\mathbf{x},t)}{\sqrt{\det(2\pi\mathcal{T}(\mathbf{x},t))}}\exp\Big(-\frac{(\boldsymbol{\xi}-\mathbf{U}(\mathbf{x},t))^T\mathcal{T}^{-1}(\boldsymbol{\xi}-\mathbf{U}(\mathbf{x},t))}{2}\Big)$$

où $\mathcal{T}(\mathbf{x},t)=\frac{1}{Pr}RT(\mathbf{x},t)I+(1-\frac{1}{Pr})\Theta(\mathbf{x},t)=\frac{1}{\rho(\mathbf{x},t)}\int_{\mathbb{R}^3}\mathbf{c}\otimes\mathbf{c}\mathcal{G}_f d\boldsymbol{\xi}$.

II Schémas numériques pour les modèles cinétiques

II.1 La discrétisation spatiale

Dans ce travail nous utilisons des grilles cartésiennes. L'avantage des grilles cartésiennes par rapport à des grilles non structurés est que les schémas sont facilement parallélisables. Le partitionnement du domaine est aussi effectué bien plus simplement et de manière efficace. De plus, dans le cas de d'écoulement autour d'objet mobile, il n'y a pas besoin de générer un nouveau maillage adapté à la géométrie à chaque pas de temps. En revanche, la difficulté est transférée sur les conditions aux bords plus compliquées à imposer. La discrétisation spatiale utilisée est strictement identique pour les deux modèles présentées et va être détaillée dans un cas générale avec f la fonction de distribution et M_f la fonction d'équilibre.

Considérons un domaine 2D $\Omega_{\mathbf{x}} = [x_{in}, x_{out}] \times [y_{in}, y_{out}]$ discrétisé par $n \times m$ mailles $\Omega_{\mathbf{x}}^{i,j}$:

$$\Omega_{\mathbf{x}} = \bigcup_{\substack{i=1..n \\ j=1..m}} \Omega_{\mathbf{x}}^{i,j}$$

Chaque maille (i,j) a comme centre de maille le point (x_i, y_i) et le point $(x_{i+1/2}, y_j)$ est le centre de l'interface entre la maille (i,j) et la maille $(i+1,j)$. On a également $\Delta x = \Delta y = \frac{x_{out}-x_{in}}{n} = \frac{y_{out}-y_{in}}{m}$ et $x_i = x_{in} + (i-\frac{1}{2})\Delta x$, $y_j = y_{in} + (j-\frac{1}{2})\Delta y$. On utilise alors un schéma volumes finis tels que :

$$\frac{\partial f_{i,j}}{\partial t} + \frac{1}{\Delta x}(F_{i+\frac{1}{2},j} - F_{i-\frac{1}{2},j} + F_{i,j+\frac{1}{2}} - F_{i,j-\frac{1}{2}}) = \frac{1}{\tau}(M_{f_{i,j}} - f_{i,j}) \tag{II.10}$$

$f_{i,j}$ et $M_{f_{i,j}}$ sont les fonctions de distribution discrétisées sur la grille cartésienne tel que :

$$f_{i,j} = \frac{1}{|\Omega_{\mathbf{x}}^{i,j}|}\int_{\Omega_{\mathbf{x}}^{i,j}} f d\mathbf{x} \quad \text{et} \quad M_{f_{i,j}} = \frac{1}{|\Omega_{\mathbf{x}}^{i,j}|}\int_{\Omega_{\mathbf{x}}^{i,j}} M_f d\mathbf{x}$$

Les flux $F_{i+\frac{1}{2},j}$ sont exprimés par (avec des notations similaires pour les autres flux):

$$F_{i+\frac{1}{2},j} = \max(0,\xi_u) f_l + \min(0,\xi_u) f_r \tag{II.11}$$

Dans le cas d'un schéma à l'ordre 1, on a $f_l = f_{i,j}$ et $f_r = f_{i+1,j}$. Pour une discrétisation à l'ordre 2, on utilise une reconstruction linéaire de la fonction de distribution à l'interface entre les deux mailles.

II.2 La discrétisation en temps

La discrétisation en temps utilise une méthode IMEX [6]. Le terme convectif est discrétisé de manière explicite alors que le terme de collision est discrétisé de manière implicite. L'avantage de ce genre de méthode est que le pas de temps est toujours déterminé par la partie convective de l'équation (la vitesse maximum considérée dans la discrétisation en vitesse). Ceci est particulièrement utile dans le cas de temps de relaxation très faible où une forte restriction apparaîtrait sur le pas de temps pour des raisons de stabilité de l'intégration du terme de collision.

Pour un schéma de type Runge-Kutta à ν étapes :

$$\begin{aligned}
f_{i,j}^{n+1} &= f_{i,j}^n - \Delta t \sum_{k=1}^{\nu} \tilde{\omega}_k \boldsymbol{\xi} \nabla_{\mathbf{x}} f_{i,j}^{(k)} + \frac{\Delta t}{\tau} \sum_{k=1}^{\nu} \omega_k (M_{f_{i,j}}^{(k)} - f_{i,j}^{(k)}) \\
f_{i,j}^{(k)} &= f_{i,j}^n - \Delta t \sum_{l=1}^{k-1} \tilde{A}_{k,l} \boldsymbol{\xi} \nabla_{\mathbf{x}} f_{i,j}^{(l)} + \frac{\Delta t}{\tau} \sum_{l=1}^{k} A_{k,l} (M_{f_{i,j}}^{(l)} - f_{i,j}^{(l)}) \\
f_{i,j}^{(1)} &= f_{i,j}^n + \frac{\Delta t}{\tau} A_{1,1} (M_{f_{i,j}}^{(1)} - f_{i,j}^{(1)})
\end{aligned} \tag{II.12}$$

où A et $\tilde{A}$ sont des matrices $\nu \times \nu$, avec $\tilde{A}_{i,s} = 0$ si $s \geq i$ et $A_{i,s} = 0$ si $s > i$. Ces coefficients sont obtenus à partir des tableaux de Butcher. Ici nous nous intéresserons uniquement à des schémas d'ordre 1 et 2.

Ces schémas requirent la connaissance de la fonction d'équilibre à l'étape k pour calculer la fonction de distribution à cette même étape. Ceci peut être fait en calculant d'abord les moments. Le fait que les moments de la fonction de distribution et de la fonction d'équilibre soit égaux permet de connaitre les grandeurs macroscopiques à l'étape k sans connaître la fonction de distribution et ainsi reconstruire la fonction d'équilibre. On peut alors en déduire la fonction de distribution par la résolution d'un système linéaire.

III Condition au bord préservant la limite asymptotique sur grilles cartésiennes

Dans le cas d'un écoulement résolu sur grille cartésienne avec un solide immergé, il faut être capable d'imposer correctement les conditions de paroi sur un interface ne coïncidant pas avec la grille. Dans un premier temps, la position du solide est identifié par une fonction signée qui, à chaque point du maillage associe la distance au solide. L'isoligne 0 de cette fonction représente alors l'interface solide-fluide. A partir de cette fonction il est aussi possible de calculer d'autres grandeurs tels que les normales ou encore la courbure de l'interface.

Pour les modèles cinétiques, deux types de conditions de parois sont utilisées. La première est dite condition diffuse f_d. Elle considère que les molécules de gaz qui impacte la paroi sont instantanément ré-émises sous la forme d'une distribution maxwelienne. Il faut alors fournir la vitesse de la paroi ainsi que sa température. La densité est elle calculée de manière à annuler le flux de masse à travers la paroi. La seconde correspond à une réflexion spéculaire f_s. Chaque particule qui impacte la paroi rebondit et est ré-émise sans perturbation thermodynamique. Ces deux types de conditions sont alors combinés pour former la condition de bord de type Maxwell :

$$f_b = \alpha f_d + (1 - \alpha) f_s \tag{III.13}$$

avec $\alpha \in [0, 1]$.

Nous allons dans un premier temps nous intéresser au comportement des conditions aux parois dans la limite hydrodynamique. Dans cette limite, la solution des modèles cinétique doit être celle des équations d'Euler compressible. En particulier, la condition de paroi qui doit être utiliser est une condition d'imperméabilité ($\mathbf{U} \cdot \mathbf{n}_w = 0$, avec $\mathbf{n}_w$ la normal à la paroi). La condition cinétique correspondante est la réflexion spéculaire. Pourtant l'implémentation de cette condition à la paroi au niveau discret fait apparaître des flux résiduels dégradant la solution (voir figure III.1a). Pour supprimer ces flux résiduels, il faut alors utiliser une grille en vitesse beaucoup plus fine ou des interpolations d'ordre élevées ce qui augmente de manière importante le coût de calcul. Nous avons donc proposer une nouvelle condition de paroi valable dans le régime hydrodynamique appelée Euler-AP. Cette condition est basée sur une fonction d'équilibre construite à partir de la vitesse et de la température extrapolés de la zone fluide en imposant une vitesse normale nulle. La densité est alors calculé de manière à obtenir un flux de masse nul. La solution correcte est alors obtenue dans le régime hydrodynamique préservant ainsi la limite asymptotique des modèles cinétiques jusqu'à la paroi (voir figure III.1b). Précisons que le même phénomène est observé et solutionné de manière équivalente pour les deux modèles cinétiques présentés

Étant valable uniquement dans le régime hydrodynamique, cette condition est incluse dans une expression plus globale intégrant la réflexion spéculaire classique qui doit être utilisée dans des régimes non hydrodynamiques. Pour cela, la condition au paroi spéculaire est écrite sous

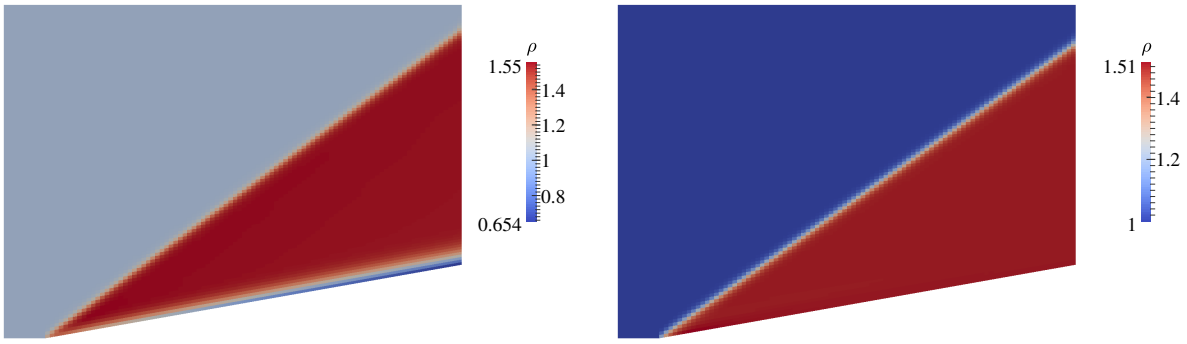

(a) Réflexion spéculaire classique.

(b) Condition de paroi Euler-AP.

Figure III.1: Densité dans le cas d'un choc oblique à Mach 3, $Kn = 10^{-5}$ pour le modèle ES-BGK.

la forme d'une combinaison convexe entre la réflexion spéculaire classique f_s et la nouvelle condition aux paroi f_{AP}.

$$f_b = \alpha f_d + (1-\alpha)(\beta f_s + (1-\beta) f_{AP}) \tag{III.14}$$

avec $\beta \in [0,1]$ un coefficient correspondant à une mesure de la distance entre la fonction de distribution et la fonction d'équilibre correspondante :

$$\beta = \min\Big(1, \frac{||f - M_f||_{L^2}}{\max(f) tol}\Big) \tag{III.15}$$

tol est un paramètre dépendant de l'ordre de l'interpolation utilisée pour le calcul de f_s. On prendra $tol = \Delta\xi_u^2$.

Nous allons maintenant tenter d'imposer cette condition aux parois à l'ordre deux dans le cas d'un objet immergé sur grille cartésienne. Pour cela il est d'abord nécessaire de reconstruire la fonction de distribution à l'interface entre le solide et le fluide. Ici, il est choisi de reconstruire la fonction de distribution de manière "upwind" en remontant les caractéristiques afin de prendre en compte la direction de l'écoulement. Ceci évite alors une extrapolation qui pourrait amener à sélectionner de l'information "downwind" et donc peu précise. La condition à la paroi est alors construite comme précédemment à l'interface solide-fluide. Afin de calculer les flux à l'ordre deux, il faut maintenant reconstruire cette condition de paroi à l'interface entre deux mailles. Pour cela, les valeurs de la fonction de distribution sont simplement extrapolées par reconstruction linéaire. Sur la figure III.2, on peut voir la solution d'un écoulement de Couette ainsi que l'ordre de précision obtenu (deuxième ordre).

IV Optimisation du temps de calcul

Les modèles cinétique étant très couteux à résoudre notamment à cause de la discrétisation de l'espace des vitesses, nous allons maintenant nous intéresser à différentes possibilités pour réduire le temps de calcul.

IV.1 Parallélisation

En vue de la parallélisation, l'utilisation de grilles cartésiennes en espace est un avantage. Le partitionnement du domaine est fait de manière immédiat en le décomposant en sous

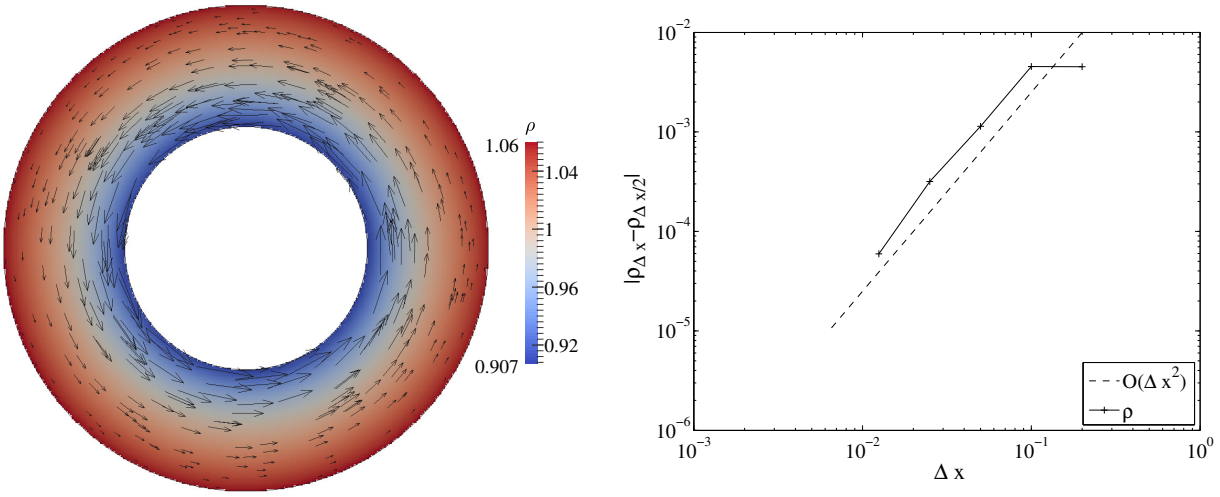

(a) Densité et vecteurs vitesse.

(b) Erreur.

Figure III.2: Solution stationnaire et erreur pour l'écoulement de Couette (modèle ES-BGK, $Kn = 10^{-2}$).

domaines attribués à chaque processeur. Les stencils utilisés dans les méthodes et schémas développés précédemment requièrent la connaissance d'un maximum de deux couches de mailles supplémentaires dans chaque direction (principalement pour obtenir l'ordre deux en espace). Ainsi chaque sous domaines possédera en plus une couche de deux mailles appartenant au sous domaine voisin. Cette couche sera communiquée par les processeurs entre eux.

Les tests montrent une bonne performance du code. Dans le cas de la scalabilité faible le rapport entre le temps CPU sur N processeurs et sur un processeur doit rester proche de 1 puisque le nombre de degré de liberté (taille du maillage) par processeur est maintenu constant. Pour la scalabilité forte, le nombre de degré de liberté est fixe dans le domaine et on augmente le nombre de processeur. Idéalement, la pente des courbes observées sur la figure IV.3 devraient avoir un coefficient directeur de 1. Dans notre cas, il est d'environ 0.7.

IV.2 Une approche aux grilles locales en vitesse

Une autre possibilité pour réduire le coût de calcul est d'éviter de calculer des flux pour des vitesses microscopique ne portant aucune information. La grille de vitesse est établit au début du calcul et ne change plus à partir de critère globaux en espace et en temps comme la vitesse maximale ou la température minimale. Dans certain cas, la grille peut être très large et très fine. Dans certaines zone de l'écoulement elle peut être très large par rapport au support de l'information. L'objectif est alors de réduire (ou d'agrandir) la zone de la grille de vitesse dans laquelle les flux sont calculés en fonction des grandeurs macroscopiques locales. A chaque pas de temps, des bornes minimum et maximum sont calculés sur la vitesse microscopique. Il est également crucial de préciser que ces bornes ne servent qu'à limiter la taille de la grille de vitesse et non d'en générer une nouvelle. Ainsi, pour un point de la grille de vitesse donné, dans une maille spatiale donnée, si ce point est entre les bornes de la grille de vitesse de la maille voisine, alors il existe. Dans le cas contraire, la fonction de distribution est nulle pour cette valeur de vitesse microscopique. Aucune interpolation n'est nécessaire entre les mailles. Les critères de

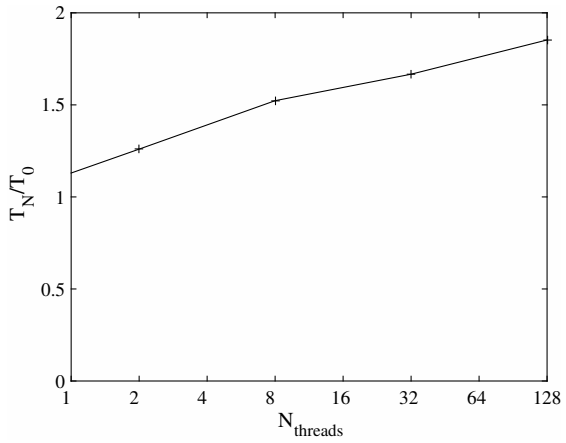

(a) Scalabilité faible : le nombre de degré de liberté est constant par processeur.

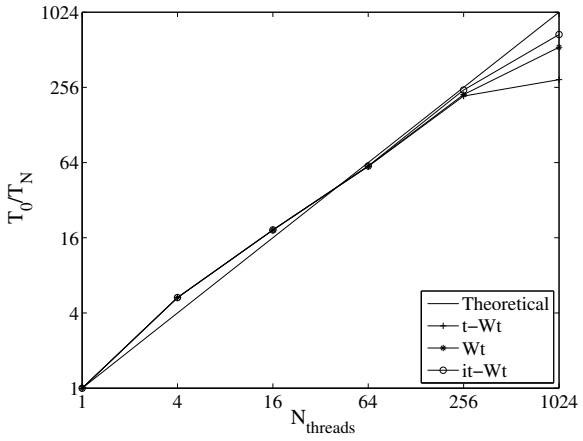

(b) Scalabilité forte : le nombre de degré de liberté est fixe dans tout le domaine.

Figure IV.3: Scalabilités.

construction de la grille de vitesse locale en 1D dans une maille i sont :

$$\begin{aligned} &\xi_{u_{min}}^{\ i} = \xi_u^l \quad \text{tel que} \quad \xi_u^l = \max_{k\in[1,N_v]}(\xi_u^k \leq u_i - \alpha\sqrt{T_i}) \\ &\xi_{u_{max}}^{\ i} = \xi_u^l \quad \text{tel que} \quad \xi_u^l = \min_{k\in[1,N_v]}(\xi_u^k \geq u_i + \alpha\sqrt{T_i}) \\ &\frac{|\int_{\mathcal{G}_i^n} f_i^n d\xi_u - \int_{\mathcal{G}_i^{n-1}} f_i^n d\xi_u|}{\int_{\mathcal{G}_i^{n-1}} f_i^n d\xi_u} < tol \end{aligned} \tag{IV.16}$$

N_v est le nombre de points dans la grille de vitesse initiale, α est un paramètre dont nous allons étudier l'influence, $\mathcal{G}_i^n$ est la grille de vitesse au temps t^n. Les deux premiers critères permettent d'agrandir ou de réduire la grille à chaque pas de temps. Le dernier critère est un critère de conservation qui contrôle que la nouvelle grille créée conserve toute l'information présente au pas de temps précédent. Le passage en deux ou trois dimensions est immédiat en appliquant le même algorithme indépendamment dans chaque direction.

La taille des grilles locales est montrée à l'état stationnaire pour le cas du Blunt Body sur la figure IV.4. Le gain en temps de calcul en fonction de α ainsi que l'erreur relative par rapport au calcul sans les grilles locales sont pésentés sur la figure IV.5.

V Méthode numérique pour le transport de particules en écoulements raréfiés

Nous allons maintenant nous intéresser au cas test présenté en introduction. Il s'agit de simuler l'éjection de particules par une tuyère en milieu raréfié. Nous avons présenté les méthodes utilisées pour simuler correctement ce type d'écoulement à partir des modèles cinétiques et en particulier comment conserver les propriétés correctes de l'écoulement jusqu'aux parois. Dans le cas de la tuyère ceci est indispensable puisque, étant donné la haute densité de gaz dans la tuyère, le régime sera proche du régime hydrodynamique alors qu'à l'extérieur, on ira jusqu'à des nombres de Knudsen de l'ordre de 10.

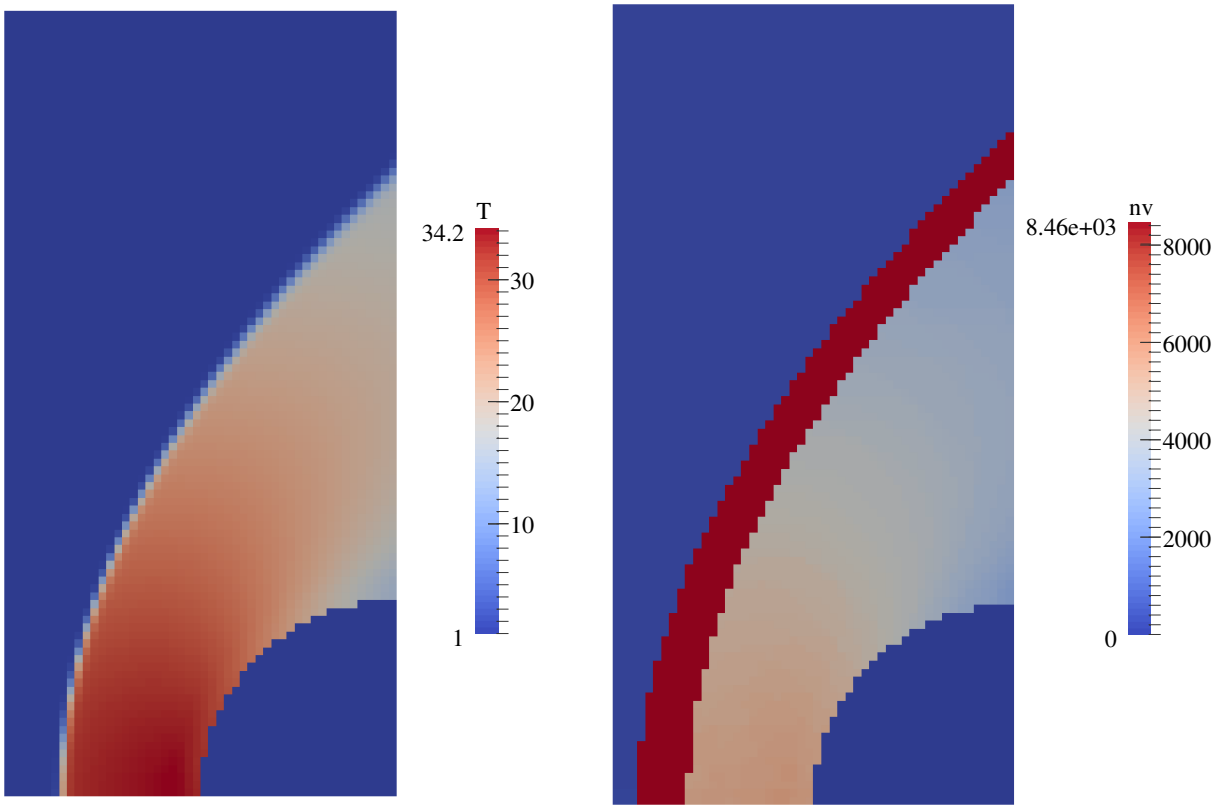

(a) Température. (b) Nombre de points en vitesse par maille.

Figure IV.4: Solution stationnaire du Blunt body à Mach 10, $Kn_\infty = 10^{-5}$.

V.1 L'équation de transport de particules

Nous nous plaçons ici dans un cas où l'écoulement de particule solide est tellement dilué qu'il n'impacte pas l'écoulement du gaz (sprays fins). Le modèle cinétique régissant l'écoulement du gaz n'est donc pas modifié. Pour la même raison nous considérons également que les particules solides n'entrent pas en collision. Le transport des particules solides va donc être modélisé à partir d'une équation de type Vlasov :

$$\frac{\partial f_p}{\partial t} + \nabla_{\mathbf{x}} \cdot \boldsymbol{\xi}' f_p + \nabla_{\boldsymbol{\xi}'} \cdot \mathbf{a} f_p = 0 \tag{V.17}$$

où f_p est la fonction de distribution de la densité de particules, $\boldsymbol{\xi}'$ est la vitesse microscopique des particules solides et $\mathbf{a}$ un terme d'accélération. C'est à travers ce terme d'accélération que le modèle de transport de particules va être couplé au modèle cinétique en considérant que l'accélération des particules est due à une force de trainé $\mathbf{a} = D(\mathbf{U}_g - \boldsymbol{\xi}')$. $\mathbf{U}_g$ est ici la vitesse macroscopique du gaz et provient donc du modèle cinétique.

V.2 La méthode numérique

La méthode utilisée pour résoudre le modèle de transport de particule est basée sur un splitting entre le transport dans l'espace physique et celui dans l'espace des vitesses. Les particules solides sont d'abord transportées dans l'espace physique puis remaillées sur le maillage cartésien

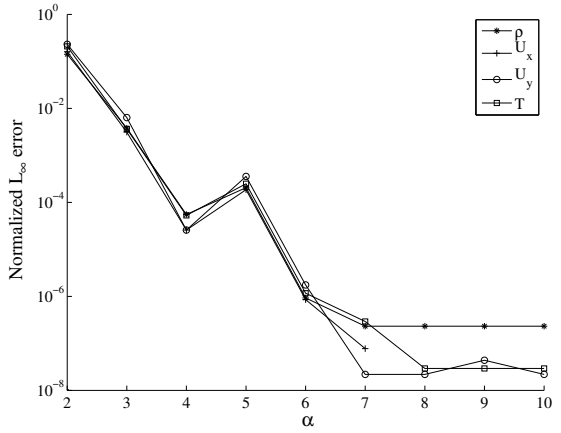

(a) Norme L_∞ de l'erreur pour la densité, la vitesse et la température.

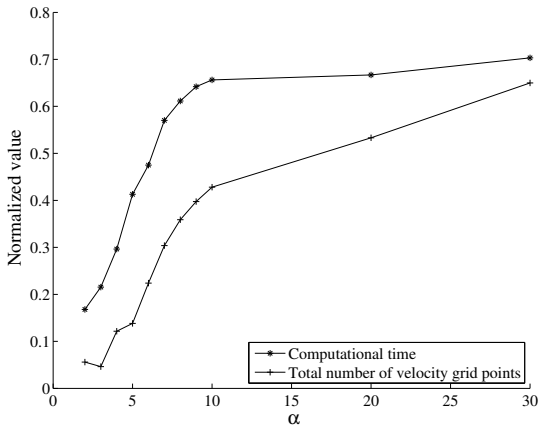

(b) Réduction du coût de calcul.

Figure IV.5: Erreur et réduction du temps de calcul pour le cas du Blunt body à Mach 10 (par rapport au cas sans grilles locales).

initiale coïncidant avec le maillage utilisé pour la résolution du modèle cinétique. On effectue ensuite le transport dans l'espace des vitesses et on remaille dans ce même espace sur la grille initiale. Comparée aux méthodes purement lagrangiennes, aux méthodes SPH (Smooth Particle Hydrodynamic) ou encore aux méthodes PIC (Particle-in-Cell), une seule grille est stockée (des particules numériques équivalentes sont créées aux centres des mailles à chaque pas de temps et les particules transportées sont supprimées), et la méthode ne souffre pas du bruit stochastique inhérent aux méthodes lagrangiennes. L'étape de remaillage est illustrée figure V.6 dans un cas 1D.

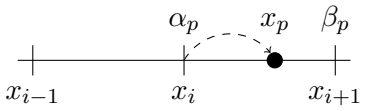

(a) Cas $\xi'_u > 0$

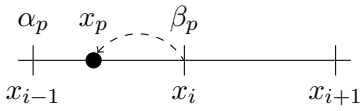

(b) Cas $\xi'_u < 0$

Figure V.6: Configuration 1D après une étape de transport dans l'espace physique (comportement similaire dans l'espace des vitesses avec $\xi'_u \equiv a_u$)

Le choix du noyau d'interpolation pour le remaillage est une étape cruciale. Dans notre cas, il doit préserver la positivité de la fonction de distribution et remailler les particules au même endroit si leur vitesse est nulle. Le meilleur compromis a été trouvé pour une fonction chapeau :

$$\Lambda_1 = \begin{cases} \alpha = 1 - y \\ \beta = y \end{cases} \tag{V.18}$$

où y est défini d'après la figure V.6 par :

$$\begin{cases} y = \dfrac{x_p - x_i}{\Delta x} & \text{si} \quad \xi'_u > 0 \\ y = \dfrac{x_p - x_{i-1}}{\Delta x} & \text{si} \quad \xi'_u \leq 0 \end{cases}$$

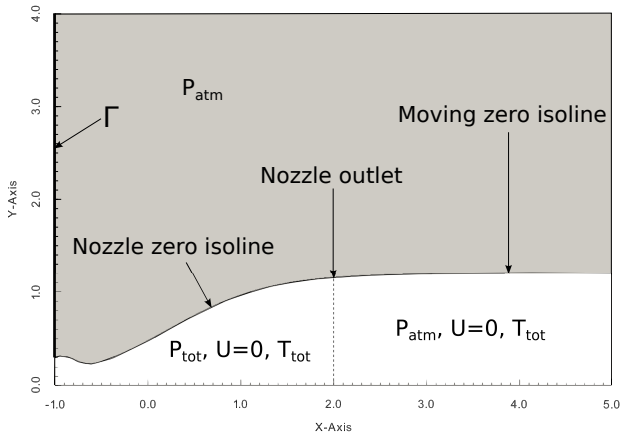

Figure V.7: Configuration initiale du domaine de calcul pour la simulation du transport de particules dans un jet de tuyère.

V.3 Le cas de la tuyère

Après validation sur plusieurs cas tests analytiques, la méthode est utilisée sur le cas de la tuyère. On considère une tuyère 2D représentée par une levelset. Le jet de la tuyère est également représenté par une levelset concentrant les effets visqueux dus à l'interface avec le gaz initialement à l'extérieur de la tuyère. La levelset est ensuite transportée à la vitesse du gaz éjecté. La géométrie initiale est présentée figure V.7

Le rapport de pression entre la pression d'adaptation de la tuyère connue P_c (qui ne dépend pas de la pression extérieure mais seulement de la géométrie et des conditions d'entrée) et la pression extérieure P_{atm} est imposé. Plus ce rapport est grand, plus la dépression est importante en sortie de la tuyère est importante. On constate alors que le jet tend à revenir en arrière le long des parois extérieures de la tuyère jusqu'au niveau de l'entrée pendant le transitoire et se stabilise ensuite formant un angle avec la sortie de la tuyère pouvant attendre plus de 90 degrés. Le régime transitoire est montré sur la figure V.8. Le modèle couplé nous permet de quantifier le nombre de particules éjectées par la tuyère jusqu'au niveau de l'entrée et qui dans le cas réel impacteraient les dispositifs optiques embarqués par le satellite (voir figure V.9).

Conclusion

Dans ce travail nous avons développé des méthodes permettant la résolution d'écoulements complexes sur grilles cartésiennes. Nous avons tenter de reproduire des phénomènes encore peu connus et difficilement reproductible expérimentalement comme le cas test de la pollution de dispositifs optiques par l'éjection de particules solides provenant d'un moteur de satellite.

Trois contributions principales sont à distinguées. La première concerne le comportement des schémas pour les modèles cinétiques dans la limite hydrodynamique. Il est indispensable pour les écoulements complexes mêlant différents types de régimes de permettre une transition continue de la solution jusqu'aux parois d'un possible solide immergé. En ce sens, une nouvelle condition de paroi a été proposée préservant la limite asymptotique des modèles cinétiques (BGK et ES-BGK) vers les équations d'Euler compressible. De plus, nous avons montré comment cette condition aux parois (et n'importe quelle condition aux parois en général) peut être imposée au second ordre sur des grilles cartésiennes.

Il a ensuite été possible d'utiliser l'avantage des grilles cartésiennes pour le calcul massive-

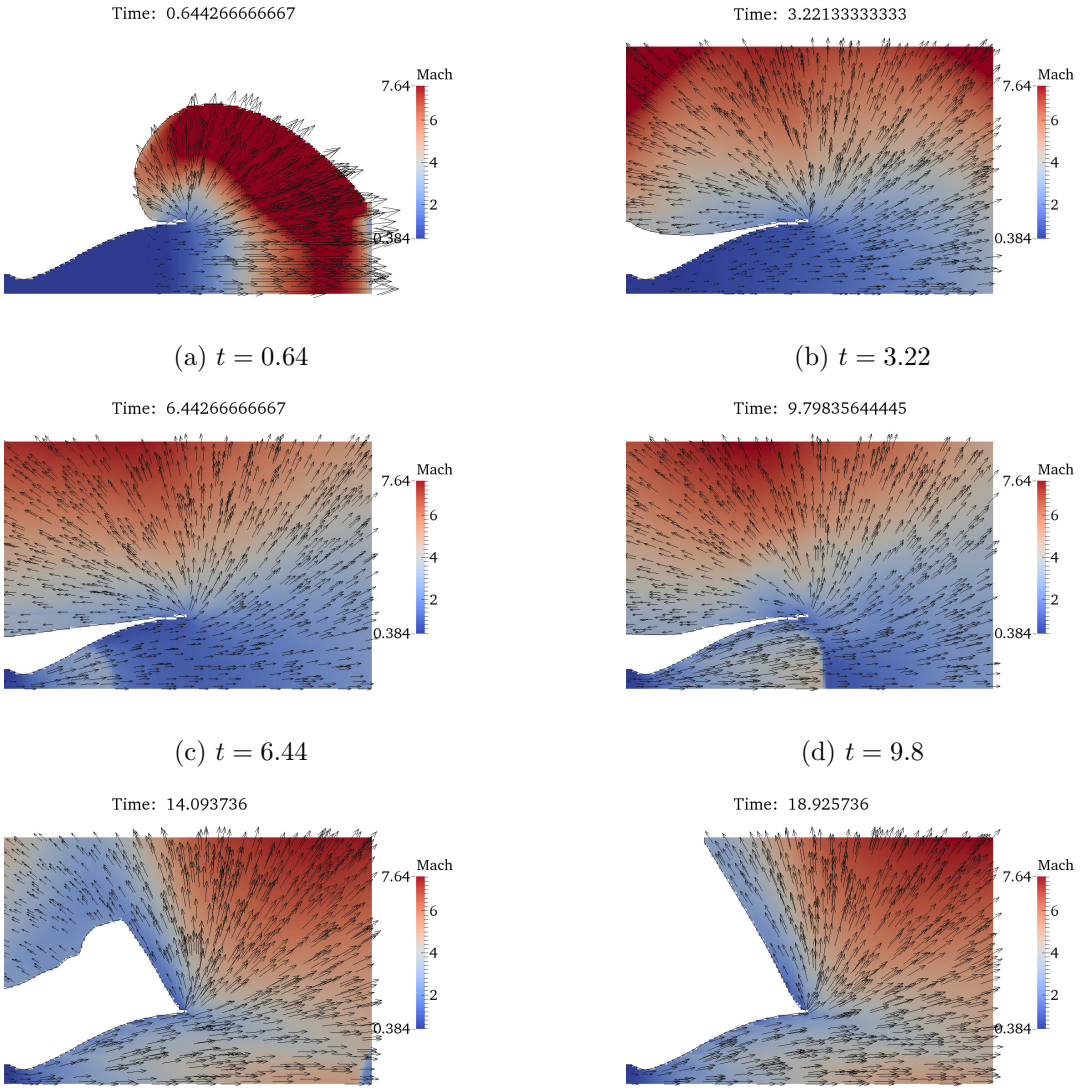

(a) $t = 0.64$ (b) $t = 3.22$

(c) $t = 6.44$ (d) $t = 9.8$

(e) $t = 14.09$ (f) État stationnaire

Figure V.8: Nombre de Mach et vecteurs vitesse pour $P_c/P_{atm} = 200000$ avec le modèle BGK.

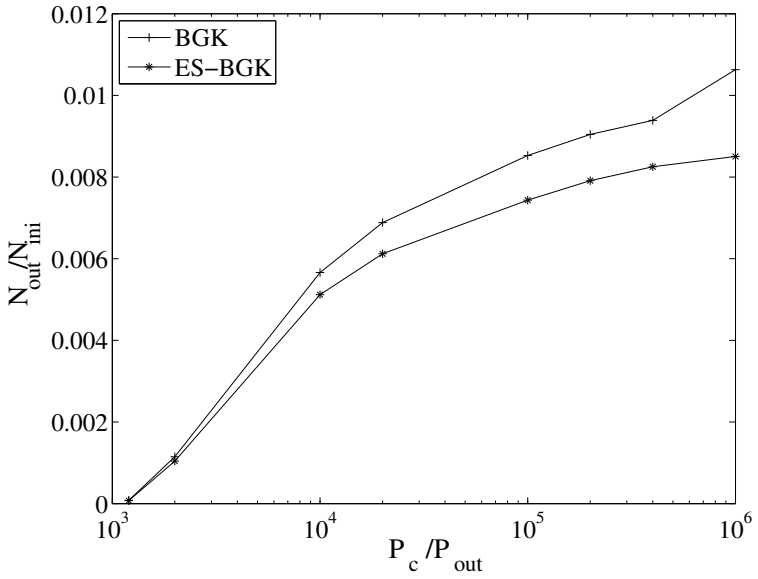

Figure V.9: Nombre de particules sortant du domaine au dessus de l'entrée de la tuyère.

ment parallèle et donc de réduire considérablement le temps de calcul. C'est également dans une optique de réduction du coût de calcul qu'une approche aux grilles locales en vitesse a été proposée et constitue la deuxième contribution de cette thèse. De très bon résultats ont été obtenues avec une réduction du temps de calcul allant jusqu'à 80%.

Enfin, les modèles cinétiques ont été couplés avec un modèle de transport de particules afin de simuler l'éjection de particules solides par une tuyère en environnement raréfié. Là encore, une méthode a été proposée pour résoudre de manière efficace l'équation de type Vlasov modélisant le transport de particules solides dans un écoulement de gaz.

Nous avons pu également montré l'adaptabilité de ces méthodes à du calcul 3D notamment grâce à l'effort d'intégration des schémas dans un environnement HPC (High Parallel Computing). Il serait maintenant intéressant de comparer quantitativement les résultats obtenues sur des cas test avec des données expérimentales. Pour cela une extension à des modèles cinétiques plus complexes (polyatomiques, poly-espèces) est probablement nécessaire. De même, si nous avons commencé à traiter la réduction du temps de calcul, un travail similaire pourrait être effectué pour réduire la consommation en mémoire (méthodes AMR par exemple). Enfin, le modèle de transport de particules peut être enrichi en intégrant les collisions entre particules solides mais aussi en ajoutant un terme dans les modèles cinétiques modélisant l'effet de ces particules sur l'écoulement (sprays épais).

Schemi preservanti il limite asintotico per i modelli BGK e ES-BGK su griglia Cartesiana

Contents

Introduzione

Una particolarità dei flussi complessi è la presenza di due tipi di regimi : il regime idrodinamico e il regime rarefatto. Troviamo questo tipo di coesistenza nelle pompe a vuoto oppure nel caso di rientro ipersonico di un veicolo in atmosfera. Il regime rarefatto è caratterizzato da una importante distanza tra le molecole di gas rispetto alla dimensione caratteristica del problema. Nel caso di dispositivi microscopici, anche se la densità di molecole non è bassa (e quindi la distanza media tra le molecole è piccola), il regime può essere definito rarefatto a causa della ridotta lunghezza caratteristica del problema. In questi casi, il comportamento microscopico delle molecole di gas può essere diverso dal comportamento medio del flusso (macroscopico). Se la distanza tra le molecole diventa molto piccola, il regime è chiamato idrodinamico.

L'obiettivo di questa tesi è la simulazione di flussi in cui coesistono i due tipi di regimi. In un contesto industriale, la realizzazione di esperimenti in condizione reali, come il rientro di capsule in atmosfera, diventa difficile a causa delle basse pressioni e delle alte velocità che devono

essere riprodotte. È a fronte di questo tipo di problema che la simulazione numerica diventa importante. I modelli numerici usati devono essere capaci di assicurare una transizione continua della soluzione da un regime all'altro. Inoltre, è necessario che tale proprietà che consiste nel preservare il limite asintotico sia soddisfatta anche in presenza di solidi immersi nel dominio. In questa tesi, considereremo sia geometrie fisse (gradino, Blunt body) che geometrie mobili e deformabili (capsula, getto di un ugello). Svilupperemo i metodi e gli schemi necessari in un contesto HPC (High Parallel Computing) per ridurre il più possibile il costo computazionale.

Ci interesseremo più particolarmente a due casi test applicati : il trasporto di particelle nel getto di un ugello in mezzo rarefatto (per esempio nel caso di ugelli di manovra di un satellite) ed il rientro di una capsula in atmosfera. Il primo caso test viene da esperimenti in laboratorio in cui si è osservato che particelle solide possono sporcare un corpo posto al livello dell'ingresso dell'ugello al momento della sua accensione. In condizioni operative, queste particelle colpiscono dispositivi ottici che possono essere montati su satelliti.

Dal punto di vista dei modelli, le equazioni classiche della meccanica dei fluidi (Eulero, Navier-Stokes) non descrivono correttamente la dinamica di un flusso rarefatto a causa della loro natura macroscopica. Per lo studio di questi fenomeni è più adatta una descrizione statistica dello stato termodinamico delle molecole mediante una funzione di distribuzione. Ad un dato instante di tempo, questa funzione descrive la densità di molecole di gas che hanno una certa velocità microscopica in un determinato punto dello spazio (di dimensione D). Si rende quindi necessaria l'introduzione di uno spazio di velocità di dimensione d. L'equazione di evoluzione temporale di questa funzione di distribuzione è l'equazione di Boltzmann. Essa è derivata considerando due fenomeni fisici : la conservazione della massa nello spazio delle fasi e le collisione tra le molecole di gas. A causa dell'elevato numero di variabili indipendenti (per un caso 3D, tre in spazio, tre in velocità, più il tempo) della funzione di distribuzione, il costo di risoluzione dell'equazione di Boltzmann è molto alto. Tra i metodi usati per risolvere l'equazione di Boltzmann il più famoso, conosciuto sotto il nome di "Direct Simulation Monte Carlo" (DSMC, [16]), è efficiente nel regime rarefatto ma difficilmente applicabile vicino al regime idrodinamico. Un ulteriore svantaggio è il rumore stocastico generato dall'approccio probabilistico.

Risolvere l'equazione di Boltzmann con modelli deterministici non soffre di questi svantaggi. Abbiamo scelto quindi di concentrarci su due di questi modelli : il modello BGK [15] e il modello ES-BGK [64], [65]. Risolviamo entrambi modello con un metodo alle velocità discrete ("Discrete Velocity Method", DVM) che considera una discretizzazione dello spazio delle velocità microscopiche. Dopo una breve presentazione dei modelli e degli schemi numerici usati per risolverle, ci interesseremo al limite asintotico dei modelli verso le equazione di Eulero e più in particolare alla preservazione di questo limite in presenza di un corpo immerso. Proporremo una nuova condizione a parete permettendo una transizione continua della soluzione tra i due regimi. Presenteremo poi, diverse tecniche per ridurre il costo computazionale della simulare in casi 3D con geometrie mobili. In questo senso, le griglie cartesiane sono più adatte e quindi sceglieremo questo tipo di griglie. L'ultima parte del lavoro riguarderà un modello e un metodo per il trasporto di particelle in un flusso rarefatto per trattare il caso della contaminazione di dispositivi ottici montati su satelliti.

I Modelli cinetici

In questa sezione, introduciamo l'equazione di Boltzmann che permette di risolvere flussi sia nel regime idrodinamico che nel regime rarefatto. Quindi verranno presentati due modelli deterministici usati in questa tesi.

I.1 L'equazione di Boltzmann

Un indicatore per definire se il flusso è rarefatto è il numero di Knudsen, definito come il rapporto tra il percorso libero medio tra le molecole di gas λ e la dimensione caratteristica del problema L :

$$Kn = \frac{\lambda}{L} \tag{I.1}$$

Se il numero di Knudsen è piccolo ($< 10^{-2}$), il regime è detto idrodinamico e le equazioni classiche della meccanica dei fluidi (Eulero, Navier-Stokes) sono adatte alla sua descrizione. Se tale numero è grande, queste equazioni non sono più valide.

L'equazione valida per ogni regime è l'equazione di Boltzmann :

$$\frac{\partial f}{\partial t} + \boldsymbol{\xi} \cdot \nabla_{\mathbf{x}} f + \mathbf{a} \cdot \nabla_{\boldsymbol{\xi}} f = Q(f, f) \tag{I.2}$$

dove f è la funzione di distribuzione di densità dipendente dal tempo t, dalla posizione $\mathbf{x} = (x, y, z)^T$, e dalla velocità microscopica $\boldsymbol{\xi} = (\xi_u, \xi_v, \xi_w)^T$. Q è l'operatore collisionale.

Le grandezze macroscopiche come la densità ρ, la velocità $\mathbf{U} = (u, v, w)^T$ e l'energia E sono calcolate a partire dai momenti della funzione di distribuzione f :

$$\begin{pmatrix} \rho(\mathbf{x},t) \\ \rho(\mathbf{x},t)\mathbf{U}(\mathbf{x},t) \\ E(\mathbf{x},t) \end{pmatrix} = \int_{\mathbb{R}^d} f(\mathbf{x},\boldsymbol{\xi},t)\mathbf{m}(\boldsymbol{\xi})d\boldsymbol{\xi} \quad \text{con} \quad \mathbf{m}(\boldsymbol{\xi}) = \begin{pmatrix} 1 \\ \boldsymbol{\xi} \\ \frac{1}{2} \mid \boldsymbol{\xi} \mid^2 \end{pmatrix} \tag{I.3}$$

L'energia totale E può anche essere calcolata introducendo la temperatura T :

$$E(\mathbf{x},t) = \frac{d}{2}\rho(\mathbf{x},t)RT(\mathbf{x},t) + \frac{1}{2}\rho(\mathbf{x},t) \mid \mathbf{U}(\mathbf{x},t) \mid^2 \tag{I.4}$$

dove R è la costante specifica del gas esprimibile a traverso la costante universale dei gas $\mathcal{R}$ e la massa molare $\mathcal{M}$ del gas :

$$R = \frac{\mathcal{R}}{\mathcal{M}}$$

In questo lavoro, consideriamo gas monoatomici ($d = 3$) con un rapporto di calori specifici :

$$\gamma = 1 + \frac{2}{d} = \frac{5}{3}$$

I momenti di ordine più elevato permettono di calcolare il tensore dei sforzi Θ e il flusso di calore $\mathbf{q}$:

$$\begin{aligned} \Theta(\mathbf{x},t) &= \frac{1}{\rho(\mathbf{x},t)} \int_{\mathbb{R}^d} \mathbf{c} \cdot \mathbf{c}^T f(\mathbf{x},\boldsymbol{\xi},t)d\boldsymbol{\xi} \\ \mathbf{q}(\mathbf{x},t) &= \int_{\mathbb{R}^d} \frac{1}{2}\mathbf{c} \cdot |\mathbf{c}|^2 f(\mathbf{x},\boldsymbol{\xi},t)d\boldsymbol{\xi} \end{aligned} \tag{I.5}$$

dove $\mathbf{c} = \boldsymbol{\xi} - \mathbf{U}(\mathbf{x},t)$.

I.2 Il modello BGK

Il modello BGK di Bhatnagar, Gross e Krook [15] è un approssimazione dell'equazione di Boltzmann dove il termine collisionale è linearizzato attorno a una funzione d'equilibrio maxwelliana

$$\frac{\partial f}{\partial t}(\mathbf{x},\boldsymbol{\xi},t) + \boldsymbol{\xi} \cdot \nabla_{\mathbf{x}} f(\mathbf{x},\boldsymbol{\xi},t) = \frac{1}{\tau}(M_f(\mathbf{x},\boldsymbol{\xi},t) - f(\mathbf{x},\boldsymbol{\xi},t)) \tag{I.6}$$

dove τ è il tempo di rilassamento e M_f è la funzione d'equilibrio maxwelliana tale che :

$$M_f(\mathbf{x},\boldsymbol{\xi},t)=\frac{\rho(\mathbf{x},t)}{(2\pi T(\mathbf{x},t))^{d/2}}\exp\Big(-\frac{|\,\boldsymbol{\xi}-\mathbf{U}(\mathbf{x},t)\,|^2}{2T(\mathbf{x},t)}\Big) \tag{I.7}$$

nella sua forma adimensionalizzata. Il tempo di rilassamento è legato alle quantità macroscopiche e al numero di Knudsen all'infinito definito con le grandezze di riferimento :

$$\frac{1}{\tau}=\frac{1}{Kn_{local}}=\frac{1}{Kn_\infty}\rho T^{1-\delta}\quad \text{où}\quad Kn_\infty=\frac{\mu_0}{\sqrt{RT_0}\rho_0 L}$$

μ_0 è la viscosità di riferimento del gas alla temperatura di riferimento T_0, ρ_0 è la densità di riferimento e δ è l'esponente della legge di viscosità del gas.

Il principale svantaggio di questo modello è che non rispetta i coefficienti di trasporto per un gas monoatomico. Facendo un espansione di Chapman-Enskog [29] che permette di ricavare le equazione nel limite idrodinamico, il numero di Prandtl ottenuto è 1 invece di 2/3. Ricordiamo che il numero di Prandtl è definito come :

$$Pr=\frac{\mu c_p}{\kappa}=\frac{2}{3} \tag{I.8}$$

dove κ è la conduttività termica e c_p è il calore specifico a pressione constante.

I.3 Il modello ES-BGK

Il modello ES-BGK [64, 65, 3], è basato su un operatore collisionale simile a quello del modello BGK pero dà un corretto numero di Prandtl uguale a 2/3. In questo modello la funzione di equilibrio è una gaussiana isotropa. L'equazione di questo modello si scrive :

$$\frac{\partial f}{\partial t}+\boldsymbol{\xi}\cdot\nabla_{\mathbf{x}}f=\frac{1}{\tau}\Big(\mathcal{G}_f-f\Big) \tag{I.9}$$

Il tempo di rilassamento τ diventa :

$$\frac{1}{\tau}=\frac{Pr}{Kn_{local}}=\frac{Pr}{Kn_\infty}\rho T^{1-\delta}\quad \text{dove}\quad Kn_\infty=\frac{\mu_0}{\sqrt{RT_0}\rho_0 L}$$

La funzione d'equilibrio in forma adimensionalizzata è :

$$\mathcal{G}_f(\mathbf{x},\boldsymbol{\xi},t)=\frac{\rho(\mathbf{x},t)}{\sqrt{\det(2\pi\mathcal{T}(\mathbf{x},t))}}\exp\Big(-\frac{(\boldsymbol{\xi}-\mathbf{U}(\mathbf{x},t))^T\mathcal{T}^{-1}(\boldsymbol{\xi}-\mathbf{U}(\mathbf{x},t))}{2}\Big)$$

dove $\mathcal{T}(\mathbf{x},t)=\frac{1}{Pr}RT(\mathbf{x},t)I+(1-\frac{1}{Pr})\Theta(\mathbf{x},t)=\frac{1}{\rho(\mathbf{x},t)}\int_{\mathbb{R}^3}\mathbf{c}\otimes\mathbf{c}\mathcal{G}_f d\boldsymbol{\xi}$.

II Schemi numerici per i modelli cinetici

II.1 La discretizzazione spaziale

In questo lavoro abbiamo scelto di usare griglie cartesiane. Il vantaggio di questo tipo di griglie rispetto alle griglie non strutturate è che gli schemi sono più facilmente parallelizzabili. Il partizionamento del dominio tra i processori è più semplice e più efficiente. In caso di oggetti mobili, la griglia è generata una sola volta, senza il bisogno di creare una nuova griglia ad ogni passo di tempo come nel caso di griglia non strutturate. Tuttavia, la difficoltà si sposta nell'imporre le condizioni a parete con opportuna precisione.

Le discretizzazione spaziale è identica per i due modelli presentati e viene descritta senza perdita di generalità in un caso 2D con f, la funzione di distribuzione e M_f, la funzione di equilibrio.

Consideriamo un dominio 2D $\Omega_{\mathbf{x}} = [x_{in}, x_{out}] \times [y_{in}, y_{out}]$ discretizzato con $n \times m$ celle $\Omega_{\mathbf{x}}^{i,j}$:

$$\Omega_{\mathbf{x}} = \bigcup_{\substack{i=1..n \\ j=1..m}} \Omega_{\mathbf{x}}^{i,j}$$

Ciascuna cella (i,j) ha come centro cella (x_i, y_i) e il punto $(x_{i+1/2}, y_j)$ è il centro dell'interfaccia tra la cella (i,j) e la cella $(i+1,j)$. Definiamo $\Delta x = \Delta y = \frac{x_{out}-x_{in}}{n} = \frac{y_{out}-y_{in}}{m}$ e $x_i = x_{in} + (i - \frac{1}{2})\Delta x$, $y_j = y_{in} + (j - \frac{1}{2})\Delta y$. Utilizziamo uno schema ai volumi finiti :

$$\frac{\partial f_{i,j}}{\partial t} + \frac{1}{\Delta x}(F_{i+\frac{1}{2},j} - F_{i-\frac{1}{2},j} + F_{i,j+\frac{1}{2}} - F_{i,j-\frac{1}{2}}) = \frac{1}{\tau}(M_{f_{i,j}} - f_{i,j}) \tag{II.10}$$

$f_{i,j}$ e $M_{f_{i,j}}$ sono le funzioni di distribuzione discrete cosi definite :

$$f_{i,j} = \frac{1}{|\Omega_{\mathbf{x}}^{i,j}|}\int_{\Omega_{\mathbf{x}}^{i,j}} f d\mathbf{x} \quad \text{e} \quad M_{f_{i,j}} = \frac{1}{|\Omega_{\mathbf{x}}^{i,j}|}\int_{\Omega_{\mathbf{x}}^{i,j}} M_f d\mathbf{x}$$

Il generico flusso $F_{i+\frac{1}{2},j}$ è definito :

$$F_{i+\frac{1}{2},j} = \max(0, \xi_u) f_l + \min(0, \xi_u) f_r \tag{II.11}$$

dove nel caso di uno schema all'ordine uno, imponiamo $f_l = f_{i,j}$ e $f_r = f_{i+1,j}$. Per ottenere uno schema del secondo ordine, la funzione di distribuzione è ricostruita linearmente all'interfaccia tra le due celle.

II.2 La discretizzazione in tempo

Per la discretizzazione in tempo scegliamo un metodo IMEX [6]. Il termine convettivo è discretizzato esplicitamente mentre il termine collisionale è discretizzato in modo implicito. Grazie a questo metodo, il passo di tempo è determinato solo dalla parte convettiva dell'equazione. Questa particolarità diventa molto utile per tempi di rilassamento piccoli che imporrebbero una forte restrizione sul passo di tempo per motivi di stabilità nell'integrazione del termine di collisione.

Per uno schema Runge-Kutta con ν tappe :

$$\begin{aligned}
f_{i,j}^{n+1} &= f_{i,j}^n - \Delta t \sum_{k=1}^{\nu} \tilde{\omega}_k \boldsymbol{\xi} \nabla_{\mathbf{x}} f_{i,j}^{(k)} + \frac{\Delta t}{\tau} \sum_{k=1}^{\nu} \omega_k (M_{f_{i,j}}^{(k)} - f_{i,j}^{(k)}) \\
f_{i,j}^{(k)} &= f_{i,j}^n - \Delta t \sum_{l=1}^{k-1} \tilde{A}_{k,l} \boldsymbol{\xi} \nabla_{\mathbf{x}} f_{i,j}^{(l)} + \frac{\Delta t}{\tau} \sum_{l=1}^{k} A_{k,l} (M_{f_{i,j}}^{(l)} - f_{i,j}^{(l)}) \\
f_{i,j}^{(1)} &= f_{i,j}^n + \frac{\Delta t}{\tau} A_{1,1} (M_{f_{i,j}}^{(1)} - f_{i,j}^{(1)})
\end{aligned} \tag{II.12}$$

dove A e $\tilde{A}$ sono matrici $\nu \times \nu$, con $\tilde{A}_{i,s} = 0$ se $s \geq i$ e $A_{i,s} = 0$ se $s > i$. Questi coefficienti sono ottenuti a partire dalle tavole di Butcher. In questo lavoro l'interesse è posto su schemi di ordine uno e due.

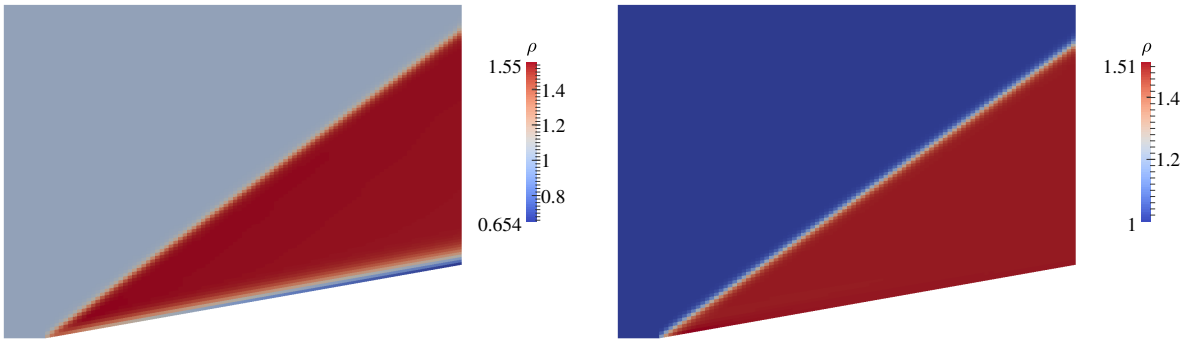

(a) Riflessione speculare classica.

(b) Condizione di parete Euler-AP.

Figure III.1: Densità per un urto obliquo a Mach 3, $Kn = 10^{-5}$ per il modello ES-BGK.

III Condizione a parete preservante il limite asintotico su griglia cartesiana

Se un solido è immerso in flusso risolto su griglia cartesiana, bisogna imporre correttamente le condizioni a parete su un'interfaccia flusso-solido non allineata con la griglia. La posizione del solido è identificata da una funzione caratteristica che associa ad ogni punto della griglia la distanza dal solido. L'isolinea zero di questa funzione rappresenta l'interfaccia fluido-solido. Da questa funzione, è possibile calcolare grandezze come le normale o la curvatura del interfaccia.

Per i modelli cinetici, due tipi di condizioni a la parete sono utilizzate. La prima è una condizione diffusiva f_d che considera il fatto che le molecole di gas che impattano la parete vengono riemesse con lo stato termodinamico della parete stessa (distribuzione maxwelliana). È necessario quindi fornire a parete la velocità e la temperatura. La densità viene calcolata tale che il flusso di massa sia nullo a traverso la parete. Le seconda è una condizione di riflessione speculare f_s per cui ogni molecola rimbalza sulla parete. Questi due condizioni possono essere combinate per diventare la condizione di Maxwell :

$$f_b = \alpha f_d + (1 - \alpha) f_s \tag{III.13}$$

con $\alpha \in [0, 1]$.

Consideriamo innanzitutto il comportamento delle condizioni a parete nel limite idrodinamico dove la soluzione deve essere quella delle equazioni di Eulero. La condizione corretta è una condizione di impermeabilità ($\mathbf{U} \cdot \mathbf{n}_w = 0$, con $\mathbf{n}_w$ la normale a la parete) che per i modelli cinetici, corrisponde alla riflessione speculare. Ciò nonostante, l'implementazione di questa condizione al livello discreto crea flussi spuri che degradano la soluzione (figura III.1a). La soppressione di questi flussi richiede interpolazioni di alto ordine o un raffinamento della griglia di velocità. Tuttavia, il costo computazionale cresce molto.

Proponiamo allora una nuova condizione a parete valida nel regime idrodinamico chiamata Euler-AP. Questa condizione è basata su una funzione di equilibrio costruita a partire dalle velocità e temperatura estrapolate dal fluido ; successivamente, imponiamo la velocità normale nulla. Come per la condizione diffusiva, la densità è calcolata annullando il flusso di massa. La soluzione ottenuta è corretta nel regime idrodinamico e preserva il limite asintotico dei modelli cinetici anche a parete (figura III.1b). Lo stesso fenomeno è osservato in entrambi modelli cinetici presentati ed è risolto nello stesso modo.

Dal momento che questa condizione a parete è valida solo nel regime idrodinamico, essa è combinata con la riflessione speculare classica che deve essere usata in regimi non idrodinamici,

in un'espressione unica. Se f_{AP} è la nuova condizione per il regime idrodinamico, l'espressione della condizione a parete generale diventa :

$$f_b = \alpha f_d + (1-\alpha)(\beta f_s + (1-\beta) f_{AP}) \tag{III.14}$$

con $\beta \in [0,1]$ un coefficiente corrispondente a una misura della distanza tra la funzione di distribuzione e la funzione di equilibrio corrispondente :

$$\beta = \min\Big(1, \frac{||f - M_f||_{L^2}}{\max(f) tol}\Big) \tag{III.15}$$

dove tol è un parametro dipendente dall'ordine dell'interpolazione utilizzata per il calcolo di f_s. Prendiamo $tol = \Delta\xi_u^2$.

Proviamo a imporre la condizione a parete all'ordine due su una griglia cartesiana nel caso di un oggetto immerso. La posizione dell'interfaccia è nota grazie alla funzione levelset. È necessario ricostruire la funzione di distribuzione su questa interfaccia, e per farlo, scegliamo una ricostruzione upwind lungo le caratteristiche per prendere in considerazione le direzioni principali del flusso, evitando un estrapolazione che introdurrebbe imprecisioni dovute all'uso di valori downwind. La condizione di parete all'interfaccia è costruita come spiegato precedentemente. Per calcolare i flussi all'ordine due bisogna trasferire questa condizione dall'interfaccia fluido-solido all'interfaccia tra le due celle : Utilizziamo un'estrapolazione lineare. In figura III.2 mostriamo la soluzione nel caso di un flusso di Couette risolto con la nuova condizione a parete e lo schema al ordine due.

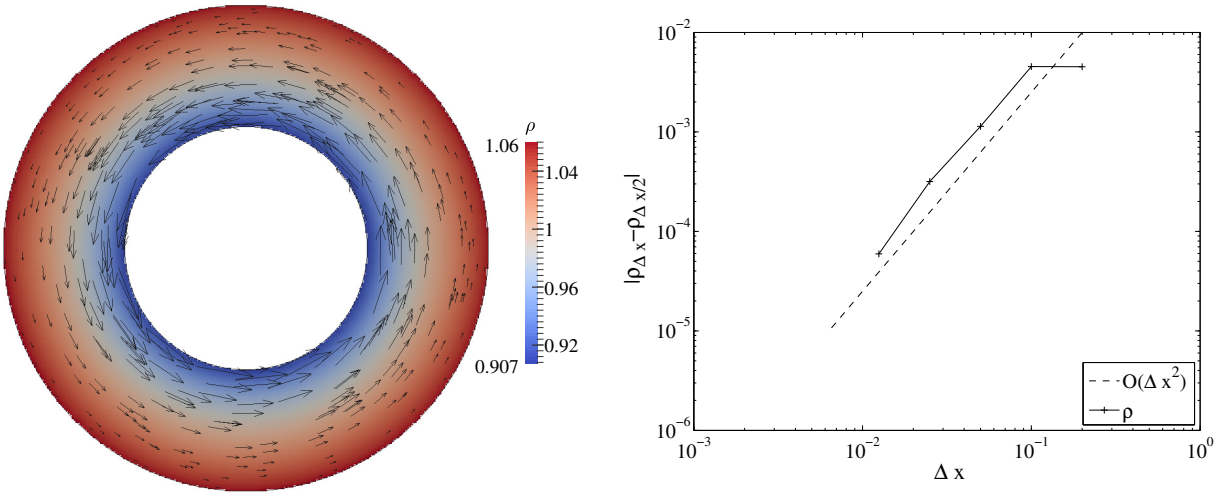

(a) Densità e vettore velocità.

(b) Errore.

Figure III.2: Soluzione stazionaria ed errore per il flusso di Couette (modello ES-BGK, $Kn = 10^{-2}$).

IV Ottimizzazione del tempo di calcolo

IV.1 Parallelizzazione

Per la parallelizzazione, l'uso di griglie cartesiane è un vantaggio. Il partizionamento del dominio è immediato poiché i sotto domini assegnati ai processori seguono la struttura della griglia. Gli

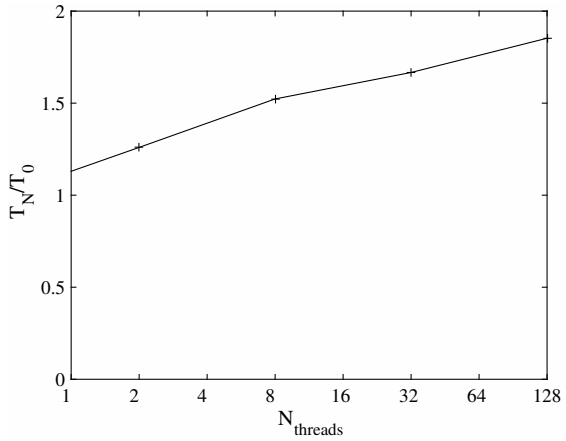

(a) Scalabilità debole : il numero di gradi di libertà è costante per processore.

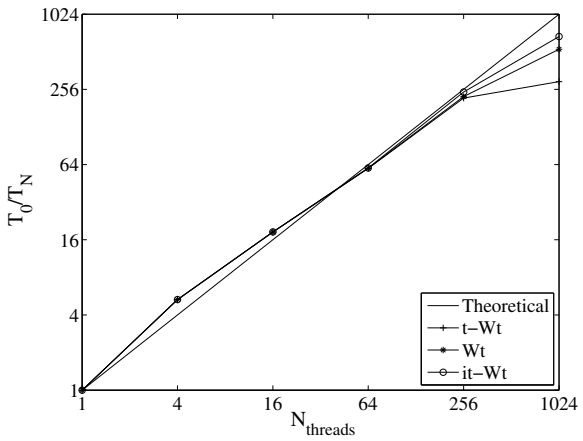

(b) Scalabilità forte : il numero di gradi di libertà è fisso per tutto il dominio.

Figure IV.3: Scalabilità.

schemi usati richiedono l'aggiunta di due strati di celle "ghost" in ciascuna direzione al fine di ottenere l'ordine due in spazio. Perciò, ogni processore comunica due strati di celle al processore vicino e vice versa.

I test di scalabilità mostrano una buona performance del codice. Per avere una buona scalabilità debole, il rapporto tra il tempo CPU su N processori e su un processore deve essere prossimo a 1 poiché il numero di gradi di libertà in questa valutazione è mantenuto costante per ogni precessore. Per valutare la scalabilità forte, il numero di gradi di libertà globale è tenuto fisso mentre il numero di processori viene aumentato. Per un'ottima scalabilità forte, la pendenza della curva in figure IV.3b dovrebbe essere 1. Nel nostro caso, otteniamo 0.7.

IV.2 Un approccio alle griglie locali

Un'altra possibilità per ridurre il costo computazionale è calcolare i flussi solo dove c'è informazione, ovvero dove il valore della funzione di distribuzione è non trascurabile. La griglia di velocità è creata all'inizio del conto su criteri globali sia in tempo che in spazio (velocità massima, temperatura minima). In certi casi, la griglia deve essere molto fine e estesa. In alcune zone del flusso, può risultare molto più larga del necessario. L'obbiettivo è quindi di estendere o di ridurre la zona della griglia dove i flussi vengono realmente calcolati ; i criteri usati sono gli stessi che hanno portato alla generazione della griglia globale ma utilizzando grandezze locale. Ad ogni passo di tempo, determiniamo i nodi della griglia globale che definiscono i estremi della griglia locale, ovvero, non generiamo una nuova griglia ma definiamo una restrizione della griglia globale come regione di interesse. Il vantaggio consiste nel fatto che nel calcolo del flusso per ogni velocità microscopica, non utilizziamo interpolazione ne tra le griglie di velocità ne tra i passi di tempo : se quella velocità microscopica è presente nella griglia locale, la funzione di distribuzione è nota, altrimenti il suo valore è 0. I criteri per costruire la griglia locale nel caso

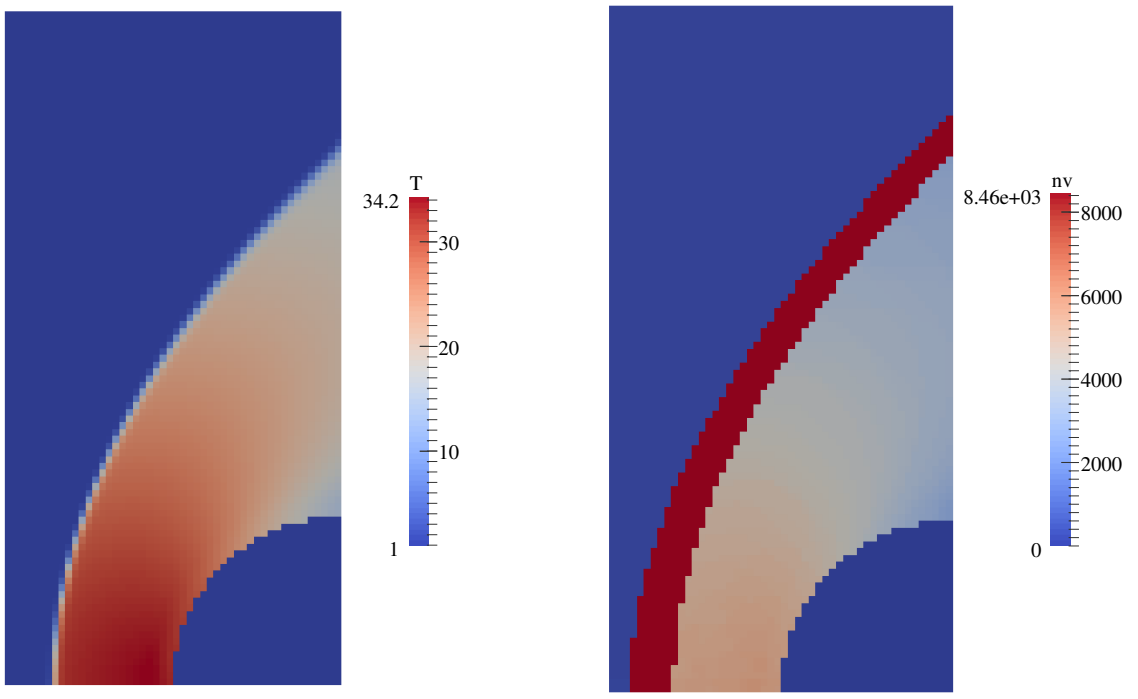

(a) Temperatura. (b) Numero di punti in velocità.

Figure IV.4: Soluzione stazionaria del Blunt body a Mach 10, $Kn_\infty = 10^{-5}$.

1D di una cella i sono :

$$\begin{aligned} &\xi_{u}{}^{i}_{min} = \xi_u^l \quad \text{tale che} \quad \xi_u^l = \max_{k\in[1,N_v]}(\xi_u^k \leq u_i - \alpha\sqrt{T_i}) \\ &\xi_{u}{}^{i}_{max} = \xi_u^l \quad \text{tale che} \quad \xi_u^l = \min_{k\in[1,N_v]}(\xi_u^k \geq u_i + \alpha\sqrt{T_i}) \\ &\frac{|\int_{\mathcal{G}_i^n} f_i^n d\xi_u - \int_{\mathcal{G}_i^{n-1}} f_i^n d\xi_u|}{\int_{\mathcal{G}_i^{n-1}} f_i^n d\xi_u} < tol \end{aligned} \tag{IV.16}$$

dove N_v è il numero di punti in velocità nella griglia in velocità globale (iniziale), α è un parametro di cui studiamo l'influenza e che dà la larghezza della griglia locale, $\mathcal{G}_i^n$ è la griglia in velocità al tempo t^n. I due primi criteri permettono di allargare o di ridurre la larghezza della griglia locale ad ogni passo di tempo. L'ultimo criterio controlla che non ci sia una perdita di informazione tra le griglie a due passi di tempo successivi.

Il passaggio a due o a tre dimensioni è immediato. L'algoritmo deve essere applicato direzione per direzione.

Sulla figura IV.4 vediamo la soluzione del Blunt body per la temperatura e il numero di punti in velocità usati in ogni griglia locale. L'errore relativa rispetto a un conto senza le griglie locale e il guadagno in tempo computazionale è mostrato sulla figura IV.5.

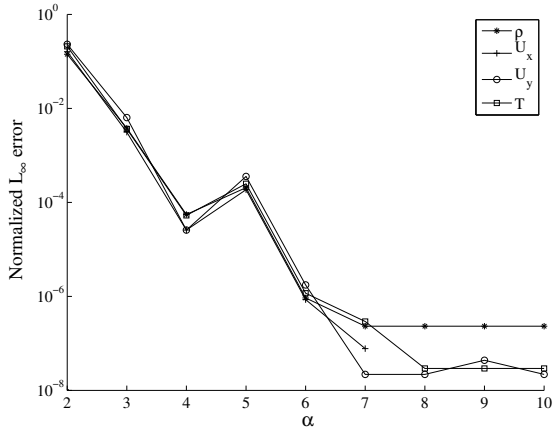

(a) Norma L_∞ dell'errore per la densità, la velocità e la temperatura.

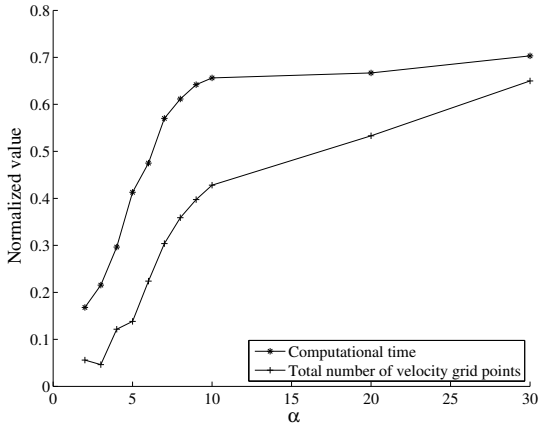

(b) Riduzione del costo di calcolo (rispetto al caso senza le griglie locale).

Figure IV.5: Errore e riduzione del tempo di calcolo per il caso del Blunt body a Mach 10.

V Metodo numerico per il trasporto di particelle in flussi rarefatti

Ci interessiamo adesso al caso test presentato in introduzione. Si tratta di simulare l'eiezione di particelle da un ugello in ambiente rarefatto. Abbiamo prima presentato i modelli cinetici usati per simulare questo tipo di flusso e come conservare la soluzione corretta nel limite idrodinamico anche in presenza di oggetti. Nel caso dell'ugello preservare il limite idrodinamico è indispensabile perché abbiamo sia il regime idrodinamico all'interno (dove la densità di gas è alta) che il regime rarefatto all'esterno dell'ugello dove il numero di Knudsen potrà andare fino a 10.

V.1 L'equazione di trasporto delle particelle

Consideriamo che il flusso di particelle solide è talmente diluito che non influenza il flusso di gas. Per questo motivo, il modello cinetico che governa il flusso non è modificato. E per lo stesso motivo, consideriamo particelle solide non collidono. Rappresentiamo il trasporto di queste particelle solide con un equazione di tipo Vlasov :

$$\frac{\partial f_p}{\partial t} + \nabla_{\mathbf{x}} \cdot \boldsymbol{\xi'} f_p + \nabla_{\boldsymbol{\xi'}} \cdot \mathbf{a} f_p = 0 \tag{V.17}$$

dove f_p è la funzione di distribuzione della densità di particelle, $\boldsymbol{\xi'}$ è la velocità microscopica delle particelle solide e $\mathbf{a}$ è un termine di accelerazione. I due modelli sono accoppiati tramite questo termine di accelerazione dovuto a una forza di resistenza $\mathbf{a} = D(\mathbf{U}_g - \boldsymbol{\xi'})$. $\mathbf{U}_g$ è la velocità macroscopica del gas e viene dal modello cinetico.

V.2 Il metodo numerico

Il metodo usato per risolvere il modello di trasporto delle particelle è basato su uno splitting tra il trasporto nello spazio fisico e il trasporto nello spazio delle velocità. Le particelle solide sono prima trasportate nello spazio fisico e poi, redistribuite sulla griglia cartesiana iniziale che coincide con la griglia usata per la risoluzione del modello cinetico. Successivamente, le particelle vengono trasportate nello spazio delle velocità e quindi redistribuite sulla griglia di

velocità. Rispetto ai metodi lagrangiani, ai metodi SPH (Smooth Particle Hydrodynamic) o ai metodi PIC (Particle-in-Cell), una griglia sola è memorizzata e non soffre del rumore stocastico dei metodi lagrangiani. Lo step di ridistribuzione delle particelle è illustrato figura V.6 in un caso 1D.

(a) Caso $\xi'_u > 0$ (b) Caso $\xi'_u < 0$

Figure V.6: Configurazione 1D dopo una tappa di trasporto nello spazio fisico (comportamento simile nello spazio delle velocità con $\xi'_u \equiv a_u$)

La scelta del nucleo di interpolazione è importante. Nel nostro caso, deve conservare la positività della funzione di distribuzione è redistribuire le particelle nello stesso posto se la loro velocità è 0. Il miglior compromesso è stato trovato con la seguente funzione Λ_1 :

$$\Lambda_1 = \begin{cases} \alpha = 1 - y \\ \beta = y \end{cases} \tag{V.18}$$

dove y è definito dalla figura V.6 come :

$$\begin{cases} y = \dfrac{x_p - x_i}{\Delta x} & \text{se} \quad \xi'_u > 0 \\ y = \dfrac{x_p - x_{i-1}}{\Delta x} & \text{se} \quad \xi'_u \leq 0 \end{cases}$$

V.3 Caso dell'ugello

Dopo una validazione su casi test analitici, abbiamo applicato il metodo al caso test dell'ugello. Consideriamo un ugello 2D e il suo getto rappresentati da una funzione levelset la quale è quindi trasportata alla velocità del gas eiettato. La geometria è presentata in figura V.7

Il rapporto di pressione tra la pressione d'adattamento nota P_c dell'ugello (che non dipende dalla pressione esterna all'ugello ma solo dalla geometria e dalle condizioni all'ingresso) e la pressione all'esterno dell'ugello P_{atm} è imposto. Più questo rapporto è alto, più la rarefazione

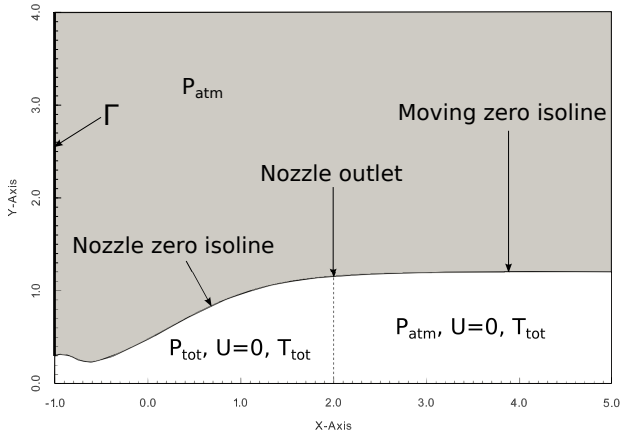

Figure V.7: Configurazione iniziale del dominio di calcolo per la simulazione del caso dell'ugello.

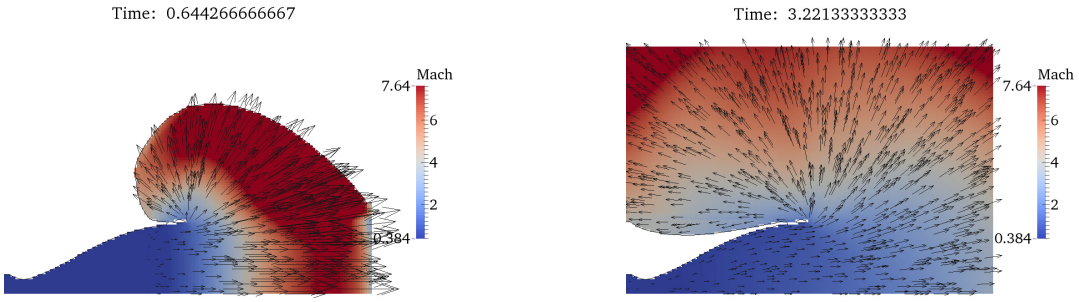

(a) $t = 0.64$

(b) $t = 3.22$

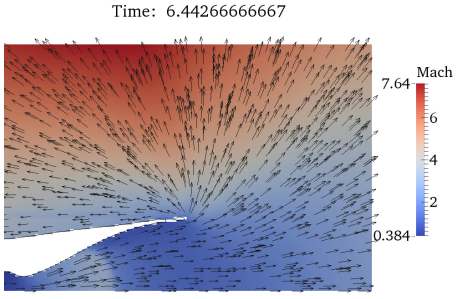

(c) $t = 6.44$

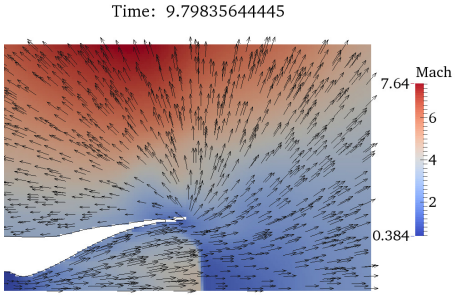

(d) $t = 9.8$

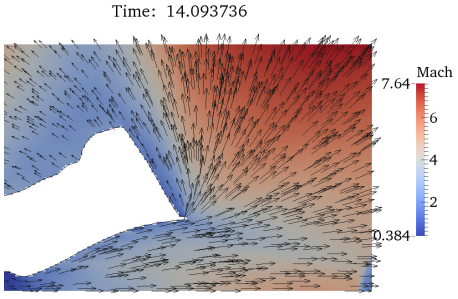

(e) $t = 14.09$

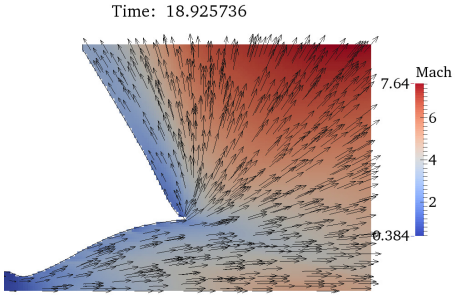

(f) Stato stazionario

Figure V.8: Numero di Mach e vettori velocità per $P_c/P_{atm} = 200000$ con il modello BGK.

in uscita dell'ugello è importante. In quel caso, osserviamo che, durante il transitorio, il getto torna indietro verso le pareti esterne dell'ugello fino all'ingresso, stabilizzandosi successivamente e creando un angolo con l'ugello che può essere maggiore di 90 gradi.

Il regime transitorio è presentato in figura V.8. Il modello accoppiato permette di quantificare il numero di particelle (figura V.9) che impatta la zona sopra l'ingresso dell'ugello, che corrisponde in un caso reale alla posizione dei dispositivi ottici.

Conclusione

In questa tesi, abbiamo sviluppato metodi per la risoluzione di flussi complessi su griglia cartesiana. Abbiamo cercato di riprodurre fenomeni ancora poco conosciuti e difficili da riprodurre in condizione sperimentali come il caso test della contaminazione di dispositivi ottici dovuta all'eiezione di particelle solide da motori di satelliti.

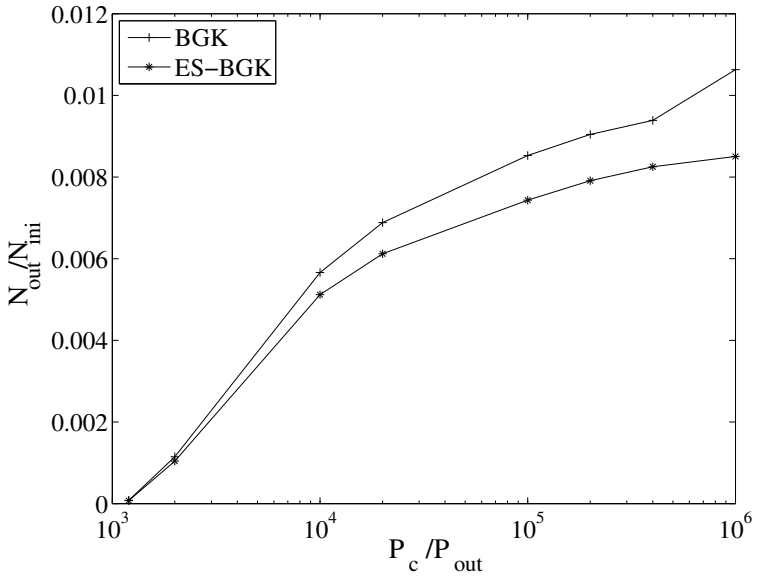

Figure V.9: Numero di particelle uscente del dominio sopra l'ingresso dell'ugello.

Possiamo estrarre tre contributi principali. Il primo riguarda il comportamento degli schemi per modelli cinetici nel limite idrodinamico. Abbiamo proposto una nuova condizione a parete che rispetta le proprietà asintotiche verso le equazione di Eulero della soluzione per i modelli BGK e ES-BGK. Questo comportamento è indispensabile per trattare flussi dove sono presenti sia il regime idrodinamico che il regime rarefatto in presenza di solidi immersi. Questa nuova condizione al contorno è stata integrata in uno schema al secondo ordine su griglia cartesiana.

Abbiamo poi sfruttato il vantaggio delle griglie cartesiane per il calcolo parallelo in modo da ridurre il costo computazionale. In questo stesso senso, è stato sviluppato un approccio alle griglie locali in velocità. Sono stati ottenuti risultati interessanti con una riduzione del tempo computazionale fino all'80%.

Il terzo contributo riguarda l'accoppiamento dei modelli cinetici con un modello di trasporto di particelle. Sono stati proposti un metodo di risoluzione per risolvere l'equazione di tipo Vlasov e una prima spiegazione nel fenomeno di contaminazione dei dispositivi ottici su satellite.

Grazie a questi metodi particolarmente adatti a contesti di calcolo HPC (High Parallel Computing), è stato possibile realizzare simulazione 3D. In futuro, ci proponiamo di introdurre modelli cinetici più complessi per gas poliatomici o con diverse specie chimiche al fine di paragonare i risultati numerici con dati sperimentali. Inoltre, ci prefiggiamo un intervento sulla riduzione del impronta di memoria. In fine, sarà nostro obbiettivo completare il modello di trasporto di particelle con un termine di collisione e con un termine d'interazione delle particelle/gas nel modello cinetico.

Résumé

Dans cette thèse, nous nous sommes interessés à des écoulements complexes où les régimes hydrodynamique et raréfiés coéxistent. On retrouve ce type d'écoulements dans des applications industrielles comme les pompes à vide ou encore les rentrées de capsules spatiales dans l'atmosphère, lorsque la distance entre les molécules de gaz devient si grande que le comportement microscopique des molécules doit être pris en compte. Pour ce faire, nous étudions 2 modèles de l'équation de Boltzmann, le modèle BGK et le modèle ES-BGK. Dans un premier temps, nous développons une nouvelle condition au bord permettant une transition continue de la solution du régime raréfié vers le régime hydrodynamique. Cette nouvelle condition permettant de préserver l'asymptotique vers les équations d'Euler compressible est ensuite incluse dans une méthode de frontière immergée pour traiter, à une précision raisonnable (ordre 2), le cas de solides immergés dans un écoulement, sur grilles cartésiennes. L'utilisation de grilles cartésiennes permet une parallélisation aisée du code de simulation numérique afin d'obtenir une réduction considérable du temps de calcul, un des principaux inconvénients des modèles cinétiques. Par la suite, une approche dites aux grilles locales en vitesses est présentée réduisant également le temps de calcul de manière importante (jusqu'à 80%). Des simulations 3D sont également présentées montrant l'efficacité des méthodes. Enfin, le transport passive de particules solides dans un écoulement raréfié est étudié avec l'introduction d'un modèle de type Vlasov couplé au modèle cinétique. Grâce à une résolution basée sur des méthodes de remaillage, la pollution de dispositif optiques embarqués sur des satellites dues à des particules issues de la combustion incomplète dans les moteurs contrôlant d'altitude est étudiée.

Abstract

This work is devoted to the study of complex flows where hydrodynamic and rarefied regimes coexist. This kind of flows are found in vacuum pumps or hypersonic re-entries of space vehicles where the distance between gas molecules is so large that their microscopic behaviour differ from the average behaviour of the flow and has be taken into account. We then consider two models of the Boltzmann equation viable for such flows: the BGK model dans the ES-BGK model. We first devise a new wall boundary condition ensuring a smooth transition of the solution from the rarefied regime to the hydrodynamic regime. We then describe how this boundary condition (and boundary conditions in general) can be enforced with second order accuracy on an immersed body on Cartesian grids preserving the asymptotic limit towards compressible Euler equations. We exploit the ability of Cartesian grids to massive parallel computations (HPC) to drastically reduce the computational time which is an issue for kinetic models. A new approach considering local velocity grids is then presented showing important gain on the computational time (up to 80%). 3D simulations are also presented showing the efficiency of the methods. Finally, solid particle transport in a rarefied flow is studied. The kinetic model is coupled with a Vlasov-type equation modeling the passive particle transport solved with a method based on remeshing processes. As application, we investigate the realistic test case of the pollution of optical devices carried by satellites due to incompletely burned particles coming from the altitude control thrusters.